NORTHWESTERN UNIVERSITY

Surface Stabilization Mechanisms in Metal Oxides

A DISSERTATION

SUBMITTED TO THE GRADUATE SCHOOL
IN PARTIAL FULFILLMENT OF THE REQUIREMENTS

for the degree

DOCTOR OF PHILOSOPHY

Field of Materials Science and Engineering

By

Andrés Enrique Becerra Toledo

EVANSTON, ILLINOIS

December 2011

ABSTRACT

Surface Stabilization Mechanisms in Metal Oxides

Andrés E. Becerra Toledo

Metal oxide surfaces play a central role in modern applications, ranging from heterogeneous catalysis to electronic devices, yet little is known about the processes determining their structural stabilization. Several such stabilization mechanisms are explored via a combination of theoretical and experimental methods. The processes of periodic reconstruction, adsorption and segregation are studied through case studies of model material systems.

The evaluation of structural models of periodic $SrTiO_3(001)$ reconstructions via bonding analysis and simulated scanning tunneling microscopy images supports the family of "DL" models terminating in two consecutive layers of TiO_2 composition, and discards alternative proposals such as the models based on periodic Sr adatoms.

Experimental and simulated scanning tunneling microscopy images and complementary spectroscopic data are used to determine the structure of linear Ti-rich $SrTiO_3(001)$ nanostructures. The structural solution exemplifies the recurrence of locally stable motifs across numerous surfaces. In particular, the arrangement of edge-sharing TiO_5 surface polyhedra is a trait is shared by (001) nanostructures and DL reconstructions. This is a flexible framework which allows for optimal bonding in surface atoms.

Modeling of water adsorption on reconstructed $SrTiO_3(001)$ surfaces reveals that water plays two major roles in the stabilization of oxide surfaces: it may mediate the formation of certain ordered structures, or it may be part of the ultimately stable structures themselves. This

can be understood in terms of the inevitable presence of chemisorbed water on defective surfaces. Since the surface mobility of cationic species is relatively low, the kinetics associated to water diffusion and desorption dominate the surface ordering process.

High-temperature annealing of $SrLaAlO_4$ single crystals leads to the segregation of SrO to the surfaces, in the form of islands. This process is in fact a bulk stabilization mechanism, due initially to the increasing number of bulk Sr-O vacancy pairs. This material enables a second accommodation mechanism for further surface segregation and increasing bulk non-stoichiometry, consisting of the formation of low-energy stacking faults. In spite of previous speculation of a similar fault-based compensation process taking place in $SrTiO_3$, this is found to be decidedly unviable in perovskite systems.

Approved by

Professor Laurence D. Marks

Department of Materials Science and Engineering

Northwestern University, Evanston, IL 60208, U.S.A.

Acknowledgments

I must start by thanking the Boss, Professor Laurie Marks, for his insight, guidance and encouragement throughout my years at Northwestern. Thanks for being what a Ph.D. advisor should be, and for knowing what a graduate student should learn and do.

I would like to thank all the other members of my dissertation committee for the time invested and support: Professor Scott Barnett, Professor Donald Ellis and Professor Mark Hersam. Similarly, I cannot forget Professor Randall Snurr, who jumped aboard my qualification examination committee a few years ago on short notice.

I am also very grateful to my collaborators at the University of Oxford: Professor Martin Castell and now-Dr. Matthew Marshall. They provided the scanning tunneling microscopy, Auger electron spectroscopy and X-ray photoelectron spectroscopy data for Chapter 4. It was a pleasure to host Matt for a couple of weeks in Evanston and to make a good friend.

I would also like to thank the staff at the Electron Probe Instrumentation Center at Northwestern University, in particular Dr. Shuyou Li and Dr. Jinsong Wu, for their help with the electron microscopes and sample preparation instruments. I am also indebted to the staff at the Department of Materials Science and Engineering, especially to Ms. Peggy Adamson, who was always happy to help despite being swamped by similar requests from every other student in the department.

I sincerely appreciate the access to the Carbon High-Performance Computing Cluster at the Argonne National Laboratory and to the Quest computing cluster, administered by Northwestern University Information Technology, which were of great use for many demanding

calculations. Similarly, I must profusely thank the United States government for funding my research through the Department of Energy and the National Science Foundation.

I thank all members (past and present) of the Marks research group, for their friendship, wisdom and open minds. Special thanks go to: Yingmin, Courtney, Jim C, Jim E and Brian, for teaching me how to use and maintain SPEAR; Jim Ciston, for leading the group by example, making me dread the day he graduated; Jim Enterkin, for the experimental work that served as complement to some of my computational results; Dani, for her help and shared memories of overlapping projects; Ariel, Emilie and Yifeng, for listening and sharing, and being great fun. Best of luck, and many thanks to those still in their early years, for making me feel useful: Yuyuan, Chuandao and Shuangping.

I am also very thankful for the other many friends I have made while at Northwestern, who helped me enjoy the grad school experience. At the risk of forgetting someone, and in no particular order, these are some of them: Nikhil, Kevin, Eddie, Kunal, Joe, Alix, Kvar, Aurora, Ryan, Danielle, Hunter, Daniel, Alicia, Praneet, David, Katie, Sheldon, Alex, Mitch, Ted, Nicola and Arpun.

I must thank my family for their enduring support and love, for listening and caring, and for sharing the sacrifice of long goodbyes and infrequent get-togethers. The partial exception was Gabriel, who came to Evanston more often than I went to Madison, which I truly appreciate.

Finally, a deep thank-you to Diana, for teaching me something new every day and making these the very best years of my life.

List of Abbreviations

AES	Auger electron spectroscopy
AFM	atomic force microscopy
APW+lo	augmented plane wave plus local orbital
BHF	buffered NH_4:HF solution
BVS	bond valence sum
CIF	Crystallographic Information File
DFT	density functional theory
DL	double layer
EDX	energy-dispersive X-ray spectroscopy
GII	global instability index
HREM	high-resolution electron microscopy
ICP-AES	inductively coupled plasma atomic emission spectrometry
LEED	low-energy electron diffraction
ML	monolayer
PIPS	precision ion polishing system
RHEED	reflection high-energy electron diffraction
RP	Ruddlesden-Popper
RT2	$(\sqrt{2}\times\sqrt{2})R45^{\circ}$
RT5	$(\sqrt{5}\times\sqrt{5})R26.6^{\circ}$
RT13	$(\sqrt{13}\times\sqrt{13})R33.7^{\circ}$

SCF	self-consistent field
SEM	scanning electron microscopy/microscope
SII	surface instability index
SIMS	secondary ion mass spectroscopy
STEM	scanning transmission electron microscopy/microscope
STM	scanning tunneling microscopy/microscope
TCS	TiO_2 crystallographic shear
TED	transmission electron diffraction
TEM	transmission electron microscopy/microscope
UHV	ultra-high vacuum
xc	exchange-correlation
XPS	X-ray photoelectron spectroscopy
XRD	X-ray diffraction

Table of Contents

List of Tables

List of Figures

Depth must be hidden. Where? On the surface.
Hugo von Hofmannsthal

In science there are no 'depths'; there is surface everywhere.
Rudolf Carnap

Chapter 1. Introduction

1.1. Motivation

Metal oxides are underappreciated in a modern world which depends heavily on them. They find use in heterogeneous catalysis, sensing, fuel cells, thin film growth and (increasingly so) in electronic devices, among other practical applications. Heterogeneous catalysts increase the efficiency and selectivity of chemical reactions, enabling the affordable synthesis of medical drugs, structural materials and fuels, among countless essential products. Moreover, metal oxide catalysts are routinely used in order to reduce air and water pollution [1]. Naturally, their usefulness crucially depends on their surface, as the catalytic process occurs at the interface of the solid catalyst with the liquid or gaseous medium. Meanwhile, as the characteristic dimensions of other technological devices continue to shrink, the ratio of surface area to bulk volume increases, so even for technologies in which performance is dictated by bulk properties,

surface effects become increasingly significant. Therefore, the focus of this work is on metal oxide surfaces.

In order to do fundamental materials science, by searching for structure-property relations, the structure must of course be known, not guessed. This truth extends into the realm of surface science, but often bulk-like truncations are assumed for metal oxides surfaces when interpreting experimental data or modeling surface phenomena, such as the interaction with adsorbates.

In reality, surface atoms in solids often behave differently from atoms deep in the bulk, since they are subject to different boundary conditions or environments. Surface atoms in bulk-like positions are likely to be undercoordinated and possess "dangling" bonds, so the simplistic truncations are often unstable. Noguera identifies three main stabilization mechanisms for polar oxide surfaces [2], but these are generally applicable to all oxide surfaces:

1. The redistribution of atoms at the surface, typically producing a surface stoichiometry unlike the bulk;
2. The adsorption of foreign species from the environment; and,
3. The redistribution of the electron density, accompanied by minor atomic relaxation.

In this dissertation, various stabilization mechanisms in metal oxides are studied via a combination of experimental and computational methods. Case studies for each of the following surface processes will be presented: periodic reconstruction, surface segregation, and water adsorption. The first two are examples of atomic redistribution, with segregation being a more drastic process involving significant bulk diffusion. The case study for the third process, water adsorption, also considers periodic reconstruction.

There are two main objectives for the present work: first, the identification of stable surface structures resulting from the aforementioned processes, through examination of model material systems; and second, the development of a basic understanding of the driving forces behind the formation of specific surface morphologies.

These two objectives are crucial steps towards two longer-term goals which are beyond the scope of this work. One of these goals is to comprehend how particular surface structures affect the properties and performance of a material for a given application; for example, a structural feature may enhance the catalytic performance of a surface for a specific chemical reaction. The other ultimate goal is to be able to engineer surfaces by deriving predictive rules that enable surface optimization for particular applications, thereby exploiting the entire materials science paradigm that connects processing, structure, property and performance.

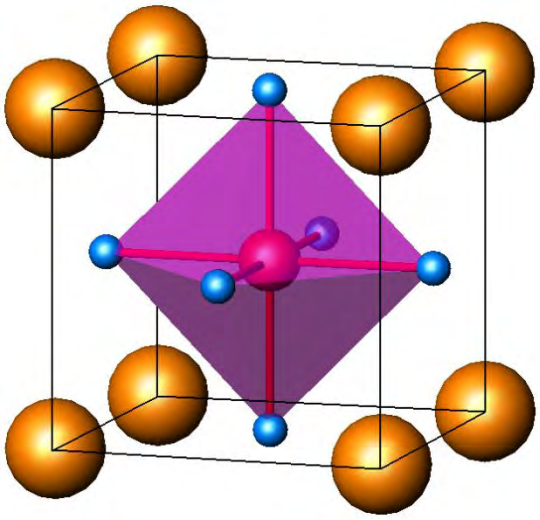

Fig. 1.1. $SrTiO_3$ perovskite structure.
Sr in orange, Ti in red at the centered of polyhedron in coordination to six O atoms (in blue).

The main material studied in this work is strontium titanate ($SrTiO_3$). This versatile oxide has the potential for use in a wide range of technological applications. For example, it has been used as a substrate for thin film growth of high-T_c superconducting cuprates and other ceramics, due to good lattice matching, especially with its (001) surface [3-5]. Also, it has been exploited as a catalytic support, for example for Pt nanoparticles for hydrocarbon combustion [6, 7]. In fact, it is a catalytic material itself, with demonstrated use for the photocatalytic splitting of water molecules to generate hydrogen fuel and gaseous oxygen [8-12].

Recently, $SrTiO_3$ has also evolved as a cornerstone material in the novel field of oxide-based electronics [13]. This is largely due to the observed formation of a 2-dimensional electron gas at the cleaved (001) surface [14, 15] and also at interfaces with other oxides such as $LaAlO_3$ [16, 17], which allows for the design of devices based on heterostructures. Additionally, the crystalline strontium titanate has been used as a buffer dielectric interfaced to Si in Si-based electronics due to its large dielectric constant, which allows for the construction of nanoscale devices [18-20]. This buffer layer can also act as an interface between Si and GaAs, which can be epitaxially grown on $SrTiO_3$ [21-23].

Further practical applications include use of its ordered, nanostructured (001) surfaces as templates for the self-assembly of molecules [24, 25], as an oxygen gas sensor [26-28] and as an anode material in Li-ion batteries and solid-oxide fuel cells [29-31]. Most importantly in the context of this dissertation, it is regarded as the archetypal perovskite oxide and it shall be treated as a model system not only for this family of materials, but also for the broader class of metal oxides with mixed cation valence states. At room temperature, $SrTiO_3$ adopts the perovskite structure, generally defined by the formula ABO_3 and by a cubic unit cell with a Ti atom at its

center (B site), Sr atoms at the corner site (A site), and O atoms at the face-centered positions (see Figure 1.1); this results in alternating SrO and TiO_2 (001) planes.

The performance of strontium titanate in almost every technological application listed above is critically dependent on its surface structure. This dissertation will focus on its (001) surface, which is the most technologically relevant orientation and is expected to dominate in nanoparticles. Moreover, a wealth of literature on the $SrTiO_3$(001) system exists, which can be exploited. For example, numerous periodic reconstructions and nanostructures have been observed and characterized on this surface, which allows for the realistic modeling of adsorption processes. Also, (001) stacking faults define the non-stoichiometric phases that will play a large role in segregation processes that will be discussed in Chapter 6.

A more complex oxide, strontium lanthanum aluminate ($SrLaAlO_4$), will also be explored, in the specific context of surface segregation. As detailed in Chapter 6, the crystal structure of this material is an intergrowth of perovskite and rocksalt layers and is isostructural with a secondary strontium titanate phase, Sr_2TiO_4. Experimental observations in $SrLaAlO_4$ will be discussed in the context of some of the literature on $SrTiO_3$.

1.2. Organization

The present dissertation is structured as follows:

Chapter 2 describes the experimental and computational techniques used in the work detailed in subsequent chapters. Some general background concepts are also introduced. The next four chapters will explore the stabilization mechanisms of metal oxide surfaces, largely in the form of case studies.

Chapter 3 discusses the numerous periodic surface reconstructions for the $SrTiO_3$(001) orientation. First-principles simulations of scanning tunneling microscopy (STM) images and bonding analysis serve as tools to evaluate structural models that have been proposed as alternatives to the double-layer (DL) TiO_2 models derived from diffraction data.

In Chapter 4, simulated STM micrographs are again used in combination with supporting experimental data to decipher the atomic-level structure of the so-called $SrTiO_3$(001) nanolines and related defects. These large-periodicity nanostructures are found to exploit the same characteristic structural motif found in the c(4×2) surface reconstruction.

In Chapter 5, the issue of water adsorption on the TiO_2-rich DL $SrTiO_3$(001) reconstructions is addressed using density functional theory. The thermodynamics of bare and hydrated structural models are presented and STM image simulations are generated for comparison to experiment. Taking into account the surface interaction with water vapor solves several longstanding puzzles regarding the presently accepted structural solutions.

Chapter 6 explores the topic of surface segregation in mixed-metal oxides, and in particular in the perovskite-like $SrLaAlO_4$ oxide. The segregation of rocksalt SrO to (100) and (001) surfaces is reported and characterized, and it is explored in conjunction with the appearance of stacking faults in the bulk. It is argued that this phenomenon must be driven by the configuration entropy of bulk defect formation and explore this idea in the context of $SrTiO_3$ surfaces.

The seventh chapter summarizes the findings in this work and discusses several avenues for future related research. Several appendices follow; the most important one outlines the theory behind (and the implementation of) the high-bias STM image simulations.

A determined soul will do more with a rusty monkey wrench
than a loafer will accomplish with all the tools in a machine shop.
Robert Hughes

Chapter 2. Methods and General Background

This chapter describes in detail the different techniques, both experimental and theoretical, which have been used to gather the results described in the following chapters. Further information specific to particular chapters will be specified there. Also, some notation and concepts which are important throughout the rest of this dissertation are introduced.

2.1. Experimental Techniques

2.1.1. Transmission Electron Microscopy and Diffraction

By analogy to an optical microscope, which lets us observe the interaction of matter with light, a transmission electron microscope (TEM) allows us to see the interaction of matter with electrons. The typical setup of a TEM is shown schematically in Figure 2.1. In essence, it produces an electron beam which is directed towards the sample, while several magnetic lenses are used to guide and focus the beam.

The biggest advantage of a TEM over an optical microscope is its spatial resolution. While the resolution attainable in optical microscopy is comparable to the wavelength of visible light (in the order of 500 nm), modern TEMs can routinely resolve individual atomic columns; at present, the best achieved resolution is around 0.5 Å [32]. As the name implies, TEM works in transmission mode, meaning that the electrons going through the sample are detected. Therefore, thin, electron-transparent specimens are necessary, which often requires potentially invasive preparation steps (more on that below).

Another big advantage of using a TEM is the ability to switch back and forth between the real-space imaging and diffraction modes. Transmission electron diffraction (TED) is a very useful technique in itself, as the resulting two-dimensional patterns yield information on the crystallography of the illuminated area, or lack thereof. Moreover, TED enables the formation of bright and dark field images. This is done by inserting an objective aperture and blocking a portion of the diffraction pattern (see Fig. 2.1). Upon switching to imaging mode, an image different from the unfiltered case is seen, arising only from allowed beams. If only the direct beam is allowed, then this corresponds to a bright-field image, whereas if it is blocked, a dark-field image is seen. The choice of image can help enhance and identify the type of contrast observed.

TEM is not conventionally thought of as being a surface-sensitive technique; since the collected electrons have gone through the specimen of interest, typically it is the bulk information that dominates. Traditionally, TEM has been used extensively to observe and examine bulk defects. However, it has found much use in surface studies, allowing for surface structures to be observed in profile view (orientations perpendicular to zone axis) [33] or in plan view if the sample is very thin (see, for example, Ref. [34]). Moreover, transmission electron

diffraction (TED) can be used to monitor the formation of non-bulk structural periodicities at the surface, as this will result in the appearance of low-intensity spots in the diffraction pattern, in addition to the bright bulk reflections. Since the energy of the electrons is much larger than in reflection-mode diffraction techniques, TED data is much more kinematical (closer to a single scattering event per electron), which makes it more suitable for structure determination efforts. Further details on this technique may be found in Ref. [35].

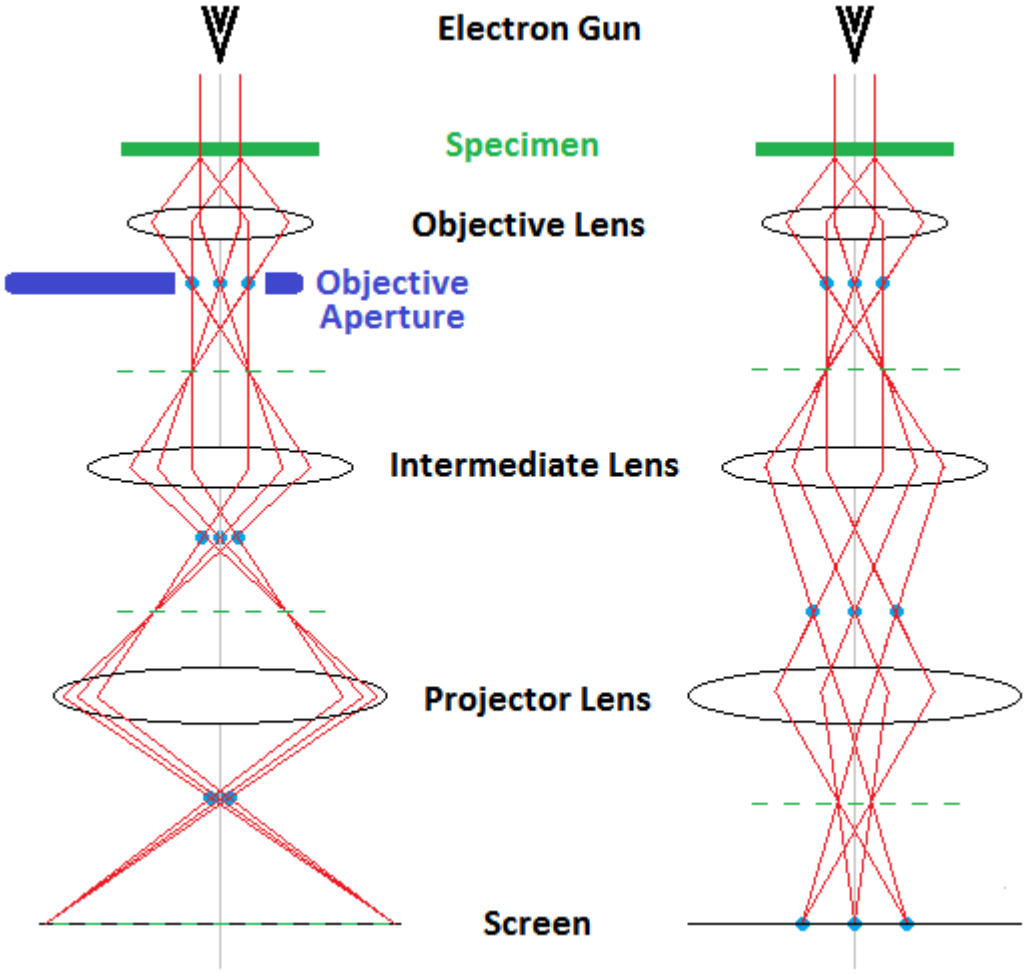

Fig. 2.1. Schematic representation of the two basic TEM operation modes: (left) real-space imaging and (right) diffraction. Parallel-beam illumination is attained with condenser lenses, not shown here. Light blue circles denote planes of focused diffraction patterns, while dashed green lines denote planes of focused real-space imaging. Adapted from Ref. [35].

For the particular case of TEM studies of oxide surfaces, relevant to this dissertation, the most convenient experimental approach is to examine one particular crystallographic orientation in a material. Therefore, a single-crystalline sample must be grown or purchased; in the experimental work of this dissertation, the latter was chosen, with each crystal wafer being roughly 0.5 mm thick. Since TEM sample holders have standardized 3 mm slots, disks of this diameter must be cut out of the wafer. In order to get areas that are electron transparent, while still allowing for the easy manipulation of a self-supporting TEM sample, the center of the crystal must be thinned. This is done in three steps: mechanical polishing, dimple polishing and low-angle ion milling. This process will be described in more detail where relevant.

2.1.2. Scanning Transmission Electron Microscopy

Scanning transmission electron microscopy (STEM) is a special operation mode of TEM. Certain microscopes are equipped with this capability, while others are designed to be used in STEM mode only. Unlike the traditional parallel beam illumination mode, STEM uses a converged probe which is rastered across a specified area of the sample. This allows for different types of data to be obtained, with good control of the sample area being probed.

In terms of imaging, there are generally two simple detection modes. One is bright-field imaging, where the electrons in the direct beam are detected and counted for a given position of the beam on the sample, which defines a pixel in the final image. The image is then composed by the intensity at each pixel; of course, vacuum appears bright in this case. The other is high-angle annular dark-field imaging, where an annular electron detector is used to integrate the number of electrons scattered at significantly large angles with respect to the optic axis. The intensity in this case is proportional to the mass density seen by the beam, so heavier elements

will scatter more strongly and appear brighter than lighter elements. Therefore, these images are also referred to as *Z*-contrast images (as in *Z*, the atomic number). Vacuum appears dark in this mode.

STEM has also great use for spectroscopic techniques. The most relevant example is energy-dispersive X-ray spectroscopy (EDX, see subsection 2.1.4), which can be performed in STEM mode, measuring chemical composition as a function of position. This allows for elemental line scans or area maps. For this application, the X-ray detector is placed near the sample.

2.1.3. Scanning Electron Microscopy

Scanning electron microscopy (SEM) is qualitatively similar to STEM, in that a focused electron beam is rastered across an area. However, it does not work in transmission mode; instead, it has two modes of operation. The most common one is the secondary-electron detection mode. As the name implies, it consists of the detection of electrons ejected due to the high energy of the incoming electron beam. Secondary electrons must overcome the ionization potential, so they will in general have relatively low kinetic energies. That means that most secondary electrons from atoms buried deep below the surface will never be detected, as they are more likely to be stopped by other matter. Therefore, detected secondary electrons mostly originate from the surface or near-surface regions, so this operation mode yields mostly topographical information. This was the imaging mode used in the SEM work presented in this dissertation.

The alternative detection method is the backscattered electron (BSE) mode. Backscattered electrons are a result of elastic scattering and are therefore more energetic than

secondary electrons. Of course, heavy nuclei backscatter more electrons, so the contrast in BSE image correlates with the density of the material.

SEM imaging of insulating samples (such as ceramic oxides) can be problematic, as it is easy for them to accumulate charge; this can be avoided by applying a thin coat of gold on the sample. EDX can also be easily implemented inside an SEM, although the spatial resolution is lower than in a TEM. Charging can distort the EDX results, but this can be remedied by using a low accelerating voltage.

2.1.4. Energy-dispersive X-ray Spectroscopy

Energy-dispersive X-ray Spectroscopy (EDX) is a chemical characterization technique which can be implemented with an electron beam, although other irradiation sources can be used. Within each atom in the specimen, electron irradiation temporarily excites electrons to higher-energy states (or ejects them). An excited electron will eventually drop back to a state of lower energy and, in accordance to the principle of energy conservation, will in the process emit an X-ray of energy equal to the energy it loses, which is defined by the specific levels involved in the transition. Since each element has a unique set of energy transitions, the X-ray intensity plotted as a function of energy acts as a chemical signature. EDX, therefore, can be used to figure out which elements are present in a specimen. Quantification of element concentration is also possible. As a caveat, however, it is well known that EDX-based quantification of light elements (notably hydrogen, oxygen, carbon) is not very reliable.

Since EDX can use an electron source, it can be implemented both in a TEM, as well as in a SEM. Area and line scans can be performed inside a TEM when using the STEM mode.

The former allows for the generation of elemental maps, while the latter allows for a linear profile, which is especially useful for interfaces.

2.1.5. Inductively Coupled Plasma Atomic Emission Spectrometry

An inductively coupled plasma (ICP) is an argon plasma that is sustained via a magnetic field produced by a radiofrequency induction coil, after being initially ignited with a Tesla coil [36]. The ICP-based atomic emission spectrometry capability allows for the detection of trace metals and for very accurate stoichiometry determination. For this, the plasma excites electrons from the sample and the subsequent de-excitation yields photons with energies characteristic to the element of origin. This is similar to EDX, except for the energy source (plasma, not electrons). The other large difference is the form of the sample. The specimen to be analyzed must be in aqueous solution. In the case of a solid oxide, it must be dissolved completely in a suitably chosen acid. A suspension does not work, as there is no guarantee that all cations have been dissolved proportionally. The liquid is then fed through a nebulizer directly into the plasma, where it is fully atomized at high temperatures and the electronic excitation occurs. Of course, this is a destructive technique, so a representative specimen is necessary for accurate results.

The stoichiometry quantification requires the careful calibration of the equipment. This can be done by using commercially available standard solutions for each element in question. When dissolving the sample of known mass in a given solvent volume, one should be able to estimate the expected concentration of each element. Therefore, calibration solutions should be prepared spanning a wide range of concentrations (for each element) around the estimated values. Further details on ICP-AES may be found in Ref. [37].

2.1.6. X-ray Photoelectron Spectroscopy

X-ray photoelectron spectroscopy (XPS) is in a way the opposite of EDX, in that the incident radiation is an X-ray beam (not electrons) and the detected particles are electrons (not X-rays). The physical process involved is somewhat different, however. Monochromatic X-rays generated from a characteristic transition of one material (typically Al K_α) irradiate the sample, causing some electrons to be ejected, provided enough energy has been transferred to them to overcome their binding energy. These so-called photoelectrons are the particles of interest. Within the detector, the photoelectrons are sorted by kinetic energy. In general, however, the energy distribution is not plotted in terms of the kinetic energy (E_K) of the photoelectrons, but instead as a function of their binding energy (E_B). These are related by the equation

$$E_\mathrm{B} = h\upsilon - E_\mathrm{K} - \phi_s, \qquad \text{(Eq. 2.1)}$$

where $h\upsilon$ is the (known) energy of the X-rays and ϕ_s is the workfunction of the spectrometer [38].

Binding energies are a chemical signature of particular orbitals for particular elements, and since these are independent of the X-ray energy, they are more meaningful than kinetic energies. XPS, therefore, allows us to identify which elements are present. Moreover, XPS provides information on the chemical environment of each element. Let us take, for example, the case of titanium. When in a 4+ valence state, Ti electrons are attracted more strongly to the nucleus than when Ti is in a metal, so the peak will be shifted towards higher binding energy. Similarly, the presence of O–H bonds on an oxide surface will give rise to a high-binding-energy shoulder in the main O-1s peak [39-42], which is important in the context of water adsorption.

This brings us to the fact that XPS is a very surface-sensitive technique. Since the escape path of an electron in a solid is typically under 10 nm, the detected electrons originate from the surface or the near-surface region. Moreover, one may change the detector position towards a more grazing collection angle (that is, closer to being parallel to the surface plane) to increase the effective escape path and therefore also the surface sensitivity. Comparing the signal intensity ratio of two elements between two different collection angles can therefore reveal whether or not a particular species is enriched or depleted at the surface. Further details on this technique can be found in Ref. [38].

2.1.7. Auger Electron Spectroscopy

Auger electron spectroscopy (AES) exploits a different de-excitation mechanism (following the excitation/ejection of an electron due to incident radiation) than EDX. Once another electron fills the unoccupied state, its energy does not have to be given off as an X-ray. Instead, it is possible for it to transfer enough energy to a third electron to overcome its own binding energy and be emitted; this is called an Auger electron. Its kinetic energy will depend on the energy of three levels: the original shell from which the first photoelectron originated, the level from which the second electron transitioned, and the level from which the Auger electron was ejected. As such, its kinetic energy will also be a characteristic signature of a particular element, which enables compositional quantification analysis. One big advantage of this technique is that Auger electrons of low kinetic energy can be detected for most elements, allowing for surface sensitivity even better than XPS. Also, as with XPS, one may exploit the collection angle to enhance this property. Moreover, shifts related to the chemical environment

can also be observed with AES. All AES work quoted was performed by collaborators at the University of Oxford, who used a collection angle normal to the surface.

2.1.8. Scanning Tunneling Microscopy

Scanning tunneling microscopy (STM) exploits the tunneling phenomenon, which is a unique prediction of quantum mechanics. The description of a particle (for example, an electron) in terms of its wavefunction allows it to have a nonzero probability of being measured on the opposite side of a potential barrier with higher energy than the particle; the electron is then said to have ―tunneled" through the barrier.

As opposed to the aforementioned types of microscopy, STM does not use radiation to sample a material. Instead, a bias is applied between a conducting physical probe and a sample. The probe is then rastered across a surface and the electron tunneling current is monitored at every position, and the collected information can be displayed as an image. There exist two STM operation modes:

- Constant-height mode: whereby the probe is rastered across a plane of fixed height and the tunneling current is measured at each point to generate the micrograph.
- Constant-current mode: whereby the tunneling current is fixed to a specified value and the tip height is adjusted via a feedback mechanism and recorded at each in-plane position to generate the image.

Typically, a sharp tip (usually made of tungsten) is used since the probe size determines the resolution of the image, which can reach the atomic scale. Due to the nature of the collected information, STM is very surface sensitive. Nonetheless, STM images do not strictly correspond

to the surface topography, but to its electronic structure; see section 2.2.3 for further discussion. The applied biasing voltage defines the density of states being sampled.

This technique requires the sample to be electrically conducting. Insulating materials can be imaged if slightly doped, but typically require much larger biasing voltages than metals. Even with a suitable material, STM imaging is not always trivial. High resolution images can only be obtained with all of the following: a sharp tip, a clean surface, a clean medium (UHV environment) and vibration dampening.

Historically, STM was the first scanning probe microscopy. Other such surface-sensitive techniques have been developed, such as atomic force microscopy (AFM), friction force microscopy (FFM) and magnetic force microscopy (MFM), all of which differ from STM in the physical property being measured. Further details on this technique can be found in Ref. [43].

The STM images presented in this dissertation have been collected by collaborators at the University of Oxford and are used as a reference (and target) for first-principles STM image simulations. It must be noted that the experimental images were acquired with large positive bias voltages and in constant-current imaging mode. These characteristics must be incorporated into the simulations, which are described below in subsection 2.2.3.

2.2. Theoretical Techniques

2.2.1. Density Functional Theory

Density Functional Theory (DFT) is a quantum-mechanical first-principles approach to solving Schrödinger‘s Equation for many-electron systems. Any such system is described in terms of a fictitious system of non-interacting pseudo-particles which reproduces the actual

electron density distribution upon addition of the squared magnitudes of single-particle wavefunctions. That is, the electron density ρ is accurately described by

$$\rho(\boldsymbol{r}) = \sum_i n_i |\psi_i(\boldsymbol{r})|^2 \,, \qquad \text{(Eq. 2.2)}$$

where n_i is the number of electrons in the state represented by the pseudo-eigenfunction ψ_i. From this charge density, one can extract any ground-state properties and predict macroscopic behavior. In order to find this charge density distribution, one needs to solve the Schrödinger-like Kohn-Sham equations, which need the (so far unknown) charge density as an input. Therefore, the solution is to be found iteratively, starting with an educated guess for $\rho(\mathbf{r})$. Structural relaxation is also possible by using the resulting atomic forces.

In the DFT formalism, the Hamiltonian contains an "effective" potential energy term, which in turn includes Coulombic interactions and the so-called exchange-correlation potential, μ_{xc}; this term includes complicated many-body interactions between electrons of the same spin ("exchange") and of different spin ("correlation"). The exchange-correlation contribution has a highly non-analytical functional dependence on the electron density and must be approximated. This is essentially the only significant approximation in an otherwise first-principles method, and the choice of exchange-correlation functional is the single most important parameter. This is especially important in systems like $SrTiO_3$, since even sophisticated functionals struggle to reproduce the proper degree of hybridization between O sp orbitals and Ti open-shell d orbitals. Also, surface modeling poses a further complication, as most functionals are tuned to be accurate for bulk modeling, so the charge density decay into vacuum is not always well reproduced [44, 45].

The DFT code of choice for this work is WIEN2k [46], a full-potential all-electron implementation which is more realistic than popular pseudopotential codes. The so-called

augmented plane waves + local orbitals (APW+lo) method is used to expand the single-particle wavefunctions. In this method, space is partitioned into non-overlapping spheres (each with a ~~"~~muffin-tin" radius R_{MT} and centered on an atomic nucleus) and an interstitial region. In the latter, the potential and wavefunctions use a basis set consisting of plane waves; inside the sphere, the basis set consists of spherical harmonics multiplied by radial functions. Additionally, inside each sphere a local orbital term is added for further flexibility. Naturally, a boundary condition has to be enforced at the interface between regions: each wavefunction ought to be continuous everywhere, although its slope at the sphere boundary need not be. While this is nonphysical in principle, the effects on physical observables are small and become negligible by increasing the largest wavevector used in the plane wave expansion basis.

Surfaces are modeled using the repeated slab configuration. Since WIEN2k imposes periodicity in 3 directions, this is set up by constructing a large supercell that includes a vacuum gap. This results in the periodic repetition of slabs of finite thickness but infinite lateral extent in the other 2 dimensions. This construction has to take into account some considerations. First, there must be a sufficiently large vacuum separation between the slabs, in order to avoid interaction between surfaces facing each other; however, too much vacuum makes the calculation computationally expensive. Usually, 8 to 12 Å is ideal. Also, the slab itself must be sufficiently thick, so that the atoms at its center display bulk-like behavior and there is no same-slab surface interaction. Naturally, this is countered by the expense of adding too many atoms. One way to tackle this is to run rough calculations with a varying number of planes and via surface energy calculations determine the smallest thickness that is needed. An alternative method is to use bond valence sums (see below) to quickly verify whether the atoms at the center of the slab have bulk-like bonding.

In each WIEN2k calculation an energy value can be obtained for the system modeled. However, this will be meaningless unless compared to another system using the same DFT parameters and the same number of atoms. For example, the adsorption energy of a water molecule on a given surface will be meaningful only if the energy of the "wet" system is compared to the sum of the energies of the bare system and isolated water molecules. The same idea applies to calculating a surface energy value: one must subtract energies corresponding to the obvious alternative state in which the same atoms could be (in this case, bulk energies). Obtaining meaningful energies then allows us to make proper comparisons. For example, when dealing with changes in composition, it enables the construction of a "convex-hull" construction, also called a "taut string" construction. This can be explained schematically by Fig. 2.2. In the example shown, we have the case of a binary system, where many phases of different stoichiometry exist, including end members A and B. After plotting the energy curves of each phase, one can draw a set of connected straight lines that are each tangents common to two phase curves, and with the constraint that (from left to right) they must have an increasing (more positive or less negative) slope. In this way, only the phases that fall on the convex hull construction will be the stable ones. In Fig. 2.2, the sole exception is phase Y and it is easy to see why it is unstable: given its stoichiometry, the system would have less energy if it decomposed into a mixture of phases X and Z.

DFT modeling is also the first step towards calculating bond valence sums and generating simulations of STM images; see below for further details.

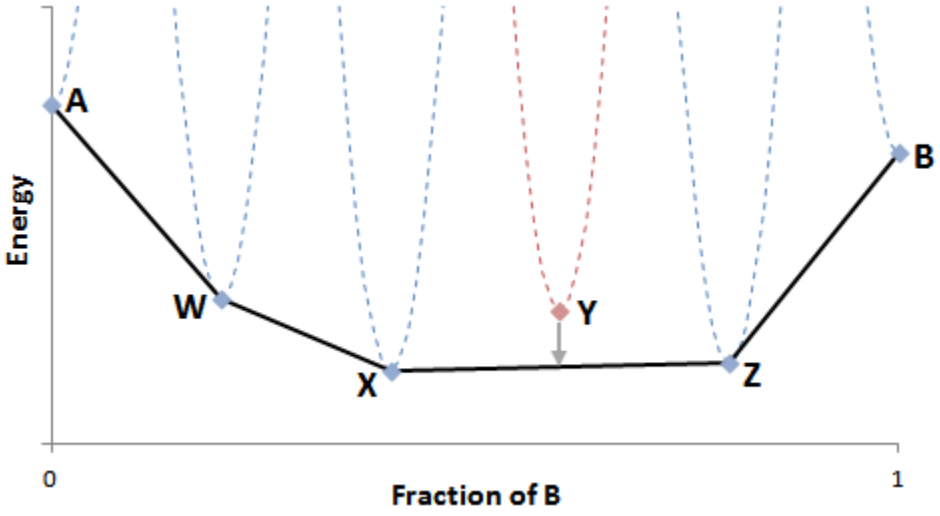

Fig. 2.2. Example of a convex-hull construction for a binary system.

2.2.2. Bond Valence Sums

The bond valence sum of an atom/ion (defined to be positive for cations and negative for anions) is calculated as

$$\mathrm{BVS} = \pm \sum_i \mathrm{BV}_i \,. \qquad \text{(Eq. 2.3)}$$

This is a sum over all bonds of the individual bond valences, defined as

$$\mathrm{BV} = \exp((R_0 - R)/b) \,, \qquad \text{(Eq. 2.4)}$$

where R is the bond length, R_0 is an experimentally-determined standard bond distance for the particular ion pair in question, and b is an empirical constant, typically 0.37 Å. In the case of relaxed DFT structures which use optimized lattice parameters different from the experimental values, these must be changed to match the experimental figures before any BVS calculation.

A useful metric in bulk inorganic structures is the global instability index (GII), so named by Salinas-Sánchez *et al.* [47]. This is simply the root mean square average, over all atoms, of the deviation of the bond valence sum from the idealized formal valence, BVS_0:

$$\mathrm{GII} = \left(\overline{(\mathrm{BVS} - \mathrm{BVS}_0)^2}\right)^{1/2} . \qquad \text{(Eq. 2.5)}$$

Typically, stable room-temperature bulk structures have a GII below 0.2 valence units [48]. By analogy to the GII, the surface instability index (SII) was introduced by Enterkin *et al.* as the figure of merit for relaxed surfaces [49]. The SII is calculated in the same way as its bulk counterpart, but only taking into account the atoms in the topmost layers. As Enterkin *et al.* proved, the usefulness of BVS analysis in predicting structural stability extends very well to surfaces and this is exploited in the present dissertation.

Since BVS are dependent only on the atomic positions, they can also be used to save computational time in DFT surface calculations, by nudging atoms into good starting positions, without large deviations from the formal valences. It must also be noted that the choice of exchange-correlation functional has a large effect on the accuracy of the BVS calculations. As shown in Appendix C, the PBEsol0 functional is very adequate and was used throughout this work whenever BVS analysis was performed, unless stated otherwise.

2.2.3. Scanning Tunneling Micrograph Simulations

The simulation of STM images allows for direct comparison to available experimental images, which is a real-space complement to surface structure determination efforts via diffraction methods. Generating simulated STM micrographs from *ab initio* methods (such as DFT) was first enabled by Tersoff-Hamann imaging theory [50], which leads to the following approximation for the tunneling current I_t from a tip (at position $\boldsymbol{r}$) into the sample:

$$I_\mathrm{t} \propto \rho(\boldsymbol{r}, E_\mathrm{F}) \equiv \sum_\mu \left|\psi_\mu(\boldsymbol{r})\right|^2 \delta\left(\varepsilon_\mu - E_\mathrm{F}\right), \qquad \text{(Eq. 2.6)}$$

where ψ_μ is the wavefunction of the μ^{th} sample state, with energy ε_μ. As should be clear from the equation above, this implies that the tunneling current is essentially proportional to the local

density of states around the Fermi energy of the specimen, E_F. The appeal of this formulation is that it is independent of the tip states. However, Tersoff-Hamann theory is not strictly applicable in the high-bias regime (>100 meV), which is important since imaging oxides, or other insulators, requires a large bias. Nonetheless, many publications [51, 52] resort to the same approach.

What is actually imaged under a large bias voltage? Let us examine this, in terms of energy bands. When the tip and the sample are far away from each other, they are independent. When they are close enough that tunneling can occur, but no external bias is applied, the respective Fermi energies will align. In the case of a positive bias voltage V_b, the Fermi level of the sample will be shifted down by $e \cdot V_b$ with respect to the Fermi level of the tip (e is the charge of an electron), as illustrated in Figure 2.3. This means that tip electrons will be able to tunnel into any unoccupied sample state with energy up to $E_F + e \cdot V_b$. If the bias is small and the sample is metallic, these states will be close to the Fermi level, so the Tersoff-Hamann approximation makes sense. However, if the bias is large, elastic tunneling will be allowed into sample states with a wide range of energies. Just as importantly, the tip electrons of highest energy (closest to the tip‘s Fermi level) will observe a smaller tunneling barrier than those of lower energy, so the tunneling probability into sample states of energy near $E_F + e \cdot V_b$ should be larger than into states near the sample‘s Fermi level. Obviously, then, simulating high-bias STM images by sampling the local density of states around E_F is not appropriate. The opposite approach, sampling the states around $E_F + e \cdot V_b$, is also inadequate and yet often done (e.g. Ref. [53]).

Instead, one must sample the range of possible sample states into which tip electrons may tunnel, applying an appropriate weighting term. Appendix A contains a more detailed derivation, but the main result is that the modified Tersoff-Hamann approximation, which is used

for all STM simulations in this dissertation and has been used successfully by collaborators [54, 55], takes the following form:

$$I_{\mathrm{t}} \propto \int_{E_{\mathrm{F}}}^{E_{\mathrm{F}}+e\cdot V_{\mathrm{b}}} \kappa(\varepsilon)^{-2}\, \rho(\boldsymbol{r},\varepsilon)\, d\varepsilon\,, \qquad \text{(Eq. 2.7)}$$

where

$$\kappa(\varepsilon) = \hbar^{-1}\sqrt{2m_e(\phi_t + E_{\mathrm{F}} + e\cdot V_{\mathrm{b}} - \varepsilon)} \qquad \text{(Eq. 2.8)}$$

is the inverse decay length of the electron states in vacuum of energy ε. Also, ϕ_t is the tip workfunction and m_{e} is the mass of an electron. Here, it is assumed that the voltage is not large enough that the range of allowed tunneling energies encompasses the region where the barrier shape is triangular (see Fig. 2.3 for clarity); such a case would require an even stronger weighting of high-energy states. The implementation of this formalism in the particular case of the WIEN2k code is described in detail in Appendix A. In what follows, the basic stages for generating a simulated STM image with large positive bias and in constant-current mode are outlined.

The structure to be tested is first allowed to relax and reach charge density convergence. The unoccupied states from $\varepsilon = E_{\mathrm{F}}$ up to $E_{\mathrm{F}} + e\cdot V_{\mathrm{b}}$ are then artificially populated, with the regular population multiplied by a weighting factor proportional to $\kappa(\varepsilon)^{-2}$. This artificial density is then sampled over a volume near the surface, typically with 0.2 Å in-plane and 0.3 Å out-of-plane sampling intervals, thereby generating a 3D array of densities. Blurring due to tip size, vibration and thermal effects is incorporated by convolving the density at each voxel with an in-plane radially-symmetric motif. Upon specification of a density value, an isosurface of constant density is produced, analogous to the generation of a surface of constant current in experimental STM. Grayscale coloring, scaled with height at each in-plane position, is applied. The

simulated STM image is thus a representation of the colored isosurface down the direction normal to the sample surface.

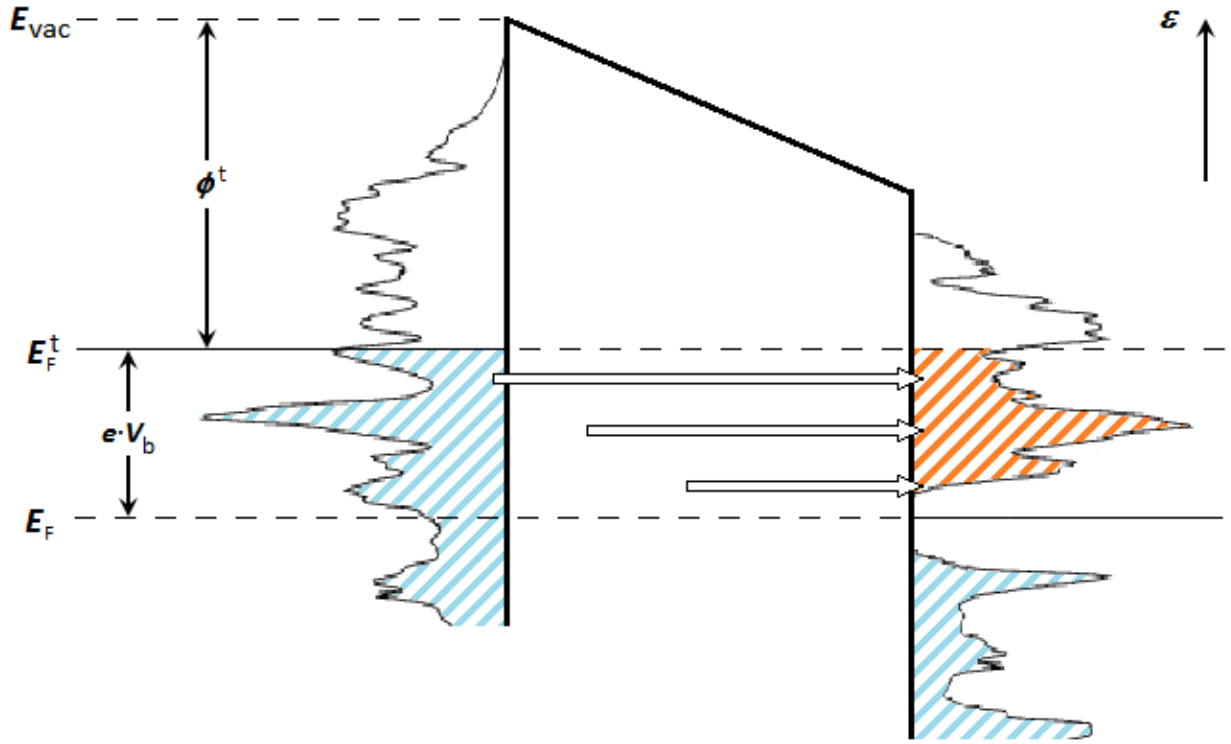

Fig. 2.3. Schematic of tunneling process upon a large positive external bias. Density of states is shown for the tip (left side) and the sample (right side). Occupied states are indicated by light blue stripes. Unoccupied sample states into which electrons may tunnel are indicated by orange stripes. The length of each white arrow correlates with the tunneling probability as a function of energy.

2.3. General Background

2.3.1. Wood's Notation

Wood's notation, the most common nomenclature system for periodic surface reconstructions, shall be consistently used in this dissertation. In general, any such reconstruction is labeled ($m \times n$)Rθ, or simply $m \times n$ if $\theta = 0°$. Here, m and n are the main indices and are multiples of the bulk-like periodicities; these need not be integers. In the case of

$SrTiO_3$(001), for example, a reconstruction labeled 2×1 has a surface period twice as large as a bulk-like truncation along the <100> direction, but preserves the original periodicity along <010>. A bulk-like truncated surface would of course be labeled 1×1.

If the axes defining the unit cell of the reconstructed surface are different from the bulk-like truncation coordinate system, angle θ represents the rotation between these two. One example of this is the $SrTiO_3$(001) ($\sqrt{13}\times\sqrt{13}$)R33.7º reconstruction.

Another important case is that of centered unit cells. If a reconstruction has $m\times n$ periodicity but the atom at the corner of the unit cell is crystallographically equivalent to the atom at the center of it, then the $m\times n$ cell is not the primitive unit cell. Therefore, said reconstruction is better labeled c($m\times n$), using the smaller centered cell. $SrTiO_3$(001) again provides an example, the c(4×2) surface, to be discussed in several of the following chapters.

As shall be seen, multiple different surface structures may have the same periodicity, so care must be taken to avoid confusion.

2.3.2. Non-Stoichiometric Perovskite-Related Phases

One recurring concept is that of Ruddlesden-Popper (RP) phases, which are compounds of $AO\cdot(ABO_3)_n$ composition, resulting from the intergrowth of perovskite (ABO_3) and rocksalt layers. Its end members are indeed the rocksalt oxide ($n = 0$) and the perovskite phase ($n = \infty$). RP phases ($n = 1, 2$ are shown in Fig. 2.4) were first observed in the SrO–$SrTiO_3$ pseudobinary system by Ruddlesden and Popper [56, 57] but have been seen in many other systems. This homologous series is defined by the periodic ordering of RP stacking faults, which can each be described (with respect to a perovskite matrix) as the insertion of an extra (001) AO plane; alternatively, an equivalent description is the subtraction of a (001) BO_2 layer. Regardless, this

results in a crystallographic shear with vector ½<111>. The periodicity of RP faults along the <001> axis defines the specific ordered phase, with larger periodicities corresponding to larger *n*. Every RP phase has a tetragonal I4/mmm space group.

Numerous computational reports [58-64] have been published regarding the RP strontium titanates, but only a few of these phases have been synthesized. Tilley [65] attempted to produce the n = 1-7 phases by annealing SrO-rich powder mixtures, but only managed to obtain the first two, although the n = 2 crystal exhibited lamellar intergrowth of higher order phases. Sturm *et al.* [66-68] had a similar powder-based approach and a mixture of nominal n = 3 composition produced crystalline regions of n = 2 and 3. Over a wide range of composition, numerous isolated faults, as well as SrO inclusions and SrO grain boundary segregation were observed. Tian *et al.* [69] grew RP thin films on a $SrTiO_3$ substrate via molecular beam epitaxy, targeting the n = 1-5 phases. The first three phases were produced with good quality, and the fourth and fifth phases, while ordered enough to produce coherent transmission electron diffraction patterns, were very defective. Zschornak *et al.* [64] used chemical solution deposition to grow similar films which produce the first three RP family members.

In analogy to the Ruddlesden-Popper phases, a set of hypothetical Ti-rich strontium titanate phases of $TiO_2{\cdot}(SrTiO_3)_n$ stoichiometry has been examined in the literature, albeit in much less detail. This homologous series, instead of having periodically ordered stacking faults consisting of contiguous (001) SrO planes, would have similar faults, but each with two consecutive (001) layers of bulk-like TiO_2, with qualitatively similar stacking as in anatase along its <001> axis. These hypothetical phases have been referred to as Magnéli phases [63], which is a confusing misnomer, since this label is usually reserved for phases of Ti_nO_{2n-1} ($n \geq 4$) composition. Instead, these phases shall be referred to in this dissertation as the TCS (TiO_2

crystallographic shear) phases. It must be noted that while the shear vector (with respect to the $SrTiO_3$ matrix) in RP faults is ½<111>, the analogous shear vector in TCS faults is ½<101> and results in edge-sharing Ti-centered octahedra, as seen in Fig. 2.4(c).

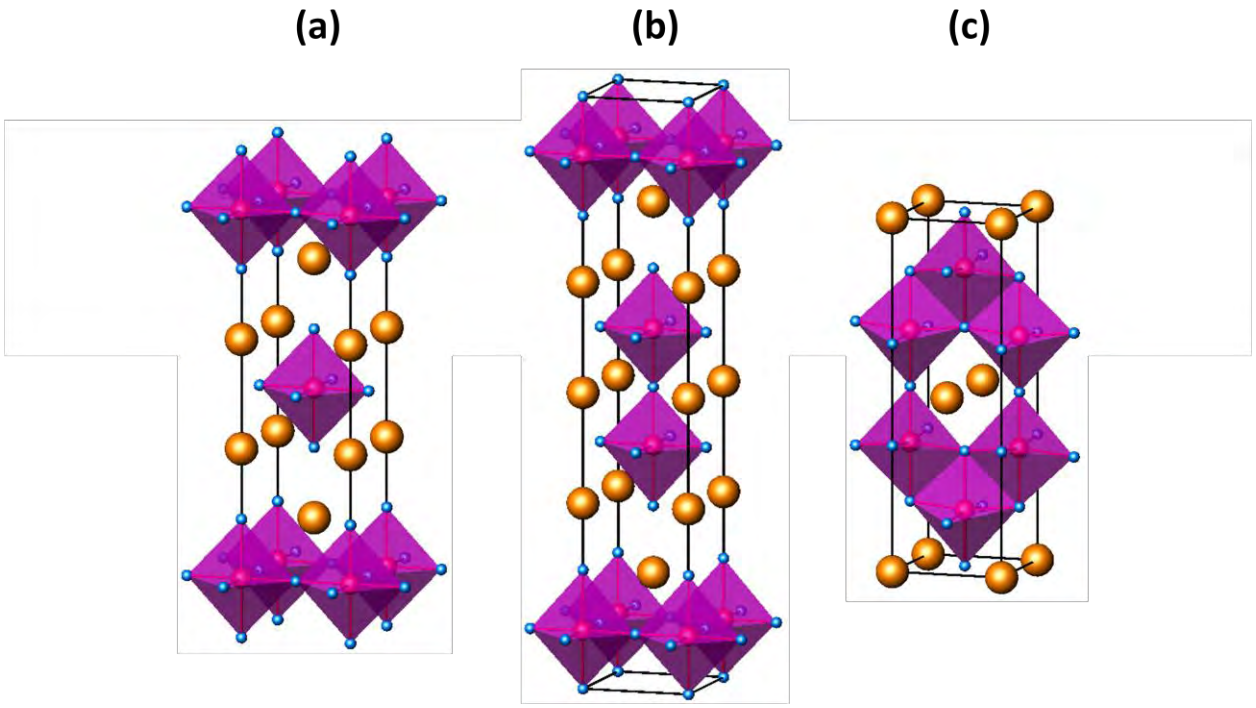

Fig. 2.4. Polyhedral representation of perovskite-like phases: (a) Sr_2TiO_4, n = 1 RP phase; (b) $Sr_3Ti_2O_7$, n = 2 RP phase; (c) $SrTi_2O_5$, n = 1 TCS phase. Sr in orange, Ti-centered octahedra in purple, O in blue.

Among several other non-stoichiometric planar defects in $SrTiO_3$, Suzuki *et al.* [60] studied (via *ab initio* computations) the energetics of a TCS-type fault, exemplified by the n = 2 case. As the authors point out, the anisotropic shear vector implies that the TCS phases would not have a tetragonal space group in their hypothetical bulk structure, but rather orthorhombic. The difference in the lattice constants in the directions parallel to the TCS faults strongly suggests that this phase (in TiO_2-doped $SrTiO_3$) would be less coherent with the perovskite matrix than RP phases (in SrO-doped $SrTiO_3$). The reaction $2\ SrTiO_3 + TiO_2 \rightarrow Sr_2Ti_3O_8$ is

found to be endothermic, with an enthalpic cost of 0.57 eV per formula unit. The only other theoretical study on a TCS phase (n = 3), by Benedek *et al.* [63], dealt with its dielectric properties. It must be pointed out that no TCS have been observed [70] although individual TCS faults have been proposed as an accommodation mechanism for excess TiO_2 in $SrTiO_3$ [71].

If observed facts of undoubted accuracy will not fit any of the alternatives it leaves open, the system itself is in need of reconstruction.
Talcott Parsons

Oh see, first off you gotta realize – everything for me is a reconstruction or deconstruction.
Danny Elfman

Chapter 3. Periodic Reconstruction: $SrTiO_3(001)$

3.1. Introduction

Many metallic surfaces are stabilized through electronic and atomic relaxation alone, without significant rearrangement of atoms with respect to their ideal bulk-like positions. This, however, is not generally the stable solution for insulating materials, including metal oxides. As mentioned in Chapter 1, one common stabilization mechanism is that of periodic reconstruction, whereby surface ordering with periodicities larger than bulk-like truncations takes place through substantial mass transport at the surface. The determination of the exact atomic-scale structure of surfaces is a prerequisite for understanding their effect on properties exploited for technological applications.

The focus in this chapter is on the numerous periodic reconstructions observed or predicted for the $SrTiO_3(001)$ surface. Experimental diffraction methods have consistently

supported structural models consisting of consecutive TiO_2 layers at the surface. Numerous alternative models have been proposed in the literature, generally requiring much less atomic redistribution. In this chapter, bonding analysis and first-principles scanning tunneling microscopy simulations are used to evaluate the feasibility of these models.

3.2. Background

Naito and Sato [72] explored $SrTiO_3$(001) surfaces following different thermal treatments using reflection high-energy electron diffraction (RHEED). Annealing in the 750-800 ºC range in a 1×10^{-8} Torr vacuum for 1 hour was reported to generate a two-domain 2×1 surface, while a 15-hour anneal at 800-1100 ºC in O_2 produced coexisting ($\sqrt{13}\times\sqrt{13}$)R33.7º (–RT13" hereafter) and c(6×2) surface reconstructions. The authors speculated that the 2×1 structure results from the ordering of surface O vacancies, while no structural models were presented for the other surfaces.

Jiang and Zegenhagen published a series of reports combining low-energy electron diffraction (LEED) and scanning tunneling microscopy (STM) to study annealed $SrTiO_3$(001) surfaces [73-75]. According to their first paper, annealing for 30-120 min at 900-950 ºC in a vacuum pressure below 10^{-7} Torr was found to give rise to a combination of a 2×1 reconstruction and a weak 2×2, while 1000-1200 ºC led only to a –square" 2×2 surface, although only partially ordered. Indeed, the resolution in the published STM images is poor and no substantial long-range order is shown. Annealing at 950-1100 ºC for 4-5 hours in 1 atm of O_2 followed by 2 hours at 950 ºC in UHV produced rows in the STM images, separated by 1.2 nm (three unit cells). LEED patterns identified this as a c(6×2) reconstruction, which was also found to be air stable. Auger electron spectroscopy (AES) indicated this surface was Ti-rich. The third paper

tracked the formation of the 2×1, c(4×2) and c(6×2) reconstructions under UHV annealing at 950 ºC, with or without a small pressure of H_2, and with or without a pre-anneal in O_2. AES data was used to argue that the surfaces with larger unit cells are more TiO_2-rich. However, Jiang and Zegenhagen also developed a simple unifying model whereby these reconstructions, as well as the "square" 2×2 and the (√5×√5)R26.6º ("RT5" hereafter) would arise from periodic O vacancies in a TiO_2 bulk-like truncation.

Several $SrTiO_3$(001) reconstructions were imaged via STM by Castell [76], after slightly doping crystals with 0.5 at.% Nb to provide some conductivity, as required by the experimental technique; LEED was used as a complement to STM. After treating crystals with a buffered NH_4:HF (BHF) solution, which is known to etch away SrO and lead to TiO_2-rich surfaces [77], samples were annealed in UHV. Annealing in the 600-900 ºC range for 30 min was found to lead to a 2×1 reconstruction, with the higher end of temperatures inducing stronger ordering. The reconstruction appears in STM as parallel bright rows, with the features along the short periodicity direction not resolved and the rows slightly wider than the valleys separating them. Also, two domain orientations were observed, as well as wavy step edges with 0.4 nm height, which corresponds to one bulk $SrTiO_3$ unit cell. Two 2×1 structural models were proposed, based on the removal of surface atoms from a TiO_2 bulk-like truncation; these will be described in more detail in subsection 3.4.1. Further annealing at higher temperatures (900-1100 ºC) led to the gradual transformation of the 2×1 surface into a surface with c(4×4) periodicity, with these two coexisting up to 1400 ºC for several minutes. This structure appears in STM as a "brickwork" pattern, with an elongated bright feature at the corner of each primitive cell. Since this reconstruction also shows two domains and has the same step morphology as (and evolves from) the 2×1 reconstruction, Castell proposed two "brickwork" c(4×4) structural models, each

derived from his proposed 2×1 structures, through further removal of atoms. The formation of a c(4×2) reconstruction was also reported, as a result of Ar^+ sputtering, followed by UHV annealing at 1200 ºC for 15 min. Normally, the STM images show one round feature per primitive surface cell, but replacing the tip halfway through an image was reported to occasionally lead to two slightly elongated features per primitive cell, ordered with 2×1 periodicity. Castell argued that the c(4×2) was likely TiO_2-rich and proposed a structure on the basis that the tip effects could be due to the imaging of either the Ti or the O surface sublattice. The three reported reconstructions were also observed on La-doped crystals, which rules out the possibility of either Nb (B-site dopant) or La (A-site dopant) mediating their formation.

Silly *et al.* [78] observed via STM the appearance of a –square" 2×2 reconstruction in 0.5 at.% Nb-doped $SrTiO_3$(001) crystals, following BHF etching and UHV annealing at 950 ºC for 2 hours. Annealing this surface for 1 hour at 1030 ºC induced the formation of linear arrangements of bright dots. These appeared as single or double rows of dots aligned along <110>-type directions and seem to form as an overlayer on the 2×2 surface, but should not be confused with the <100>-oriented nanolines to be discussed in Chapter 4. Further annealing at this temperature for another hour produced a disordered –square" arrangement of similar dots, essentially as a c(4×4) reconstruction, not to be confused with the –brickwork" structure. AES indicated that these surface structures, especially the –square" c(4×4), are Ti-rich when compared to the surface of cleaved crystals.

Another STM study of Nb-doped (0.1 at.%) $SrTiO_3$ crystals was published by Iwaya *et al.* [79]. After BHF treatment and subsequent UHV annealing at 800 ºC for 6 hours, flat (001) terraces and step heights mostly matching 1 bulk unit cell were seen. A minority of terraces half a unit cell in between were assumed to be SrO terminations and set as the focus of the paper. No

actual chemical verification was performed, however, which renders the claim dubious. Within these terraces, empty-state STM images were interpreted as a combination of c(2×2) order due to alternate buckling of octahedra and 3-unit-cell periodicity due to zigzag chains of Ti^{3+} ions. The analysis is plagued by leaps of faith. In all likelihood, this was simply a c(6×2) reconstruction.

3.2.1. The RT5 Reconstruction and Sr-Adatom Models

Matsumoto *et al.* [80] originally reported the formation of a $SrTiO_3$(001) 2×2 reconstruction which appeared in unoccupied-states STM images as a square arrangement of bright round features and formed after annealing in UHV at 1200 ºC. A structural model based on periodic oxygen vacancies on a bulk-like TiO_2 surface layer was proposed. In a subsequent paper [81], the periodicity was corrected to RT5, but the same type of structure was assumed.

Martín González *et al.* [82] used photoelectron spectroscopy and LEED to monitor the process of UHV annealing of (001)-oriented $SrTiO_3$ single crystals. A RT5 reconstruction was observed at 830 ºC, as well as the simultaneous appearance of a conduction band. This was once again interpreted as arising from the ordering of oxygen vacancies at the surface, supported by an increase in the Ti^{3+} and Ti^{2+} signals.

Kubo and Nozoye [51] used non-contact atomic force microscopy (AFM) and STM to observe the RT5 surface, a result of BHF etching followed by annealing at 1200 ºC in UHV for a few seconds. STM images are described as changing only in contrast while changing the voltage in the range from –3 to +3 V. A structural model was proposed by the authors, consisting of one Sr adatom per surface cell, sitting on top of the hollow site of a bulk-like TiO_2 layer. DFT calculations were used to generate AFM and STM simulations, the latter using traditional

Tersoff-Hamann theory in spite of the large biases. The Sr-adatom structure was shown to match the simulations significantly better than the model based on periodic O vacancies.

In a follow-up manuscript [52], these authors described the STM observation of numerous $SrTiO_3$(001) reconstructions and transitions between them, all after BHF etching and subsequent UHV annealing. All reconstructions appear in unoccupied-state STM images as periodic arrangements of bright round features. The following periodicities were observed upon short anneals in the 1000-1250 ºC range, often with multiple ones coexisting: RT5, RT13, 4×4, a c(2×2) (seen very locally), two types of ~~–s~~quare" 2×2 and two types of ~~–s~~quare" c(4×4). The two 2×2 reconstructions differ from each other in the number of bright dots per cell, as do the two c(4×4) surfaces (which are also different from the ~~–b~~rickwork" seen by Castell). The authors also claim to see a c(4×2) surface after a combination of annealing steps and air exposure, although the published image is unconvincing. Kubo and Nozoye extended their RT5 model to propose similar structural models for all these reconstructions. According to these models, every bright spot corresponds to a Sr adatom. Analogous Sr-adatom models were also proposed for the the 2×1-to-~~–b~~rickwork"-c(4×4) transition seen by Castell. Again, simplistic STM image simulations were presented for most of the structures.

Several of these Sr-adatom models were examined theoretically by Liborio *et al.* [83], along with the TiO_2 bulk-like truncation. The authors predicted that among adatom models, only one ~~–s~~quare" 2×2 and the RT5 could possibly be stable under the experimental conditions used by Kubo and Nozoye, but only in (or close to) equilibrium with SrO; this corresponds to densities of 0.25 and 0.2 Sr adatoms per 1×1 cell. Lower adatom densities were concluded to be possible only far away from equilibrium, as hypothetical transient states leading to Sr loss to the environment. Larger adatom densities were found to always be unstable.

Later, Newell *et al.* [84] studied 0.5 wt.% Nb-doped $SrTiO_3$(001) samples, which were polished and then UHV annealed at 1000ºC for 1 hour. STM was used to detect the formation of a disordered –square" c(4×4) surface, similar to that seen by Silly *et al.* and to one of the c(4×4) structures observed by Kubo and Nozoye. Treating this as a precursor surface and annealing it above 1350 ºC led to an increase in conductivity, first slowly but eventually leading to a sharp rise. This coincided with the partial appearance of a RT5 reconstruction, seen by LEED. Terraces were observed by STM to have two domains, with roughly 1.5 Å height difference, the higher domains showing an array of bright round features with RT5 periodicity. This was interpreted as being consistent with the Sr-adatom model, as an overlayer on bare surfaces. For low tunneling currents, no STM bias dependence was found in the range from –3.5 to +3.5 V, similar to the finding by Kubo and Nozoye; this implies the RT5 is metallic. For tunneling currents above 1 nA, however, the features looked less round and much more like slanted squares. Also, bias dependence was observed in this tunneling current régime: for positive bias (imaging unoccupied states), the features were bright, whereas the contrast was inverted with negative bias (occupied states), with the square features appearing dark. On top of this, SEM was used to observe needle-like surface islands of ~50 nm width, oriented along <100> directions; based on the rise in a Ti AES shoulder (attributed to Ti^{2+}) and on one past report in the literature [85], these islands were ascribed to TiO. The authors explain the whole process as a decomposition of $SrTiO_3$ into Sr (as RT5 adatoms) and TiO upon severe loss of O to the environment. Interestingly, AES data also shows that the RT5 surface is more Ti-rich than the already Ti-rich –square" c(4×4). While the authors point out that a Sr-adatom model will still be Ti-rich (due to the exposed surface Ti), it should certainly be *less* Ti-rich than a c(4×4), even if the latter were also a Sr-adatom structure (1/5 vs. 1/8 adatoms per 1×1).

Most recently, (001)-oriented crystals with the same Nb doping level were examined again by STM by Shiraki and Miki [86]. An overnight UHV anneal at 500 ºC, followed by several hours at 1200-1400 ºC, gave rise to the RT5 surface. Unlike the previous reports, filled states were imaged. At large negative bias voltages, a checkerboard pattern was observed, with an alternation of dark and bright square-like features. Within the dark areas, the authors claimed to see (the images published are unconvincing) small protrusions which were argued to match what would be expected from a TiO_2 bulk-like termination. Initially, it was also claimed that the bright squares were consistent with Kubo and Nozoye's model of a Sr adatom on a hollow site of a TiO_2 layer. However higher tunneling current reveals asymmetry in the bright regions, which contradicts the fourfold symmetry.

3.2.2. TiO_2-Rich DL Reconstruction Models

Erdman *et al.* [34] produced a two-domain 2×1 reconstruction via Ar^+ sputtering, followed by annealing under flowing O_2 in the 950-1000 ºC range for several hours. This was detected via transmission electron diffraction (TED), while electron micrographs revealed terracing. A structural solution was reached by using the relative intensities of TED reflections and using direct methods to solve the phase problem [87, 88]. This structure was further refined using DFT calculations. The model consists of an overlayer of TiO_2 composition sitting on a bulk-like TiO_2 plane and was shown to be consistent with high-resolution TEM images. A similar structural solution was found through similar methods for the c(4×2) reconstruction [89], formed by lowering the annealing temperature into the 850-930 ºC range. Like the 2×1, this surface has a double layer (DL) TiO_2 structure. The study of these DL structures and similar

ones will be an important component of this dissertation, and these will be described in more detail in section 3.4.

In light of the 2×1 and c(4×2) structural solutions, Warschkow *et al.* [90] used DFT to examine these and other hypothetical periodic reconstructions with the same DL stoichiometry. These included a 1×1 reconstruction (where both TiO_2 surface layers are bulk-like in nature), a (√2×√2)R45º (–RT2" hereafter), three 2×2 structures, three 4×1 structures and one additional c(4×2). The RT2 surface was found to be the most stable of these surfaces, although it has not been observed experimentally, while the 2×1 was among the structures of highest energy.

Similar methods to those used by Erdman *et al.* were exploited for two more (001) reconstructions. Lanier *et al.* [91] used them, in combination with surface X-ray diffraction and STM image simulations, to reach a structural solution for the c(6×2) surface, detected after annealing at 1050-1100 ºC for 2-5 hours in O_2. This reconstruction was determined to be rather complex, with microscopic domains of four similar, but distinct TiO_x motifs and additional, randomly distributed TiO_2 units. Meanwhile, Kienzle *et al.* [92] reached a structural solution for the RT13 reconstruction. Like the DL structures, this has an overlayer of TiO_2 stoichiometry on a TiO_2 bulk-like plane. However, in this case the top layer has a composition of 10 TiO_2 units per RT13 cell. The authors highlighted the fact that an infinite number of structures can be constructed with little variation in the surface energy by using simple tiling of TiO_5 polyhedra; this points to the possibility that many such surfaces can coexist and that disordered two-dimensional glass-like arrangements can form and subsist for long times.

Herger *et al.* [93, 94] used surface X-ray diffraction to probe the $SrTiO_3$(001) surface, after submersion in water, followed by BHF etching and O_2 annealing at 950 ºC for 1 hour; this treatment has been found to yield near perfect single-termination surfaces [95]. Given the

observed superstructure rods, numerous 1×1, 2×1 and 2×2 structures were considered. It was found that the best fit to the data was given by a combination of Erdman *et al.*'s DL 2×1 model [34], one of the hypothetical 2×2 DL models proposed by Warschkow *et al.* [90] and a DL 1×1 model (where the surface terminates in two consecutive bulk-like (001) TiO_2 layers). For this same treatment, followed by typical conditions for thin film growth (annealing at 750 ºC in 10^{-3} Pa of O_2), the larger reconstructions appear to vanish and a DL 1×1 appears to be the best fit. However, the authors speculate that since this is a high energy structure, it is possible that it actually corresponds to a disordered DL structure, largely a mix of the 2×1 and 2×2; the lack of long-range order would explain the lack of superstructure rods in the diffraction data.

More recently, Lin *et al.* [55] used STM image simulations to test several structural models for a "square" 2×2 reconstruction against experimental micrographs. The simulations were performed with the same method used in several portions of the present dissertation (see Chapter 2 for details). The best match to experiment was obtained with one of the DL models examined by Warschkow *et al.* [90], which is consistent with complementary experimental data. The corresponding Sr-adatom model was discarded.

Several theoretical papers have addressed the DL structures. Heifets *et al.* [96] carried out hybrid Hartree-Fock/DFT calculations to examine Erdman *et al.*'s DL 2×1 model, as well as the DL 1×1 and a SrO double-layer surface. While the 2×1 DL structure was found to be slightly more stable than the TiO_2-rich DL 1×1, it was predicted to be less favorable than bulk-like truncations under all experimental conditions. Similar modeling by Johnston *et al.* [53] pointed to the relative instability of the 2×1 DL structure; this will be reviewed in more detail in subsection 3.4.1. The topic of TiO_2-rich DL reconstructions was revisited by Iles *et al.* [97], by performing DFT calculations for several of them, not only for $SrTiO_3$, but also for other

perovskites. The structures under study were the DL 1×1, the 2×1, the "zigzag" 2×2 observed by Herger *et al.* [93, 94], and the RT2; it was confirmed that these follow, in that order, a trend of increasing stability.

3.3. Methods

The periodic reconstructions studied here are evaluated with two theoretical methods: STM image simulations and bond valence sum (BVS) analysis. Both of these use density functional computations as the first step, modeling surfaces with the repeated slab configuration. All DFT calculations were carried out with the full-electron-potential WIEN2k code [46], using an augmented plane wave + local orbital (APW+lo) basis set. The atomic positions were allowed to relax so that the residual force on any atom was under 0.1 eV/Å. Muffin-tin radii of 2.36, 1.70 and 1.20 bohr were used for Sr, Ti and O, respectively, along with a maximum K value for the plane wave expansion of 5.5/1.2 bohr^{-1} and a k-point mesh equivalent to a 6×6×6 mesh for a bulk $SrTiO_3$ unit cell. At least 13 atomic layers per slab were used, except for Sr-adatom models, since pre-converged structures with nine layers were obtained from Dr. James Enterkin. Contiguous slabs were separated by at least 10 Å of vacuum.

3.3.1. STM Image Simulations

For the STM image simulations, the PBE [98] form of the generalized gradient approximation to the exchange-correlation functional was used, as explained in Appendix A. The $SrTiO_3$ bulk lattice parameter was optimized and a value of $a_{SrTiO_3}^{PBE} = 3.944$ Å was obtained, which was subsequently enforced in slab calculations along the in-plane directions.

The constant-current STM images were simulated by exploiting the WIEN2k outputs, using a modified Tersoff-Hamann approach, as described in subsection 2.2.3 (see Appendix A for more detail). The artificial density of unoccupied states was sampled at intervals of $a_{SrTiO_3}^{PBE}/20$ (in-plane) and 0.3 Å (out-of-plane). A radially-symmetric step-function convolution motif of characteristic radius $a_{SrTiO_3}^{PBE}/2$ (~2 Å) was used for the blurring stage, following tests.

3.3.2. Bond Valence Sum Analysis

Since surface energy is composition-dependent (and many structural models have different composition), direct comparison is not immediately meaningful. For this reason, BVS analysis was performed, which supplies clues regarding the stability of individual structures. The exchange-correlation functional was changed for this analysis, because PBE does perform as well as other functionals for this purpose (see Appendix B). Instead, the PBEsol-Hybrid [99] form of the generalized gradient approximation was used, with 0.5 exact-exchange fraction for the Ti-d orbitals. The amount of exact exchange was optimized to match experimental atomization energies of TiO_x molecules, as done elsewhere [100, 101]; see Appendix B for more details. The usual term for this combination of functional and exact-exchange fraction is PBEsol0. This yields an optimized cubic lattice parameter of $a_{SrTiO_3}^{PBEsol0} = 3.893$ Å, which is very close to the experimental value.

The following standard bond length (R_0) values were consistently employed to calculate each bond valence (see section 2.2.2): 2.118 Å for Sr^{2+}–O^{2-}, 1.815 Å for Ti^{4+}–O^{2-}, 1.791 Å for Ti^{3+}–O^{2-} [102]. The usual value of 0.37 Å was used for the empirical constant b (see Eq. 2.4). Each supercell was expanded isotropically to match the lattice parameter to the experimental value of 3.905 Å. The bond valence sums were computed using the KDist software from the

Kalvados program suite [103]. The surface instability index (SII, see section 2.2.2) was calculated by only taking into account the atoms in the topmost two layers (unless otherwise indicated).

The bond valence sums have been calculated in the past for many Sr-adatom models by Dr. James Enterkin [104]. However, this was done with the PBE exchange-correlation functional. Whenever BVS analysis is presented for Sr-adatom models, Enterkin‘s calculated structures were used and relaxed again with the PBEsol0 functional.

3.4. Results

Proposed structural models for certain $SrTiO_3$(001) reconstructions are described and evaluated below. All structures discussed are available in Appendix D in the Crystallographic Information File (CIF) format.

3.4.1. The 2×1 Reconstruction

As mentioned above, Castell proposed two structural models for the 2×1 reconstruction based on a TiO_2 bulk-like truncation [76]. These are:

- $\underline{2\times1TiO_2}$ (Fig. 3.1(a)): This model removes every other <010> TiO row, as well as one third of the remaining O. The rest of the O atoms are displaced so as to be directly on top of a Sr atom from the underlying layer, as described by Castell. However, upon relaxation the top-layer O atoms move so as to shorten the Ti–O bonds. Overall, the top-layer composition is TiO_2 (not Ti_2O_4) per 2×1 cell. This arrangement yields <010> rows of edge-sharing TiO_5 polyhedra. The appeal of this structure is that it preserves the overall $SrTiO_3$ stoichiometry with no surface excess of any species.

- 2×1Ti_2O_3 (Fig. 3.1(b)): In this case, every other <010> O-only row is removed from the top TiO_2 plane, with all other atoms roughly preserving their bulk-like positions. This model produces <010> rows of corner-sharing TiO_4 surface polyhedra; these rows pair up through further edge-sharing. This structure is also the most logical form of the suggestion by Naito and Sato [72] that the 2×1 is due to vacancy ordering.

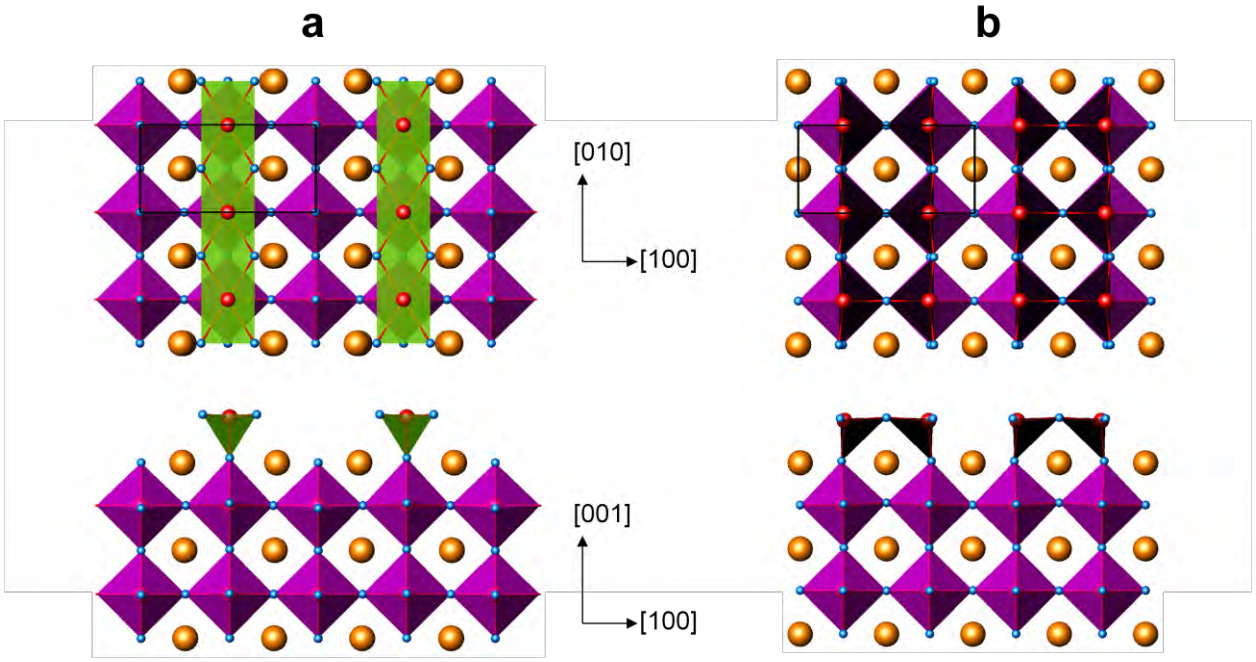

Fig. 3.1. Polyhedral representation of DFT-relaxed Castell 2×1 reconstruction models, in (top) plan view and (bottom) profile view: (a) 2×1TiO_2, and (b) 2×1Ti_2O_3. All polyhedra are Ti-centered. Purple polyhedra are 6-fold coordinated, green polyhedra are 5-fold coordinated and black polyhedra are 4-fold coordinated. Sr atoms in orange, Ti in red, O in blue.

Meanwhile, The DL model by Erdman *et al.* [34] can be described as follows:

- 2×1DL (Fig. 3.2(a)): Zigzagging <010> rows of edge-sharing TiO_5 polyhedra on top of a bulk-like TiO_2 plane. This leads to one distinctive ~~"d~~angling" O per surface cell, in single

coordination; this feature is one of the main contributors to the relatively high energy of this structure.

Kubo and Nozoye, while not observing the 2×1 themselves, extended their Sr adatom models to propose a similar structure with this periodicity [52]:

- 2×1-Sr (Fig. 3.2(b)): Starting with a TiO_2 bulk-like truncation, this model adds a Sr adatom per 2×1 cell above a hollow site, in fourfold coordination to O atoms.

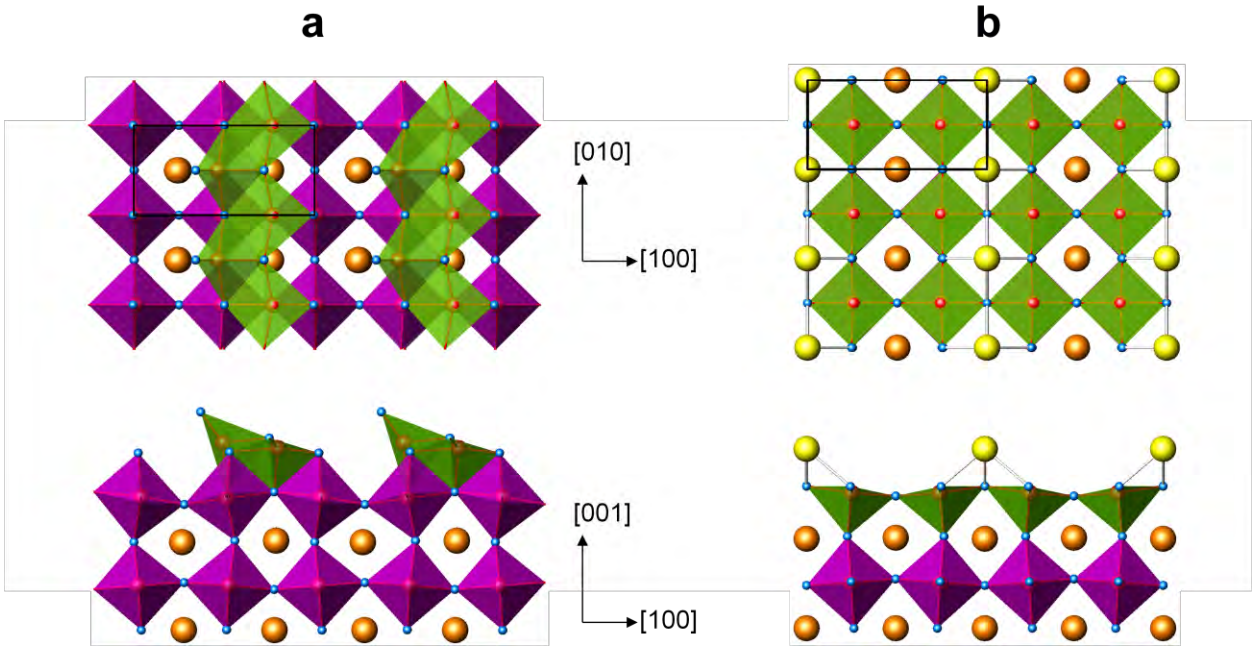

Fig. 3.2. Polyhedral representation of DFT-relaxed 2×1 reconstruction models, in (top) plan view and (bottom) profile view: (a) 2×1DL, and (b) 2×1-Sr. Legend follows Fig. 3.1, with the addition of Sr adatoms in yellow.

Johnston *et al.* [53] revisited the two 2×1 structural models by Castell and the DL model by Erdman *et al.*, along with both types of bulk-like truncation, using first-principle calculations to compute their surface energy as a function of TiO_2 chemical potential, oxygen partial pressure and temperature. It was found that the bulk-like truncations were most stable at realistically attainable pO_2 values, although the 2×1Ti_2O_3 had a window of stability for very low pO_2.

Arbitrarily removing the bulk-like truncations from consideration would lead to the 2×1DL model being favorable at 1000 K and in equilibrium with TiO_2 for $pO_2 > 10^{-8}$ atm, below which a 2×2 arrangement of O vacancies should be favored; Castell's experiments were conducted at around 10^{-13} atm [76]. The $2\times1TiO_2$ model was found to be unstable under all conditions and was therefore discarded for subsequent STM simulations. Said simulations consisted of 1 eV-wide energy windows of unoccupied states, displayed as constant-density contours. One prediction is that for the $2\times1Ti_2O_3$ the missing O rows would dominate the image.

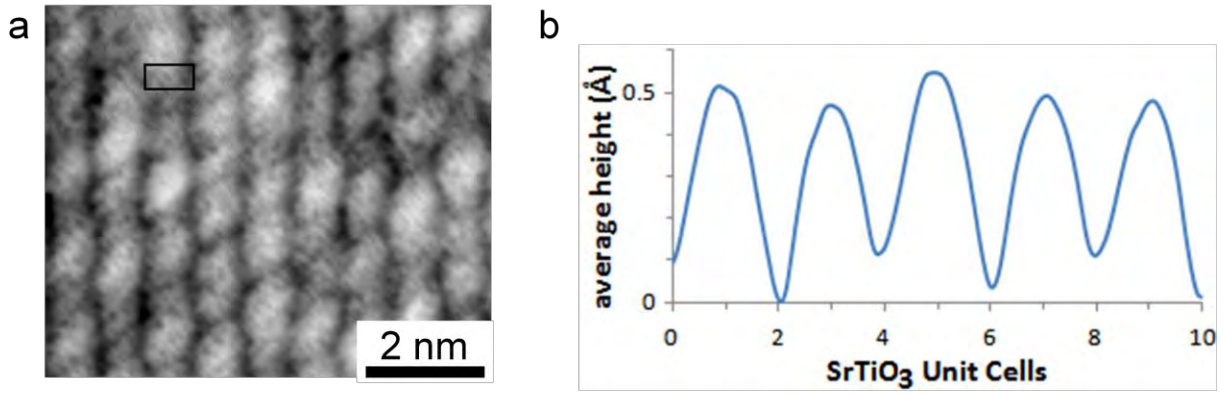

Fig. 3.3. (a) Scanning tunneling micrograph of the 2×1-reconstructed surface, with unit cell outlined; 2.0 V bias voltage, 0.5 nA tunneling current. (b) Typical average height plot, upon averaging along the rows.

Johnston *et al.* also reported a constant-current scanning tunneling micrographs of the 2×1 reconstruction. The images clearly resolve the 2-unit cell periodicity, but not the perpendicular single-cell period, so the surface appears as rows: a typical experimental STM image of the 2×1 surface is shown in Figure 3.3(a), courtesy of Prof. Martin R. Castell at the University of Oxford. The average row height is plotted in Figure 3.3(b) as a function of

position along the 2-unit cell periodicity direction with a typical corrugation height of between 0.4 and 0.5 Å.

In this context, DFT-based constant-current STM image simulations have been generated for the different 2×1 models with 2.0 V bias, specifying in each case a density value that gives the best match to the measured average corrugation, fixed at 0.45 Å. The simulated STM images are shown in Figure 3.4. The $2\times1TiO_2$ and 2×1-Sr models do the best at matching the near-sinusoidal profile of Fig. 3.3(b), with the Ti-centered surface polyhedra (in the former) and the Sr adatoms (in the latter) dominative the respective images.

The $2\times1Ti_2O_3$ structure is inconsistent with the STM experiments, as the corrugation of 0.45 Å is not attained for any specified density. At low densities, the experimental curve shape is well reproduced; one must agree with Johnston *et al.* that the dominant features correspond to the rows of O missing with respect to the TiO_2 truncation. However, the largest predicted corrugation is 0.28 Å, well below the experimental value. At higher densities, approaching the surface, the contrast is distorted dramatically (not shown).

The bond valence sums were calculated for the $2\times1TiO_2$, $2\times1Ti_2O_3$ and 2×1-Sr models; these are tabulated in Table 3.1. In the case of the $2\times1Ti_2O_3$ model, the BVS were calculated by considering the surface Ti to be in a 3+ valence state, to preserve the overall valence neutrality. Similarly, the 2nd-layer Ti atoms in the 2×1-Sr structure are also set to have a 3+ formal valence. What is found is that the models that successfully match the experimental STM images are the ones whose BVS metrics are inadequate.

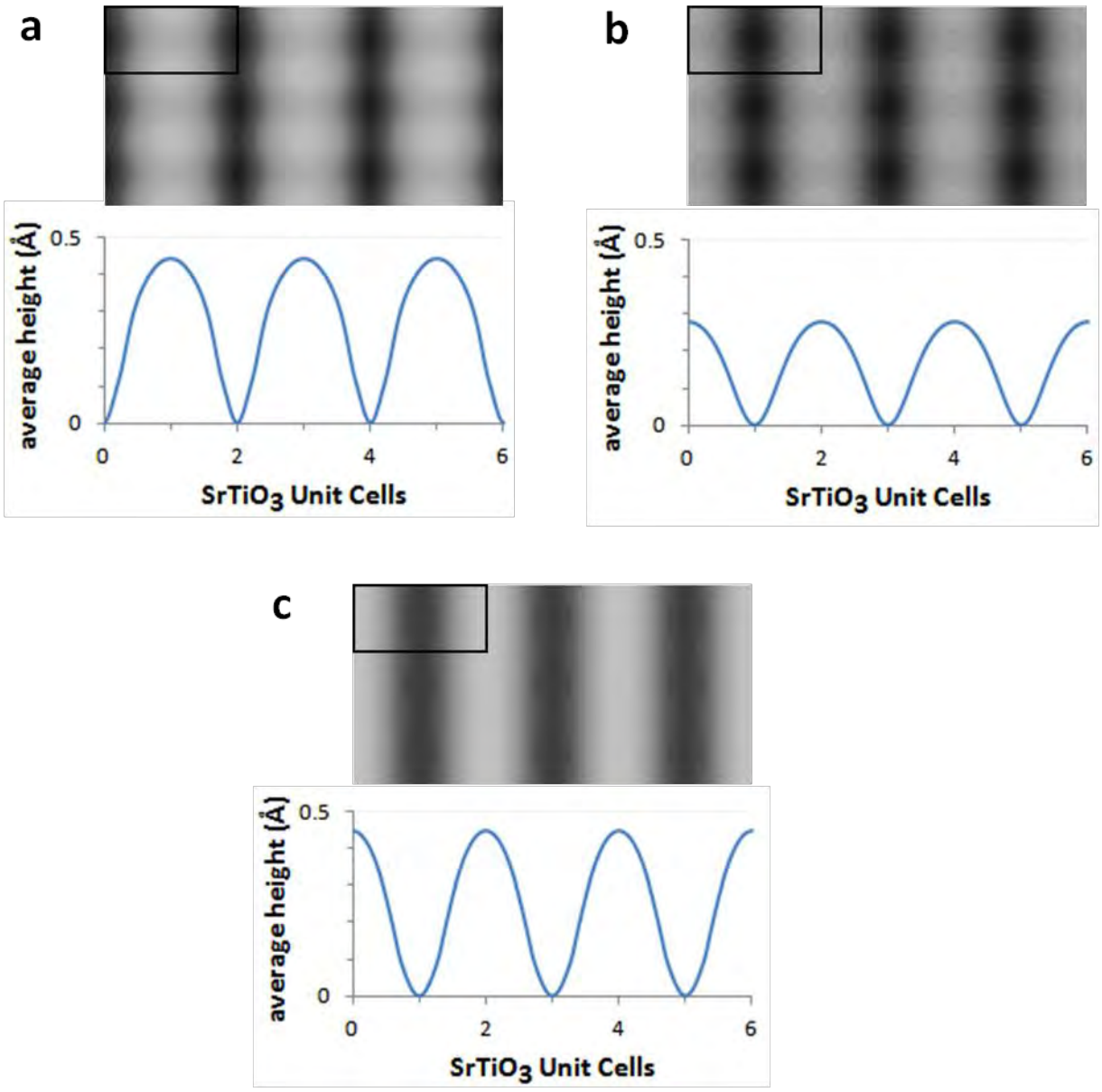

Fig. 3.4. 2.0 V STM image simulation (top) and average row height (bottom) for (a) 2×1TiO_2 model, (b) 2×1Ti_2O_3 model, and (c) 2×1-Sr model. Outlined 2×1 cells match the respective cells in Figs. 3.1 and 3.2.

For example, the 2×1TiO_2 structure has some severely underbonded atoms, especially in the top layer. Although there is some shortening upon relaxation of the surface Ti–O bonds (as compared to its original description by Castell, with each O1 atom directly on top of a Sr1 atom), these bonds are constrained to be much larger than in the bulk. This feature, which defines the

model, is the main contribution to the terrible SII value. Also, it is clear that this is intimately related to the high surface energy which led Johnston *et al.* to discard this model [53].

Similarly, the 2×1-Sr model fails due to the characteristic Sr adatom, whose BVS is only 1.26, far below the formal 2 valence. This indicates the adatom is very underbonded, which is to be expected since it is coordinated to only 4 O atoms, not to 12 like the bulk Sr. It is worth remarking the difference with respect to the PBE-based analysis by Enterkin [104], which yielded a BVS of 1.65 for the Sr adatom; this highlights the benefit of using a more accurate exchange-correlation functional. One should also refer back to the theoretical work by Liborio *et al.* [83], whose calculations predict that this large adatom density (0.5 per 1×1 cell) is very unstable; this is especially true given the initial BHF treatment by Castell, which etches SrO away, which indicates the experimental conditions were very far away from equilibrium with SrO.

The 2×1Ti_2O_3 structure, which failed to reproduce the experimental STM images, does significantly better, as evidenced by its SII, although it also exhibits undercoordination in the top layer, especially in the O atoms. Clearly, none of these three 2×1 models succeeds in both matching the observed STM images and having reasonable bonding. Moreover, all these models were among those taken into account by Herger *et al.* [93, 94] when fitting their surface X-ray diffraction data, and they were promptly discarded in favor of the 2×1DL (in combination with a ~~–z~~igzag" 2×2; see subsection 3.4.6).

In Chapter 5 it is argued that while the 2×1DL is the correct base structure, the addition of dissociatively adsorbed water leads to a model which resolves the high-energy concerns [53, 90, 96, 97] and is more consistent with STM images. Therefore, the BVS analysis and STM simulations are given in more detail in subsection 5.3.1, in comparison to hydrated models. For

reference, the SII of the 2×1DL structure (calculated with top 2 layers) is 0.28, which is relatively large and is driven by the ~~–d~~angling" O and one underbonded surface Ti. This is another indication that there is a need to tweak the presently accepted 2×1 model.

Table 3.1. Bond valence sums for the near-surface atoms of several 2×1 models. *m* is the atom multiplicity per 1×1 cell. The SII is also shown for each surface, calculated with the two outermost atomic layers. The value shown in parentheses is calculated with the three outermost atomic layers. The atom labels correspond to the CIF files.

	2×1TiO_2			**2×1Ti_2O_3**			**2×1Sr**		
SII	0.85 (0.63)			0.24 (0.19)			0.34 (0.27)		
	Atom	*m*	BVS	Atom	*m*	BVS	Atom	*m*	BVS
Top layer	Ti1	0.5	2.14	Ti1*	1	2.86	Sr1	0.5	1.26
	O1	1	–1.13	O1	1	–1.57			
				O2	0.5	–1.76			
2nd layer	Sr1	1	2.05	Sr1	0.5	1.99	Ti1*	1	3.18
	O2	0.5	–1.98	Sr2	0.5	1.98	O1	0.5	–1.87
	O3	0.5	–1.75	O3	1	–2.13	O2	0.5	–1.86
							O3	1	–1.72

*Nominal 3+ valence assumed

3.4.2. The "Brickwork" c(4×4) Reconstruction

Given the similarity in step morphology between (and the coexistence of) the 2×1 and ~~–b~~rickwork" c(4×4) reconstructions, it is likely that these are structurally similar. Castell proposed two c(4×4) models [76], each based on one of his 2×1 proposals:

- c(4×4)bw-TiO_2 (Fig. 3.5(a)): Starting with the 2×1TiO_2 structure, every fourth Ti along each row is removed, as well as two of the four surface O formerly bonded to it; the other O relax so as to make the neighboring Ti atoms 4-fold coordinated.

- c(4×4)bw-Ti_4O_5 (Fig. 3.5(b)): Starting with the 2×1Ti_2O_3 structure, every fourth pair of O along each pair of rows is removed, leaving the four neighboring Ti in 3-fold coordination.

These are shown here for completeness only and have not been DFT-relaxed or examined in detail. Since the precursor 2×1 can be discarded, these can be too. It is plain to see that these structures have many problems. The c(4×4)bw-TiO_2 model preserves many long Ti–O bonds and adds two "dangling" O, which cannot help with the high surface energy problem. Meanwhile, the c(4×4)bw-Ti_4O_5 model now has half of its surface Ti atoms in 3-fold coordination

Kubo and Nozoye also proposed a "brickwork" c(4×4) model based on Sr adatoms [52]:

- c(4×4)bw-Sr (Fig. 3.6): Every fourth Sr within the rows of adatoms is removed from the 2×1Sr structural model.

The c(4×4) surface appears in the STM micrograph (2.0 V bias) as a distinctive "brickwork" pattern of short linear units, seen in Figure 3.7, courtesy of Dr. Martin R. Castell. No corrugation value has been published for this surface, but it is reasonable to assume it to be in the order of 0.5 Å.

Let us examine the Sr-adatom c(4×4) model via STM image simulations, using the same biasing voltage. In this case, it is found that 0.5 Å corrugation cannot be reached with the vacuum thickness used in these calculations; this is due to the very large density of unoccupied states around the Sr adatoms. Using as low a density as possible (that is, so that the isosurface does not cross the middle of the vacuum region) produces the simulated micrograph shown in Fig. 3.7, superposed to the experimental image. This does match the simulation well, but the corrugation in this case is 2.2 Å, so one would need to go further away from the surface. The features seen here are not expected to change drastically.

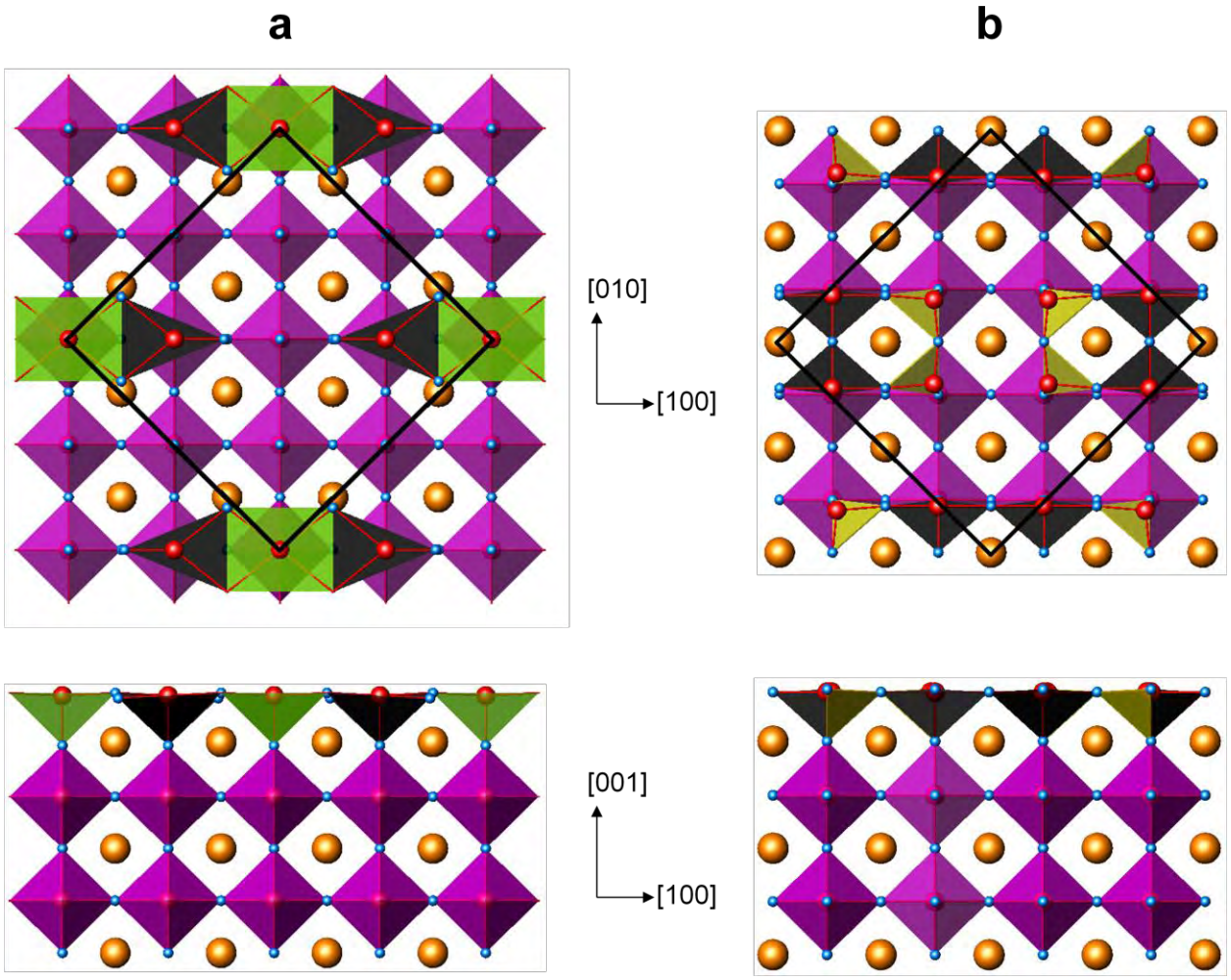

Fig. 3.5. Polyhedral representation of Castell c(4×4) surface models, in (top) plan view and (bottom) profile view: (a) c(4×4)bw-TiO_2, and (b) c(4×4)bw-Ti_4O_5. Figures are rotated 90º with respect to their 2×1 precursors in Fig. 3.1. These structures have not been relaxed by DFT; atomic positions are very roughly approximate. Legend follows Fig. 3.1, with the addition of yellow faces denoting 3-fold coordinated planar polyhedra.

However, Liborio *et al.*'s prediction that Sr-adatom models with an adatom surface density higher than 0.25 per 1×1 cell are unstable in all conditions [83] once again helps discard this model, since it corresponds to 0.375 adatoms per 1×1. Related to this is the fact that one can expect similarly low BVS for the adatoms as seen in the analogous 2×1 structure. No BVS analysis has been performed at present. Also, Enterkin did not carry out such analysis to this structure.

Ultimately, it becomes clear that no adequate structural models exist in the literature for the ~~–b~~rickwork" c(4×4), and this goes back to the fact that there are no decent 2×1 alternatives to the 2×1DL model, which is strongly supported by diffraction data. However, no ~~–b~~rickwork" c(4×4) model derived from the 2×1DL structure has been proposed, which is another shortcoming. This concern is also solved by the hydrated DL model in Chapter 5.

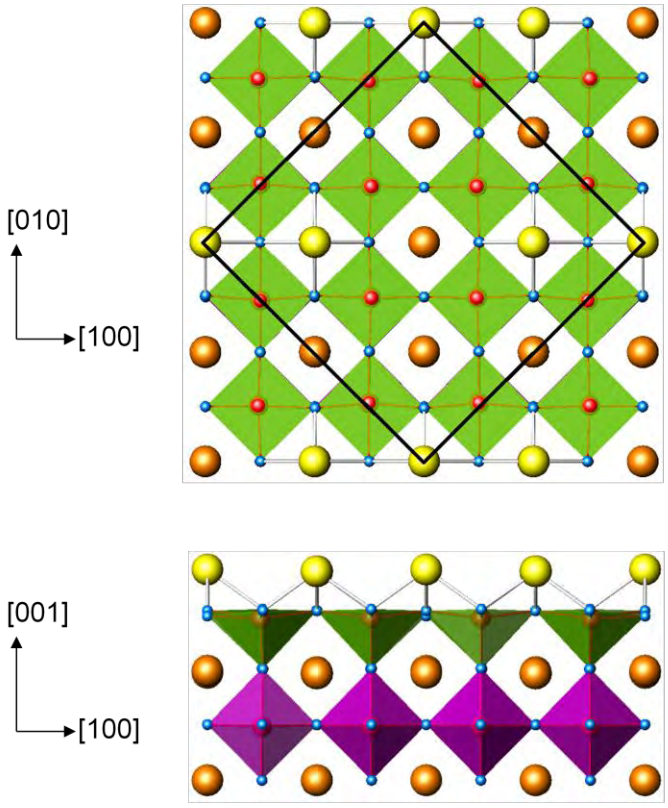

Fig. 3.6. Polyhedral representation of the DFT-relaxed c(4×4)bw-Sr structure, in (top) plan view, and (bottom) profile view. Legend follows Fig. 3.2.

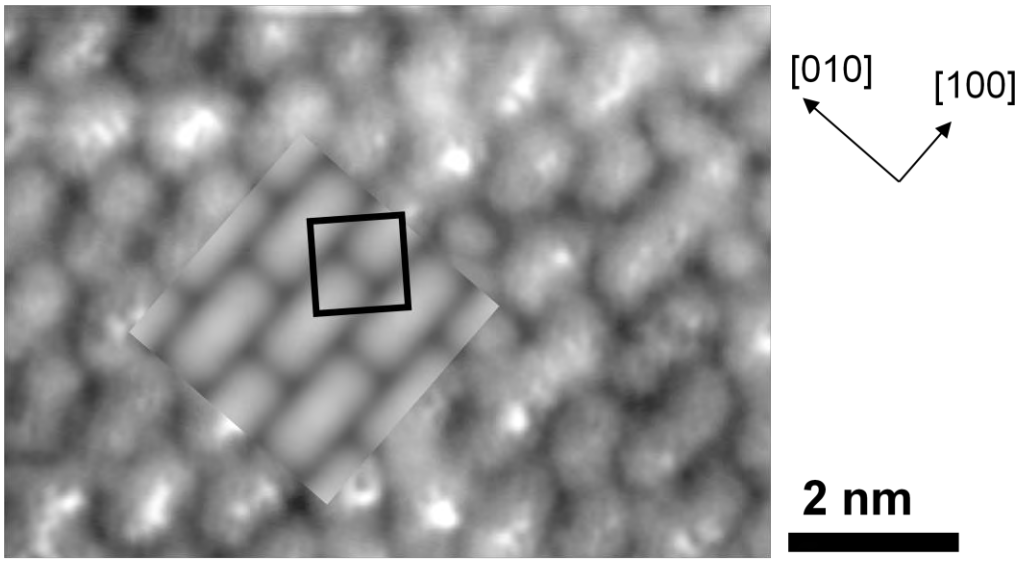

Fig. 3.7. Experimental scanning tunneling micrograph of the surface exhibiting a ~~–b~~rickwork" c(4×4) surface structure; 2.0 V bias voltage, 10 nA current. Simulated 2.0 V STM micrograph for the Sr-adatom c(4×4)A model is superposed, with the surface cell outlined.

3.4.3. The c(4×2) Reconstruction

The c(4×2) structure was also solved by Erdman *et al.* [89], using the same methods as for the 2×1. It exhibits c2mm symmetry and a distinctive surface feature consisting of a clustered quartet of edge-sharing polyhedra, as shown in Figure 3.8(a). This will be discussed in more detail in Chapter 4, were it is demonstrated that the simulations for this structure also reproduce the STM features successfully. Also, it is shown that the polyhedral quartet is a recurring feature and a central building block of more complex surface nanostructures. Also, the BVS analysis for this structure is deferred to Chapter 5, where along other DL structures, it is subjected to water vapor adsorption. For reference, the c(4×2)DL model has a SII of 0.18 (taking into account only the top two atomic layers), which is reasonable.

Earlier, Castell had proposed a structural model for the c(4×2) surface, under the premise that each of the two types of image he detected was a result of sampling different sublattices. This model is shown in Fig. 3.8(b). However, this model is unrealistic, as the topmost atoms are

extremely underbonded. In particular, each surface Ti atom is coordinated to just one O (compared to 6 in the bulk). Therefore, this model will not be pursued further.

Kubo and Nozoye also proposed a Sr-adatom model for this reconstruction, which is here labeled c(4×2)-Sr and is shown in Fig. 3.8(c). Although this structure was not examined by Liborio *et al.* [83], it has the same composition as the "square" 2×2 adatom model, which is one of the few such models with plausible stability, but only in the unrealistic regime of near-equilibrium with SrO. As mentioned earlier, the usual experimental STM image of the c(4×2) surface is characterized by one bright round feature per cell. As seen in Fig. 3.9, the STM simulation for the c(4×2)-Sr structure successfully reproduces the experimental pattern. As with other Sr-adatom models, the smallest corrugation attained within the available vacuum space is rather large (here, 2.9 Å). This is expected to decrease as one goes further away from the surface, but without significant change in the shape of the features. One other limitation of this model, however, is that it provides no plausible explanation for the alternative STM images, which show two small elongated features per c(4×2) cell [76].

Several things tip the balance in favor of the DL model. First and foremost, Erdman *et al.*'s model was derived from diffraction data. Second, the c(4×2)-Sr model is metallic, which is inconsistent with the need for a high STM bias to image it. Related to this is the fact that the c(4×2) can be formed in oxidizing conditions, which renders Sr-adatom models very unstable [83]. Finally, the DL model provides a plausible (though not definitive) explanation for the alternative STM appearance of the c(4×2). It is possible that decreased blurring due to increased tip sharpness actually splits each round feature into two elongated features. This was seen with preliminary STM modeling, although the final simulations do not quite produce this. While the polyhedral quartet feature allows for this possibility, a single adatom does not.

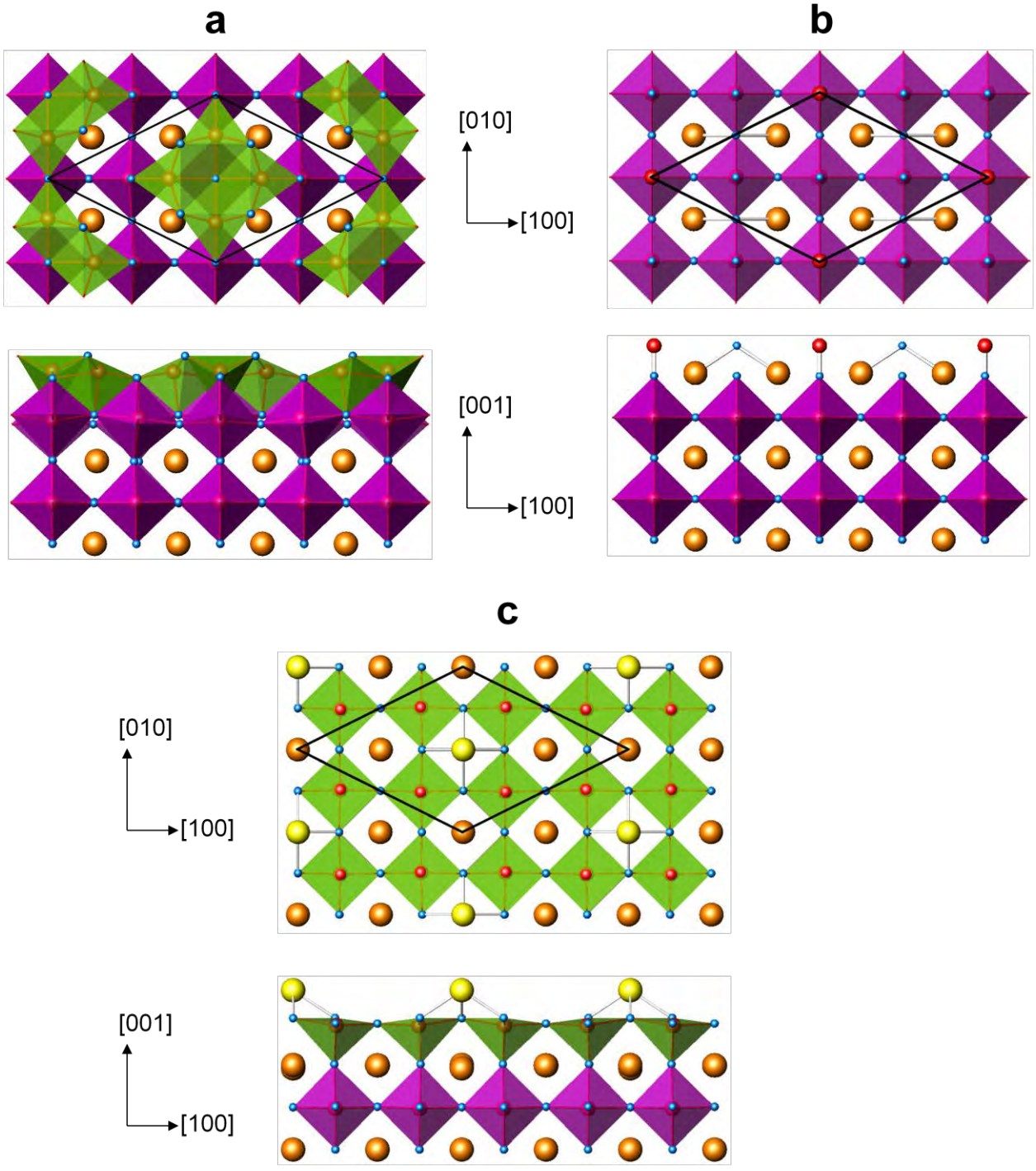

Fig. 3.8. Polyhedral representation of c(4×2) structures, in (top) plan view, and (bottom) profile view: (a) DL c(4×2) model, (b) Castell's model, and (c) c(4×2)-Sr model. Legend follows Fig. 3.2.

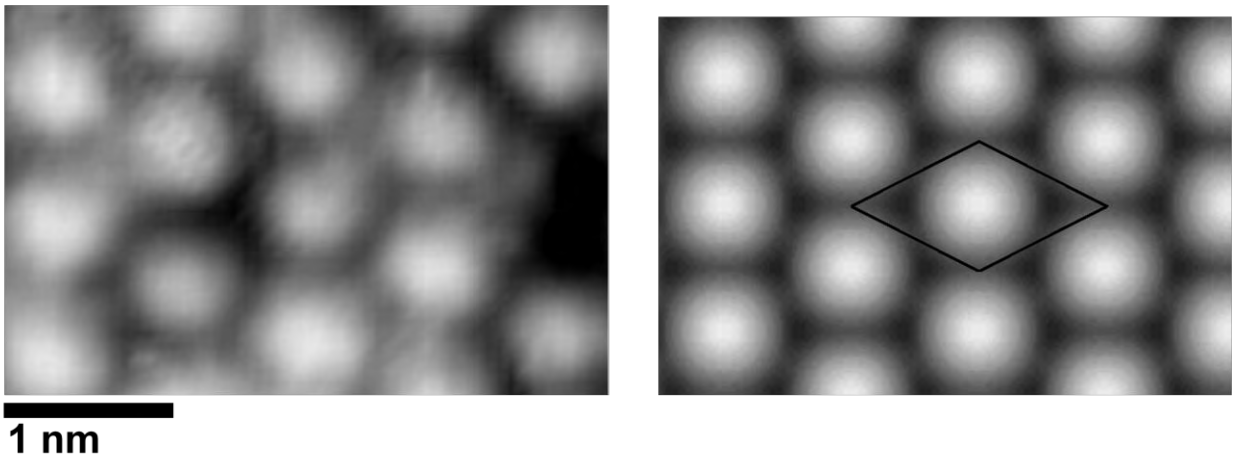

Fig. 3.9. (Left) Experimental STM image, 2.0 V bias, 0.1 nA tunneling current. (Right) Simulated STM image with 2.0 V bias voltage for the c(4×2)-Sr model. Outlined surface cell corresponds to cell in Fig. 3.8(c).

3.4.4. The RT5 Reconstruction

In empty-state STM images, this reconstruction is characterized by a single round feature per RT5 cell [51, 81, 84]. The earliest structural model for the RT5 reconstruction was based on periodic O vacancies in a Ti-rich bulk-like truncation [80, 81]. The work by Kubo and Nozoye [51, 52] makes a good case against this model, pointing out that this structure breaks the fourfold symmetry and should theoretically exhibit either an elongated feature per cell or split into two small ones [105, 106]. Also, the general decrease in the density of STM features with annealing temperature in UHV, as observed experimentally [52], disproves this structure: if the features corresponded to O vacancies, one would expect more of these to appear.

The RT5 surface was the reconstruction which led to the original Sr-adatom model by Kubo and Nozoye, shown in Fig. 3.10(a) [51]. The typical STM corrugation is in the order of 0.2-0.5 Å [51, 81]. The STM image simulation (using a 0.65 V bias, as in Ref. [51]) of the RT5-Sr model is unable to reproduce such a corrugation due to the very large density of unoccupied states, especially around the Sr adatoms. Setting the charge density as low as possible (that is,

keeping the isosurface from crossing the middle of the vacuum) produces an image like that shown in Fig. 3.11(a). This has a very large corrugation of 3.8 Å. A larger vacuum spacing (and larger tip-sample distance) would be necessary to reach reasonable values, but the features are not expected to change significantly. The simulation is generally a good match, although the individual bright features are less well resolved than in the experimental images (not shown). This can be solved by using larger densities (that is, using an isosurface that is closer to the surface), but this would make the corrugation even larger

.

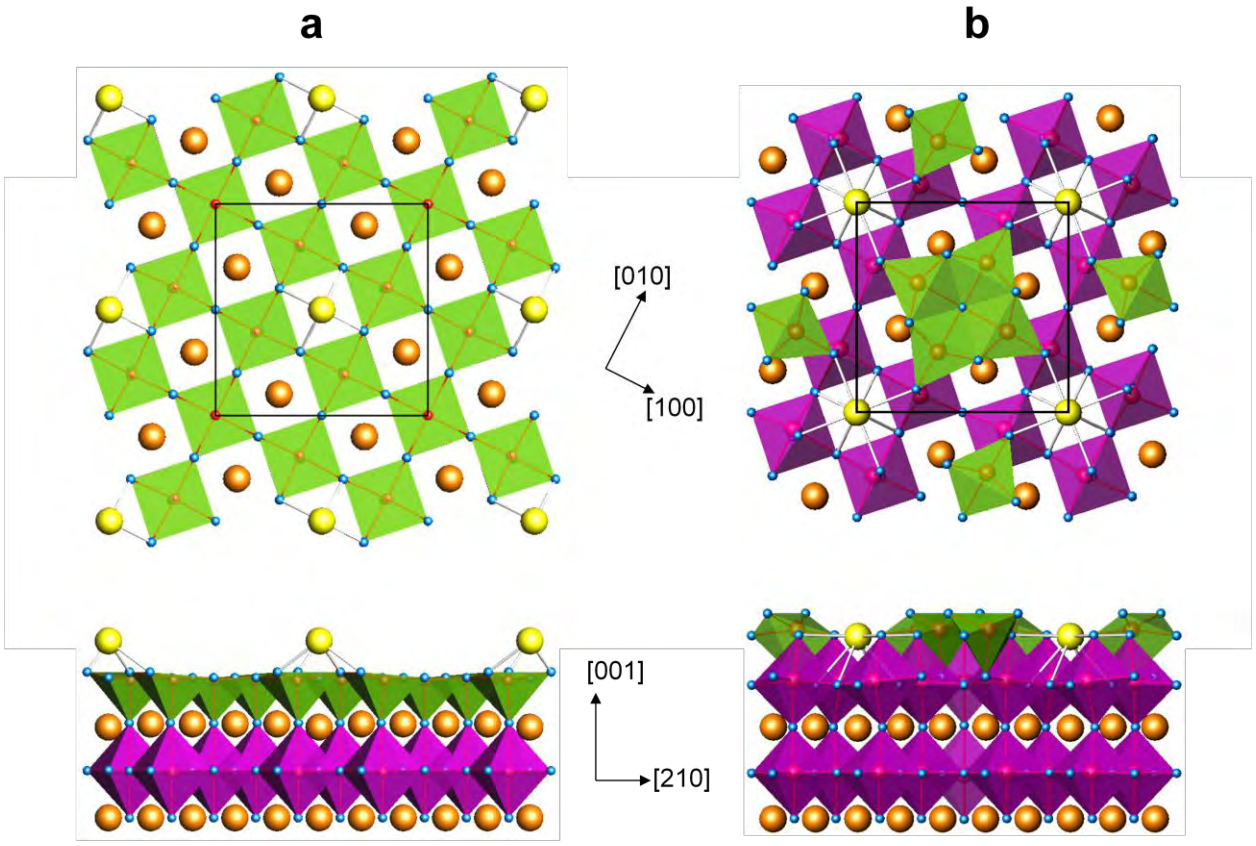

Fig. 3.10. Polyhedral representation of DFT-relaxed RT5 structures, in (top) plan view and (bottom) profile view: (a) Sr-adatom model, and (b) RT5-Q model. Legend follows Fig. 3.2.

Given the shortcomings of the Sr-adatom models for other periodicities, an alternative RT5 structure is tested in this subsection, based largely on the c(4×2)DL surface. Its characteristic polyhedral quartet is arranged on top of a bulk-like TiO_2 truncation, following the same registry as in the c(4×2). This implies that the quartet motifs are no longer corner-sharing. One Sr is added per surface cell to keep the structure valence neutral. This is dubbed the RT5-Q model and it is shown in Fig. 3.10(b).

The STM simulations of this surface have partial success. One big problem with this structure is that its large bandgap means that there are no unoccupied states into which tip electrons may tunnel, unless the bias voltage is set to roughly 2.0 V or larger. This is inconsistent with the observations by Newell *et al.* [84] and by Kubo and Nozoye [51], who can image the RT5 over wide ranges of bias voltages. Upon reaching this voltage and setting the corrugation to 0.5 Å, the simulations do reproduce the slanted squareness of the features, as detected by Newell *et al.* for large tunneling currents; see Figure 3.11(b). Of course, this is meaningless given the bias needed. Surprisingly, the square-like features do not correspond to the polyhedral quartet motif, but are centered around the Sr, with most brightness coming from the O at the corners of the quartet motifs.

BVS analysis of this model has also been performed to test its viability. As seen in Table 3.2, this surface has adequate bonding. There are some underbonded and overbonded atoms on the topmost layer, but all deviations from the formal valence are moderate. In particular the Sr is coordinated to 8 O atoms, twice as many as the Sr adatoms in the other model. Moreover, the second layer atoms are very close to having ideal bonding, so the overall SII is quite reasonable. While the RT5-Q may not be the structure seen experimentally, at present there is no reason to think this structure is unfeasible.

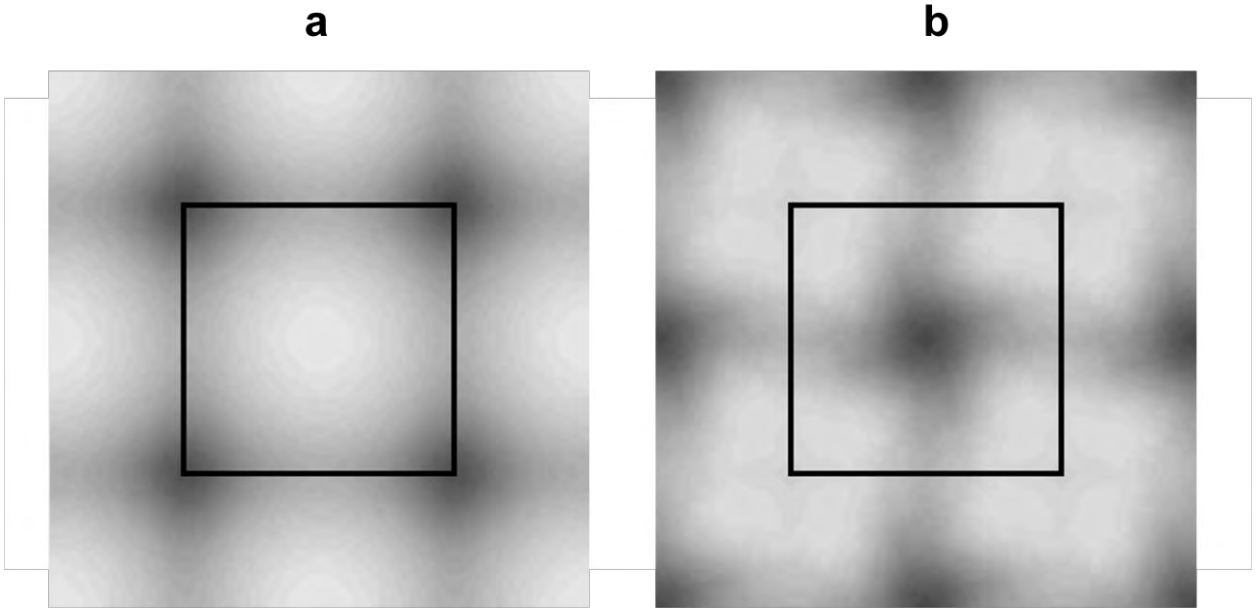

Fig. 3.11. Simulated STM images for RT5 models: (a) Sr-adatom model, 0.65 V, and (b) RT5-Q model, 2.0 V. Surface cells outlined correspond to respective cells marked in Fig. 3.10.

Table 3.2. Bond valence sums for the near-surface atoms of the RT2-Q model. The SII is also shown.

	RT2-Q		
SII	0.18 (0.17)		
	Atom	*m*	BVS
Top layer	Ti1	0.8	3.69
	Sr1	0.2	1.73
	O1	0.2	–2.26
	O2	0.8	–1.75
	O3	0.8	–1.87
2nd layer	Ti2	0.2	4.10
	Ti3	0.8	4.07
	O4	0.8	–1.96
	O5	0.4	–2.07
	O6	0.8	–2.13

Ultimately, one must refer back to the recent STM work by Shiraki and Miki [86], who discovered a surprising but unmistakable break in the fourfold symmetry, when imaging the occupied states of the RT5 reconstruction with a high tunneling current. This asymmetry was

observed at what would correspond, in Kubo and Nozoye's model, to the adatom site. Neither this model nor the RT5-Q model explored here can adequately explain this, so the RT5 structure remains a mystery.

3.4.5. The RT2 Reconstruction

As mentioned above, the RT2 reconstruction has been calculated to be the most thermodynamically stable DL structure by Warschkow *et al*. [90]. However, this surface has never been observed experimentally and was merely explored as a hypothetical structure. It has p2gg symmetry and, as seen in Figure 3.12(a), it consists of parallel rows of surface polyhedra running along a <110>-type direction. In case it is ever detected, the STM image simulation for this surface is presented here for future reference.

It is predicted that a bias voltage of ~2 V should be necessary to start imaging this surface. At this bias, the density of unoccupied states is dominated by the areas between the <110> rows of polyhedra; this is seen in Fig. 3.13(a). At higher voltages, the contrast is inverted and the polyhedral rows themselves are imaged, as seen in Fig. 3.13(b) for a bias of 2.6 V. In both cases, the lack of a (110) mirror plane is noticeable, as the bright rows are wavy in nature.

The BVS analysis is, as for other DL models, deferred to Chapter 5. However, the results may be summarized by noting that this model has a very low SII (0.13), as expected for such a low-energy structure.

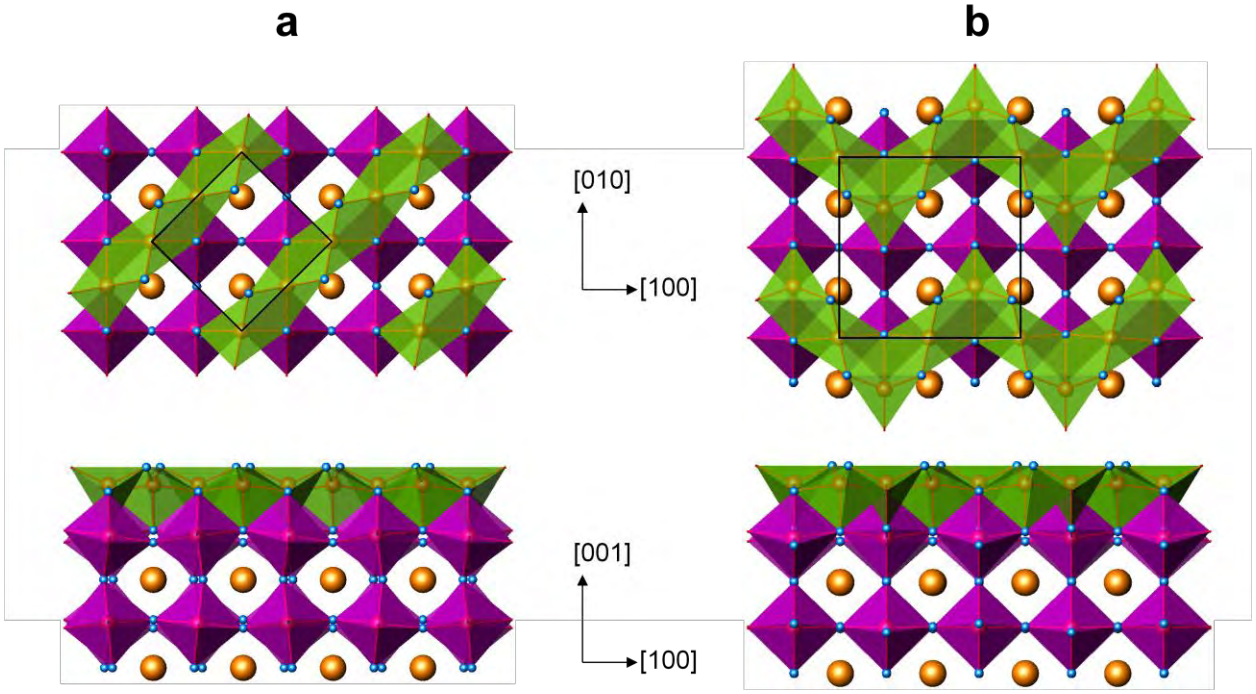

Fig. 3.12. Polyhedral representation of DFT-relaxed DL structures in (top) plan view, and (bottom) profile view: (a) RT2 reconstruction, and (b) ~~"z~~igzag" 2×2 reconstruction. Legend follows Fig. 3.1.

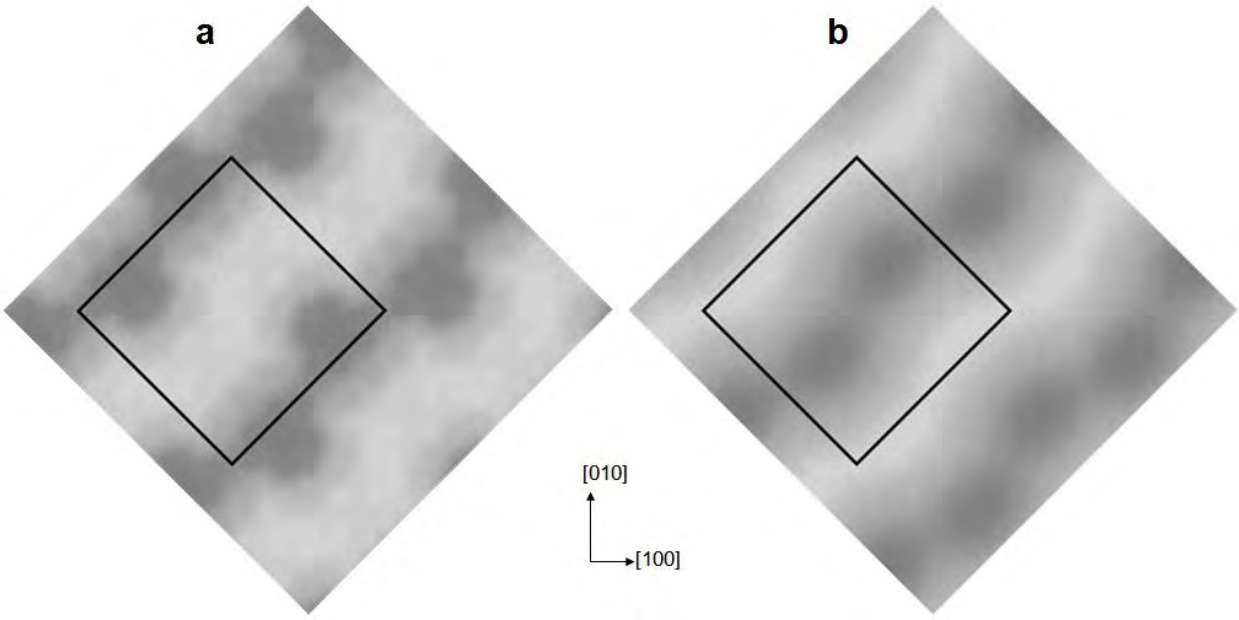

Fig. 3.13. STM image simulations for the RT2 DL reconstruction with (a) 2.0 V bias and (b) 2.6 V bias. Outlined cells correspond to surface cell marked in Fig. 3.12(a).

3.4.6. The "Zigzag" 2×2 Reconstruction

Also proposed by Warschkow *et al.* [90], this geometry was found in their report to be the most stable DL structure with 2×2 periodicity. It was also observed to coexist with the 2×1 reconstruction by Herger *et al.* via surface X-ray diffraction [93]. This surface has p2gm symmetry and can be qualitatively described as an ordered alternation of 2×1 units of opposite orientation. As can be seen in Figure 3.12(b), the 2×2 structure also yields a zigzagging row of surface polyhedra.

Since this structure yields similar diffraction patterns as the 2×1 surface, one question is whether the STM observation of the 2×1 could actually be this "zigzag" reconstruction. This is a fair concern, as no real-space reports of this 2×2 exist. It can be tackled via DFT-based STM simulations, so a typical simulated STM image with 2.0 V bias is shown in Fig. 3.14. It is clear that the periodicity of the "zigzag" 2×2 would be easily resolved along all directions, should it ever be imaged.

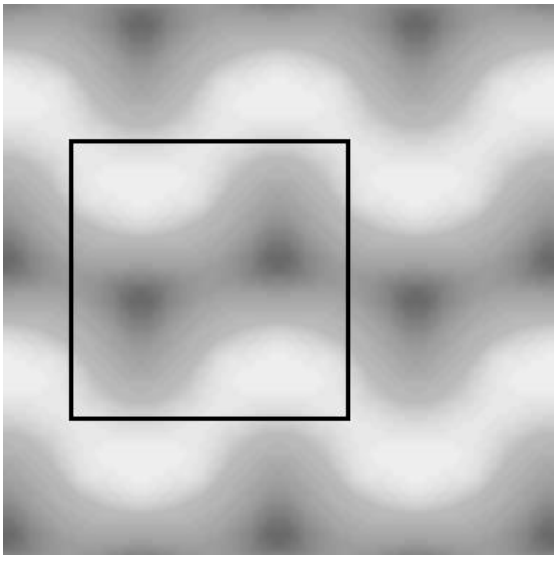

Fig. 3.14. Simulated STM image for the DL "zigzag" 2×2 reconstruction, with 2.0 V bias. Outlined cell corresponds to surface cell marked in Fig. 3.12(b).

This simulation appeared in the paper by Lin *et al.* [55], which addressed the structure of a 2×2 reconstruction that showed a square arrangement of bright, round features. Despite exhibiting only 2-fold rotational symmetry, the ―zigzag" 2×2 was included in that manuscript for completeness, since it is has a lower surface energy than the DL ―square" structure [90].

This reconstruction is explored further in Chapter 5, in the context of H_2O adsorption on DL surfaces.

3.5. Discussion

Aside from the models put forward by Castell [76], three main families of structural models have been proposed: ordered O vacancies on a TiO_2 bulk-like truncation, periodic Sr adatoms, and DL models. The first has not gained much traction, largely because of the fact that said vacancies would show up in STM images as elongated features [105, 106], which repeatedly fails to be observed. The only exception might be ―brickwork" c(4×4) reconstruction, but this is derived from a 2×1 surface, where vacancy-based models are untenable.

Among the Sr-adatom models, the ―square" 2×2 has been shown via STM image simulations to do worse than a DL model [55]. The c(4×2)Sr, while providing a good match to typical experimental STM micrographs, has several shortcomings. Among them is the fact that the anomalous STM pattern occasionally seen experimentally upon tip replacement cannot be explained with this structure. Also, the c(4×2) has been formed in oxidizing conditions and proved to be air stable, which Sr-adatom models certainly are not. More importantly, the DL model for this reconstruction was not a speculative proposal, but a direct result of electron diffraction data [89]. The last two points are similarly applicable to the 2×1 reconstruction.

The flagship Sr-adatom model, the RT5, presents other problems too. For example, Newell *et al.* [84], despite subscribing to this model, report that the RT5 is more Ti-rich than the ―square" c(4×4). Even if the latter were itself a Sr-adatom model, the adatom RT5 model would necessarily be less Ti-rich.

The biggest problem for all reconstruction models based on Sr adatoms is that they imply a severe reduction of the surface. As the theoretical study by Liborio *et al.* [83] shows, heat and ultra-high vacuum are not enough to achieve this: in a regular UHV environment, no Sr-adatom model is thermodynamically stable in the range of temperature range required to generate any of these periodic reconstructions. For any of these models to be stable (and this would encompass the problematic structures already discussed in this section), one needs to be at or near equilibrium with SrO, which in practice would entail something like annealing the $SrTiO_3$ in close proximity to strontium oxide or metal strontium. The adatom models are indefensible, then, when one considers that most reconstructions form either in SrO-poor crystals (from BHF treatment) or in oxidizing conditions.

Given the unsatisfactory proposed structures for the RT5 reconstruction, an alternative structural model, inspired by the c(4×2) DL model, has been tested here. The STM simulations do not support this model, as it is insulating, which is inconsistent with the low-bias STM imaging obtained experimentally [51, 84]. Although this structure is most probably not the same as the RT5 observed experimentally, its formation under different conditions is plausible.

Most of the discussion on DL models has been deferred to other chapters, but at present this family of reconstructions is the most consistent with the experimental evidence. The 2×1, ―zigzag" 2×2, c(4×2) and c(6×2), as well as the similar RT13, have been solved from diffraction data; one of the ―square" 2×2 surfaces also has a DL structure, as determined from STM image

simulations. Of these, the most problematic structure is the 2×1, which has a relatively high energy. This is resolved in Chapter 5, where it is shown that although the base structure is correct, the addition of chemisorbed water leads to a model more consistent with theory and experiments.

3.6. Conclusions

In this chapter, the viability of many $SrTiO_3$(001) surface structures proposed in the literature has been explored, mostly as alternatives to DL periodic reconstruction models. For this, chemical bonding analysis via bond valence sum calculations has been employed, as well as DFT-based STM image simulations. No good substitutes to the presently accepted models have been found, as Sr-adatom models and other reduced structures display too many shortcomings.

The RT5 reconstruction remains an elusive case, as no structural model at present is fully consistent with the theoretical and experimental constraints. A new model has been proposed and tested here, but while it seems energetically plausible, it is inconsistent with the experimental STM findings.

Predicted STM images for the DL "zigzag" 2×2 and RT2 reconstructions, which have never been imaged, have been presented.

Then there is the open charm felt of the structural features
which are not hidden [...], but are clearly revealed.
Gustav Stickley

Chapter 4. Recurrent Structural Motifs: $SrTiO_3(001)$

4.1. Introduction

The ability to form periodic reconstructions is clearly an important mechanism for the stabilization of surfaces in metal oxides. As has been seen, the (001) surface of strontium titanate shows much flexibility, exhibiting structures with different periodicities and characteristic features. In this chapter, one such structural motif is explored, as it recurs across several different $SrTiO_3(001)$ surface reconstructions and nanostructures, which is indicative of its stability. This feature was first discovered via a combination of transmission electron diffraction, direct methods and density functional theory (DFT) by Erdman *et al.* [89], as a crucial component of the c(4×2) surface reconstruction.

This structure was introduced in subsection 3.4.3 and, like other $SrTiO_3(001)$ reconstructions, the c(4×2) was found to have a double-layer TiO_2 (DL) termination, with the

second topmost layer qualitatively resembling the arrangement of TiO_2 planes in bulk $SrTiO_3$. The top layer consists of a periodic pattern based on a distinctive feature, which in turn consists of a clustered quartet of edge-sharing TiO_5 polyhedra. In Chapter 3, other structural models were examined, but none was found to be an adequate alternative. In the particular case of the c(4×2) reconstruction, it is well known that the quartets (which are roughly squares of c(2×2) dimensions) run in corner-sharing alignment along only one [001]-type direction, with each row of quartets "out of phase" with the next row. The structure is shown in its polyhedral representation in Fig. 3.8(a). Scanning tunneling microscopy (STM) image simulations, performed by Lin *et al.* [55], indicate that this DL motif is also central to the structure of one of the "square" 2×2 reconstructions.

The generation of a novel type of surface nanostructures upon ultra-high vacuum (UHV) annealing of a c(4×2)-reconstructed $SrTiO_3$(001) surface was first reported by Castell [107]. These were seen via high-bias STM after thermal treatment in the 850-1200 ºC range. The observed surface features included isolated and close-packed "dilines", a type of linear nanostructure, as well as arrays of small features, later termed "crossdots". These coexist with a background of c(4×2) terraces, 0.2 nm lower than the top of the nanostructures. X-ray photoelectron spectra (XPS) detected no impurities at the surface, which discards possible impurity segregation as the cause of these surface structures. Above 1200 ºC, the surface was found to revert to a c(4×2) periodicity. Castell proposed several SrO- and TiO_2-rich models, although no further chemical characterization was reported.

Deak *et al.* [108] expounded on the above report, identifying several other characteristic structures after carefully controlling the annealing time and temperature. Among these were three other kinds of <001>-oriented "nanolines", in addition to the dilines. These were called

–*m*eta-dilines", –*tr*ilines" and –*te*tralines", these names being indicative of the number of row-like features within each structure. Also, Auger electron spectroscopy (AES) showed that the surface, when covered by dilines, trilines and crossdots (the dominant nanostructures), is more Ti-rich than not only a cleaved sample, but also surfaces with DL reconstructions, such as the c(4×2) or the 2×1. Moreover, the AES peaks demonstrated that these nanostructures contained Ti predominantly in the 4+ formal valence state. The growth, formation and ordering dynamics of these nanostructures were addressed by Marsh *et al.* [109] via *in situ*, high-temperature STM. Most interestingly, trilines were consistently observed to form from pairs of dilines, never from a single diline.

Silly *et al.* [110] evaporated Pd on a $SrTiO_3$(001) surface covered in dilines, trilines and crossdots. Subsequent UHV annealing at 620 ºC for 1 hour produced Pd nanocrystals which were encapsulated by an incommensurate thin layer of TiO_x, as determined via STM, a clear example of strong metal–support interaction. Meanwhile, Deak *et al.* [24, 25] demonstrated the use of c(4×2) reconstructed surfaces, as well as surfaces covered by nanostructures, as templates for self-assembled, close-packed arrays of fullerenes. The capability of doing this reproducibly with other species would potentially enable the synthesis of nanoscale devices.

Given the strong substrate-molecule/nanoparticle interaction required for ordered nanoscale patterning, the determination of the atomic-level structure of these TiO_x-rich surface nanostructures is a crucial step towards engineering $SrTiO_3$(001) surfaces for this purpose. In this chapter, the DL structure of the c(4×2) $SrTiO_3$(001) reconstruction is verified and it is found, via high-bias STM image simulations, that its characteristic structural motif is an essential component of some of these linear nanostructures. In particular, the focus is on developing full structural models for the dilines and trilines, by further exploiting first-principles STM

simulations. These models are identified as consisting of a triple TiO_x layer termination and all surface Ti are found to form TiO_5 polyhedra in edge-sharing arrangements, which is similar to all experimentally observed DL surfaces.

4.2. Methods

4.2.1. Experimental Methods

The experimental component of this work was performed by collaborators at the University of Oxford, Prof. Martin Castell and Dr. Matthew Marshall. The techniques used include scanning tunneling microscopy (STM), Auger electron spectroscopy (AES) and X-ray photoelectron spectroscopy (XPS). Single-crystalline, 0.5 wt.% Nb-doped $SrTiO_3$(001) wafers (7×2×0.5 mm) were commercially purchased (PI-KEM Ltd, United Kingdom) for scanning tunneling microscopy (STM) studies in an ultra-high vacuum JEOL JSTM4500S. Doping was necessary to render the specimens electrically conductive for experimental analysis.

c(4×2)-reconstructed surfaces were produced in the following manner: the specimens were etched for 10 min with a buffered NH_4-HF solution, shown by Kawasaki *et al.* [111] to preferentially remove surface SrO; Ar^+-sputtering inside the UHV chamber (base pressure 10^{-8} Pa) was carried out with a VG Microtech gun for 10 min with 0.5 kV ion energy and a 45º incidence angle; finally, UHV resistive heating for 15 min at 1200 ºC was performed by applying a direct current through the samples [107].

Nanostructured surfaces were obtained via Ar^+-sputtering for 10 min with ion energy of 1.0 kV and a 45º incidence angle, followed by a 2 hr UHV anneal at 900 ºC. Auger electron spectra were obtained using a SPECS PHOIBOS 150 hemispherical electron energy analyzer attached to a JEOL TM Z9043T UHV scanning electron microscope. X-ray photoelectron

spectroscopy was performed in a Scienta ESCA 300 X-ray photoelectron spectrometer (Al K_α source, effective energy resolution of the spectrometer of 350 meV) at the National Center for Electron Spectroscopy and Surface Analysis (NCESS) at the Daresbury Laboratory, United Kingdom. The surfaces were cleaned by heating for 5-10 minutes at 600 °C prior to analysis.

4.2.2. Density Functional Theory and STM Image Simulations

First-principle density functional calculations were performed to model the different surfaces, using the repeated slab configuration. All DFT calculations were carried out using an augmented plane wave + local orbital (APW+lo) basis set with the full-electron-potential WIEN2k code [46]. Every structure modeled was relaxed until the residual force on each atom was under 0.2 eV/Å. The exchange-correlation functional of choice was the PBE [98] implementation of the generalized gradient approximation (GGA). The optimized PBE lattice parameter value of $a_{SrTiO_3}^{PBE} = 3.944$ Å was enforced in the dimensions parallel to the surface plane.

The c(4×2) slab consisted of 13 atomic layers, while the nanoline models varied in thickness, with the final slabs consisting of 11 atomic layers. Muffin-tin radii of 2.40 (Sr), 1.68 (Ti) and 1.50 (O) bohr were consistently employed, along with a maximum *K* value for the plane wave expansion of 5.25/1.5 bohr^{-1}. In each model, a *k*-point mesh equivalent to an 8×8×8 mesh for a bulk $SrTiO_3$ unit cell was used. A vacuum spacing of at least 10 Å between slabs was used. All relevant structures are included in Appendix D in the Crystallographic Information File (CIF) format.

Constant-current, high-bias STM image simulations were generated from the WIEN2k outputs, following the structural relaxation. This was done through the modified Tersoff-

Hamann method described in subsection 2.2.3 and in Appendix A; as explained there, the PBE functional is adequate for this purpose, in spite of some of its known limitations. The artificial density of unoccupied states was sampled at intervals of $a_{SrTiO_3}^{PBE}/20$ (~0.2 Å) along the in-plane dimensions and 0.3 Å along the out-of-plane direction.

4.2.3. Bond Valence Sum Analysis

Bond valence sums (BVS) were calculated for surface Ti atoms in non-defective nanoline models. The following R_0 (standard bond length) values were employed to calculate each bond valence (see section 2.2.2): 1.815 Å for Ti^{4+}–O^{2-} and 1.791 for Ti^{3+}–O^{2-} [102]. No R_0 value appears to exist in the literature for Ti^{2+}–O^{2-}. The empirical constant b (see Eq. 2.4) was kept at its usual value of 0.37 Å. The volume of each supercell was expanded isotropically to match the lattice parameter to the experimental a_{SrTiO_3} value of 3.905 Å. The bond valence sums were computed using the KDist software from the Kalvados program suite [103], allowing each Ti atom to adopt its preferred formal state (3+ or 4+) for the calculation. This was repeated for rocksalt TiO for a reference on the 2+ state, borrowing a structure from the literature [112].

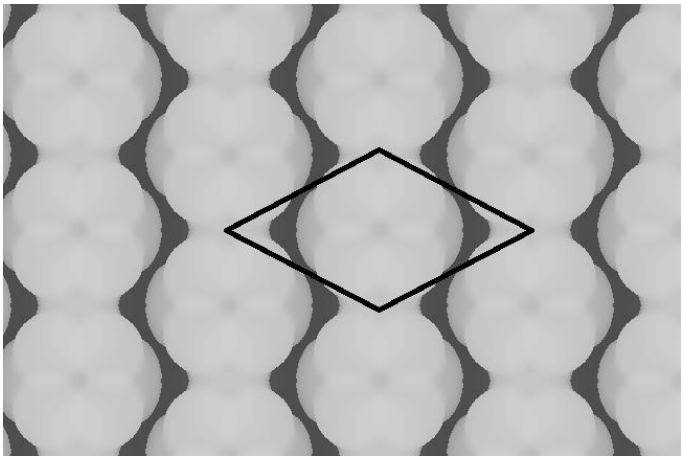

Fig. 4.1. DFT-based 2.0 V STM image simulation of the DL c(4×2) reconstruction, unit cell outlined.

4.3. Results

4.3.1. The c(4×2) Reconstruction

As expected, the STM images of c(4×2)-reconstructed samples [76] show step heights of approximately 0.4 nm (one $SrTiO_3$ bulk unit cell), implying only one type of surface termination. As shown in Fig. 4.1(c), the main feature in images with bias voltage of 2.0 V is a round bright spot which is present exactly once per c(4×2) cell; the image is courtesy of Prof. Martin Castell at the University of Oxford. Since the atomic-scale structure is known in this case, it is possible to generate a STM image simulation for direct comparison and subsequent attribution of the bright feature to a particular structural element. The 2.0 V DFT-based simulation of the relaxed c(4×2) surface is in good agreement with the experimentally observed micrographs, as can be seen in Fig. 4.1; this supports the claim that this structure is the same as the one solved via transmission electron diffraction. Moreover, one can conclusively say that the aforementioned polyhedral quartet motif is responsible for the observed round spot.

4.3.2. Dilines

The nanolines form reproducibly on $SrTiO_3$(001) surfaces as shown in the STM micrograph in Fig. 4.2, courtesy of Prof. Martin Castell and Dr. Matthew Marshall at the University of Oxford; these can also be seen in Ref. [113]. One class of nanoline which appears in the STM images is the diline. Dilines have a ridge-and-valley structure with 6×2 periodicity in close-packed domains. The latter number indicates the periodicity along the [100]-type nanoline growth direction (hereafter "longitudinal" direction) and the former labels the periodicity along its perpendicular (hereafter "transverse") direction. The STM corrugation indicates that the top layer is one atomic layer higher than the known DL TiO_2-rich

reconstructions such as the aforementioned c(4×2), often found as a precursor to (or in coexistence with) nanolines [107]. A characteristic bright round motif is the main building block of the diline structure; it is the stacking of said motifs in two parallel rows that gives the diline its name. This type of nanoline can exist in two configurations: square, where the spots from contiguous rows are aligned along the longitudinal axis; and zigzag, where the spots are ~~"o~~ut of phase" by one bulk unit cell with respect to those in the next row. The rows are 0.78 nm apart, so the separation between the centers of adjacent motifs under the square configuration is exactly two bulk unit cells. Auger electron spectra indicate that dilines are more Ti-rich than cleaved surfaces and DL reconstructed structures such as the c(4×2) surface.

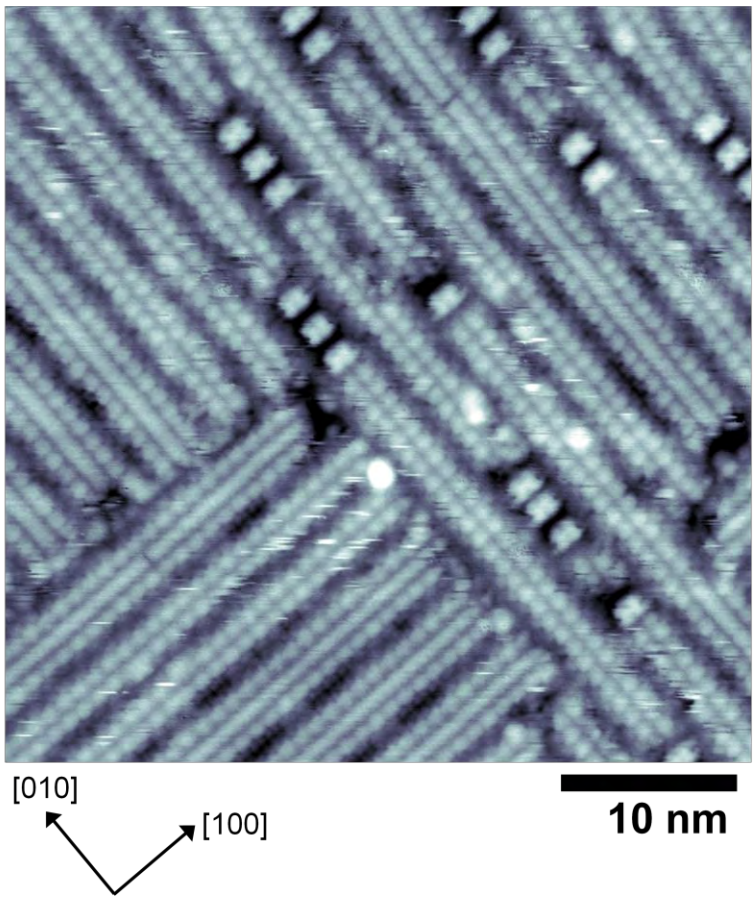

Fig. 4.2. STM image of a typical nanostructured $SrTiO_3$(001) surface dominated by dilines, trilines and crossdots (1.98 V bias, 0.23 nA tunneling current).

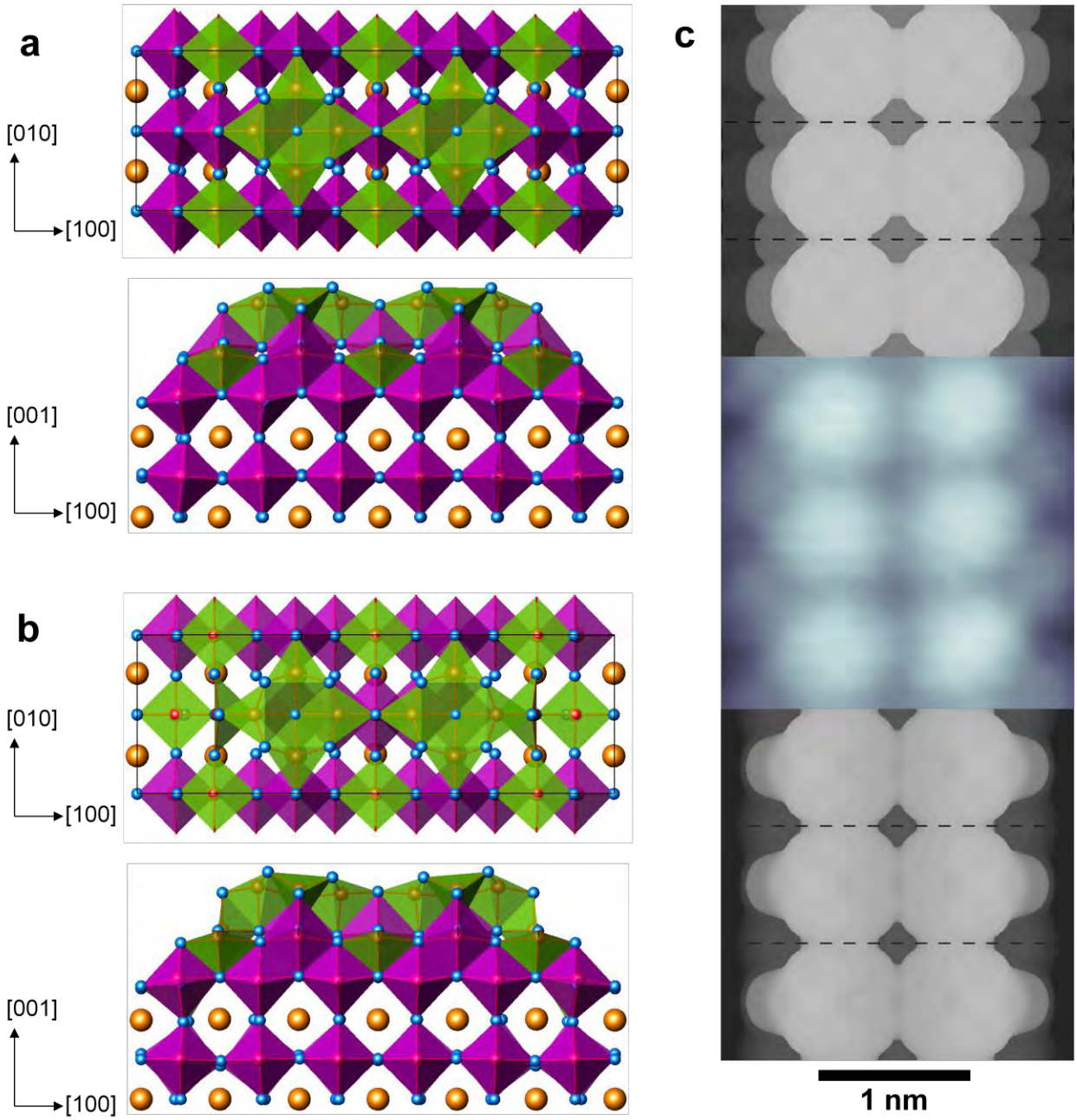

Fig. 4.3. Polyhedral representation of the DFT-relaxed (a) D1, and (b) D2 diline structures, square configuration: plan view (top) and profile view (bottom). (c) STM micrographs, unit cell outlined: D1 simulation (top, 1.5 V bias), experimental (middle, 1.7 V bias, 0.05 nA tunneling current), and D2 simulation (bottom, 1.5 V bias). All such figures show Sr in orange, Ti in red and O in blue. Ti-centered polyhedra are colored as follows: purple for 6-fold, green for 5-fold and black for 4-fold coordination.

Numerous candidate nanoline structural models were examined, but only a few are discussed here. Most candidate structures were discarded due to their high surface energy or the poor match to experiment of their simulated STM images.

Based on the observation that these bright spots are of the same size and shape as those in experimental STM images of c(4×2) surfaces, structural models containing the polyhedral quartet motif on the top layer were created and relaxed in WIEN2k; this is very reasonable, as the c(4×2) precedes and coexists with the nanolines. The quartet motif constrains the second layer structure – at least immediately underneath it – upon the assumption of a TiO_x underlayer, consistent with the AES results. Of the two registries with bulk-like TiO_2 layers, the one leading resulting in the central O being in 5-fold coordination is not only significantly lower in energy [90], but is also the observed registry for the c(4×2)-reconstructed surfaces. Nonetheless, the structure in the valley area observed via STM must be different.

Two viable models, both with a perfectly bulk-like TiO_2 layer in the third topmost atomic plane, were tested. The first one can be described as follows:

- D1 (Fig. 4.3(a)): Qualitatively bulk-like second layer, except for a row of missing TiO along the center of the valley.

A perfectly bulk-like TiO_2 second layer was not considered, as access to the third layer is necessary to match the valley corrugation measured experimentally. A simulated STM micrograph (1.5 V bias voltage) of the D1 model in the square configuration is shown in Fig. 4.3(c). While this model replicates most diline features, in the experimental micrographs the valley area exhibits a distinct semicircular feature from the second layer, always "out of phase" with the nearby top-layer round motifs, as illustrated in Fig. 4.3(c). This is not well reproduced by the D1 model, which does show similar such features, but both in phase and out of phase with

the top-layer spots, with the former extending further out into the valley. Rather, it appears that in the D1 model they are due to the 2-fold coordinated O atoms in the second layer, nearest to the center of the valley. Therefore, a modification was made to arrive at a new model:

- D2 (Fig. 4.3(b)): Qualitatively equivalent to D1, except for the removal of only those second-layer oxygen atoms that were in phase with the top-layer features; this keeps all Ti atoms in at least 5-fold coordination.

Figure 4.3(b) shows the relaxed structure, under the square configuration and the 1.5 V simulated STM image is presented in Fig. 4.3(c). This model successfully reproduces the second layer valley features. The zigzag configuration of the D2 model is shown in Fig. 4.4.

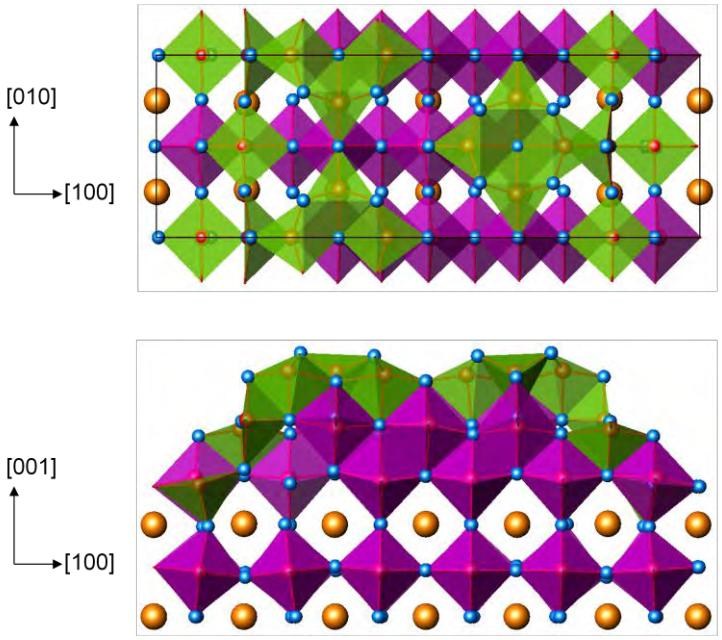

Fig. 4.4. Polyhedral representation of the DFT-relaxed D2 diline structure in the zigzag configuration in (top) plan view, with unit cell outlined, and in (bottom) profile view.

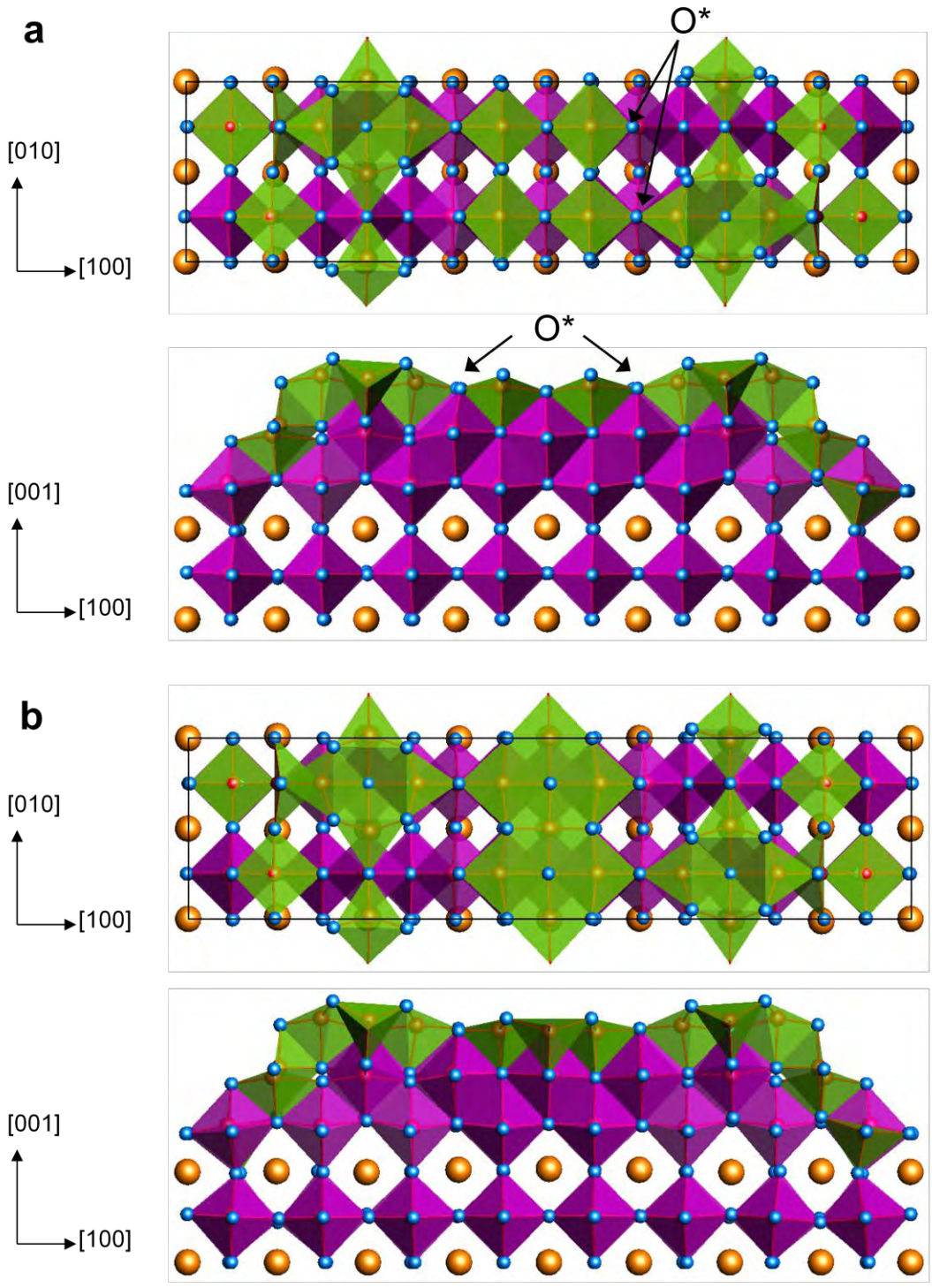

Fig. 4.5. (a) T1, and (b) T2 triline structures in the zigzag configuration: plan view (top) and profile view (bottom).

4.3.3. Trilines

Another class of nanoline is the triline, which is often observed in coexistence with the diline. Trilines are similar in STM appearance to the dilines, except for the additional presence of a ―backbone" between diline-like rows. Trilines have 8×2 or 9×2 periodicity when found in close-packed domains, with the valley size determining the transverse period. X-ray photoelectron spectra, collected by collaborators at the University of Oxford, show more Ti reduction than in diline spectra, as nominally ―2+" Ti 2p peaks, absent for dilines, show up [113]. Structural triline models based on the D2 architecture were examined, keeping the valley and diline-like top-layer motifs unchanged, and thus leaving only the backbone structure to be determined.

The backbone building blocks have single-unit-cell periodicity (0.39 nm) along the longitudinal direction [113]. Each of these units has mirror symmetry along both the longitudinal and transverse directions. Within these constraints, three structural models of 8×2 periodicity were initially constructed, relaxed and employed for STM image simulations:

- T1 (Fig. 4.5(a)): A segment of a bulk-like TiO_2 plane makes up the top layer of the backbone, via two rows of corner-sharing TiO_5 polyhedra running along the longitudinal direction. The O* atoms (labeled in Fig. 4.5(a)) are shared with the diline-like quartet motif when the nearby backbone Ti is in phase with it. Each backbone top-layer unit is thus Ti_2O_5, in this case.

- T2 (Fig. 4.5(b)): Similar to the T1, but with an additional Ti atom in the otherwise hollow sites along the central column of the backbone; this leads to a Ti/O checkerboard pattern along the backbone top layer. Therefore, the extra Ti atoms are also 5-fold coordinated and this results (as in the quartet motif) in not just corner-sharing, but edge-sharing TiO_5 polyhedra. In

this model, the repeated top-layer units are Ti_3O_5. This composition indicates some reduction, consistent with the XPS data; this shall be quantified in the next subsection.

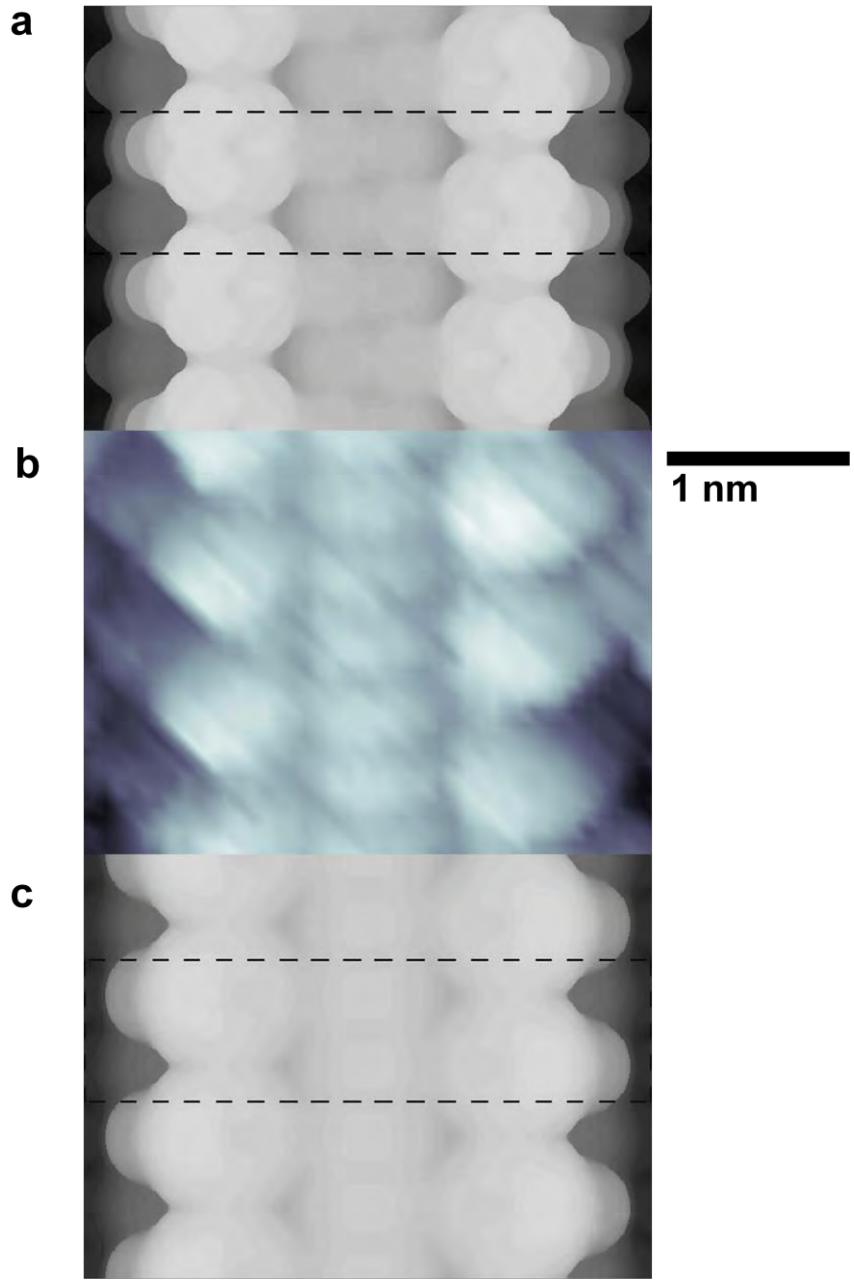

Fig. 4.6. STM micrographs: (a) T1 simulation (1.5 V bias), unit cell outlined; (b) experimental (2.23 V bias, 0.24 nA tunneling current); (c) T2 simulation (1.5 V bias).

- T3 (Fig. 4.7(a)): Similar to T1, but with additional Ti in the octahedral sites of the backbone second layer (four per triline supercell), thereby creating a local Ti/O checkerboard pattern under the backbone top layer. The top layer is still Ti_2O_5, but the reduction in the underlayer is also consistent with the XPS results.

The 1.5 V simulation for model T1 shows a less bright (less height, ie. the density isosurface is closer to the sample) backbone signal than for the adjacent diline-like features (Fig. 4.6 (a)). Furthermore, within every backbone repeat unit each Ti appears as its own distinct spot, instead of pairing up and combining as a single unit. Moreover, some of the quartet O atoms brighten up markedly more than the rest.

Model T2 gives the best match to experiment, with the backbone and diline-like features having comparable intensities and the backbone repeat units appearing each as a single feature. One such simulation, in the zigzag configuration, is shown in Fig. 4.6(c).

The corresponding simulations for model T3 (Fig.4.8(a)) present the same problem as T1, in that the top-layer backbone Ti atoms give rise to resolved small spots. Moreover, the brightness from in-phase backbone units appears to extend into part of the adjacent (and otherwise less bright) diline-like motif.

It must be mentioned that the triline backbone defect (see subsection 4.3.5) does not significantly depend on the neighboring diline-like features. That is, its existence is equally frequent under the zigzag and square configurations, and within the latter it is equally common in the in-phase and out-of-phase locations; this also holds true for its diffusion rate. This seems to suggest that the triline backbone ought to be independent of the diline-like motifs, so another structural model was generated and tested:

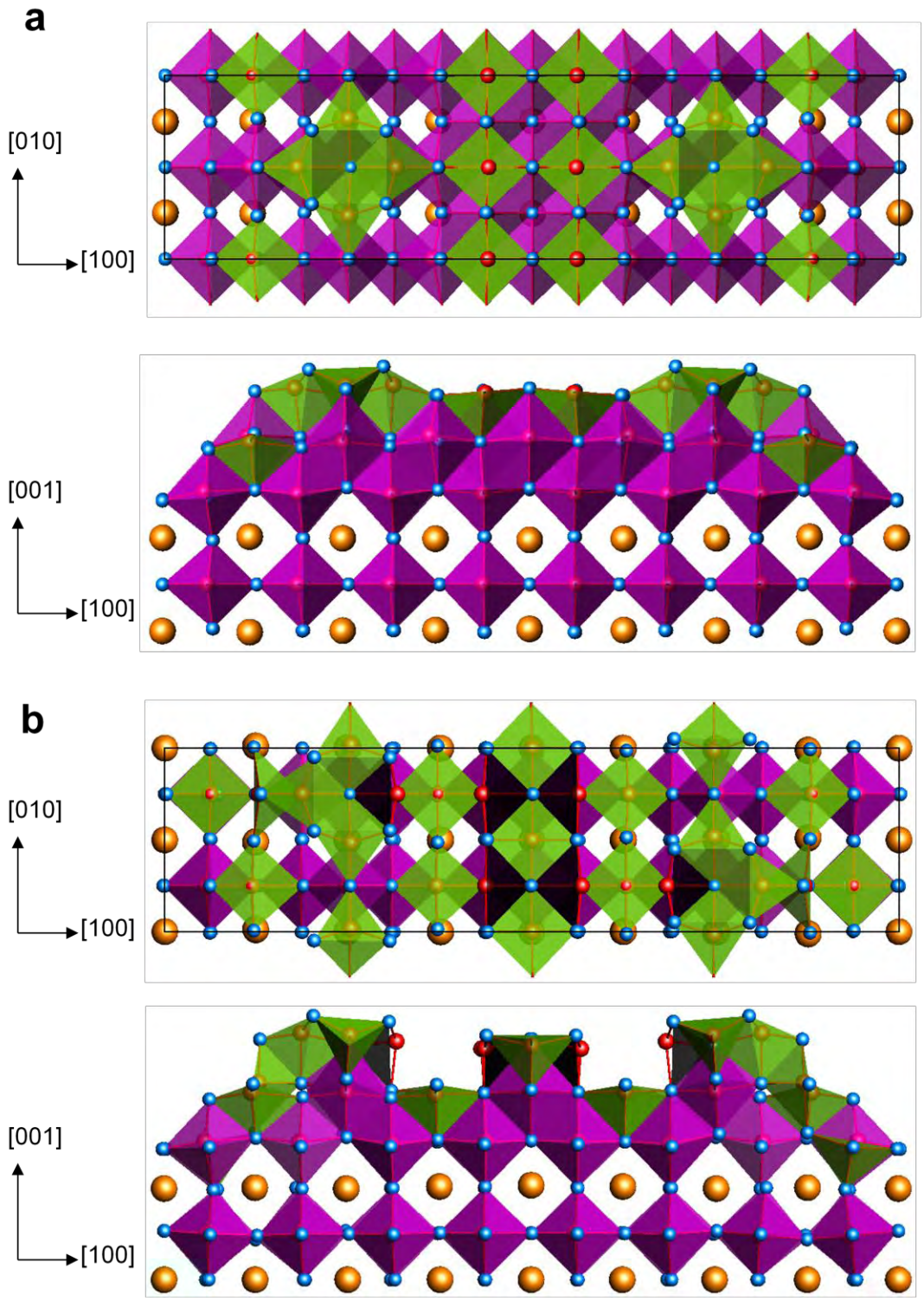

Fig. 4.7. (a) T3 triline structure in the square configuration, and (b) T4 triline structure in the zigzag configuration: plan view (top) and profile view (bottom).

- T4 (Fig. 4.7(b)): Similar to T2, it keeps the additional top-layer Ti atoms in the backbone. However, the O* atoms originally bonded to the outside of the backbone Ti (half of which bridge the backbone to the diline-like features) are no longer present. The second atomic layer remains bulk-like underneath the backbone.

The simulated micrograph (Fig. 4.8(b)) of the T4 model clearly fails to reproduce the experimental backbone features; the removal of the mentioned O leads to high brightness where the Ti–O bond existed, spuriously dominating the backbone signal.

For completeness, one must note that other structures not discussed here came close to matching the experimental STM images, but were not consistent with the backbone defect discussed in the following subsection. Model T2 provides the best fit both in itself, as well as with the constraints imposed by the backbone defect.

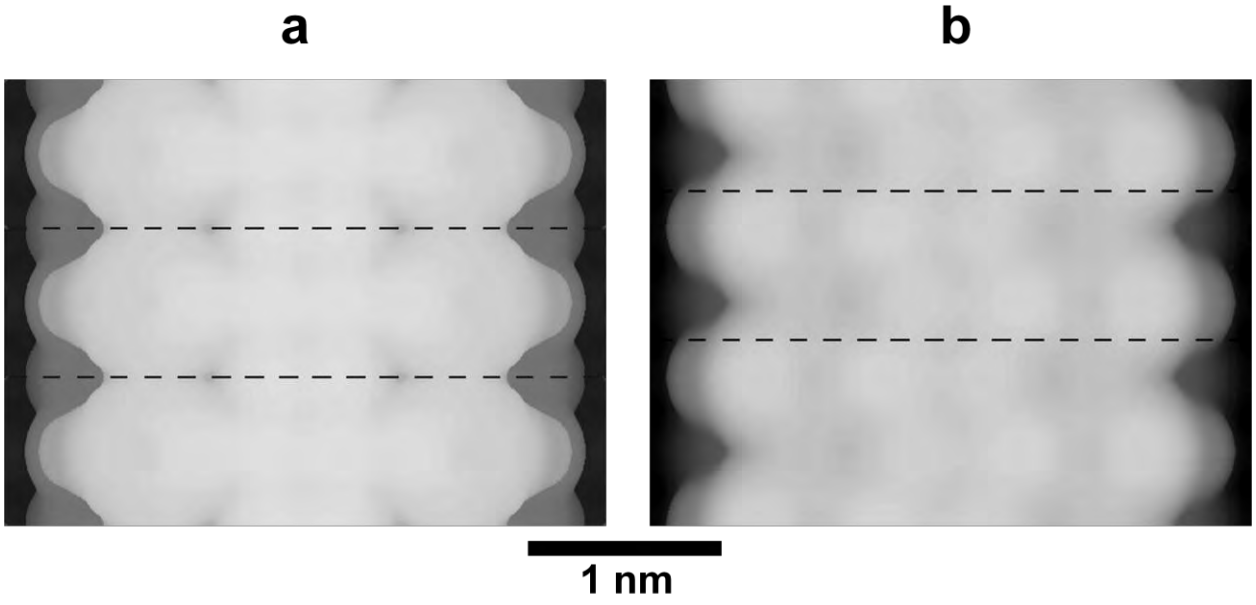

Fig. 4.8. Simulated STM micrographs (1.5 V bias) of triline models, unit cell outlined: (a) T3 and (b) T4.

4.3.4. Surface Ti Valence States

Since the chemical shift of XPS peaks actually reflects changes in bond valence sums (and not the idealized integer valence states), one can attempt to explain the appearance in trilines (and absence in dilines) of "Ti^{2+}" peak shoulders via BVS analysis. For this purpose, BVS values of the top-layer Ti atoms were computed for the favored D2 and T2 models. The results are listed in Table 4.1, and the atom labels refer to the respective CIF files (see Appendix D). For further clarity, the Ti4, Ti6 and Ti7 atoms correspond to the Ti sites in the c(4×2)-like quartet motifs. Within the T2 structure, the rest are Ti sites in the backbone. The Ti11 site is along the center row in the backbone, at the center of the TiO_5 polyhedron sharing its edges with four other polyhedra. Each Ti12 atom is in phase with the quartet motif, sharing an O with it. Finally, each Ti13 atom is out of phase with the nearby polyhedral quartets.

Table 4.1. Bond valence sums for the D2 and T2 nanoline models.

D2 Diline		T2 Triline	
Atom	BVS	Atom	BVS
Ti4	3.84	Ti4	4.00
Ti6	4.13	Ti6	4.15
Ti7	3.97	Ti7	3.97
		Ti11	3.72
		Ti12	2.87
		Ti13	3.65

The Ti atoms within the polyhedral quartets in either structure have bonding that is very close to a formal 4+ state. However, the Ti in the triline backbone are reduced, especially the Ti12 atom, since the O atoms it is bound to are heavily constrained. As a reference for the BVS of a Ti^{2+} state when calculated using the Ti^{3+}–O^{2-} R_0, Ti atoms in rocksalt TiO have a bond

valence sum of 2.69, close to the Ti12 value. The appearance of low-binding-energy shoulders in the XPS data [113] is easily explained by the T2 model.

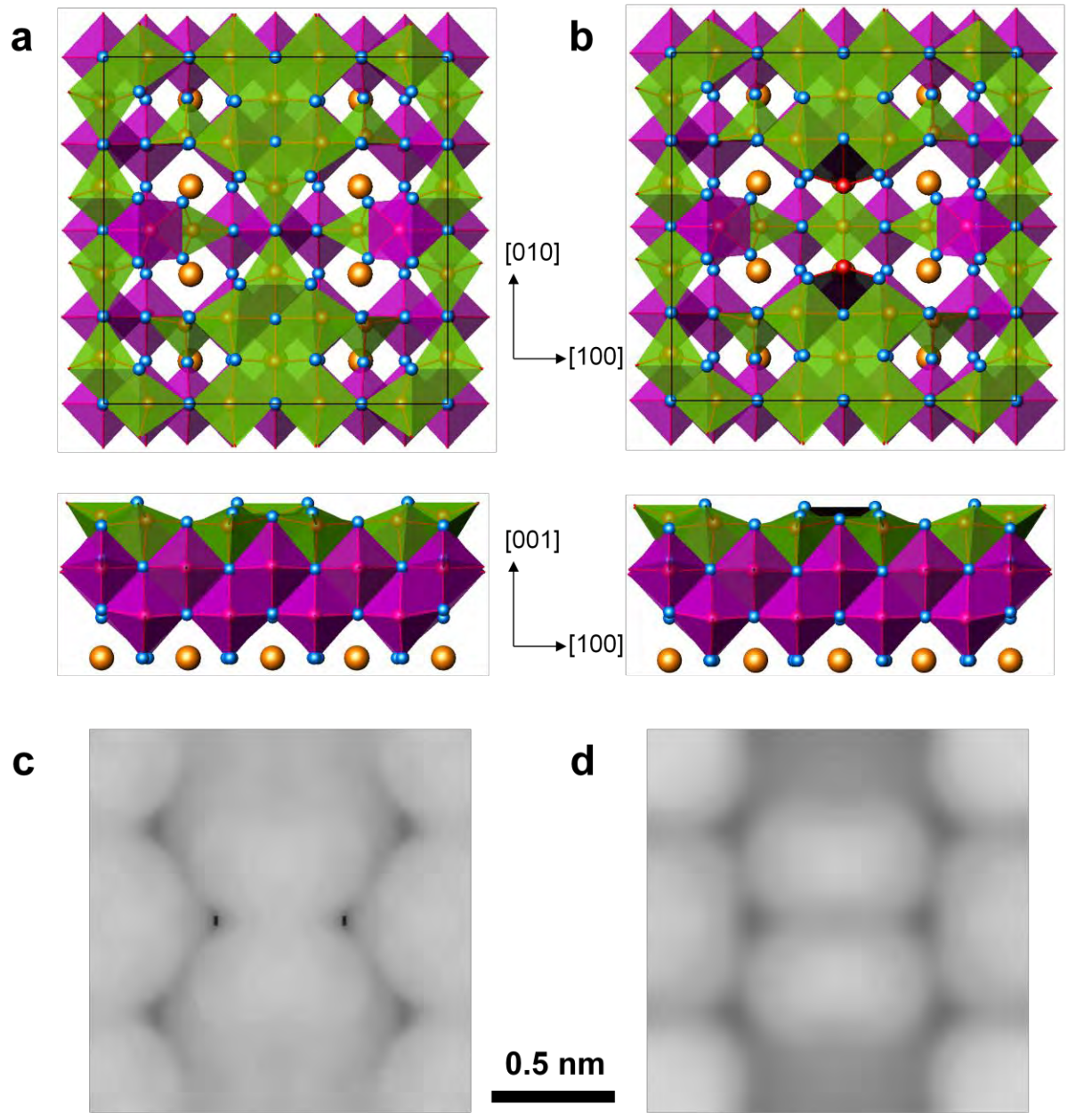

Fig. 4.9. 4×4 supercell simplified (a) BD1 and (b) BD2 models of triline backbone defect in phase with diline-like features, square configuration: plan view (top) and profile view (bottom).
1.5 V simulated STM micrographs: (c) BD1; (d) BD2.

4.3.5. Backbone Defect

A characteristic triline defect appears in experimental STM micrographs, always along the backbone. It shows up essentially as a missing repeat unit within the backbone, so it is double mirror-symmetric itself and is always in phase or out of phase with the diline-like features. Thus, the T2 model rules out the possibility that the defect is a single Ti vacancy, since the center of the diline-like spots always line up with a pair of Ti, never just one. Moreover, the STM image of a single Ti vacancy was simulated in small supercell calculations and indeed, it results in a small dark feature between repeat units, which is further reason to discard this option. All triline models indicate that most of the triline backbone brightness in experimental micrographs is due to pairs of top-layer Ti atoms. This in turn eliminates the possibility of it being a single O vacancy.

An analysis of defect position along the backbone as a function of time allowed for the extraction of its hopping rate. In turn, this was fitted by Dr. Matthew Marshall at the University of Oxford to an Arrhenius diffusion equation [113]. This yields a defect diffusion activation barrier of 4.98 ± 0.17 eV; the large value supports the conclusion that the defect cannot consist of a single atom, and must be more complex.

In order to test defect models more efficiently, 4×4 supercells (the valleys were excluded) with 7 atomic layers were generated; see Figures 4.9-4.11 for clarity. This forcibly required the use of the square configuration. Defects aligned with the diline-like motifs were initially modeled. To begin with, two structural models were constructed for the backbone defect:

- BD1 (Fig. 4.9(a)): A pair of Ti vacancies aligned ~~"in~~ phase" with the diline-like features, and the outside O*-type also missing (two Ti-O pairs removed).

- BD2 (Fig. 4.9(b)): A vacant linear Ti_2O_3 unit. That is, the same as BD1, but with the central O between the Ti also removed.

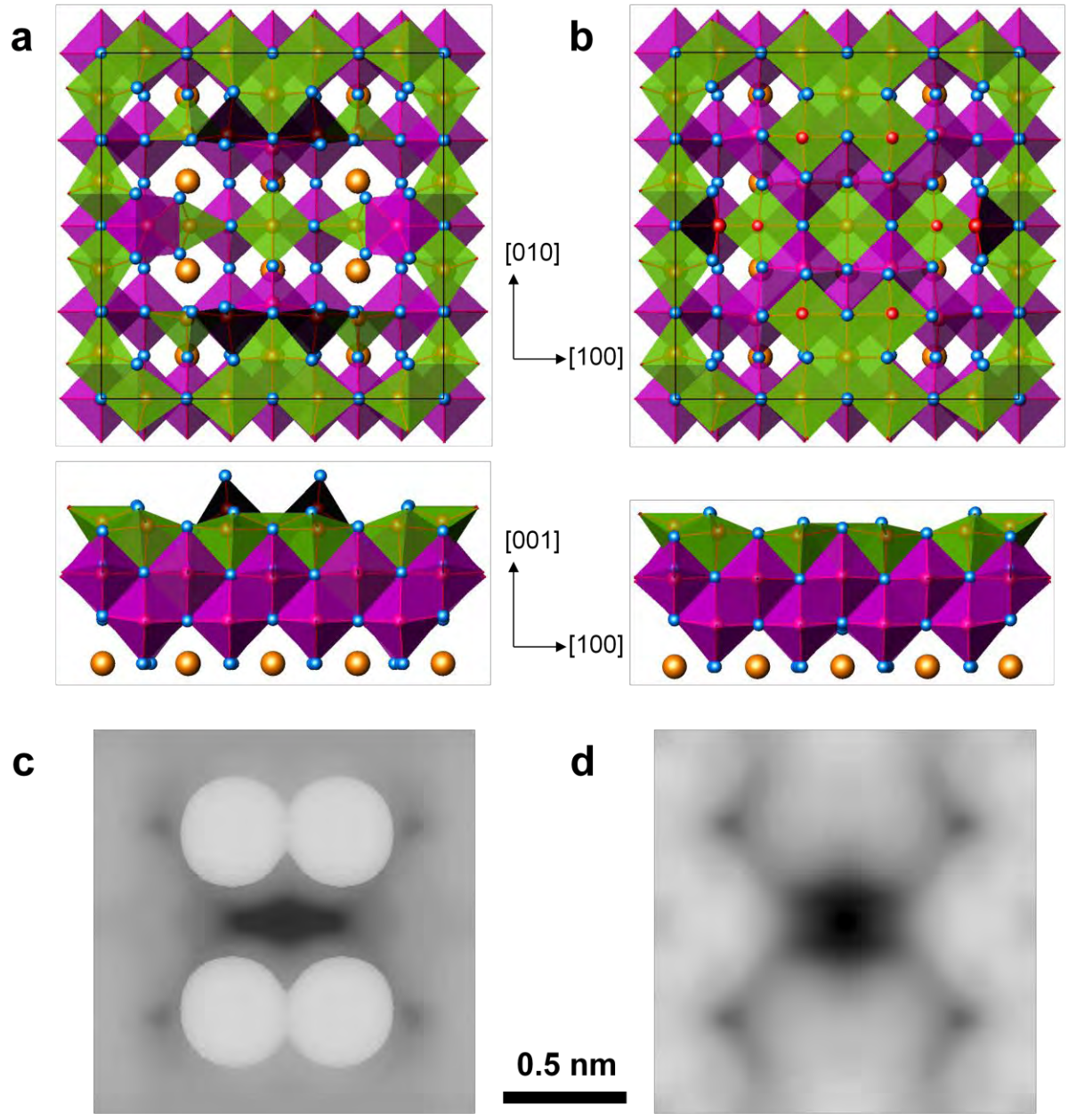

Fig. 4.10. 4×4 supercell simplified (a) BD3 and (b) BD4 models of triline backbone defect in phase with diline-like features, square configuration: plan view (top) and profile view (bottom).
1.5 V simulated STM micrographs: (c) BD3; (d) BD4.

Both BD1 and BD2 prove inadequate. The STM image simulations (Fig. 4.9(c,d)) show an enhanced signal from the nearby O atoms, as a result of their out-of-plane relaxation. Also, the simulated image for the BD1 model shows necking between the blobs on either side of the defect; the bridging O is responsible for this, as it has nonzero local density of unoccupied states. Meanwhile, while a gap exists in the defect of the BD2 simulation, it is too narrow, not the size of a repeat unit. Therefore, a third structural model was studied:

- BD3 (Fig. 4.10(a)): Similar to the BD2 defect, but with the two nearby central-row Ti atoms also vacant, thereby constituting a larger Ti_4O_3 vacancy cluster.

Upon relaxation, the four O atoms nearest to the defect core (each only bound to one Ti atom) lift up much more, resulting in rather vertical titanyl bonds. These overwhelmingly dominate the STM image simulations (Fig. 4.10(c)). However, an adequately sized gap emerges in the defect core. In order to address the remaining discrepancy, a fourth model was created:

- BD4 (Fig. 4.10(b)): The same Ti_4O_3 cluster as in model BD3 has been removed, but each of the 4 (previously removed) Ti atoms are instead placed in one of the empty octahedral sites in the layer underneath. This keeps the top-layer O from lifting up as they do in model BD3. In this arrangement, only three O are effectively missing.

The simulated STM image is a good fit to experiment, showing a dark, oval-shaped defect region – essentially a missing repeat unit (see Fig. 4.10(d)). The backbone exhibits a unit of brighter signal half-way in between contiguous defects, but this is believed to be an artifact of the small periodicity imposed.

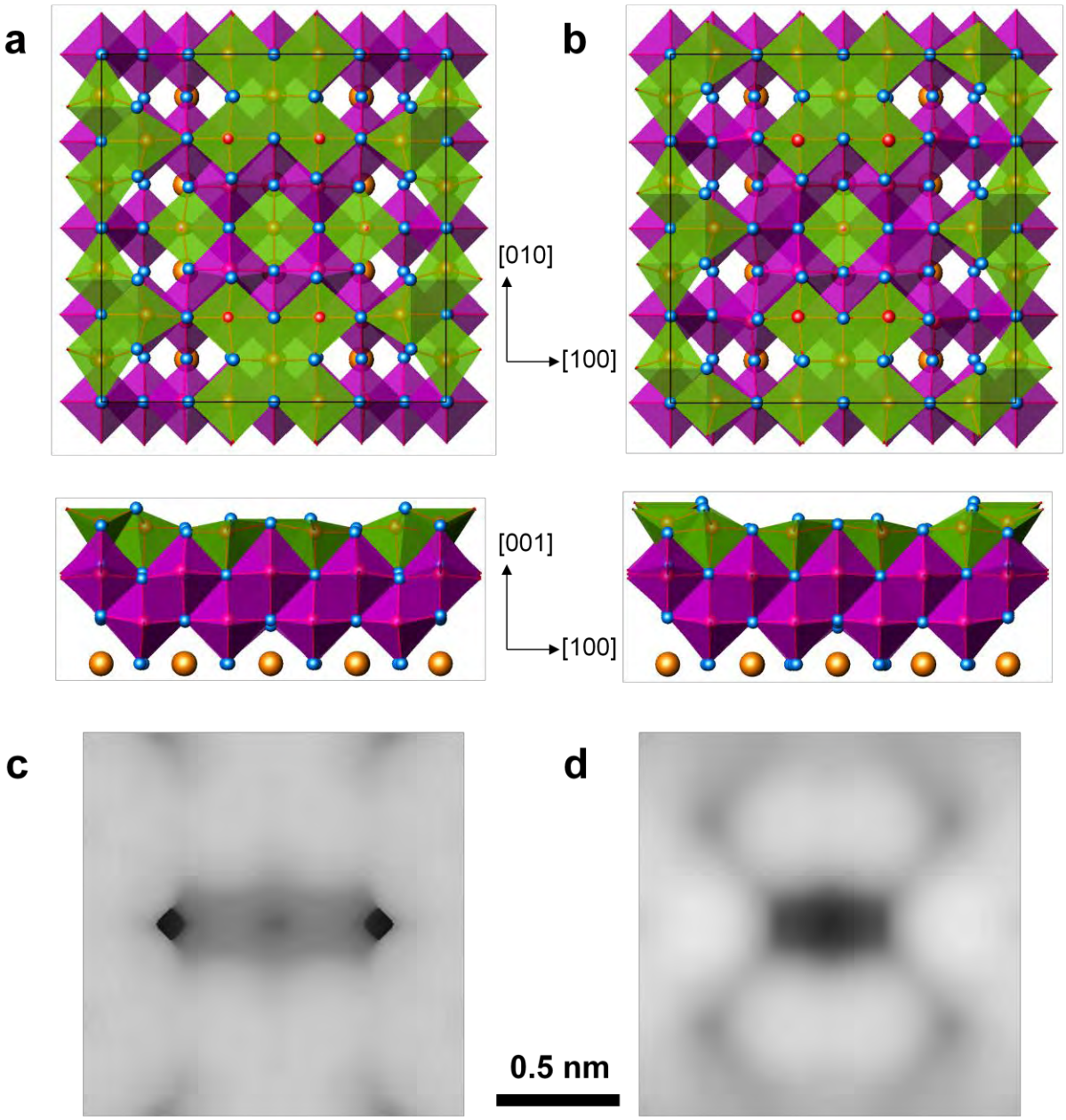

Fig. 4.11. 4×4 supercell simplified models of triline backbone defect, square configuration: (a) BD4, out of phase with diline-like features, and (b) BD5a, in phase with diline-like features. Plan view (top), profile view (bottom). 1.5 V simulated STM micrographs: (c) BD4; (d) BD5a.

One similar model was investigated:

- BD5a (Fig.4.11(b)): This is qualitatively the same as model BD4, except for the no-longer-removed O atoms which bridge (in the non-defective structure) the backbone with the diline-like features. In this scenario, only one O atom is effectively missing.

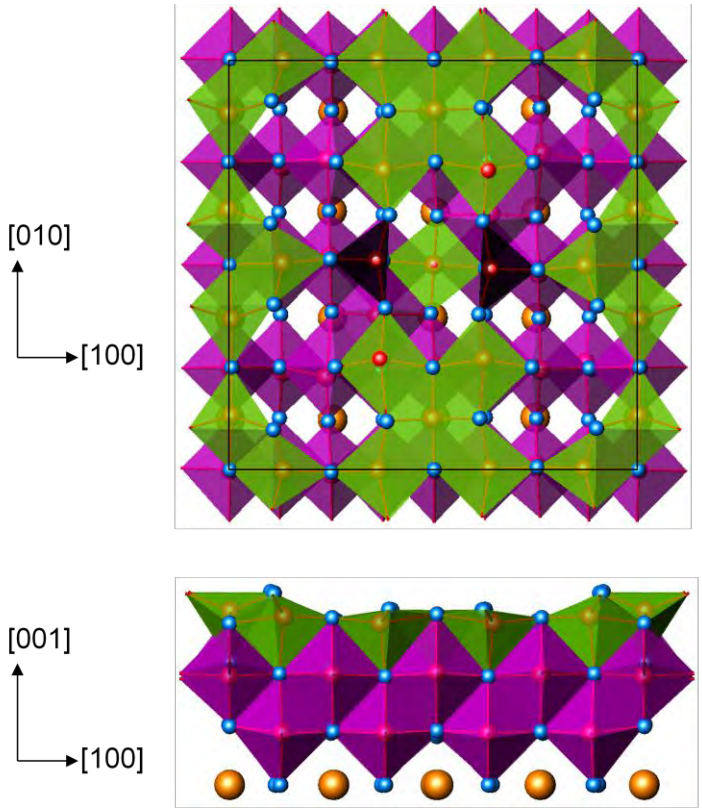

Fig. 4.12. Relaxed 4×4 supercell BD5b structural model in (top) plan view and (bottom) profile view.

The simulation of the STM micrograph (Fig. 4.11(d)) successfully reproduces the dark defect and is more elliptical than in the BD4 simulation. Nonetheless, there is plenty of undesired brightness contrast – namely, the backbone units which are immediately adjacent to the defect are more prominent than the rest. Similarly, the diline-like features which are aligned with the defect are much brighter than those near the non-defective backbone segment. While

the brightness disparity is larger and less local than that found for BD4, in principle this may be due to the artificially-imposed small periodicity. In order to indirectly test the BD5a model, another model with the same stoichiometry was examined. It must be emphasized, however, that the following structure was not itself a candidate for the defect structure, as it did not satisfy several of the known constraints:

- BD5b (Fig. 4.12): A linear Ti–O–Ti unit running along the central row of the backbone top layer is removed. Two Ti atoms are placed in two of the four nearby empty octahedral sites in the second layer. These two atoms occupy opposite sites with respect to the center of the defect, thereby breaking the mirror planes while preserving the 2-fold rotational symmetry.

This defect structure is calculated to be 1.3 eV lower in energy than model BD5a. Therefore, BD5a is not stable, since two of its subsurface Ti would quickly migrate back to the top layer. Moreover, should the BD5a defect occur at a backbone position out of phase with the diline-like features (square configuration), this would leave two highly unstable O atoms, bound only to one Ti; half as much is true at every position along the backbone under the zigzag configuration. Including these O atoms as part of the vacancy cluster is of course unviable, as the number of these varies depending on the defect position (1 in square in-phase, 2 in zigzag, and 3 in square out-of-phase). As mentioned above, the diffusion dynamics show no discernible dependence on defect position. This in itself suffices to discard all structural models (for example, just two Ti vacancies) which do not include the side O in the vacancy cluster.

Model BD4 was thereafter simulated in the out-of-phase square configuration (Fig. 4.11(a)). While not identical to the in-phase case, the simulated image of this configuration (Fig. 4.11(c)) also succeeds in reproducing the defect as a missing backbone unit. Ultimately, this

defect structure was also modeled with a larger (8×4) supercell which includes the valley areas, as well as four additional atomic layers in the bulk, for a total of 890 atoms (Fig. 4.13). A composite figure of the STM simulation of the defect under the zigzag configuration and the perfect T2 triline is shown in Fig. 4.13(c).

4.4. Discussion

It is clear that the polyhedral quartet motif which characterizes the c(4×2) reconstruction is a recurrent feature of many stable $SrTiO_3$(001) surfaces. It is the main building block in titanium-rich dilines, which in turn are the cornerstone for the formation of the trilines. As mentioned above, it is also the distinctive feature in one of the "square" 2×2 reconstructions [55]. Moreover, while this motif is likely to play a role in the stabilization of the surfaces of other perovskite (ABO_3) materials, this is constrained to BO_2-rich surfaces. The planar registry of the polyhedral quartet with a rocksalt-like AO plane is energetically unfeasible in such structures.

The non-defective structural solutions of the nanolines satisfactorily consist of Ti-centered polyhedra at the surface, where all top-layer Ti are five-fold coordinated and every polyhedron is in an edge-sharing configuration with at least two other such polyhedra. This characteristic is shared with all DL surface structures solved via diffraction methods (see Chapter 3), so it must be considered a stabilization mechanism itself. In general, the edge-sharing arrangement of surface polyhedra prevents many surface O from being in single co-ordination, given the registry of the top layer with the bulk-like layer below. The lone exception here is the DL 2×1 reconstruction model, which is characterized by one such "dangling" O per surface cell. As shall be seen in the following chapter, this instability can be reconciled by incorporating chemisorbed water in the structure.

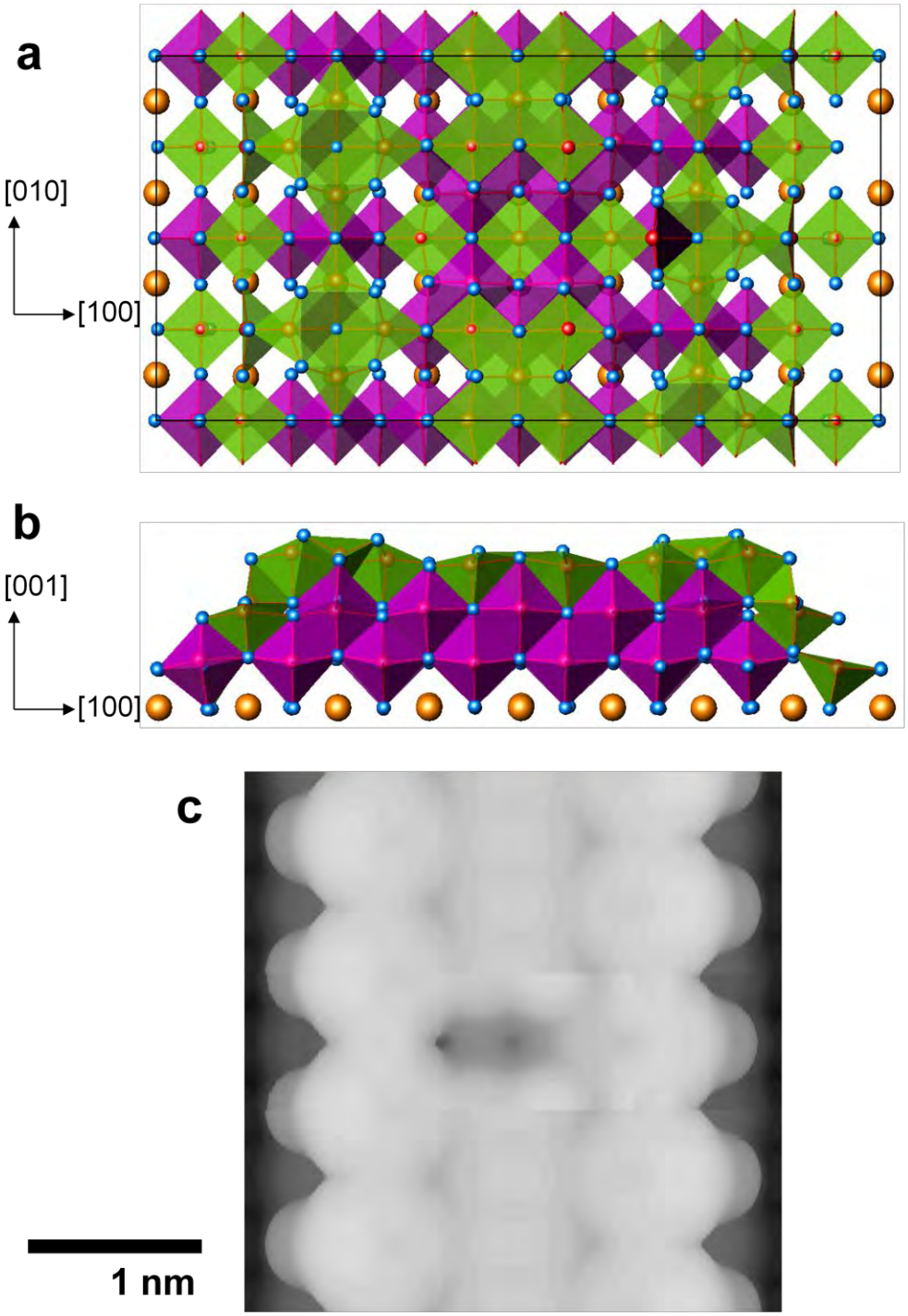

Fig. 4.13. Relaxed 8×4 supercell structural model of BD4 triline backbone defect in the zigzag configuration: (a) plan view, with cell outlined, and, (b) profile view. (c) Composite image of 1.5 V simulated STM micrographs of triline (T2 model) and BD4 zigzag model.

Regarding the surface polyhedra in the nanoline structures, it is found that the dilines borrow the characteristic c(4×2) quartet motif, but with an extra TiO_x layer. The second layer is not fully bulk-like but supports the quartet motifs and provides a valley area that successfully reproduces the experimental STM images. Moreover, it is worth noting that the zigzag and square configurations take up slightly different amounts of oxygen.

The triline builds on the diline structure, but adds a backbone with a top-layer checkerboard pattern of Ti and O, with a more Ti-rich composition than the dilines. The $SrTiO_3$(001) nanolines can adapt to small variations in Ti and O content by adopting different structures, while maintaining the quartet motif. Admittedly, one cannot be absolutely definitive about the exact composition below the outermost atoms, but the triple-layer TiO_x models proposed here are consistent with the AES data. Moreover, BVS analysis of these structures predicts the presence of reduced Ti sites only in triline-covered surfaces, in accordance to XPS results.

The triline backbone defect is large and complicated, consisting of three effective oxygen vacancies plus four relocated Ti atoms in new subsurface positions. This complexity is required by symmetry constraints, as well as by the electronic structure and observed hopping rate. No single vacancy defect can reproduce the experimentally observed defect hopping, and the diffusion activation energy of 4.98 eV is too large for a single-atom defect structure; for comparison, the barrier for single O vacancy diffusion in bulk $SrTiO_3$ is calculated to be in the range of 0.40-0.58 eV [114, 115] and the corresponding value for diffusion along a TiO_2-terminated (001) surface is ~0.11 eV [115]. The dynamics of defect motion along the length of the triline backbone, as illustrated in Fig. 4.14, require a collective effort. For a translation of one bulk unit cell to occur, three subsurface Ti atoms must hop to top-layer sites and three top-

layer Ti must hop to octahedral second-layer sites. Additionally, three surface O atoms must jump to new positions. Unfortunately, vast computational expense keeps one from being able to estimate the activation energy of such an orchestrated motion, but it is believed that this diffusion scheme explains the large observed activation barrier.

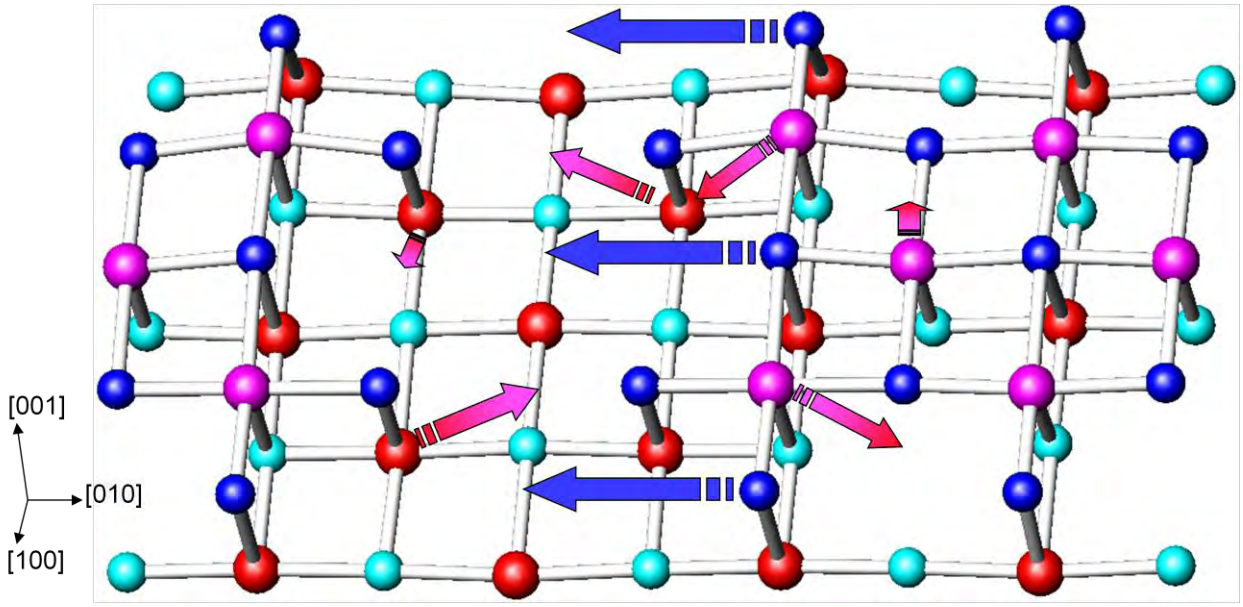

Fig. 4.14. Schematic ball-and-stick representation of diffusion mechanism of BD4 defect along triline backbone. Topmost two layers of 2×4 triline backbone supercell are shown, and structure shown is not relaxed. Longitudinal direction is [010], transverse is [100]. Surface Ti atoms are pink, subsurface Ti atoms are red, surface O atoms are blue, subsurface O atoms are light blue.

4.5. Conclusion

First-principles simulations of scanning tunneling micrographs have been used to re-examine the $SrTiO_3$(001) c(4×2) DL model. Structural models have been proposed for the dilines, trilines, and triline backbone defect, all consistent with the observed scanning tunneling micrographs and complementary experimental data. In particular, the Ti-rich nanolines on

$SrTiO_3$(001) surfaces are found to be terminated by three TiO_x layers and to exploit the polyhedral quartet feature, which is characteristic of the c(4×2) and –square" 2×2 reconstructions, as a central building block. In addition to this recurrent structural motif, the triline relies on a different edge-sharing arrangement of TiO_5 surface polyhedra along its backbone, which is itself a persistent feature among periodic $SrTiO_3$(001) surface structures.

Water, taken in moderation, cannot hurt anybody.
Mark Twain

Nothing is softer or more flexible than water, yet nothing can resist it.
Lao Tzu

Chapter 5. Water Adsorption: TiO_2-Rich $SrTiO_3$(001) Surfaces

5.1. Introduction

Water adsorption on the $SrTiO_3$(001) reconstructions with two TiO_2 surface layers is considered in this chapter. The focus lies primarily on the *ab initio* energetics and it is found that all such reconstructions can adsorb water at ambient temperature and pressure, and that the energies of the different reconstructions are almost degenerate for half-monolayer water coverage. These results are consistent with strong water chemisorption on defective surfaces formed either by ion-beam milling or cleavage, with relatively sluggish dehydration kinetics. Which reconstruction forms is therefore an issue of kinetics, not just thermodynamics. Hints from STM imaging are also exploited to test and develop structural models for some periodic reconstructions which incorporate adsorbed water.

Strontium titanate, as seen in Chapter 1, is not only a suitable model system for a broad range of materials, but also holds much promise for practical use in several technological fields. It is no surprise, then, that the topic of water interaction with strontium titanate surfaces has already merited exploration in numerous reports. This is warranted, furthermore, as H_2O in the vapor phase is truly ubiquitous, making it very difficult to avoid said interaction; even in ultra-high vacuum (UHV) environments, the presence of some residual water vapor is unavoidable. Moreover, water molecules are polar in nature, so they are likely to chemisorb on ionic oxide surfaces [116-121]. Experimentally, the consensus in the literature is that water adsorbs molecularly (i.e. non-dissociatively) on unreconstructed $SrTiO_3$ surfaces of the dominant (001) orientation [122], whereas dissociative adsorption occurs strongly on defective surfaces, be it at O vacancy sites [122, 123] or steps [124].

On the theoretical front, Wang *et al.* provided a simple geometrical model for the full monolayer (in this chapter, 1 ML ≡ 1 molecule per 1×1 surface cell) molecular H_2O adsorption on a TiO_2-truncated $SrTiO_3$(001) surface and used density functional theory (DFT) to predict the adsorption energy and bond lengths [125]. This was published in a paper describing the adsorption of methanol on this surface, as a follow-up to an experimental report on water adsorption.

Evarestov *et al.* [126] took the next step by using a hybrid Hartree-Fock/DFT approach to study the adsorption of water on bulk-like (001) TiO_2 and SrO truncations, allowing for both dissociative and molecular adsorption models; both 1 and 2 ML water adsorption were considered. On the TiO_2-terminated surface at full-monolayer coverage, the molecular configuration was indeed found to be more stable than the dissociative mode, in agreement with experimental observations. Adsorption energies and bond lengths were also reported.

Hinojosa *et al.* [127] revisited the topic of dissociative and molecular H_2O adsorption on bulk-like TiO_2 and SrO $SrTiO_3(001)$ truncations, now examining water coverage of 1 ML and below, again via DFT computations. The 1 ML results on the Ti-rich surface largely agree with Evarestov *et al.* regarding both geometry and relative energies; however, the dissociative configuration is predicted to be more stable on the TiO_2 termination at a H_2O surface coverage of 0.5 ML or less, in apparent contradiction with experiment.

Most recently, Raghavan *et al.* [128] used DFT calculations to model hydrated and hydrogenated $SrTiO_3(001)$ surfaces, focusing again on the bulk-like truncations, as well as a few defective such terminations. The discussion in this study was restricted to the electronic structure, with the emphasis on new localized states of possible importance for photocatalytic water splitting. The structural models used mostly mimic the geometries in the Evarestov *et al.* report.

It bears noting that bulk-like depictions of surfaces are often unrealistic, since oxide surfaces tend to stabilize by reconstructing. Therefore, the usefulness of assuming bulk-like truncation geometries is questionable. To date, the theoretical modeling of water adsorption on reconstructed oxide surfaces has been reported in very few studies [101, 129, 130]. The most systematic reports focused on the reconstructions in rocksalt MgO/NiO(111) surfaces [101, 130]; supported by X-ray photoelectron spectroscopy (XPS) and transmission electron diffraction (TED) data, DFT calculations revealed the crucial role played by H_2O in the formation of (and transition between) different surface structures.

The naïve assumption of bulk-like terminations is particularly disconcerting in the case of the $SrTiO_3(001)$ orientation, as this surface provides us with several experimentally-observed periodic reconstructions of known structure (solved using diffraction techniques), on which

water adsorption may and should be modeled. These include the aforementioned 2×1 surface [34], as well as the "zigzag" 2×2 [93] and c(4×2) [89] structures. All of these share the distinguishing feature that they exhibit two contiguous TiO_2 atomic layers at the surface. Moreover, an unresolved conundrum exists at present, as the reconstructions observed differ from what would be expected from the thermodynamic calculations of the dry models.

The TiO_2 double-layer (DL) model for the 2×1 reconstruction (discussed in section 3.4.1), with one "dangling" oxygen atom in single coordination and one severely underbonded surface Ti per surface cell, is regularly observed experimentally, despite having a much higher predicted surface energy (by >0.5 J/m^2) than other structures of the same stoichiometry [90]; such thermodynamic instability is arguably too large to be overcome by kinetics alone. Conversely, one of such lower-energy DL structures is the hypothetical reconstruction of (√2×√2)R45° ("RT2" hereafter) periodicity, which is calculated to be the most stable surface with this composition [90]. However, the RT2 surface has never been observed experimentally. In this chapter, it will be shown that the incorporation of adsorbed H_2O on reconstructed $SrTiO_3$(001) surfaces resolves the apparent contradiction.

It is worth noting that light atoms, especially hydrogen, are exceedingly easy to miss when using diffraction techniques to decipher atomic structures. Therefore, the distinct possibility remains that certain surface reconstructions which have been declared structurally solved are, in fact, not "dry". It has already been shown, for example, that the 2×2 and (√3×√3)R30º reconstructions of both MgO(111) and NiO(111) are hydroxylated [101, 130]. On the $SrTiO_3$(001) surface, the high-energy 2×1 model is naturally a prime candidate for this.

The structure of this chapter is as follows. First, the computational method is tested with simple adsorption cases previously modeled in the literature. 0 ML, 0.5 ML, and 1 ML water

adsorption coverages are then examined for the different DL surface periodicities via DFT calculations and chemical bonding analysis. A full thermodynamic picture is built for these structures. The 2×1 reconstruction is further explored by comparing experimental STM images to simulations for the dry and a new hydrated structural model. This is exploited to propose and test models for the "brickwork" c(4×4) reconstruction, also observed by STM. Finally, a thorough discussion follows, which includes the description of supporting experimental evidence from a collaborator.

5.2. Methods

5.2.1. Density Functional Theory

Density functional calculations were performed to model all surfaces, using the periodic slab configuration. The DFT calculations were carried out with the full-electron-potential WIEN2k code [46] with an augmented plane wave + local orbital (APW+lo) basis set. Every structure considered was allowed to relax such that the residual force on each atom was under 0.1 eV/Å. Muffin-tin radii of 2.36, 1.70, 1.20 and 0.60 bohr were used for Sr, Ti, O and H, respectively. A *k*-point mesh equivalent to a 6×6×6 mesh for a bulk $SrTiO_3$ unit cell was used, as well as a maximum *K* value for the plane wave expansion of 5.5/1.2 $bohr^{-1}$.

In the case of the structures used for total energy calculations, almost every "dry" surface slab consisted of 13 atomic layers, i.e. a double TiO_2 layer termination on each side with five bulk $SrTiO_3$ unit cells as the slab core; surfaces with adsorbed water used this same base structure. The exchange-correlation functional of choice was the PBEsol-Hybrid [99] implementation of the generalized gradient approximation, with exact exchange fraction of 0.5

for the Ti-d levels. This fraction was optimized to match atomization energies of TiO_x molecules, as done for other studies [100, 101]; see Appendix B. The PBEsol functional is known to yield good lattice constants and surface energies, but poor atomization and adsorption energies [131]. In order to address this, the final energy numbers were obtained via an on-site implementation of the revTPSS functional, which significantly corrects the shortcomings of PBEsol with little downside [132]; the conventional terms for PBEsol and revTPSS with exact-exchange corrections are PBEsol0 and revTPSSh. The $SrTiO_3$ bulk lattice parameter was optimized and a value of $a_{SrTiO_3}^{PBEsol0} = 3.893$ Å was used for the total energy and bond valence sum calculations, in very good agreement (0.3% discrepancy) with the experimental value of 3.905 Å.

Surface energies at $T = 0$ K were calculated and normalized as

$$E_{surf/1\times1}^{0} = \left(E_{slab} - n_{SrTiO_3}E_{SrTiO_3} - n_{TiO_2}E_{TiO_2} - n_{w}E_{w}\right)/2N_{1\times1}\,, \qquad \text{(Eq. 5.1)}$$

where n_{SrTiO_3} is the equivalent number of $SrTiO_3$ bulk unit cells in the slab, n_{TiO_2} is the equivalent number of TiO_2 bulk unit cells, n_w is the number of equivalent water molecules adsorbed per slab, $N_{1\times1}$ is the number of 1×1 surface cells, E_{SrTiO_3} is the energy of a bulk $SrTiO_3$ unit cell, E_{TiO_2} is the energy of a bulk rutile TiO_2 unit cell and E_w is the energy of an isolated H_2O molecule. An error estimate of 0.05 eV/1×1 cell was used for the hybrid revTPSSh surface energy values, as explained in Appendix B.

Adsorption energies per water molecule were computed as

$$E_{ads} = \left(E_{dry} + n_{w}E_{w} - E_{wet}\right)/n_{w}\,, \qquad \text{(Eq. 5.2)}$$

where the subscripts E_{dry} and E_{wet} are the slab energies for the bare surface and the relevant hydrated model.

The surface energies were also computed as a function of temperature, by including a correction for the chemical potential of water in its gaseous phase. This was done as

$$E_{\mathrm{surf/1x1}}(T,P) = E^{0}_{\mathrm{surf/1\times1}} - (n_{\mathrm{w}}/2N_{1\times1})\Delta\mu_{\mathrm{w}}^{0\,\mathrm{K}\to T}\,, \qquad \text{(Eq. 5.3)}$$

where

$$\mu_{\mathrm{w}}(T,P) = \mu_0 - (T-T_0)S(T) + RT\ln(P/P_0)\,. \qquad \text{(Eq. 5.4)}$$

Here, the zero subscript corresponds to standard temperature and pressure. The entropy $S(T)$ was obtained from Ref. [133] and a partial pressure of water of 0.02 atm is assumed, which is typical for 50% relative humidity at room temperature. With such a method the phonon entropy of the different surfaces is assumed to be very similar and to cancel to first order and, since all the models considered are insulating, there is no electronic entropy contribution. This is a reasonable approximation, as suggested by earlier calculations (see, for example, Ref. [134]).

In the case of surfaces used for DFT-based STM image simulations, the PBE [98] form of the generalized gradient approximation to the exchange-correlation functional was employed, as explained in Appendix A. The $SrTiO_3$ lattice parameter was optimized and a value of $a^{\mathrm{PBE}}_{\mathrm{SrTiO_3}} = 3.944$ Å (1% larger than the experimental figure) was used. Surface slabs of 2×1 periodicity were kept at 13 base atomic layers for the STM simulations, while slabs of c(4×4) periodicity, due to the additional computation expense, only have 9 atomic layers, plus the corresponding adsorbates. In order to compare total energy calculations, the 2×1 surfaces were also modeled with 9 base atomic layers.

High-bias, constant-current scanning tunneling micrographs were simulated using the DFT outputs via a modified Tersoff-Hamann approach, as outlined in subsection 2.2.3 (and in greater detail in Appendix A). Sampling intervals of $a^{\mathrm{PBE}}_{\mathrm{SrTiO_3}}/20$ (in-plane) and 0.3 Å (out-of-

plane) were used for the artificial density of unoccupied states. A radially-symmetric step-function convolution motif of characteristic radius $a_{SrTiO_3}^{PBE}/2$ (~2 Å) was used for the blurring stage, following tests.

5.2.2. Bond Valence Sum Analysis

The bond valence sums were calculated from the PBEsol0 relaxed structures; as shown in Appendix C, the choice of exchange-correlation functional is important for accurate BVS values. The following R_0 (standard bond length) values were consistently employed to calculate each bond valence (see section 2.2.2): 2.118 Å for Sr^{2+}–O^{2-}, 1.815 Å for Ti^{4+}–O^{2-} [102] and 0.957 Å for H^{+}–O^{2-}. The latter was set to the O–H distance in gaseous H_2O [135]. The empirical constant b (see Eq. 2.4) was kept at its usual value of 0.37 Å. The volume of each supercell was expanded isotropically to match the lattice parameter to the experimental a_{STO} value of 3.905 Å. The bond valence sums were computed using the KDist software from the Kalvados program suite [103]. The surface instability index (SII, see section 2.2.2) was calculated only taking into account the atoms in the topmost two layers, plus any adsorbed atoms.

5.2.3. Experimental Methods

The experimental portion of this work was performed entirely by collaborator Dr. James A. Enterkin, and included a combination of transmission electron diffraction, X-ray photoelectron spectroscopy and heat treatments in different environments; it is described in much more detail in Enterkin‘s doctoral dissertation [104]. For this work, single-crystalline (100)-oriented $SrTiO_3$ wafers (10×10×0.5 mm, 99.95% purity, one side epi-polished) were commercially purchased from MTI Corporation (Richmond, CA) and cut into 3 mm-diameter

disks with a rotary disk cutter. Each disk was mechanically thinned to ~100 μm thickness with abrasive SiC paper; then, its center was dimpled with a Gatan dimple grinder and a diamond slurry to ~25 μm thickness; finally, the sample was milled (with 2.5-6.0 keV Ar^+ ions) at glancing incidence angle (< 3°) using a Gatan precision ion polishing system to obtain electron transparent regions at the center of the disk.

In order to remove implanted ions and other impurities, the specimens were washed for several seconds in a concentrated HCl:HNO_3 (equal parts by volume) solution. After several rinsing cycles with deionized water and drying, samples were air-annealed to repair the damage and the preferential removal of light atoms such as O. Each sample was placed in an alumina boat in a fused silica tube, which was inserted into a Carbolite STF 15/51/180 furnace and annealed at 850-950 ºC; this temperature range was selected to target the formation of the 2×1 and c(4×2) reconstructions, following previous reports [136].

Samples were mounted in a custom-made alumina ring and secured with a tungsten spring clip, then introduced into the UHV SPEAR system at Northwestern University, which is interfaced with a UHV Hitachi H9000 transmission electron microscope (TEM) with base pressure of 1×10^{-10} Torr. After insertion into the SPEAR load lock chamber, this compartment was pumped down and wrapped with a thermal blanket filled with dry ice to act as a cold trap to help the chamber reach UHV conditions. Once inside the system, samples were transported, always *in vacuo*, between different compartments: the gas treatment cell, for anneals with a resistive heating stage; the analytical chamber, for electron-gun anneals or XPS analysis; and the TEM, for electron diffraction and real space imaging. No further exposure to air took place, unless otherwise stated.

XPS was carried out with an Al K_α source using a PHI model 05-458 hemispherical analyzer. Spectra were normalized and corrected for charging effects with the known $SrTiO_3$ Ti-$2p_{3/2}$ peak of binding energy (458.8 eV). The Sr-3d, Ti-2p, O-1s and C-1s regions were scanned in detail (0.1 eV step size, dwell time of 0.5-0.655 seconds, averaged over 5-25 scans), following a broad survey scan. Each peak was fit to a Gaussian curve, with the background signal subtracted linearly. The appearance of a high binding energy shoulder on the O-1s peak, which may indicate hydroxyl-type bonding, was monitored and quantified [40-42, 137]. It is known that Ti^{3+} also leads to a similar shoulder feature, as it does in rutile TiO_2 [40, 41]; therefore, the presence of Ti^{3+} was simultaneously tested by looking for low binding energy shoulders on the Ti-2p peaks.

Two types of heat sources were used for the annealing treatments: either an electron gun or a resistive heating stage. Electron-gun annealing was performed with a Kimball Physics EMG-14 gun. The sample was bombarded with a low-energy beam (4.28 kV accelerating voltage) and the temperature was increased by either increasing the filament current, or by focusing the beam onto the central, thinner area of the sample, which is the region analyzed by TEM. The temperature was measured with an infrared optical pyrometer. Two main concerns exist with this type of heating. First, while high temperatures are attainable, the required beam size is significantly smaller than the sample diameter, resulting in inhomogeneous heating. Second, low-energy electron bombardment is known to reduce titanium in rutile TiO_2 [138]; this was found to occur with $SrTiO_3$ even in an oxygen gas environment. Conversely, annealing with a resistive heating stage resulted in uniform heating, but the maximum achievable temperature was lower than with the electron gun. In the latter setup, a calibrated thermocouple was employed to monitor the temperature.

5.3. Results

The main new results presented here relate to the adsorption of H_2O on known TiO_2-rich $SrTiO_3(001)$ surface reconstructions. In order to test the reliability of the computational method for total energy and BVS calculations, full-monolayer water adsorption was modeled on the bulk-like $SrTiO_3(001)$ TiO_2-truncation seen in Figure 5.1(a), both in the dissociative and molecular modes. This enables a direct comparison to three previous theoretical reports [125-127]. Qualitatively, the relaxed dissociative and molecular structures are very similar to those previously examined. The molecularly-adsorbed water molecule, seen in Fig. 5.1(b), orients itself so as to generate a rough in-plane alignment of its O−H bonds with oxygen atoms at the surface. In the dissociative adsorption case, the adsorbed OH and the lone H adsorbed on a surface O tilt slightly in opposite directions. The relaxed structures are available in Appendix D in the Crystallographic Information File (CIF) format.

All interatomic distances and adsorption energies with at least two previously published theoretical values are tabulated in Table 5.1. As in the prior studies, it is found that the surface with molecularly adsorbed water is more stable than the dissociative case for water coverage of one molecule per 1×1 cell. The only significant discrepancy is found in the molecular adsorption case, where the H_2O molecule tilts more than previously predicted: one of the hydrogen atoms (H2) comes closer to —while the other (H1) goes farther away from— the surface than in the other calculations. Otherwise, the predictions agree very well with results in the literature, especially with those from the recent Hinojosa *et al.* [127] report.

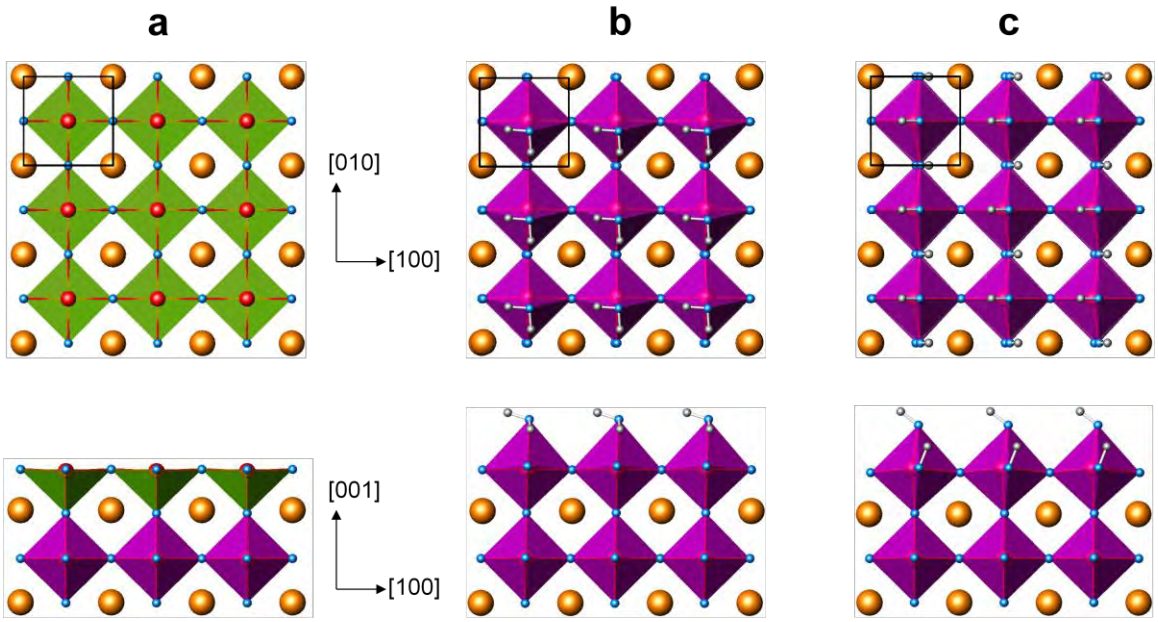

Fig. 5.1. Polyhedral representation of (a) the bulk-like TiO_2-truncated $SrTiO_3$(001) surface, (b) the favored full-monolayer molecular water adsorption geometry on this surface, and (c) the relaxed full-monolayer dissociative water adsorption geometry. Plan view on top (surface cells outlined) and profile view at the bottom. Sr = large orange, Ti = red, O = blue, and H = gray. All polyhedra are Ti-centered, with 5-fold coordination polyhedra in green and 6-fold coordination polyhedra in purple.

Table 5.1. Calculated interatomic distances (in Å) and adsorption energies (in eV/molecule) for the water adsorption structures on the bulk-like TiO_2-terminated $SrTiO_3$(001) surface. The *mol* and *diss* superscripts refer to the relaxed full-monolayer molecular and dissociative adsorption configurations, respectively. The atom labels follow the labels used in the CIF files listed in Appendix D.

	Wang *et al.* [125]	Evarestov *et al.* [126]	Hinojosa *et al.* [127]	This work
$Ti1–O_w^{mol}$	2.23	2.27	2.27	2.24
$H1–O1^{mol}$	2.59	–	2.42	2.75
$H2–O2^{mol}$	2.23	1.85	1.82	1.73
$O_w–H1^{mol}$	0.984	–	0.98	0.981
$O_w–H2^{mol}$	0.986	–	1.00	1.02
$Ti1–O_w^{diss}$	–	1.88	1.90	1.90
E_{ads}^{mol}	0.83	0.87	0.79	0.80
E_{ads}^{diss}	–	0.77	0.59	0.58

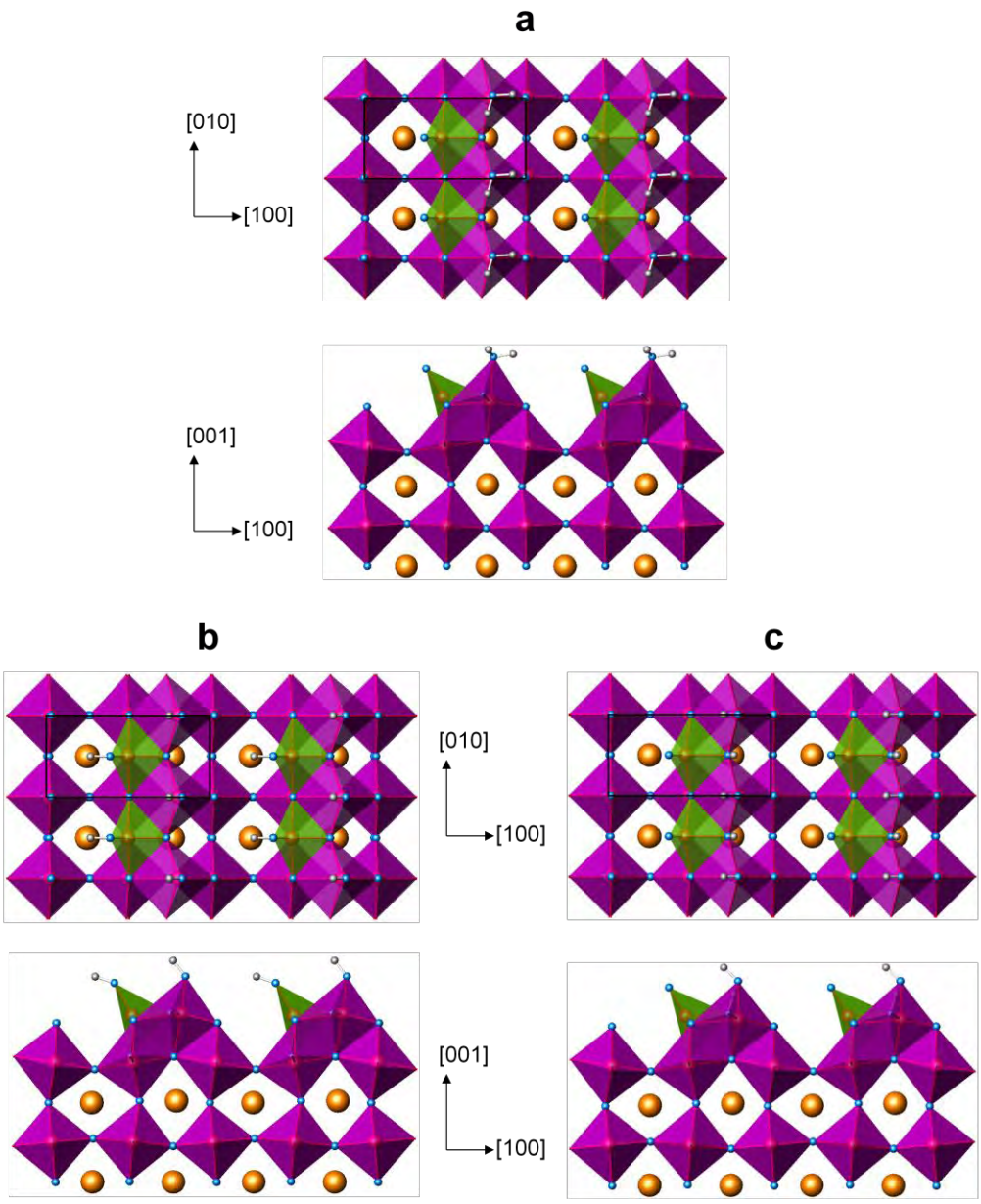

Fig. 5.2. Polyhedral representation of half-monolayer water adsorption configurations with 2×1 periodicity: (a) the 2×1Mol model, (b) the 2×1DissA model, and (c) the 2×1DissB model. Plan view on top (surface cells outlined) and profile view on the bottom. Legend follows Fig. 5.1.

The 2×1, RT2, 2×2 and c(4×2) DL TiO_2 reconstructions are now examined in more detail. For each case, additional structures with 0.5 and 1 ML H_2O adsorption are explored; please note that 1 ML is defined differently than in the previous studies [126-128]. It must be emphasized that the number of possible geometric configurations is prohibitively large. Therefore, the set of structures studied herein is not an exhaustive list and it is certainly possible that other structures of the same stoichiometry are of lower surface energy. However, the aim is to tackle the most likely low-energy candidate structures, as dictated by chemical intuition and reasoning, making use of bond-valence analysis of the dry structures to screen out many implausible adsorption configurations.

Bond valence sums and the surface instability index (SII) are calculated for the lowest-energy structure of each periodicity and water coverage; these structural models are ultimately used for further thermodynamic analysis.

5.3.1. The 2×1 Surface

The presently accepted structural solution to the 2×1 reconstruction [34], discussed in subsection 3.4.1, exhibits a characteristic "dangling" oxygen (in single coordination, O1 in Table 5.2) and one mirror plane. The polyhedral representation is displayed in Figure 3.2(a). As can be seen in Table 5.2, several top-layer atoms in the dry 2×1 reconstruction are very undercoordinated, including both Ti and the "floating" O (those which are not bound to subsurface Ti, borrowing the nomenclature by Warschkow *et al.* [90]). These drive the relatively large SII, which correlates with the high surface energy, both of which are unusual for an experimentally observed structure.

Table 5.2. Bond valence sums for the near-surface atoms of the 2×1 dry structure and low-energy hydrated models. *m* is the atom multiplicity per 1×1 cell. The SII is also shown for each surface. For the hydrated models, the SII shown in parentheses is calculated without taking the adsorbed atoms into account. Atom labels follow labels in CIF files listed in Appendix D.

	2×1			**2×1DissA**			**2×1SatB**		
ML H_2O	0			0.5			1		
SII	0.28			0.10 (0.11)			0.12 (0.14)		
	Atom	*m*	BVS	Atom	*m*	BVS	Atom	*m*	BVS
Adsorbed Atoms				O_w1	0.5	–1.93	O_w1	0.5	–1.96
				H1	0.5	0.96	H1	0.5	0.97
				H2	0.5	0.95	H2	0.5	1.04
							O_w2	0.5	–1.84
							H3	0.5	0.96
							H4	0.5	1.01
Top layer	Ti1	0.5	3.64	Ti1	0.5	3.95	Ti1	0.5	3.90
	Ti2	0.5	3.45	Ti2	0.5	3.83	Ti2	0.5	3.89
	O1	0.5	–1.54	O1	0.5	–1.97	O1	0.5	–1.95
	O2	0.5	–1.68	O2	0.5	–2.04	O2	0.5	–1.92
	O3	0.5	–2.20	O3	0.5	–2.06	O3	0.5	–2.12
	O4	0.5	–1.88	O4	0.5	–1.88	O4	0.5	–2.30
2nd layer	Ti3	0.5	4.01	Ti3	0.5	3.93	Ti3	0.5	4.00
	Ti4	0.5	4.15	Ti4	0.5	4.04	Ti4	0.5	3.90
	O5	0.5	–2.05	O5	0.5	–1.80	O5	0.5	–1.82
	O6	0.5	–1.91	O6	0.5	–2.08	O6	0.5	–1.83
	O7	0.5	–1.95	O7	0.5	–2.01	O7	0.5	–1.99
	O8	0.5	–2.31	O8	0.5	–2.17	O8	0.5	–2.13

Several 0.5 ML configurations (1 H_2O per 2×1 cell) were modeled:

- 2×1Mol (Fig. 5.2(a)): In the dry case, it is clear that of the two surface Ti, atom Ti2 is more exposed (and more undercoordinated, as seen in Table 5.2); therefore, Ti2 is the natural choice for the adsorption site of molecular water. Much like the full-monolayer molecular adsorption on bulk-like TiO_2, the O−H bonds align with surface O atoms (in this case, O2 and O4). This structural model, however, is unstable – its surface energy is 0.37 eV/1×1 higher than the following case.

- 2×1DissA (Fig. 5.2(b)): Dissociative adsorption, where an OH group adsorbs to the aforementioned Ti2 site. The remaining H binds to the dangling O1 atom, previously in single

coordination. This preserves the original mirror plane and is the lowest energy structure among half-monolayer –wet" 2×1 surfaces.

- 2×1DissB (Fig. 5.2(c)): Dissociative adsorption, similar to 2×1DissA, except for the adsorption of the lone H on O2, which is the second most undercoordinated anion. This is also unstable, 0.59 eV/1×1 higher in energy than 2×1DissA.

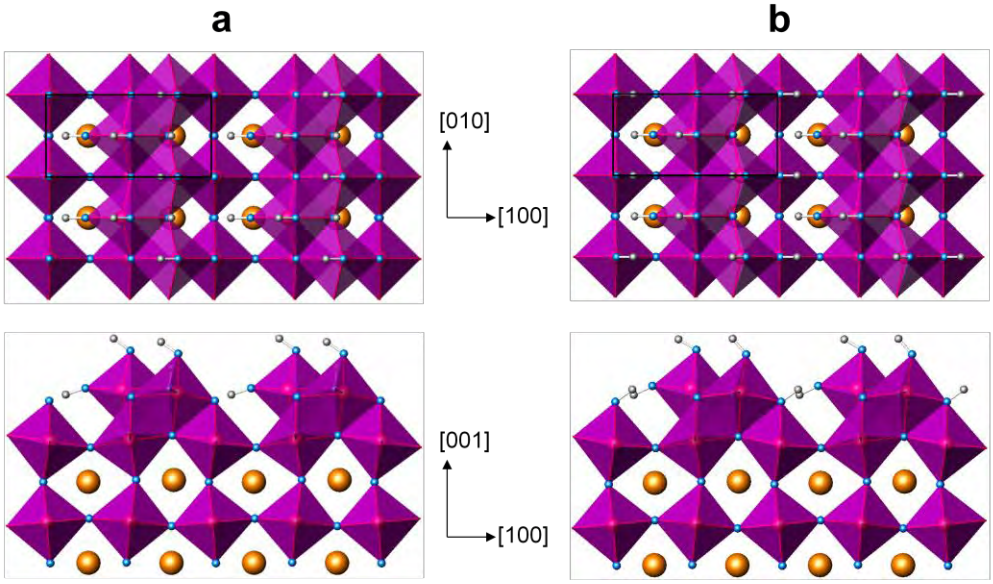

Fig. 5.3. Polyhedral representation of full-monolayer water adsorption configurations with 2×1 periodicity: (a) the 2×1SatA model, and (b) the 2×1SatB model. Plan view on top (surface cells outlined) and profile view on the bottom. Legend follows Fig. 5.1.

Model 2×1DissA provides a very low SII (Table 5.2), as a result of the almost ideal BVS of the surface atoms. This fact is suggestive that this structural model may be a more accurate description of the experimentally observed 2×1 reconstruction; as previously mentioned, diffraction experiments are not very sensitive to light atoms. The 2×1DissA model shall be revisited in section 5.3.7 in the context of experimental and simulated STM images.

Two full-monolayer cases of 2×1 periodicity were studied:

- 2×1SatA (Fig. 5.3(a)): Double dissociative adsorption. Similar to 2×1DissA, this structure adds an OH group to the previously shielded Ti1 atom, while the other lone H binds to O2, which is the second most underbonded oxygen atom in the dry 2×1 model. This renders all Ti 6-fold coordinated and forces the distinctive titanyl bond from the dry structure to be parallel to the surface. It is worth noting that the mirror plane is also preserved here even when no symmetry constraint is applied, and that upon relaxation all four O−H bonds lean in the same direction.

- 2×1SatB (Fig. 5.3(b)): Double dissociative adsorption. Similar to 2×1SatA, except that the second lone H binds not to O2, but to O4, which is the most underbonded surface oxygen in 2×1DissA, the favored 0.5 ML case. This new O−H leans in the direction opposite to all the others. This structure was found to be more stable than 2×1SatA by 0.24 eV/1×1.

With the exception of O4, which is now overbonded, the BVS remain near the expected values (Table 5.2). The SII of 2×1SatB, while slightly higher than for the half-monolayer case, is significantly lower than for the bare 2×1.

5.3.2. The RT2 Surface

As mentioned above, this DL reconstruction has the lowest surface energy, but has not been observed experimentally; see Figure 3.12(a) for its polyhedral representation. Table 5.3 shows that the BVS upon relaxation are mostly reasonable and the SII of the RT2 is better than for all other dry DL reconstructions. While some of the surface atoms are somewhat undercoordinated, their divergence from the expected BVS is relatively small.

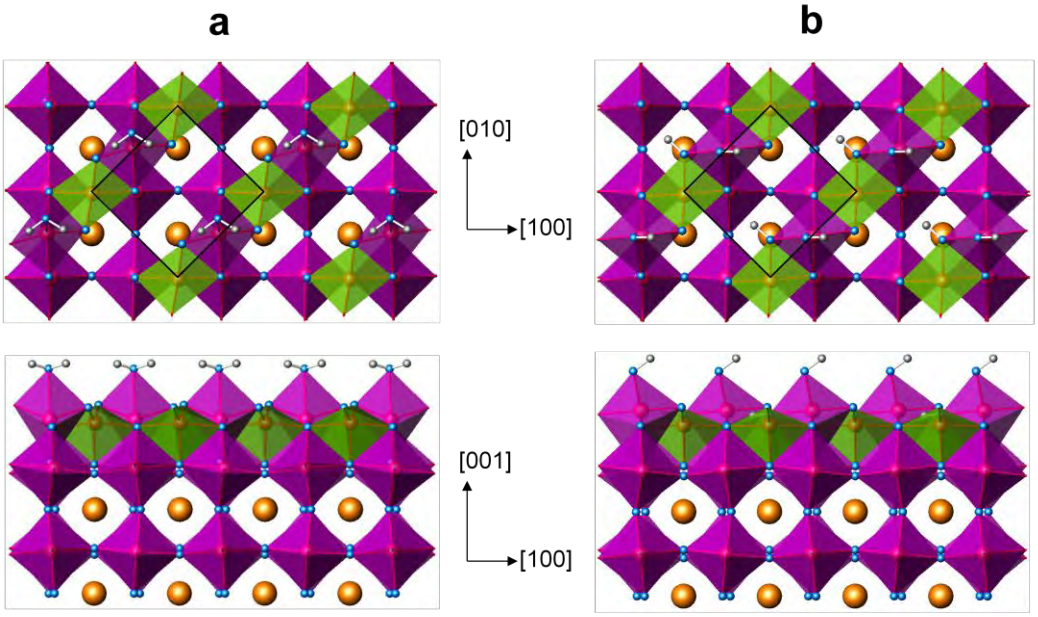

Fig. 5.4. Polyhedral representation of half-monolayer water adsorption configurations with RT2 periodicity: (a) the RT2Mol model, and (b) the RT2Diss model. Plan view on top (surface cells outlined) and profile view on the bottom. Legend follows Fig. 5.1.

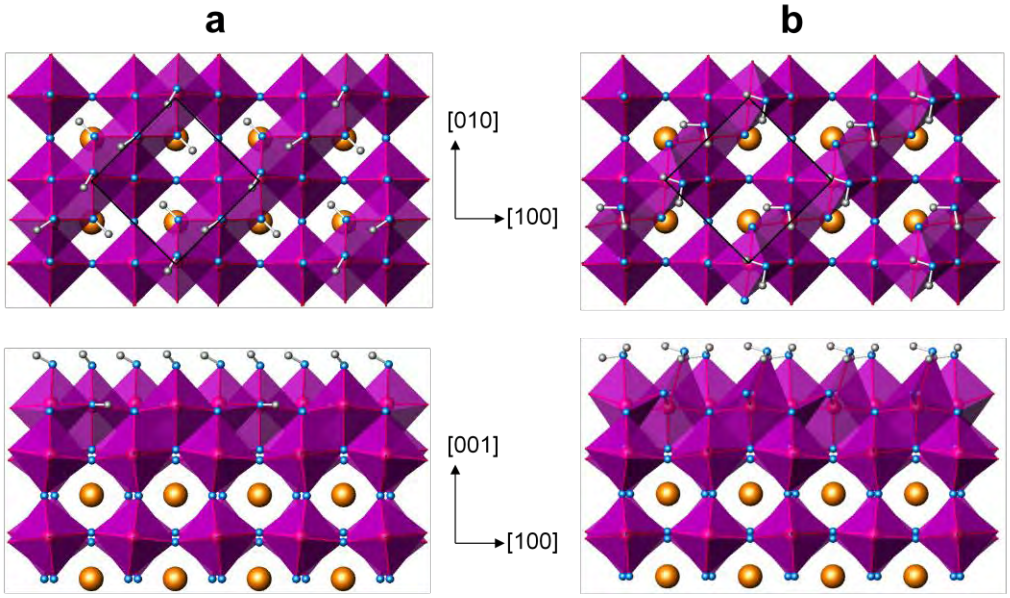

Fig. 5.5. Polyhedral representation of full-monolayer water adsorption configurations with RT2 periodicity: (a) the RT2SatD model, and (b) the RT2SatM model. Plan view on top (surface cells outlined) and profile view on the bottom. Legend follows Fig. 5.1.

Table 5.3. Bond valence sums for the near-surface atoms of the RT2 dry structure and low-energy hydrated models. The SII is also shown for each surface.

	RT2			RT2Diss			RT2SatD		
ML H_2O	0			0.5			1		
SII	0.13			0.14 (0.15)			0.13 (0.15)		
	Atom	*m*	BVS	Atom	*m*	BVS	Atom	*m*	BVS
Adsorbed Atoms				O_w	0.5	−1.87	O_w1	0.5	−1.90
				H1	0.5	0.95	H1	0.5	0.99
							H2	0.5	1.00
							O_w2	0.5	−1.89
							H3	0.5	1.01
							H4	0.5	0.97
Top layer	Ti1	1	3.82	Ti1a	0.5	4.04	Ti1a	0.5	4.17
				Ti1b	0.5	3.90	Ti1b	0.5	4.14
	O1	1	−2.04	O1a	0.5	−2.01	O1a	0.5	−2.03
				O1b	0.5	−1.97	O1b	0.5	−2.05
	O2	1	−1.84	O2a	0.5	−2.26	O2a	0.5	−2.28
				O2b	0.5	−1.88	O2b	0.5	−2.31
2nd layer	Ti2	1	4.08	Ti2a	0.5	4.04	Ti2a	0.5	3.99
				Ti2b	0.5	4.02	Ti2b	0.5	3.97
	O3	1	−1.98	O3a	0.5	−2.17	O3a	0.5	−1.94
				O3b	0.5	−1.84	O3b	0.5	−1.87
	O4	1	−2.19	O4a	0.5	−2.31	O4a	0.5	−2.10
				O4b	0.5	−1.88	O4b	0.5	−2.05

Two 0.5 ML structures (1 H_2O per RT2 cell) were examined:

- RT2Mol (Fig. 5.4(a)): Since all surface Ti are equivalent in the dry structure, the adsorption site for molecular H_2O is arbitrary. The new Ti−O bond tilts so as to favor a rough alignment of the each O−H bond towards a neighboring O2 atom. The O2 have lower coordination than O1 since they are not bound to a Ti beneath and hence they lift up slightly. This structure was examined with no enforced in-plane symmetry.

- RT2Diss (Fig. 5.4(b)): Dissociative adsorption, where an OH group binds to an arbitrary surface Ti, with the O−H bond tilting towards one of the neighboring O2 atoms (O2b in Table 5.3). The extra lone H binds to the other O2 (O2a), and this new O−H bond points towards an O1 atom (O1b) from the next diagonal row of surface polyhedra so as to form a H-

bond (2.07 Å). Like in the previous case, no in-plane symmetry was enforced. Although the difference is within error, this structure is calculated to be lower in energy by 0.03 eV/1×1.

Two full-monolayer structures with RT2 periodicity were modeled:

- RT2SatD (Fig. 5.5(a)): Double dissociative adsorption. A hydroxyl group binds to each surface Ti. Upon relaxation, all these O−H bonds roughly align in-plane, leaning towards the same <110>-type direction. Each lone H binds to an O2 atom; as in RT2Diss, each new O−H bond points towards an O1 from the next row of surface polyhedra, forming a H-bond (H2−O1b = 1.85 Å; H3−O1a = 1.86 Å).

RT2SatM (Fig. 5.5(b)): Double molecular adsorption. A water molecule adsorbs on each surface Ti site. No in-plane symmetry enforced. Each O−H bond originally points towards a nearby O2, but this is no longer true upon relaxation. This structure is found to be 0.28 eV/1×1 higher in energy than RT2SatD.

Model RT2Diss largely corrects the BVS shortcomings of the bare RT2 surface. However, it does leave the top-surface O2a and the subsurface O4a atoms overcoordinated. Meanwhile, RT2SatD does the same to top-surface Ti and all O2-type atoms. Neither hydrated model has comparably better metrics than the dry RT2 structure.

5.3.3. The "Zigzag" 2×2 Surface

The "zigzag" 2×2 reconstruction, discussed in section 3.4.6 and depicted in Figure 3.12(b), shows some underbonding for most of its top layer atoms, but as its SII indicates (Table 5.4), the BVS numbers are clearly better than the dry 2×1 model, as expected from a structure with lower surface energy.

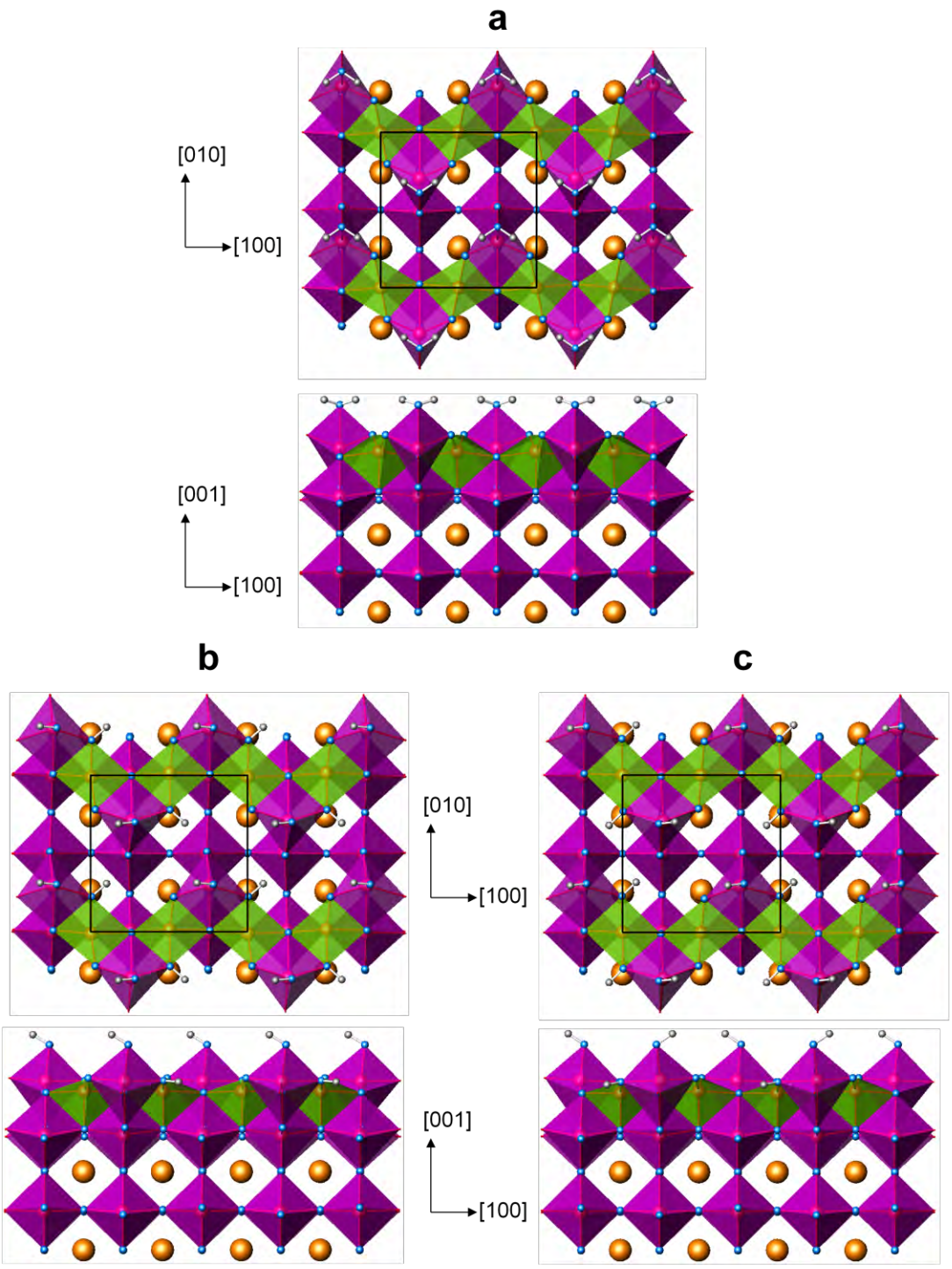

Fig. 5.6. Polyhedral representation of half-monolayer water adsorption configurations with 2×2 periodicity: (a) the 2×2Mol model, (b) the 2×2DissA model, and (c) the 2×2DissB model. Plan view on top (surface cells outlined) and profile view on the bottom. Legend follows Fig. 5.1.

Table 5.4. Bond valence sums for the near-surface atoms of the 2×2 dry structure and low-energy hydrated models. The SII is also shown for each surface.

	2×2			**2×2Mol**			**2×2SatD**		
ML H_2O	0			0.5			1		
SII	0.17			0.15 (0.16)			0.10 (0.11)		
	Atom	*m*	BVS	Atom	*m*	BVS	Atom	*m*	BVS
Adsorbed Atoms				O_w	0.5	–2.14	O_w1	0.5	–1.88
				H1	1	0.97	H1	0.5	0.98
							H2	0.5	0.96
							O_w2	0.5	–1.90
							H3	0.5	1.03
							H4	0.5	1.01
Top layer	Ti1	0.5	3.78	Ti1	0.5	3.86	Ti1	0.5	3.96
	Ti2	0.5	3.70	Ti2	0.5	3.72	Ti2	0.5	3.94
	O1	1	–1.83	O1	1	–1.81	O1a	0.5	–2.21
							O1b	0.5	–2.19
	O2	0.5	–2.09	O2	0.5	–2.05	O2	0.5	–2.04
	O3	0.5	–1.87	O3	0.5	–1.88	O3	0.5	–1.87
2nd layer	Ti3	0.5	3.88	Ti3	0.5	3.88	Ti3	0.5	3.99
	Ti4	0.5	4.16	Ti4	0.5	4.13	Ti4	0.5	3.90
	O4	0.5	–1.93	O4	0.5	–1.83	O4	0.5	–1.89
	O5	0.5	–2.06	O5	0.5	–2.12	O5	0.5	–1.87
	O6	0.5	–1.93	O6	0.5	–1.95	O6	0.5	–2.00
	O7	0.5	–2.24	O7	0.5	–2.21	O7	0.5	–2.11

The following 0.5 ML structures (2 H_2O per 2×2 cell) were studied:

- 2×2Mol (Fig. 5.6(a)): Molecular adsorption, where the H_2O molecules adsorb at Ti2, which is more undercoordinated than Ti1. A p2gm symmetry constraint was imposed and upon relaxation the Ti−O bond tilts so as to favor a rough alignment of each O−H bond towards the nearby O1 at the surface. This is the low-energy structure for this periodicity and water coverage.

- 2×2DissA (Fig. 5.6(b)): Dissociative adsorption. A hydroxyl group adsorbs at Ti2, with its O−H bond tilting towards one of the two neighboring O1. All such O−H bonds point towards the same direction. The corresponding lone H binds to the other O1 and this new O−H bond tilts so as to form a H-bond (1.87 Å) with an O3 from the next zigzag row of surface

polyhedra. In this structure, the glide planes are preserved, but not the 2-fold rotational symmetry. Its energy is slightly higher than that of 2×2Mol, by a margin of 0.07 eV/1×1.

- 2×2DissB (Fig. 5.6(c)): Dissociative adsorption. Similar to 2×2DissA, except that (going along each zigzag) the adsorbed hydroxyl O−H bonds alternate orientations. Therefore, in this case the 2-fold rotational symmetry is preserved, while the glide planes are not. The energy of this model is higher than for the 2×2Mol by 0.10 eV/1×1.

The 2×2Mol model, despite its relatively low energy, does not bring the Ti2 BVS dramatically closer to its optimal +4 value (Table 5.4); the same can be said for virtually every atom. While the bond valence metrics do get better, the improvement is modest, as evidenced by the comparable SII values.

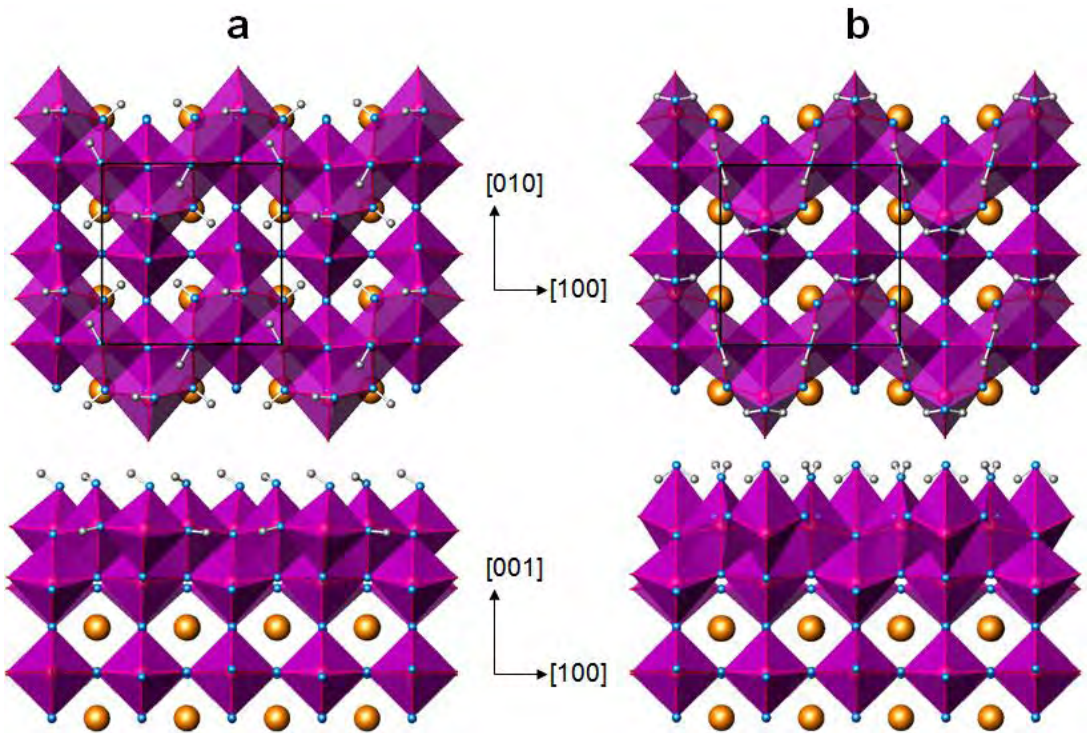

Fig. 5.7. Polyhedral representation of full-monolayer adsorption geometries with 2×2 periodicity: (a) the 2×2SatD model, and (b) the 2×2SatM model. Plan view on top and profile view on the bottom. Legend follows Fig. 5.1.

In addition to the above, two full-monolayer structural models were tested:

- 2×2SatD (Fig. 5.7(a)): Double dissociative adsorption. Every surface Ti acts as an adsorption site for hydroxyl groups. Each of the four lone H atoms binds to a surface O1 and this bond points towards an O3 from the next zigzag row of surface polyhedra so as to form H-bonds (H3−O3 = 1.59 Å; H4−O3 = 1.63 Å). In this case, the 2-fold rotational symmetry is not preserved, but the glide planes are. In spite of this constraint, the energy of 2×2Mol is the lowest of all the full-monolayer structural models.

- 2×2SatM (Fig. 5.7(b)): Double molecular adsorption. This model is similar to 2×2Mol, with an additional water molecule adsorbed on every Ti1. The original p2gm is enforced. This adsorption configuration yields a surface energy 0.78 eV/1×1 higher than the 2×2SatD model.

The 2×2SatD configuration succeeds in improving the bond-valence sums for almost every atom in the surface region, including the adsorbates. While there is some overcoordination of the O1-type atoms, it is comparable to the undercoordination exhibited in the lower H_2O coverage cases.

5.3.4. The c(4×2) Surface

This reconstruction was discussed in subsection 3.4.3. Figure 3.8(a) clearly shows its characteristic surface polyhedral quartet feature, which was central to the discussion in Chapter 4. As Table 5.5 shows, the relaxed c(4×2) reconstruction shows both overcoordination (noticeably for atom O4, which sits at the center of the polyhedral quartet, bound to five Ti) as well as undercoordination (Ti1, Ti2 and O1, which are the surface atoms surrounding O4) in its

top layer. However, its SII is comparable to that of the ~~"~~zigzag" 2×2 surface, much like their respective surface energies.

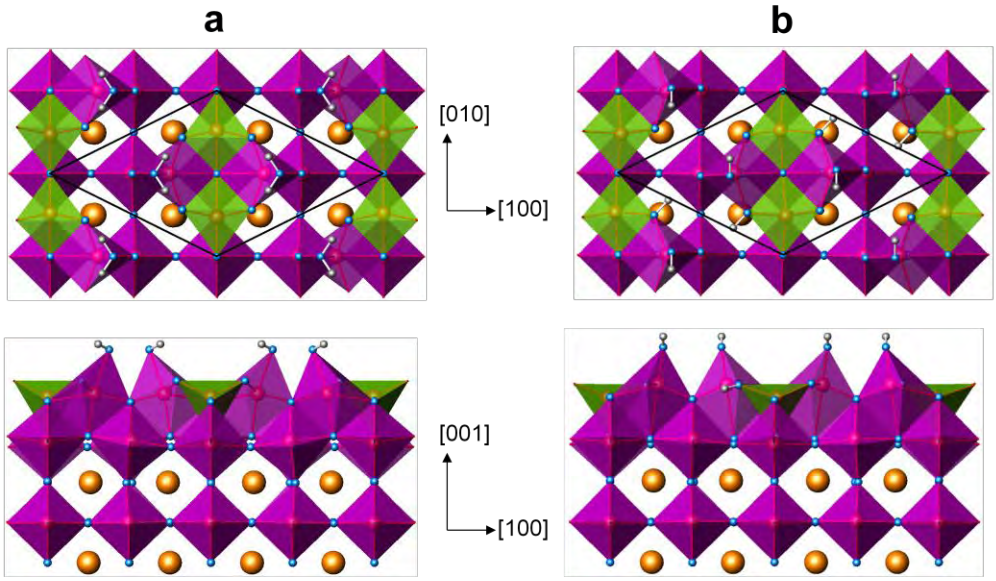

Fig. 5.8. Polyhedral representation of half-monolayer water adsorption configurations with c(4×2) periodicity: (a) the c(4×2)Mol model, and (b) the c(4×2)Diss model. Plan view on top (surface cells outlined) and profile view on the bottom. Legend follows Fig. 5.1.

Two 0.5 ML models (2 H_2O per c(4×2) cell) were examined:

- c(4×2)Mol (Fig. 5.8(a)): Molecular adsorption. Of the surface Ti atoms, the Ti2 are more undercoordinated than the Ti1 and, therefore, molecular water should preferentially adsorb on Ti2. The two H_2O groups of each polyhedral quartet tilt away from each other favoring the in-plane alignment of each O−H bond towards a surface O1. The symmetry was constrained to the original c2mm.

- c(4×2)Diss (Fig. 5.8(b)): Dissociative adsorption. One hydroxyl group adsorbs on each Ti2 atom. Each of these O−H bonds tilts slightly towards one of the nearby surface O1 atoms. A lone H binds to the other neighboring O1 and this new O−H bond aligns towards an

O3 at the corner of a nearby polyhedral quartet, so as to form a H-bond (1.99 Å). Only the 2-fold rotational symmetry, not the mirror planes, is preserved. The energy of this model is 0.08 eV/1×1 higher than that of c(4×2)Mol.

Model c(4×2)Mol yields better BVS numbers than the dry case for the top-layer atoms (see Table 5.5), nudging them closer to their ideal values; however, it makes them worse for several atoms in the layer beneath. The net outcome is a slightly lower (yet certainly comparable) SII than for the bare surface.

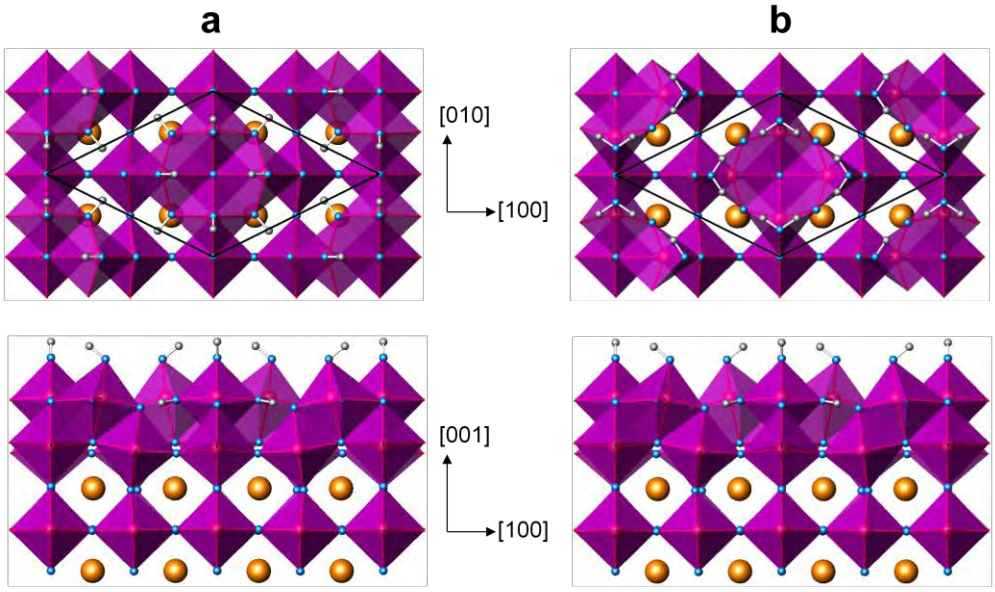

Fig. 5.9. Polyhedral representation of full-monolayer water adsorption configurations with c(4×2) periodicity: (a) the c(4×2)SatD model, and (b) the c(4×2)SatM model. Plan view on top (surface cells outlined) and profile view on the bottom. Legend follows Fig. 5.1.

Also, two full-monolayer structures were studied:

- c(4×2)SatD (Fig. 5.9(a)): Double dissociative adsorption. Every surface Ti has a hydroxyl group adsorbed on it. While the O−H bonds above Ti1 point away from the center of the polyhedral quartet, the O−H bonds above Ti2 relax to point towards it. Every O1 atom has a

lone H bound to it, with this new bond tilting towards an O3 from a nearby polyhedral quartet so as to form a H-bond (1.61 Å). This is the low-energy c(4×2) structure for 1 ML water coverage.

- c(4×2)SatM (Fig. 5.9(b)): Double molecular adsorption. Similar to c(4×2)Mol, with the addition of an adsorbed H_2O molecule on every Ti1, with all O−H pointing towards an O1 atom. The original c2mm symmetry was preserved. This was found to have a surface energy 0.60 eV/1×1 higher than c(4×2)SatD.

Table 5.5. Bond valence sums for the near-surface atoms of the c(4×2) dry structure and low-energy hydrated models. The SII is also shown for each surface.

	c(4×2)			**c(4×2)Mol**			**c(4×2)SatD**		
ML H_2O	0			0.5			1		
SII	0.18			0.16 (0.17)			0.11 (0.13)		
	Atom	*m*	BVS	Atom	*m*	BVS	Atom	*m*	BVS
Adsorbed atoms				O_w	0.5	–2.17	O_w1	0.5	–1.91
				H1	1	0.97	H1	0.5	0.97
							O_w2	0.5	–1.92
							H2	0.5	0.97
							H3	1	1.04
Top layer	Ti1	0.5	3.86	Ti1	0.5	3.93	Ti1	0.5	4.02
	Ti2	0.5	3.70	Ti2	0.5	3.75	Ti2	0.5	3.85
	O1	1	–1.81	O1	1	–1.78	O1	1	–2.20
	O2	0.25	–2.18	O2	0.25	–2.20	O2	0.25	–2.15
	O3	0.5	–1.89	O3	0.5	–1.92	O3	0.5	–1.94
	O4	0.25	–2.39	O4	0.25	–2.27	O4	0.25	–1.83
2nd layer	Ti3	0.25	4.20	Ti3	0.25	4.17	Ti3	0.25	3.91
	Ti4	0.5	3.96	Ti4	0.5	3.98	Ti4	0.5	4.02
	Ti5	0.25	4.23	Ti5	0.25	4.27	Ti5	0.25	4.06
	O5	0.5	–1.94	O5	0.5	–1.85	O5	0.5	–1.78
	O6	0.5	–2.06	O6	0.5	–2.13	O6	0.5	–1.93
	O7	0.5	–2.16	O7	0.5	–2.15	O7	0.5	–2.15
	O8	0.5	–1.95	O8	0.5	–1.96	O8	0.5	–1.98

Model c(4×2)SatD has the lowest SII among the low-energy c(4×2) structures, as shown in Table 5.5. While a couple of top-layer O sites flip drastically from undercoordinated to overcoordinated (or vice versa), the overall shift is towards the ideal BVS values. The SII numbers for this periodicity and the trend with varying water coverage are similar to the 2×2 structures.

5.3.5. The 2Ti Surface

For completeness, a hypothetical 1×1 reconstruction is explored here, which would not be detectable via diffraction methods as its reflections would overlap with bulk reflections. This structure essentially consists of 2 bulk-like TiO_2 layers at the surface, qualitatively resembling the stacking along the <001> direction in anatase, as shown in Figure 5.10(a). For brevity, this is dubbed the ―2Ti" structure and it is studied here for comparison to DL surfaces since it has same stoichiometry. It was also examined in the theoretical study by Warschkow *et al.* [90] and tentatively found via surface X-ray diffraction to be present at $SrTiO_3$(001) surfaces by Herger *et al.* [93, 94], although the authors cautioned that this might correspond to a disordered DL surface.

As Table 5.6 illustrates, the 2Ti surface is not viable in its ―dry" form, as its top layer has very poor bond valence sums; in particular, Ti1 and O1 (which is not bound to any subsurface Ti) are severely underbonded, with Ti1 closer to a 3+ than a 4+ formal valence state. As a result, the SII is dramatically large.

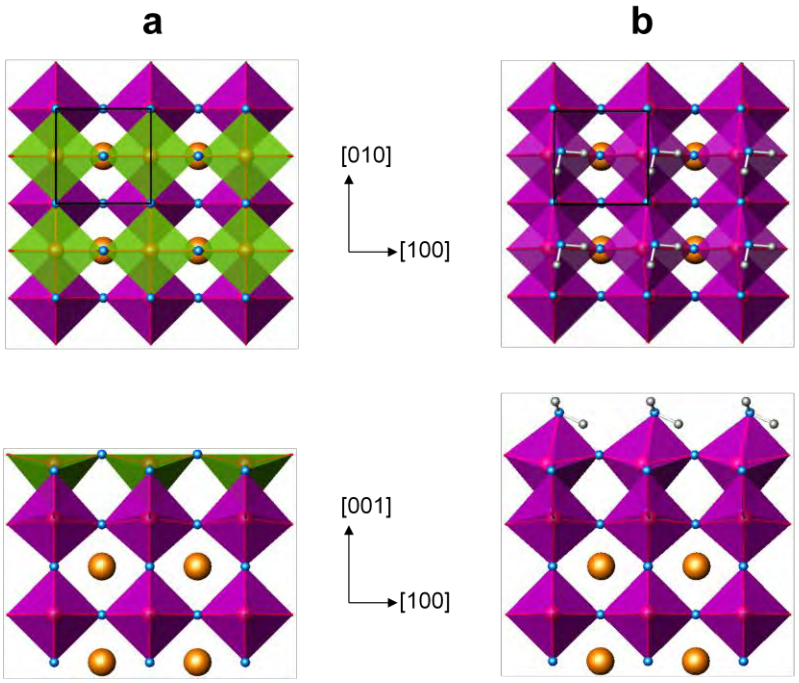

Fig. 5.10. Polyhedral representation of (a) the 2Ti surface, and (b) the relaxed full-monolayer molecular water adsorption geometry. (Top) Plan view, surface cells outlined and (bottom) profile view. Legend follows Fig. 5.1.

Table 5.6. Bond valence sums for the near-surface atoms of the 2Ti structure and hydrated models. The SII is also shown for each surface.

	2Ti			**2TiRT2**			**2TiMol**		
ML H_2O	0			0.5			1		
SII	0.46			0.12 (0.13)			0.19 (0.21)		
	Atom	*m*	BVS	Atom	*m*	BVS	Atom	*m*	BVS
Adsorbed atoms				O_w	0.5	–2.01	O_w	1	–2.04
				H1	0.5	1.07	H1	1	1.00
				H2	0.5	0.95	H2	1	0.95
Top layer	Ti1	1	3.21	Ti1a	0.5	3.78	Ti1	1	3.65
				Ti1b	0.5	3.73			
	O1	1	–1.24	O1a	0.5	–1.95	O1	1	–1.66
				O1b	0.5	–2.06			
	O2	1	–1.96	O2a	0.5	–1.89	O2	1	–1.93
				O2b	0.5	–1.90			
2nd layer	Ti2	1	3.96	Ti2a	0.5	4.00	Ti2	1	3.97
				Ti2b	0.5	4.00			
	O3	1	–1.86	O3a	0.5	–1.86	O3	1	–1.88
				O3b	0.5	–1.86			
	O4	1	–2.17	O4a	0.5	–2.04	O4	1	–2.12
				O4b	0.5	–2.05			

The first —wet" structure examined was the following:

- 2TiMol (Fig. 5.10(b)): Full monolayer molecular adsorption case; the analogous configuration had been found to be more stable than the dissociatively adsorbed structure for the simpler bulk-like truncation with a single TiO_2 surface layer. No in-plane symmetry was enforced. Indeed, the arrangement resembled closely the similar single-TiO_2-layer case, with both OH bonds roughly aligning towards pre-existing surface O.

While the Ti1 and O1 BVS values improve significantly, they both remain far from optimal. Additionally, a half-monolayer structure was considered:

- 2TiRT2: This structure started as the same as 2TiMol, except for the removal of half of the molecularly adsorbed H_2O groups. This was done by selecting the adsorption sites following a checkerboard pattern, which maximizes the distance between such sites at this coverage and results in a $(\sqrt{2}\times\sqrt{2})R45°$ periodicity; see Figure 5.11(a). Unexpectedly, however, the structure changes dramatically upon relaxation, as every adsorbed H_2O unit dissociates (Figure 5.11(b)). Atom O1a, which was originally bound to a hydrated Ti (Ti1b) but was closest among all surface O to any of the H atoms (as well as undercoordinated), pulls said atom (H1) and takes it, while the O1a-Ti1b is broken.

This results in rings of six 5-fold coordinated surface Ti atoms plus two hydroxyl groups to cap the otherwise undercoordinated surface O. More importantly, this is a very low energy structure, as shall be seen in the next section; this is consistent with the improved BVS (especially the O1-type atoms) and lowered SII, listed in Table 5.6. It bears noting that this structure is decidedly unviable in the full monolayer case due to the higher adsorbate density.

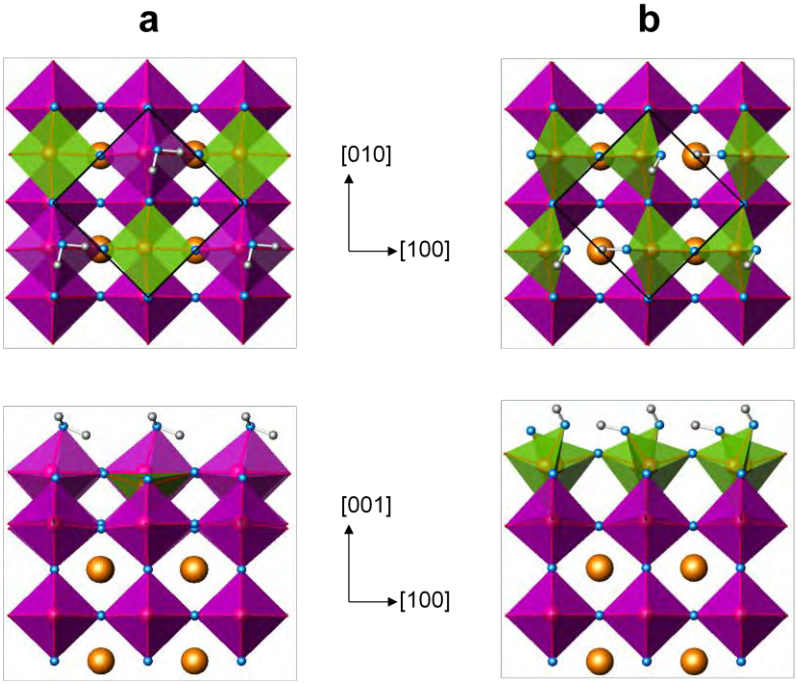

Fig. 5.11. Polyhedral representation of (a) the initial positions for the 2TiRT2 model, with 0.5 ML of molecularly adsorbed water on the 2Ti surface, and (b) the relaxed, final positions, showing the spontaneous dissociation of each water molecule. Plan view on top (surface cells outlined) and profile view on the bottom. Legend follows Fig. 5.1.

Before reporting the surface energy calculations in the next section, one ought to mention that the PBEsol0 and revTPSSh calculations for the bare 2Ti surface lead to a spuriously low surface energy. One way to visualize this is by plotting the SII versus the calculated surface energy at 0 K (which will be discussed in more detail in the next subsection). There is a strong correlation between these two, as expected [49], except for the 2Ti case, which is an unequivocal outlier (see Figure 5.12). More specifically, these calculations predict that the 2Ti has a lower surface energy than the dry 2×1 model, which is: (a) implausible, considering the strong undercoordination of the surface Ti, as a result of the symmetry constraints, (b) inconsistent with the results by Warschkow *et al.* [49], and (c) inconsistent with our own results using other exchange-correlation functionals. As can be seen in Figure 5.13, the energy of the 2Ti follows a

trend very different from the rest of dry reconstructions. This can be explained in terms of what the functionals do. The reason to use hybrid functionals such as PBE0 or PBEsol0 is that they address a significant shortcoming of PBE for materials with open-shell d/f orbitals, as it tends to overestimate the hybridization between them and p orbitals; in the particular case of $SrTiO_3$, PBE overestimates the covalency of Ti–O bonds. The hybrid functionals are more ~~–i~~onic" in the sense that they raise the energy of the Ti-3d states, thereby reducing the degree of hybridization with O-2p orbitals. In the on-site implementation of these functionals, however, this exact-exchange correction is applied only within the muffin-tin Ti spheres. The 2Ti is an exceptional case, however. In every other dry structure, some relaxation of the top-layer O bound to surface Ti is allowed, which shortens such Ti–O bonds. For the 2Ti, in contrast, all such O are constrained, and the bond lengths remain close to the bulk value: this means that, compared to the other dry structures, there is less of the O charge density tails within the Ti spheres. Therefore, the correction will increase the energy significantly less for the dry 2Ti calculation; this case, therefore, embodies an anomalous limitation to the method used. One solution would be to extend the exact-exchange correction to all space, although this would be computationally expensive. How about the hydrated 2Ti models? These should actually be exempt from the above limitation: both 2TiRT2 and 2TiMol do allow for some surface O relaxation.

The adsorption energies at 0 K for the low-energy wet structures (i.e. those listed in Tables. 5.2-5.6) are shown in Table 5.7, where the 2Ti case is excluded, given the uncertainty in the dry energy calculation. These correlate strongly with the change in SII with respect to the dry models, as shown in Figure 5.14. While this should be an expected result, this supports the use of bond valence sum analysis as a straightforward tool to examine surface structures.

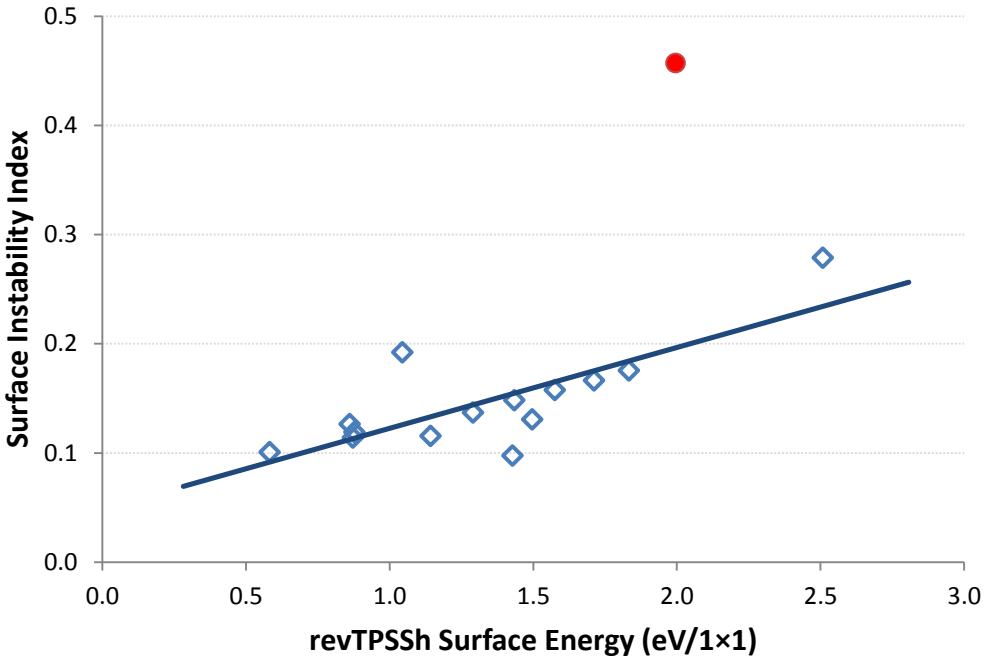

Fig. 5.12. SII as a function of revTPSSh surface energy for the low-energy structures. Red circular marker corresponds to the bare 2Ti surface, a significant outlier. The trendline is the best linear fit to the other data.

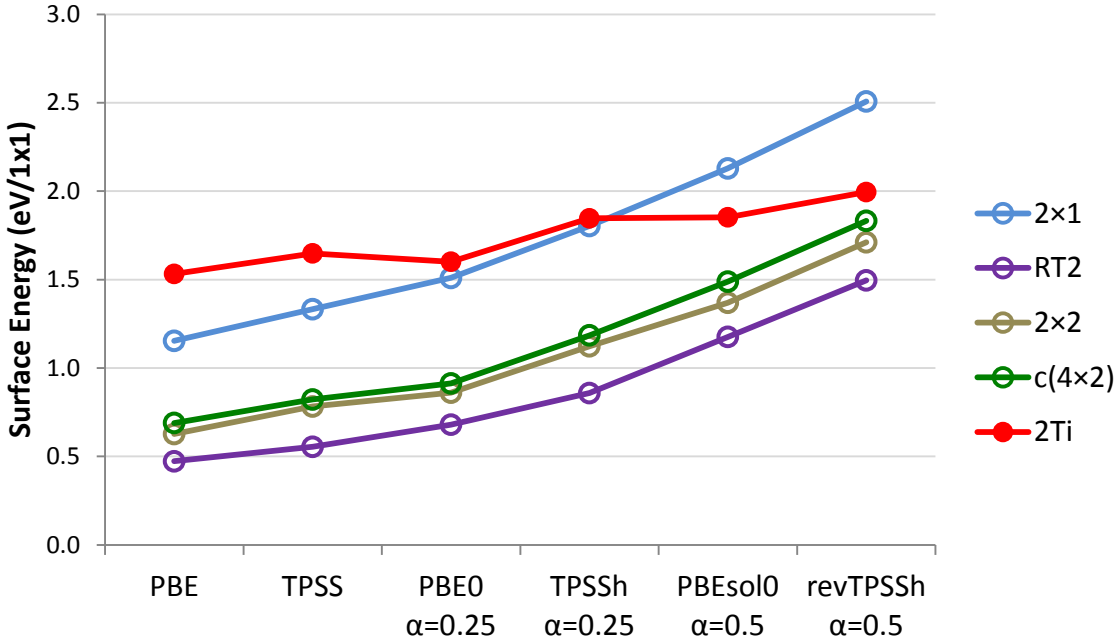

Fig. 5.13. Surface energy for dry surfaces for six different exchange-correlation functionals. α is the fraction of exact exchange, optimized for each hybrid functional.

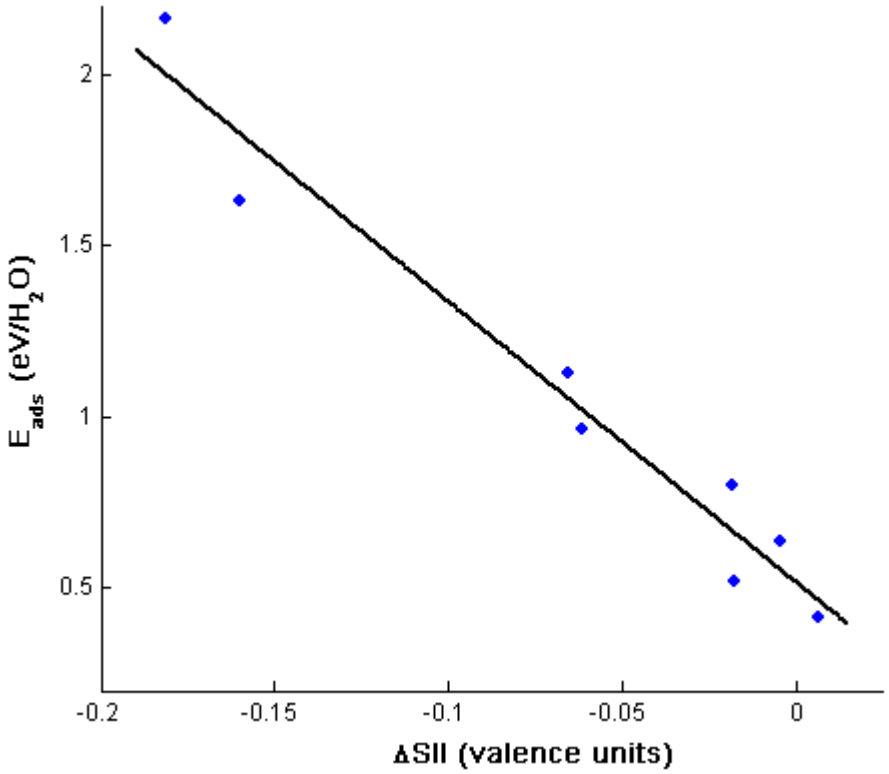

Fig. 5.14. Adsorption energies as a function of change in the surface instability index ($\Delta SII = SII_{wet} - SII_{dry}$). The linear fit has an R^2 coefficient of 0.95.

5.3.6. Thermodynamics

There are two main ways to look at the thermodynamics in question. The first is to examine the energetics as a function of the surface stoichiometry, keeping the chemical potential fixed (e.g. $T = 0$ K), while the second compares energies as a function of temperature. The items of interest in the first approach are the energies within each fixed water coverage, as well as the convex-hull construction (see subsection 2.2.1); the latter is most useful as errors in the energy of reference states (e.g. bulk $SrTiO_3$, TiO_2 and molecular H_2O) only rotate the convex hull and they do not change the predicted stable state for a given composition. As mentioned earlier, phonon entropy terms should cancel out to first order.

For this purpose, the surface energy was calculated for the lowest-energy structure for each water coverage and base periodicity. The revTPSSh values are plotted in Figure 5.15, which largely resembles the trends of the SII numbers. Here, the revTPSSh 2Ti surface energy has been discarded; instead, it has been estimated by adding the TPSS [139] difference between the 2Ti and the dry 2×1 to the revTPSSh 2×1 surface energy. Also, given the increased uncertainty in this value, the error bars have been tripled in magnitude, as compared to the other structures.

Ignoring the 2Ti anomaly, the energies of the dry structures follow the same hierarchy as in the calculations by Warschkow *et al.* [90], which was already apparent in Figure 5.13. While the RT2 reconstruction definitely has the lowest energy among the bare structures, this is no longer true upon adsorption of H_2O. At half-monolayer coverage, all periodicities yield similar energies, nearly becoming degenerate; RT2Diss has a slightly higher energy than the relaxed 2TiRT2 geometry, and only slightly lower than the other periodicities. At full-monolayer water adsorption, RT2SatD has a surface energy comparable to the 2×1SatB and c(4×2)SatD configurations, with the 2×2SatD as the most stable arrangement. A strict convex-hull construction skips all half-monolayer structures, and predicts the coexistence of RT2 and 2×2SatD on the surface. The adsorption energies (Table 5.7) highlight that, even at full-monolayer coverage, the bare RT2 adsorbs H_2O more weakly than the other reconstructions and the bulk-like TiO_2 truncation (Table 5.1).

It is also clear that the 2×1 models follow an odd trend, since the 0.5 ML water adsorption is stronger than the full-monolayer case. Unlike the dry RT2, "zigzag" 2×2 and c(4×2) reconstructions, the bare 2×1 structure has a surface Ti site (Ti2) where the position of every neighboring O is heavily constrained, inhibiting any significant bond shortening or

outward relaxation. The environment around Ti2 is thus similar to octahedral Ti sites in the bulk, but with only 5 surrounding oxygen atoms, rendering it an ideal site for adsorption. This atom is also very exposed, which makes it easy for foreign molecules to approach it, as compared to the more concealed surface Ti elsewhere; Table 5.7 lists the solid angle subtended by the four neighboring top-layer O with respect to the worst-BVS Ti in each bare structure. Adsorption on the dry 2×1 is further enhanced by the severely undercoordinated ~~–d~~angling" oxygen (O1), an ideal site for H from dissociated water. Similar geometric arguments can be easily applied to the 2Ti surface, which is even more unstable when dry.

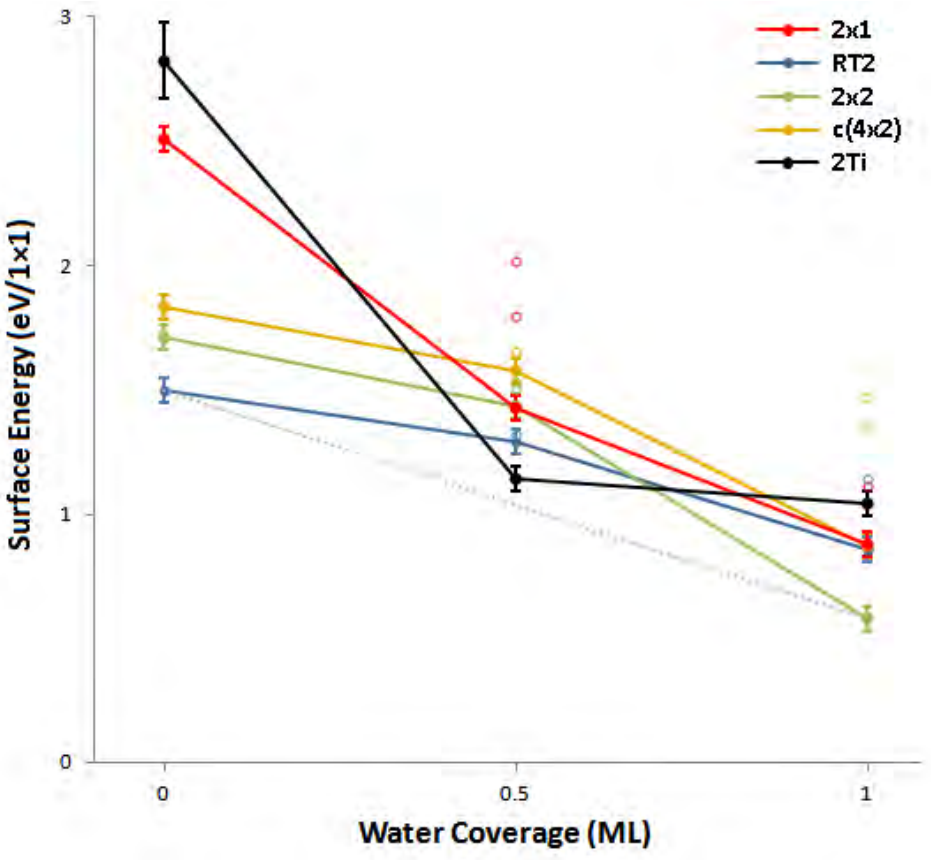

Fig. 5.15. Normalized revTPSSh surface energies for low-energy structures, listed in Tables. 5.2-5.6. Convex-hull construction is shown with the dotted black line. Hollow circles represent high-energy geometries.

The second approach uses the temperature as the main variable. Figure 5.16 shows the energy of all low-energy structures (split by periodicity) as a function of temperature, upon correction due to the chemical potential of water; one must note that this assumes the surface is in full equilibrium with the water vapor. Within each periodicity, this method allows us to predict approximate transition temperatures, ignoring any inherent activation energy. While the plots in Figure 5.16 include the errors in the DFT errors, some of the simplifications used (e.g. the treatment of water vapor as an ideal gas for Eq. 5.4) hide some additional uncertainty to the estimated transition temperatures. However, this does not affect the relative stability of different periodicities within the same stoichiometry. Table 5.7 lists the predicted temperatures above which the dry surface becomes more stable than its "wet" counterparts; it is no coincidence that this metric follows the same trend as the solid angle discussed above. It is worth remarking that for the RT2, 2×2 and c(4×2) periodicities, the half-monolayer structure is never predicted to be favored. On the other hand, 2×1DissA has the lowest 2×1-periodicity energy in the 410-769 ºC range and the 2TiRT2 model is the most stable 2Ti surface between 66 and 1145 ºC. This is associated to the sharp energy drops mentioned above. All full-monolayer structures are stable at low temperatures, including room temperature, except potentially the 2TiMol.

Table 5.7. Predicted drying temperature, adsorption energies and solid angle (with respect to first adsorption Ti site) subtended by four surrounding surface O, for different DL periodicities.

	E_{ads} (eV/H_2O)		Ti–O_4	
	0.5 ML	1 ML	Solid Angle (π sr)	T_{dry} (°C)
2×1	2.16	1.63	2.16	769
RT2	0.41	0.64	1.63	240
2×2	0.80	1.13	1.67	420
c(4×2)	0.52	0.96	1.66	360

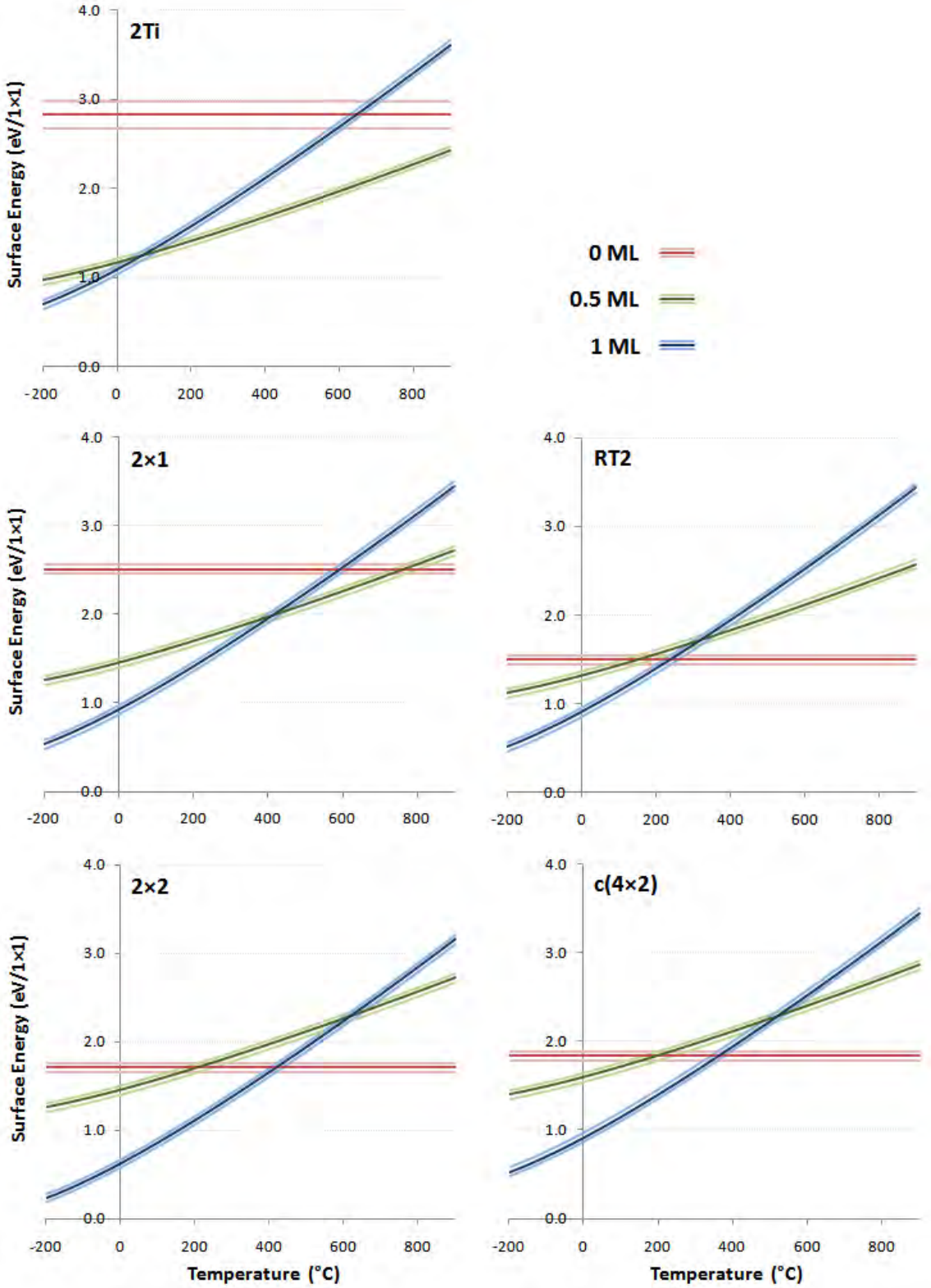

Fig. 5.16. Surface energies for low-energy structures as a function of temperature. Light-colored lines correspond to bounds from DFT errors.

At this point, there is some indication that the hydrated 2×1DissA model may be the correct structural description of the 2×1 surface reconstruction, as opposed to the accepted dry DL model. In order to test this hypothesis, experimental scanning tunneling micrographs are examined in the following subsection.

5.3.7. STM of the 2×1 Surface

As mentioned in Chapter 3, Johnston *et al.* [53] reported constant-current STM images of the 2×1-reconstructed $SrTiO_3$ (001) surface, showing a series of parallel bright rows. A typical image, courtesy of Prof. Martin Castell, is shown in Fig. 3.3, along with a plot of the corrugation, averaged along the direction of the rows. The latter profile had a near-sinusoidal shape and typical corrugation in the 0.4-0.5 Å range.

In order to test structural models by simulating constant-current STM image simulations, DFT calculations were carried out for two structures: the bare 2×1 DL structure; and the low-energy 2×1DissA model, which adds one dissociatively-adsorbed H_2O molecule per surface cell. For the STM simulation of each structure, the density was set so as to match the average corrugation above, fixed at 0.45 Å. The corresponding images are shown in Figure 5.17(a) and 5.17(b).

As can be seen, neither image successfully reproduces the experimental image or the average row height plot. While in the bare 2×1 simulation the ―dangling" O atom dominates the image, in 2×1DissA it is the adsorbed OH group that is the most salient feature. As the strict average height constraint is relaxed, changing the specified isosurface density produces simulations that are closer to the experiment. An isosurface at a lower density leads to the dry 2×1 qualitatively matching well with the image itself, although the average height curve shape is

too broad and the corrugation necessary is 0.29 Å; see Figure 5.17(c). On the other hand, the 2×1DissA model also matches well with the image, but does reproduce very successfully the sinusoidal average height curve, as can be seen in Figure 5.17(d); even the relative sharpness of the troughs, compared to the peaks, is discernible in the simulation. In this case, the average corrugation was 0.49 Å, which is within the observed experimental range.

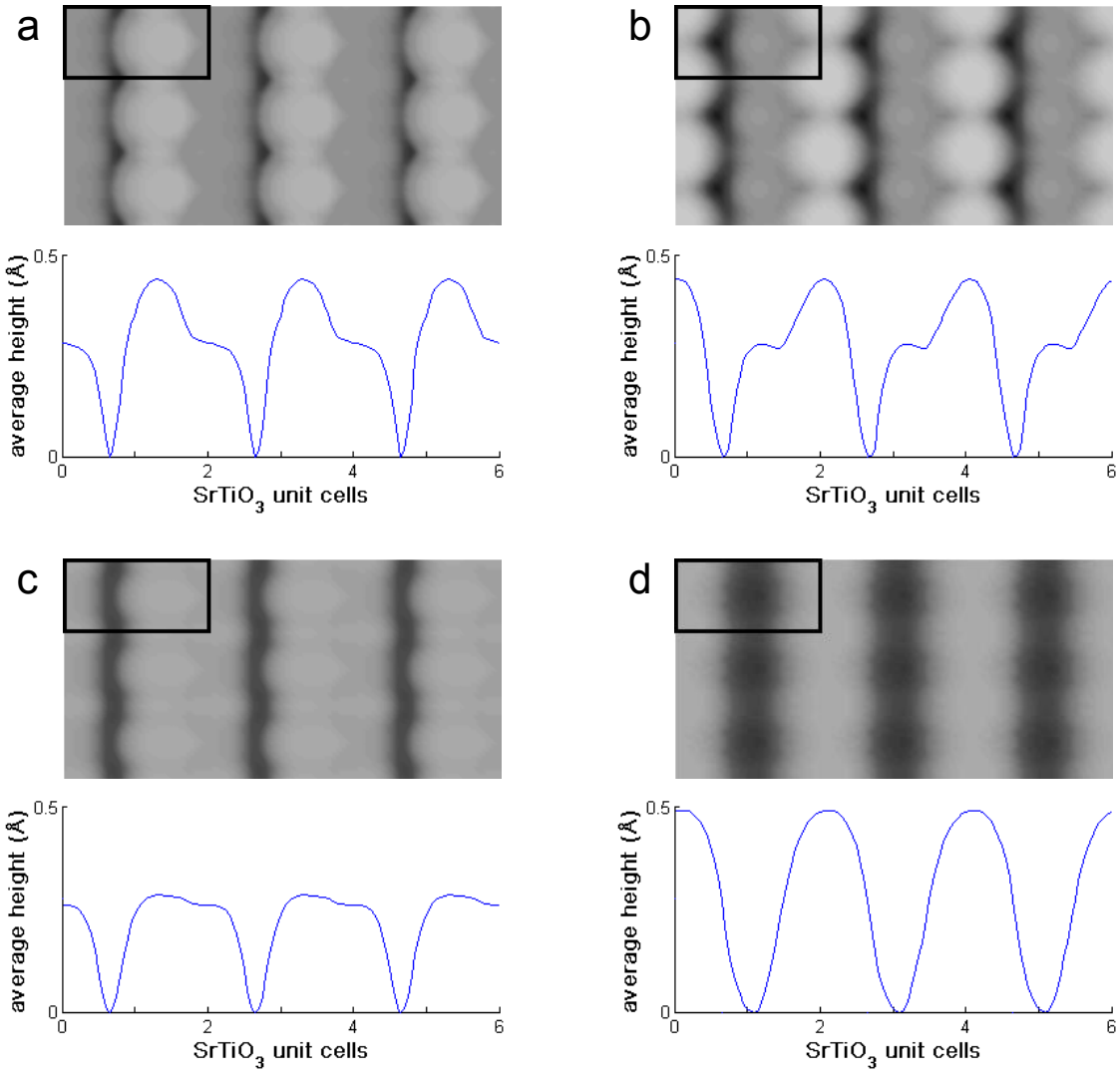

Fig. 5.17. Simulated STM image at 2.0 V bias voltage (top) and average row height plot (bottom) for (a, c) the dry 2×1, and (b, d) the 2×1DissA model. Panels (a, b) result from the constraint of fixing the average row corrugation to 0.45 Å. Panels (c, d) are the best matching simulations upon relaxing said constraint.

These results strongly suggest that the 2×1 structure contains adsorbed H_2O, but there is some ambiguity so more evidence is needed to be unconditional, which comes from a second structure, a c(4×4) reconstruction.

5.3.8. STM and Energy of the c(4×4) Surface

A report by the same research group [76] describes the gradual evolution from a 2×1 surface reconstruction to a "brickwork" c(4×4) surface upon further annealing, as described in subsection 3.4.2; a typical STM image, courtesy of Prof. Martin Castell, is shown in Fig. 5.18. The coexistence of these two reconstructions and similar step edge morphology strongly suggests that they should be structurally related. The promising 2×1DissA model insinuates that the c(4×4) reconstruction may only differ from the 2×1 in the amount of adsorbed H_2O. In such a scenario, the change would be due to the partial desorption of H_2O, and ordering of the remaining adsorbates. Naturally, this would imply that the 2×1 is indeed hydrated.

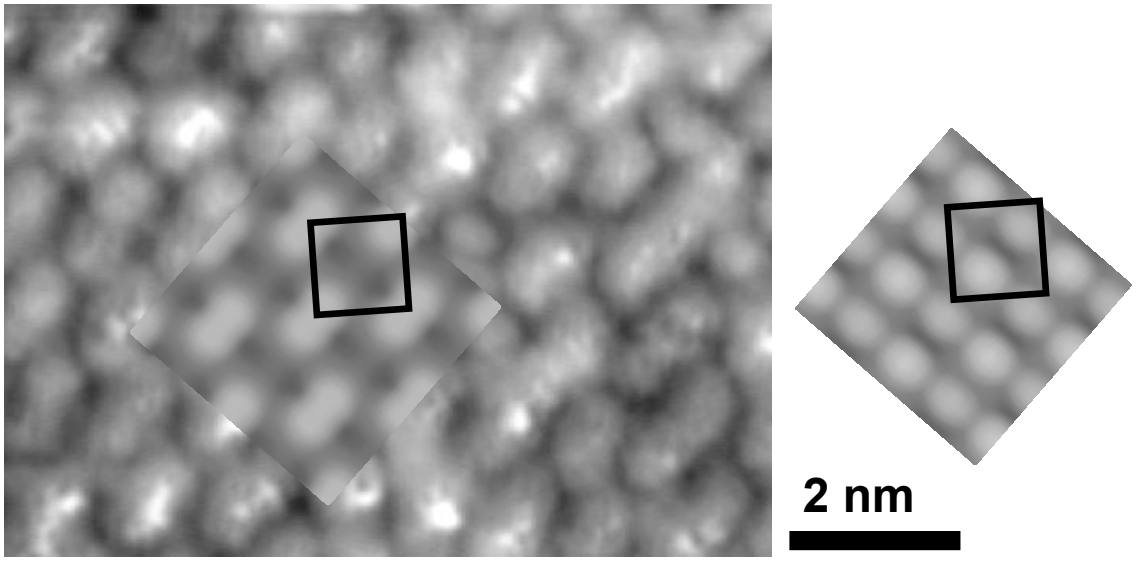

Fig. 5.18. (Left) Experimental scanning tunneling micrograph of the surface exhibiting a "brickwork" c(4×4) surface structure, courtesy of Dr. Martin Castell; 2.0 V bias, 10 nA current. Simulated 2.0 V STM micrograph for the c(4×4)A model is superposed, with the surface cell outlined. (Right) Simulated 2.0 V STM micrograph for c(4×4)B.

Two c(4×4) models based on an underlying bare 2×1 structure were constructed, both with two dissociatively-adsorbed H_2O molecules per c(4×4) cell, following the favored adsorption sites of the 2×1DissA model, which has twice as much adsorbed water. These models are available in Appendix D in the CIF format.

- c(4×4)A (Fig. 5.19(a)): The adsorbed OH pair up, with each pair member being one bulk unit cell away from its partner. The lone H atoms are evenly spread out, each one sitting roughly halfway between two OH pairs.

- c(4×4)B (Fig. 5.19(b)): This model is based on a different orientation of the underlying 2×1, perpendicular to the one used in the first model. The adsorbed OH are evenly spread out, each of them two unit cells away from the closest such units. The lone H atoms pair up, with each pair joining two adsorbed OH groups to form a large unit which could potentially give rise to the characteristic linear feature seen in the STM images.

The corresponding DFT-based STM micrograph simulations (bias voltage of 2.0 V) are shown in Figure 5.18. It is clear that model c(4×4)B can be easily discarded, as the individual OH units dominate the image. However, the simulation for the c(4×4)A model, superposed to the experimental image in Figure 5, is highly successful. Each pair of adsorbed OH forms a single linear STM feature, of comparable size to what is observed experimentally.

Moreover, total energy calculations show that the proposed c(4×4)A model is slightly lower in energy than a combination of structures of 2×1 periodicities:

$$\Delta H[{}^1\!/_2[(2\times1) + (2\times1\text{DissA})] \rightarrow \text{c}(4\times4)\text{A}] = -0.04 \text{ eV}/1\times1. \qquad \text{(Eq. 5.5)}$$

Meanwhile, the alternative c(4×4)B structural model, already discarded due to its poor STM simulation, is calculated to be a little higher in energy (0.03 eV/1×1). All these energies are

admittedly within error, but this highlights that the c(4×4)A model is certainly energetically reasonable.

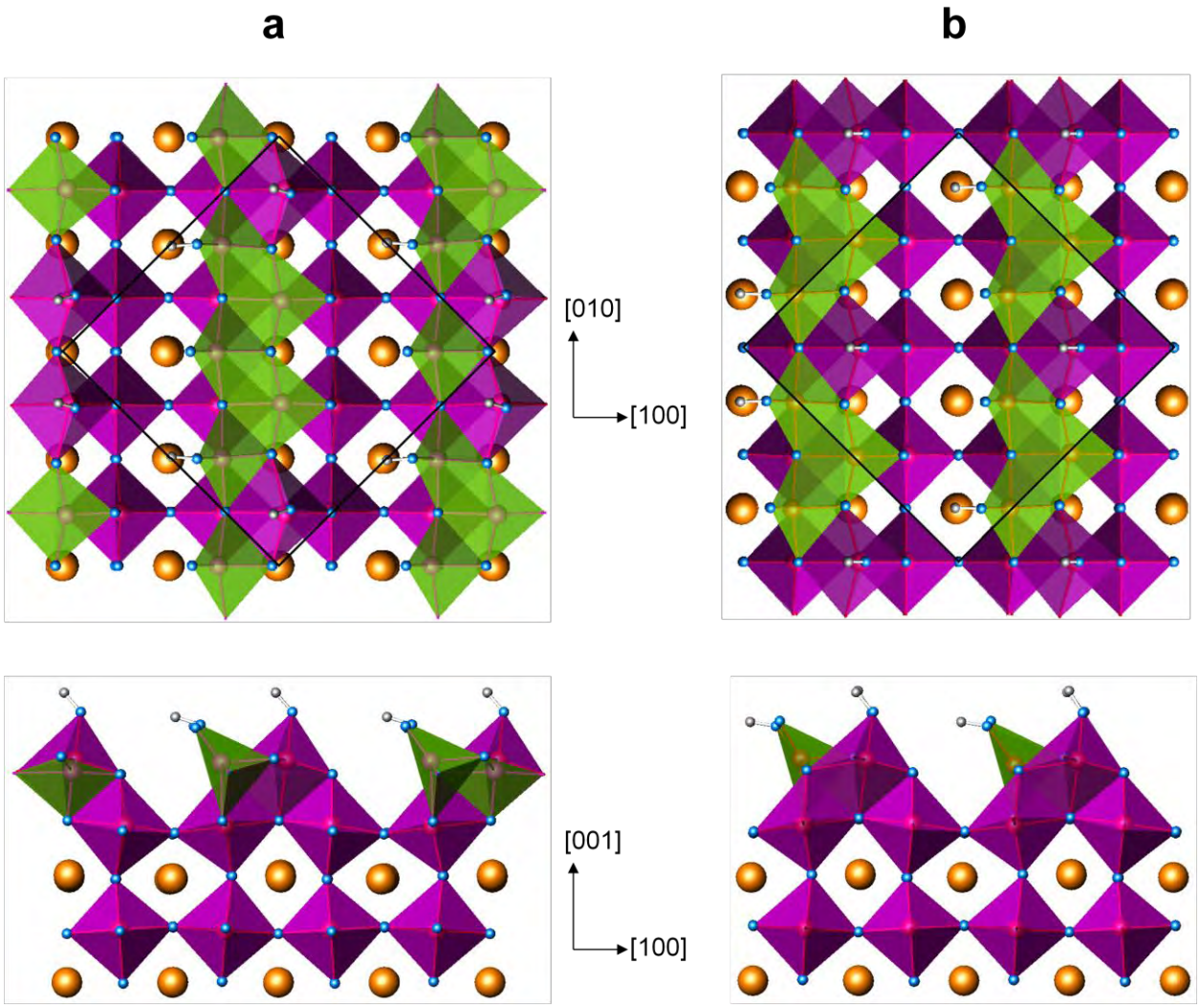

Fig. 5.19. Polyhedral representation of (a) the c(4×4)A model and (b) the c(4×4)B model: plan view (top) and profile view (bottom). Surface cells outlined.

5.3.9. X-Ray Photoelectron Spectroscopy & Transmission Electron Diffraction

Collaborator Dr. James A. Enterkin obtained XPS data that generally support the computational findings presented here. The following $SrTiO_3$(001) reconstructions were observed via TED after annealing multiple samples: 2×1, c(4×2) and (√13×√13)R33.7º. All results can be found in detail in Enterkin's doctoral dissertation [104], but here the relevant results for the DL surfaces are reviewed.

5.3.9.1. The c(4×2) Surface

A sample annealed at 950 ºC for 5 hours in air showed a strong c(4×2) transmission electron diffraction pattern. The XPS spectrum showed a high binding energy shoulder on the O-1s peak, as well as a significant C-1s peak. Several electron-gun annealing steps followed; the XPS and TED results are summarized in Table 5.8 and all relevant XPS spectra are shown in Figure 5.20. It must be noted that a feature in the O-1s spectra is attributed to differential charging between the sample and the holder, as addressed in Ref. [130].

As mentioned by Enterkin, the fact that the c(4×2) pattern was slightly less intense after the 400 and 300 ºC steps does not necessarily does not necessarily imply a structural change; a difference in the tilt condition or the sample thickness with respect to the air-annealed sample could be responsible.

More importantly, it should be highlighted that, following annealing at 300 ºC, the Ti-2p region showed a pair of extra peaks with low binding energy, corresponding to the reduction of Ti (Ti^{3+}). Since Ti^{3+} also contributes to the high binding energy O-1s shoulder, the portion attributable to hydroxylation is thus smaller than the already very small measured value. Few if any hydroxyl groups remain, but the c(4×2) subsists.

Table 5.8. Summary of XPS results following the treatment of a c(4×2)-reconstructed $SrTiO_3$(001) surface.

Temperature (°C)	Environment	Time (min)	c(4×2) TED Pattern	O-1s XPS Shoulder*	Ti^{3+}-2p Shoulders?	C-1s Peak*
950	air	300	very strong	0.36	no	0.34
400	8×10^{-7} Torr O_2	20	strong	0.55	no	0.30
300	4×10^{-6} Torr O_2	180	strong	0.08	yes	0.15
800	9×10^{-7} Torr O_2	20	weak	0.07	yes	0.18

*Area defined relative to main O-1s peak area.

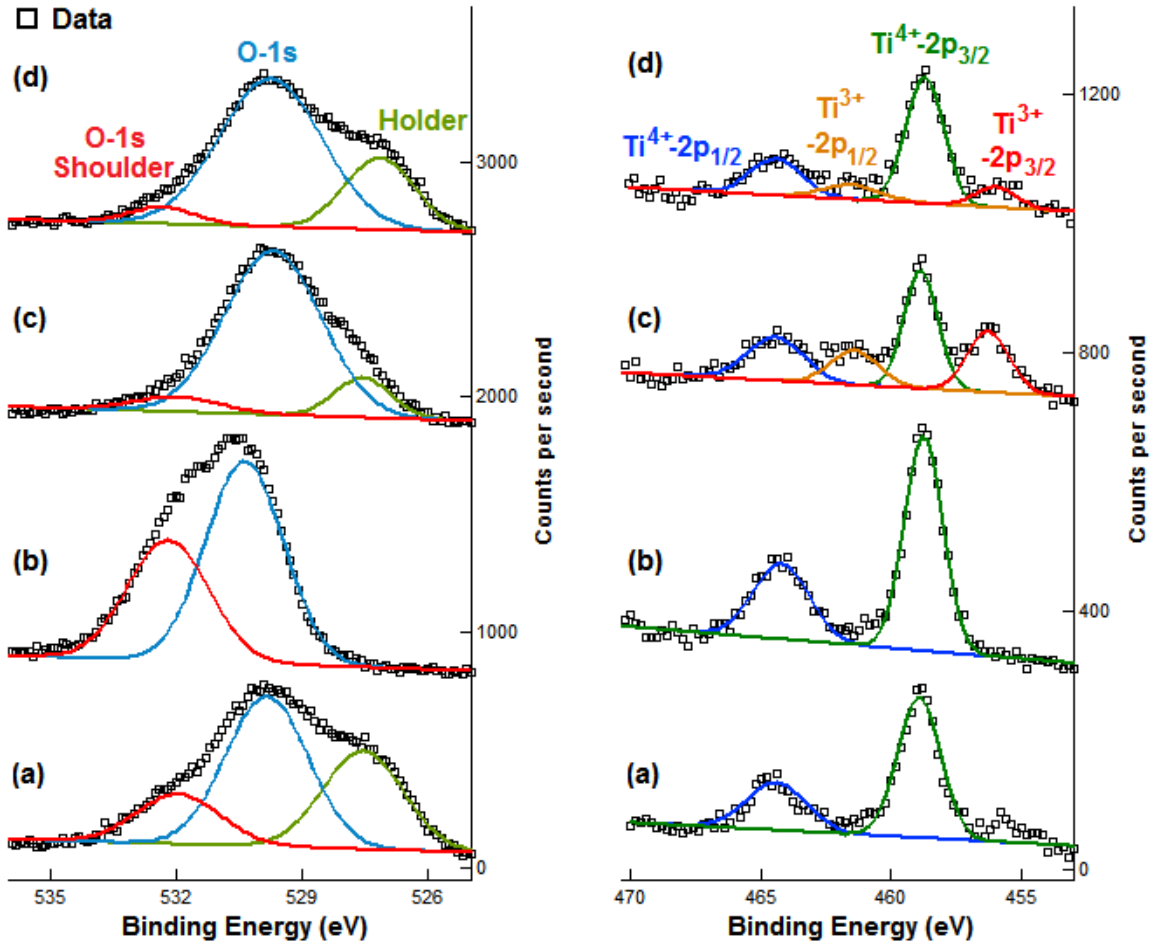

Fig. 5.20. O-1s (left) and Ti-2p (right) XPS peak regions from a sample with the c(4×2) reconstruction. Counts per second for each spectrum offset for ease of viewing. After: (a) air anneal for 5 hours at 950 °C, (b) anneal in 8×10^{-7} Torr O_2 for 20 min at 400 °C, (c) anneal in 4×10^{-6} Torr O_2 for 3 hours at 300 °C, and (d) anneal in 9×10^{-7} Torr O_2 for 20 min at 800 °C.

5.3.9.2. The 2×1 Surface

A different specimen, also annealed at 950 ºC for 5 h in air, exhibited a weak 2×1 TED pattern, with streaks along the {100}-type directions, which partially resolve into a 5×1 periodicity. The XPS spectrum showed a O-1s shoulder, with higher binding energy than the main peak, as well as a sizable C-1s peak. Several annealing steps followed, using a resistive heating stage when needed; the XPS and TED results are summarized in Table 5.9 and all relevant XPS spectra are shown in Figure 5.21.

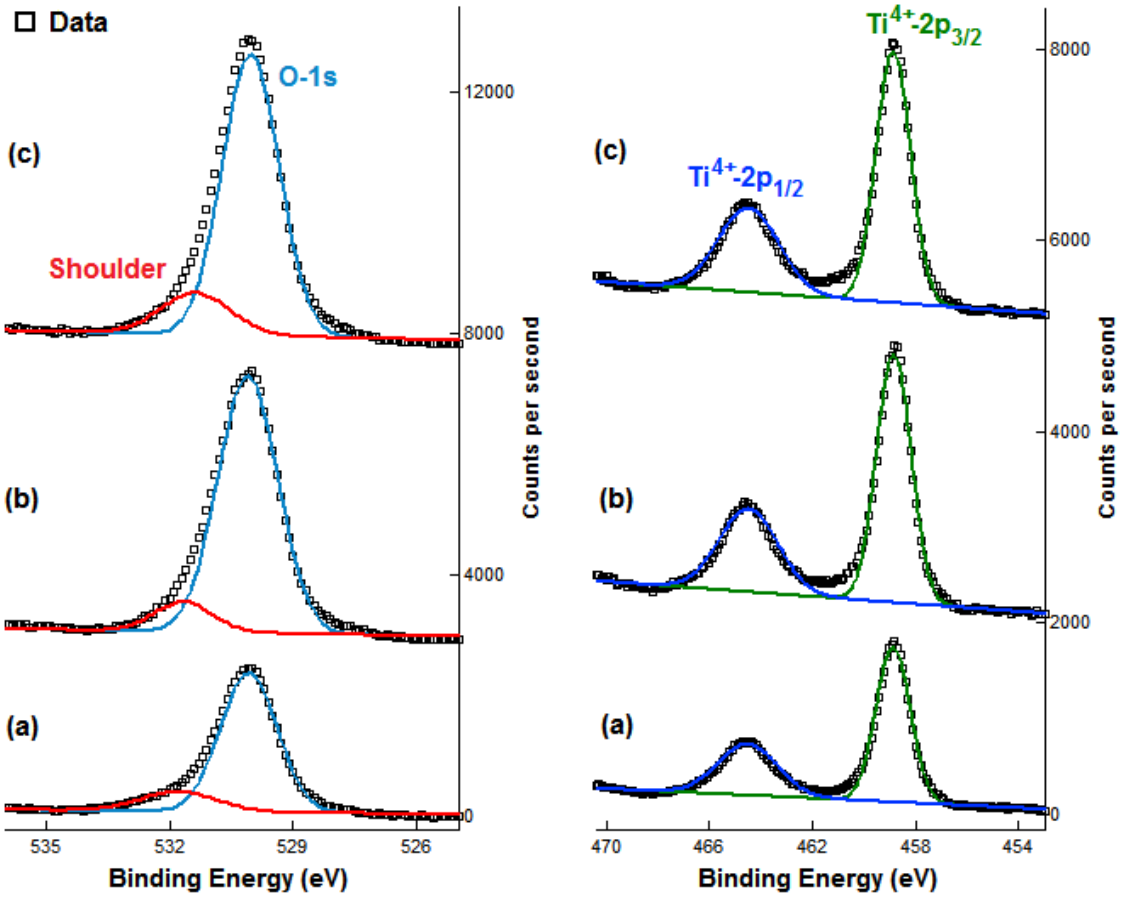

Fig. 5.21. O-1s (left) and Ti-2p (right) XPS peak regions of a sample which began with the (2×1) reconstruction. Counts per second for each spectrum offset for ease of viewing. After: (a) air anneal for 5 h at 950 °C, (b) anneal in 2×10^{-2} torr O_2 for 5 hours at 750 °C, and (c) exposure to air.

It should be clarified that for the last treatment, this specimen was simply exposed to air for 1 hour before being re-inserted into the UHV system. While XPS spectra were recorded, no TED analysis was performed, as the sample was unfortunately lost while being transported. However, the 2×1 is known to be air-stable, so it expected that this reconstruction would remain.

Table 5.9. Summary of XPS results following the treatment of a (2×1)-reconstructed $SrTiO_3$(001) surface.

Temperature (°C)	Environment	Time (min)	2×1 TED Pattern	O-1s XPS Shoulder*	Ti^{3+}-2p Shoulders?	C-1s Peak*
950	air	300	weak, streaks	0.19	no	0.29
750	2×10^{-2} Torr O_2	300	strong	0.11	no	–
~25	air exposure	60	–	0.18	no	–

*Area defined relative to main O-1s peak area.

5.4. Discussion

It is important to recognize that as-prepared surfaces will invariably start with some amount of chemisorbed water. In the particular case of $SrTiO_3$ crystals, no preparation method yields perfectly flat surfaces. For specimens to be analyzed by TEM/TED or by scanning probe microscopies, the sample preparation steps typically include ion bombardment and/or chemical etching with aqueous solutions. For the STM report of the 2×1 reconstruction [76], for example, the sample was initially prepared by submerging it in a buffered NH_4F−HF solution bath, followed by rinsing in water and drying with N_2 gas; it is known that carbonaceous surface contamination occurs, and it is hard to envision all H_2O (or hydroxyl groups) being removed. This is true regardless of the specific treatment, as surface defects (step edges or point defects)

will act as strong adsorption sites for environmental water, mostly in a dissociative fashion [122-124]; even cleaving $SrTiO_3$ crystals in UHV will generate surface vacancies [14].

Subsequent annealing steps will induce a competition between desorption of the water and ordering of the surface to stabilize it. As long as the surface is not fully ordered, defect sites (and thus strong H_2O adsorption sites) will remain. Therefore, it is not the thermodynamics of bare surface reconstructions that govern the stabilization process; it is the ―wet" kinetics that do. This is especially clear once one recognizes that the easy diffusion of oxygen and (especially) hydrogen will dominate over the slow rearrangement of surface Ti. Ultimately, the local inhomogeneities developed during the processing stages will determine which particular structure forms, with the coexistence of multiple reconstructions as a distinct possibility.

In this context, the theoretical modeling of water adsorption configurations on periodic $SrTiO_3$(001) surface reconstructions yields new insights into the factors governing the preferential formation of some structures over others. It becomes apparent, for example, that the RT2 reconstruction is kinetically inaccessible and that the inescapable interaction of the surface with environmental water vapor favors other configurations, since its distinguishing standing as the lowest energy DL structure vanishes upon water adsorption. This finding is similar to the case of the low-energy Wolf octapole MgO(111) structure, which has not been experimentally observed either; Ciston *et al.* [130] showed that the high surface mobility of hydrogen atoms, with respect to the slow cationic diffusion, favors the formation of other structures.

Regarding the 2×1 surface reconstruction, the DFT-based simulations of scanning tunneling micrographs support the idea that it carries dissociatively-adsorbed water at least sometimes, if not always. For the dry 2×1 model, no choice of isosurface density yields a satisfactory match to the experimental data. The average height curve fails to mimic the

measured curve, with its shape only vaguely approaching the observed sinusoidal nature at densities with which the average corrugation is too small. The hydroxylated 2×1DissA model is a better match, as the predicted average corrugation does not decay as fast with density. As seen in Figure 5.17(d), it is possible to find a range of densities in which the image, average corrugation and sinusoidal height curve shape are reproduced faithfully.

Moreover, total energy calculations indicate that the strongest H_2O adsorption on the periodic 2×1 surface occurs at half-monolayer coverage, in agreement with the STM results. As seen quantitatively in terms of BVS in subsection 5.2.2, the characteristic dangling O is not the only undercoordinated atom in the bare 2×1 surface model. The top-layer Ti not bound to the dangling O is 5-fold coordinated, but due to the coordination of the four top-layer O it is bound to, every Ti−O bond length is constrained. As a result, that Ti is quite exposed and is not very stable. It is no coincidence that these two atoms (the dangling O and the exposed surface Ti) are the preferred adsorption sites for dissociated water. Each of the two sites is quantifiably much more stable upon the adsorption of H or OH. This conclusion solves the question of the instability of the previously accepted, dry 2×1 structural solution; whether a stable, dry 2×1 reconstruction could form in the absence of any water vapor is an open question, but it appears unlikely, considering the energetic constraints.

The examination of hydroxylated 2×1-based models for the brickwork c(4×4) reconstruction supports the previous finding by explaining the observed 2×1-to-c(4×4) transition as a simple dehydration process. The structural models analyzed are both (stoichiometrically) halfway between the dry and hydrated 2×1 models above. The main difference lies in the position of the adsorbed OH groups, which dominate the simulated STM micrographs. In the c(4×4)A model, they pair up and within each pair the OH–OH in-plane distance is roughly one

bulk unit cell; in the c(4×4)B model, they are spread out, qualitatively arranged with 2×2 periodicity. It is evident from the simulations that a 2×1-based c(4×4) model requires the former hydroxyl arrangement to reproduce the observed linear STM features. As for the lone adsorbed H atoms, their exact position is hard to decipher, since their presence is shadowed in the simulated micrographs by the adsorbed OH groups; it is expected that each lone H will bind to a dangling O, however. While it is straightforward to come up with a structure that differs from the c(4×4)A only in the arrangement of these lone H, the adsorption sites chosen above do appear to yield a good match to the less bright regions of the experimental image. Equally encouraging is the fact that the feasibility of the c(4×4)A model is further supported by the total energy calculations, as described above.

Naturally, there are inherent limitations in comparing STM image simulations with experimental data, which tends to be restricted to qualitative evaluation. One of the main issues is that tip-sample interactions are not accounted for in the simulations, and this can be particularly relevant for surfaces with adsorbed molecules that are easily moved by the STM tip, such as dangling OH groups. Nevertheless, the significant differences in the simulated images presented herein and the good match of only one of the 2×1 and one of the c(4×4) simulations to the experiments allow us to be confident that the correct structures have been identified.

In the context of the hydroxylated 2×1 structure, it is relevant now to discuss the experimental results by collaborator Dr. James A. Enterkin, described in subsection 5.3.9. The most relevant results are the following: (1) for surfaces exhibiting the c(4×2) reconstruction, all water and hydroxyl groups desorb in the 300-400 ºC range in a pO_2 ~10^{-6} Torr; and (2) the 2×1 reconstruction will remain hydrated at temperatures at least as high as 750 ºC (pO_2 ~10^{-2} Torr). Unfortunately, Enterkin‘s 2×1 sample was prematurely lost, so it is not certain whether or not a

dry 2×1 structure is attainable. Meanwhile, although the treatment conditions were not strictly the same, one can conclude that a dry c(4×2) can exist, and these results are certainly consistent with the theoretical predictions regarding the relative H_2O adsorption strength on these two reconstructions.

Returning to the computational results, a few other predictions can be inferred. For example, the chemical-potential correction indicates that water favorably adsorbs on all $SrTiO_3$(001) DL reconstructions at ambient temperature and pressure. For most periodicities, the full-monolayer models appear to be the most thermodynamically stable, with the potential exception of the 2Ti surface, since the uncertainty in the transition temperature between the 2TiRT2 and 2TiMol encompasses room temperature. More generally, the transition temperatures presented should be taken as a rough estimate, especially considering that no activation energies for adsorption/desorption and dissociation/re-association processes are available at present.

Another common feature observed is that hydrogen bonding plays a significant role in the stabilization of most hydrated DL surfaces, especially upon dissociative water adsorption. This is true for several low-energy structures: RT2Diss, RT2SatD, 2×2SatD, c(4×2)SatD, 2TiMol and 2TiRT2. With a few exceptions, this "internal" H-bonding is usually a result of lone H adsorption upon H_2O dissociation, with the H bridging top-layer O atoms from different Ti-centered surface polyhedra.

As a general point, it is imperative to stress that adsorbates (such as H_2O) on a surface can no longer be assumed to be absent or irrelevant, and this likely applies not just to $SrTiO_3$(001), but to a broad range of metal oxide surfaces. Not only are adsorbates likely to be

present, even at high temperatures and in ultra high vacuum, but they also play an important role in the formation of stable surface structures.

5.5. Conclusions

A wide variety of H_2O adsorption configurations on reconstructed $SrTiO_3(001)$ surfaces have been explored via DFT, which elucidates the factors favoring the formation of certain structures. For example, the "dry" surface thermodynamics predict the RT2 reconstruction to be much more stable than the 2×1, yet the former has never been detected and the latter repeatedly has. Accounting for the interaction with H_2O molecules leads to surface energies which are much more consistent with the experimental observations; at half- and full-monolayer water adsorption, the RT2 periodicity is no longer the most favorable. Therefore, it is the kinetics that rule over the simplistic dry-surface thermodynamics by favoring ordering with other periodicities.

It has been shown via DFT-based simulations that the experimental STM images of the $SrTiO_3(001)$ 2×1 surface reconstruction are more consistent with a structural model that differs from the presently accepted model by the addition of one dissociatively-adsorbed H_2O molecule per 2×1 cell. Additionally, the 2×1-to-c(4×4) transition upon annealing is easily explained as a simple dehydration mechanism, by using the new 2×1 structural model as the starting surface and examining c(4×4) models based on it. One of these is proposed as the structural solution to the c(4×4) surface reconstruction, given the striking agreement of its simulated STM micrograph to the experimental data.

What was once underground is now coming to the surface.
Gavin Bryars

Segregation never brought anyone anything except trouble.
Paul P. Harris

Chapter 6. Surface Segregation: $SrLaAlO_4$ & $SrTiO_3$

6.1. Introduction

In this chapter, the (observed or hypothetical) segregation of simple unary oxides at the surfaces of two oxide materials is studied. The first oxide is strontium lanthanum aluminate ($SrLaAlO_4$), for which there is a general dearth of surface-related literature. Experimental observations of SrO surface segregation in $SrLaAlO_4$ are reported here for the first time, as well as the related formation of stacking faults in the bulk as an accommodation mechanism for the resulting non-stoichiometry.

The second oxide of interest is the now-familiar strontium titanate, for which there are already numerous reports on SrO surface segregation, typically upon high-temperature annealing. Interestingly, it has been speculated that a fault-based compensation mechanism (analogous to that observed in $SrLaAlO_4$) occurs in the $SrTiO_3$ bulk. A computational approach

is exploited to assess the viability of such a process in this material. An alternative fault-based mechanism in $SrTiO_3$ is similarly tested as a possible explanation for the TiO_2 surface-richness required for DL reconstructions. Both processes are found to be unrealistic.

Given the dissimilar approach to these two metal oxides, the organization of this chapter is unorthodox. After the present introduction, there is a section dedicated to $SrLaAlO_4$ alone, followed by one for $SrTiO_3$; each of these sections has background, methods and results subsections. A joint discussion follows, as well as a short section devoted to general conclusions.

6.2. Strontium Lanthanum Aluminate

6.2.1. Background

Strontium lanthanum aluminate, $SrLaAlO_4$, has become one of the favored substrate materials for epitaxial growth of high-T_c superconducting thin films for microwave and far-infrared applications [140-142]. It exhibits excellent lattice match with superconducting cuprates, remarkable dielectric, elastic and optical properties [142-146], as well as high chemical stability [147]. Its single-crystal bulk properties have been widely studied, as well as the effects of its crystal growth method and growth conditions [148-154]. However, there is a surprising lack of surface-specific literature on this material.

Studying surface stabilization phenomena in metal oxides is essential in order to fully understand these mechanisms at the nanoscale and to enhance the potential of metal oxides in applications such as thin film growth and heterogeneous catalysis. $SrLaAlO_4$ crystallizes in the perovskite-like K_2NiF_4 structure ($a = b = 3.756$ Å, $c = 12.64$Å [143]) with space group I4/mmm, as shown schematically in Fig. 6.1(a). This is the same crystal structure as the Sr_2TiO_4

Ruddlesden-Popper phase, depicted in Fig. 2.4(a), and it is an ordered intergrowth of perovskite and rocksalt layers. Strontium lanthanum aluminate offers an additional degree of complexity due to the shared occupancy of the nine-fold coordination site by Sr and La cations, which are distributed statistically. In this context, $SrLaAlO_4$ goes beyond simpler systems that have been studied to date, opening the door to new questions. Is the surface behavior similar to what goes on in relatively simple systems such as perovskite $SrTiO_3$ [34, 89, 91] or $LaAlO_3$ [155], or does the mixture of 2+ and 3+ cations allow different phenomena to occur at the surface? What role do bulk defects play in the stabilization of the surface if there is a change in stoichiometry, either as point or extended defects? The aim of this work is to examine the behavior of the $SrLaAlO_4$ (001) and {100} surfaces upon thermal treatment under oxidizing conditions. Unlike comparable oxides, no sign of periodic surface reconstruction is found at present. $SrLaAlO_4$ does show strong surface segregation of strontium oxide at high temperatures, in the form of islands, as demonstrated by transmission electron microscopy (TEM), scanning electron microscopy (SEM) and energy-dispersive X-ray spectroscopy (EDX). While this has been observed in $SrTiO_3$, a fundamentally different compensation mechanism for the bulk non-stoichiometry is found in the form of stable stacking faults.

6.2.2. Experimental Methods

Single-crystal $SrLaAlO_4$ (001)- and (100)-oriented wafers ($10\times10\times0.5$ mm^3, 99.99% purity, grown by the Czochralski method, one side EPI polished) were purchased from a commercial vendor, MTI Corporation.

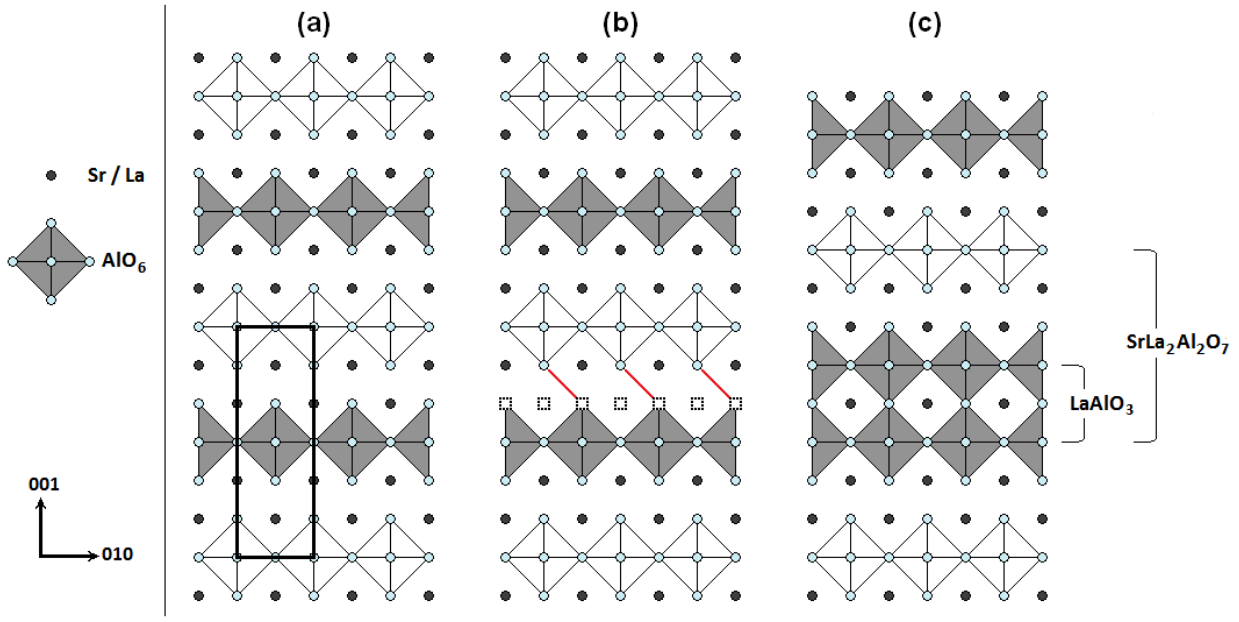

Fig. 6.1. (a) [100] projection of bulk $SrLaAlO_4$, unit cell outlined. (b) Removal of a layer of SrO and diagonal lines indicating subsequent <½ ½ *z*> crystallographic shear. (c) Resulting structure with inverse RP stacking fault. All octahedra are Al-centered; white octahedra indicate an out-of-page half-unit-cell shift with respect to gray octahedra. Dotted empty squares denote vacant sites.

6.2.2.1. Ionized couple plasma atomic emission spectrometry

Inductively coupled plasma atomic emission spectrometry (ICP-AES) measurements were performed on some of the material with a Varian Vista-MPX instrument and an Ar plasma for stoichiometry verification. The first step was to find a suitable acid to fully dissolve $SrLaAlO_4$. After HNO_3 failed to achieve this, it was found that hydrochloric acid dissolved the material completely, with no heating necessary.

A controlled dissolution followed. For this, a small piece of the crystal was chipped off, crushed, weighed (~1.75mg) and dissolved in 1 mL HCl. This was then diluted by adding 24 mL of deionized water. The elemental atomic weights were used to estimate the expected Sr/La/Al concentration in such a solution in ppm (µg/mL) to use as guiding values for the preparation of calibration standards.

For the calibration, the following standard aqueous solutions for atomic absorption spectroscopy were purchased from a commercial vendor, Sigma-Aldrich Corporation: 1020 ppm Sr in 1.2% HCl, 1021 ppm La in 1% HNO_3, and 1000 ppm Al in 2% HNO_3. These were diluted accordingly with deionized water to prepare six calibration solutions (all 50 mL, with 0.2 mL of total acid) at roughly 0.3, 0.6, 0.9, 1.1, 1.4 and 1.7 times the expected cationic concentrations. These, plus a blank deionized water sample were measured 3 times each to generate calibration curves; the emission lines that yielded the best linear fits were employed for the sample measurement, which was recorded six times and averaged. The following emission wavelengths were used: 460.733 nm (Sr), 492.178 nm (La), 308.215 nm (Al). The measured concentrations were then converted to cation ratios.

6.2.2.2. Transmission electron microscopy

The (001) wafers were cut into 3 mm-diameter disks using an ultrasonic disk cutter. Each disk was then mechanically thinned with SiC polishing paper to a thickness of ~100 μm, dimpled, and finally ion milled to attain electron transparency at the center of the disk (~100 nm) using 3.8-4.5 kV Ar^+ ion beams in a Gatan precision ion polishing system (PIPS). Samples were subsequently annealed in a Carbolite STF 15/51/180 tube furnace in a flow of O_2 gas in two steps: first, a preliminary anneal for 3 hours at 650-700 ºC, in order to revert most of the damage induced during preparation and to recover the original stoichiometry; and second, a longer 6-hour anneal at a specified temperature in the 900-1300 ºC range, which was the main variable. There was no active external cooling afterwards, but the cooling rate was capped at –10 ºC/min. Transmission electron microscopy and diffraction experiments were carried out on a JEOL JEM-2100F microscope, operated at 200 kV and equipped with an Oxford Instruments INCAx-stream

EDX detector. EDX microanalysis was performed in scanning transmission (STEM) mode, while high-resolution imaging was done under conventional parallel-beam illumination. Measurement of lattice features in high-resolution mode was calibrated to the known bulk spacings in $SrLaAlO_4$. Also, an as-received crystal was crushed, sonicated in methanol, placed on a TEM grid with a holey carbon film, allowed to dry and examined by TEM.

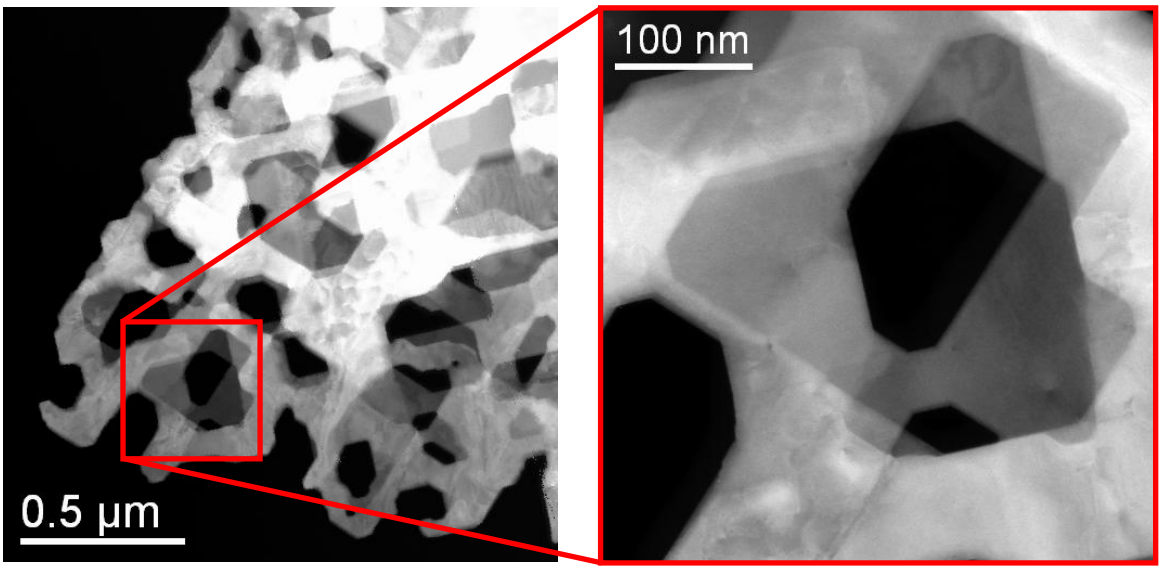

Fig. 6.2. *Z*-contrast STEM image with $SrLaAlO_4$ [001] zone axis, after annealing at 1300 ºC in O_2.

6.2.2.3. Scanning electron microscopy

The strong (001) cleavage in $SrLaAlO_4$ [142, 143] made it unviable to thin the (100)-oriented samples to electron transparency. Therefore, (100)- and (001)-oriented as-received crystals were annealed at the same high temperature and same environment as the TEM specimens for subsequent SEM-EDX analysis with a Hitachi S-3400N-II microscope, operated at 5 kV and outfitted with an Oxford Instruments INCAx-act EDX detector. SEM imaging was performed in secondary-electron detection mode for topographical information.

6.2.3. Results

As determined via electron diffraction, there was no evidence of surface ordering with non-bulk periodicity at any of the annealing conditions explored during these experiments. Temperatures below 1200 ºC did not yield any apparent morphological changes. However, annealing at 1250-1300 ºC for 6 hours in oxidizing conditions typically resulted in the microstructure shown in Fig. 6.2 in a (001)-oriented sample. In thin regions of the sample, numerous holes in them formed, but the specimen remained a single crystal, as indicated by the diffraction patterns. Distinct faceting, mostly along {100} and {110}-type surfaces, is clearly observable. This microstructure is similar to what has been seen in previous studies of metal oxides [34, 89, 91, 155].

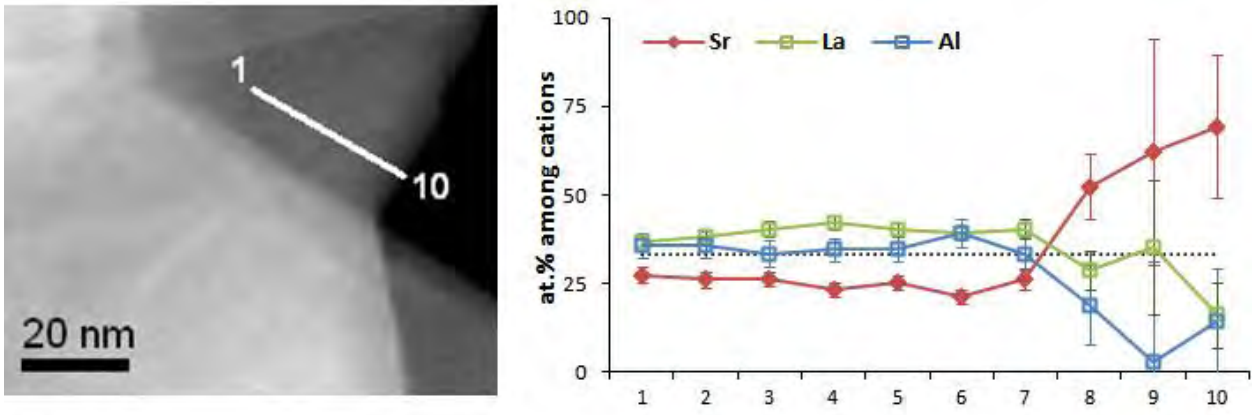

Fig. 6.3. (Left) *Z*-contrast STEM image with $SrLaAlO_4$ [001] zone axis. The white line defines the EDX scan, ending at a {110}-type edge at position 10. (Right) EDX line scan, showing the cationic species distribution as a function of position. The dotted line corresponds to the stoichiometric 1:1:1 cation ratio.

STEM-EDX line scans were performed on (001)-oriented samples, scanning from the bulk towards the edges. A semi-quantitative analysis followed which showed a marked increase

in Sr content, relative to La and Al, near some {100} and {110} surfaces (see, for example Fig. 6.3); this was highly suggestive of strontium surface enrichment. Note that the error bars shown correspond only to the statistical fluctuations and do not include calibration errors, as the built-in, software-specific *K*-factors were used. Also, the large uncertainty as the edge is approached is due to the lowered signal in this thinner region. Therefore, further evidence was necessary, although this Sr-rich surface in oxidizing conditions was presumed to be due to SrO surface segregation.

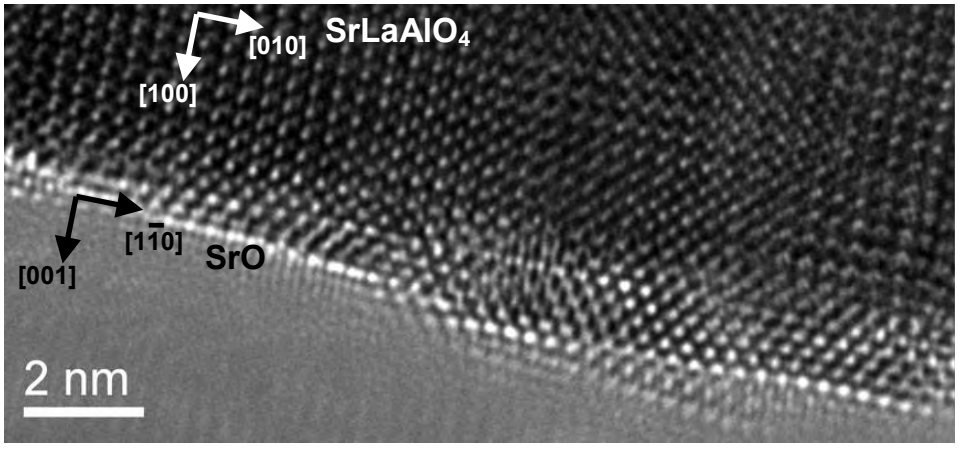

Fig. 6.4. High-resolution electron micrograph, showing formation of layers of SrO on a $SrLaAlO_4$(100) surface.

High-resolution TEM images validated the hypothesis of SrO presence at these surfaces. For example, Fig. 6.4 reveals periodic lattice features which match –within a few percent error– a {110}-type rocksalt SrO orientation on a {100} $SrLaAlO_4$ surface; there is some slight distortion in the SrO lattice in order to accommodate for the lattice mismatch of ~3%. However, it must be noted that the edges, which correspond to surfaces perpendicular to <001> are not uniformly covered in a few monolayers of this Sr-rich material; many segments remain clean of it.

Aside from the segregation of a few monolayers of strontium oxide on some surfaces, there were also some regions where relatively large amounts of SrO formed as a separate phase. This occurred both in the form of precipitates within the $SrLaAlO_4$ matrix as well as exposed areas (as shown in Fig. 6.5). EDX elemental mapping confirmed that these secondary phases consist predominantly of strontium and oxygen. The weak Al and La signals from said areas imply that these elements were present, but merely in solid solution within the SrO matrix. High-resolution TEM imaging of these secondary phases support this finding: lattice spacings matching within less than 2% error the {110}, {111} and {210} rocksalt SrO interplanar distances were visible within these phases, which were not single-crystalline.

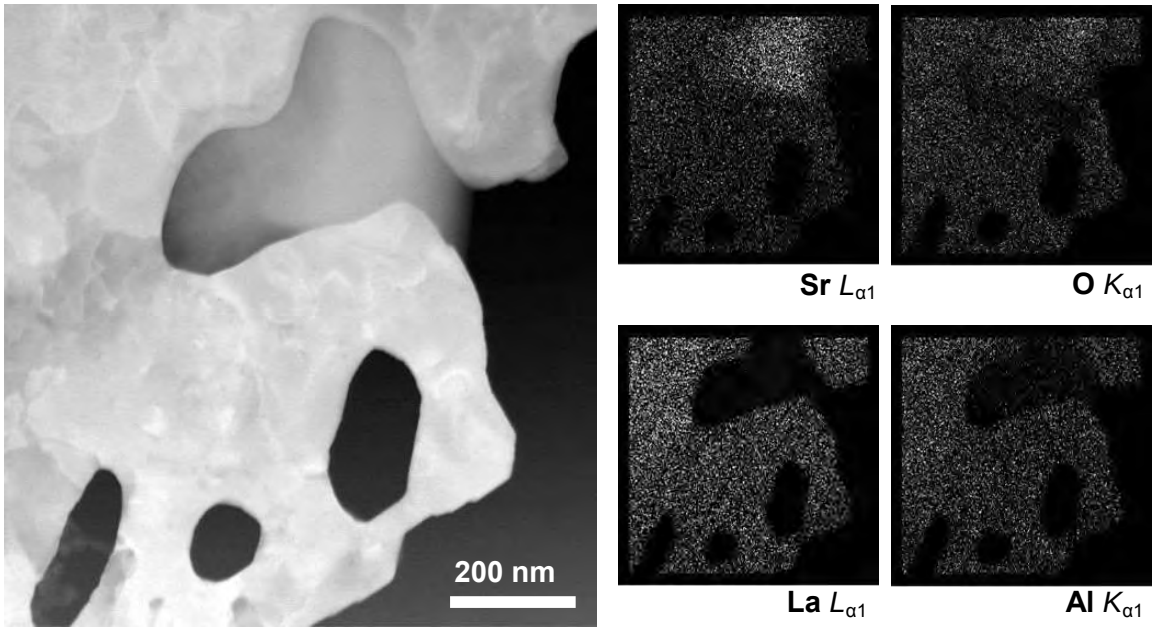

Fig. 6.5. (Left) High-angle annular dark-field STEM image with [001] zone axis. (Right) EDX elemental maps, showing the presence of a Sr-rich secondary phase.

Thermal treatment of (100)-oriented as-received samples under the same annealing conditions confirmed the segregation of SrO at this surface. Surface features, absent prior to

annealing, were easily visible via optical microscopy (see Fig. 6.6). SEM imaging revealed these to be surface islands with random positional distribution and a broad range of sizes, as large as 50 μm. The (001)-oriented as-received samples showed a similar behavior upon annealing, except that the surface islands were as large as 500 μm wide and very few small features were observed. Figure 6.7 shows a large island on this surface, with obvious signs of agglomeration of multiple particles. The estimated island coverage was 4% on the (100) surface and 2.5% on the (001) surface, with a 1% margin of error.

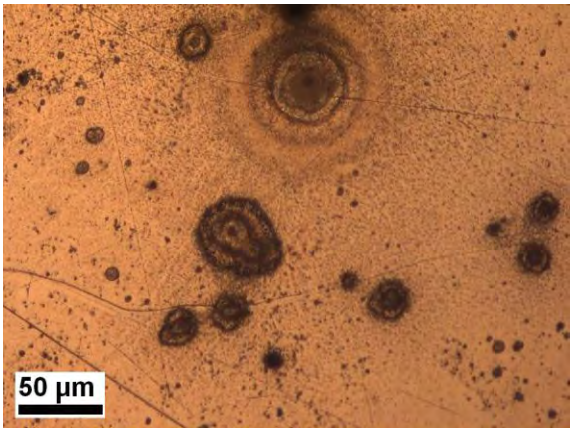

Fig. 6.6. Optical micrograph of $SrLaAlO_4$(001) surface after annealing at 1300 ºC for 6 hours.

SEM-EDX elemental mapping was carried out on the islands with the electron beam perpendicular to the surface plane, with the accelerating voltage set to the relatively low value of 5 kV. This minimized the effects of sample charging and enhanced the surface sensitivity of the technique, while still allowing for the detection of all relevant elements. The results were qualitatively the same for both surface orientations. A typical set of elemental maps is presented in Fig. 6.7. These results verify that the aforementioned features correspond to the formation of SrO-rich islands on low-index $SrLaAlO_4$ surfaces.

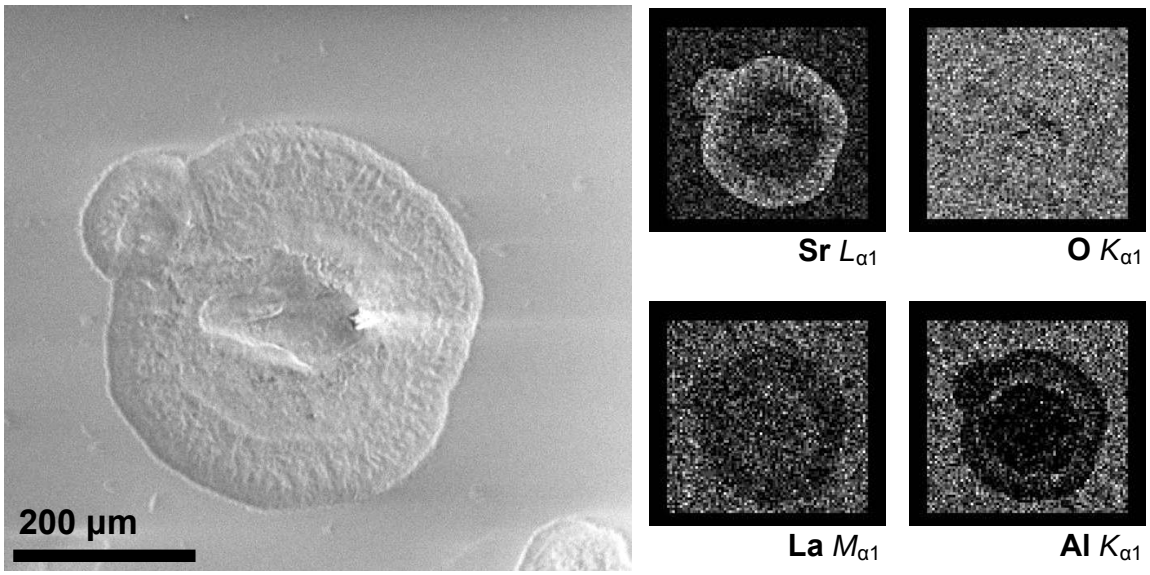

Fig. 6.7. (Left) Plan-view scanning electron microscopy image of feature on a $SrLaAlO_4$(001) surface. (Right) EDX elemental maps corresponding to the same feature.

It is also possible to address the mechanism by which the $SrLaAlO_4$ bulk remains stable in spite of the substantial preferential migration of Sr and O to the surface and the consequent non-stoichiometry. Said bulk stabilization is linked to the appearance, in (001)-oriented TEM samples, of a large number of planar defects after the high temperature anneal (see, for example, Fig. 6.8(a)); no such features were observed with lower annealing temperatures, and a crushed as-received crystal was also examined via HREM and no pre-existing faults were found.

These defects exhibit jagged boundaries, always along [100]-type directions. Upon closer examination in high-resolution mode, one finds that the lattice contrast in these planar defects exhibits half-unit-cell shifts with respect to the rest of the crystal (Fig. 6.8(b)). Therefore, these features are aptly explained as disordered stacking faults. The observed shifts correspond to a <1/2 1/2 *z*> crystallographic shear ($z \sim 1/6$), as can be seen schematically in Fig. 6.1(b-c); the loss of a (001) SrO layer in $SrLaAlO_4$ favors said effect. Similar crystallographic

shear mechanisms have been observed in perovskite systems [65, 156, 157], as well as the broader Ruddlesden-Popper family [158] (introduced in subsection 2.3.2), although they have rarely been discussed in combination with surface segregation and never before have both phenomena been coupled through direct observation.

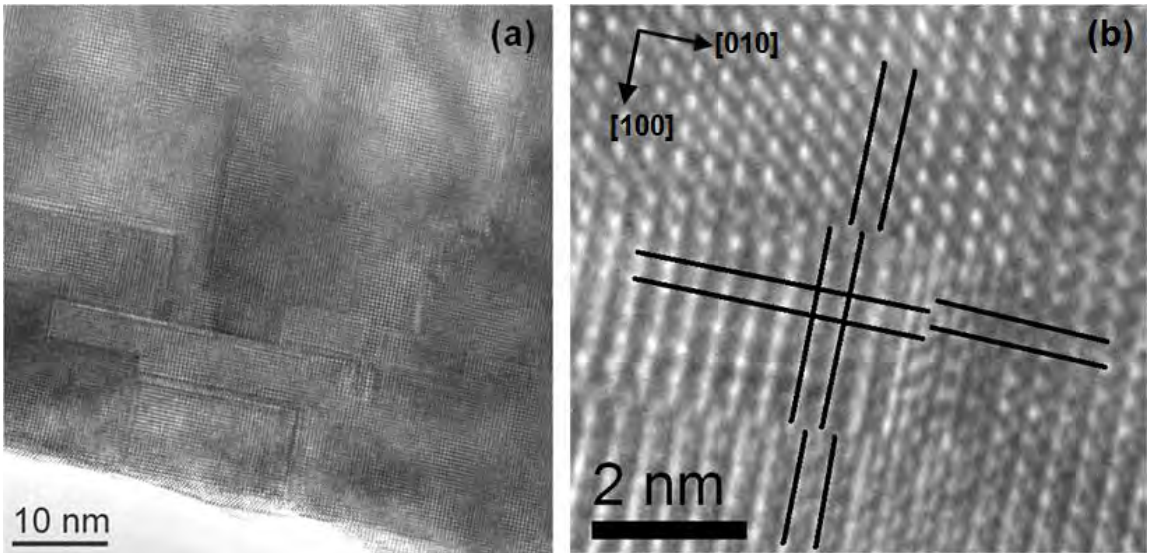

Fig. 6.8. (a) High-resolution [001]-axis TEM image of planar defects in the $SrLaAlO_4$ bulk. (b) Higher magnification of one such defect, with solid black lines highlighting half-unit-cell shifts with respect to the bulk.

6.3. Strontium Titanate

6.3.1. Background

A significant number of reports of Sr or SrO surface enrichment in pure and doped $SrTiO_3$ have been published. Moreover, one set of authors [159, 160] has proposed a bulk mechanism involving the formation of planar defects similar to those reported here for $SrLaAlO_4$, also to accommodate the ensuing bulk non-stoichiometry, although no direct

observation has been made. The relevant literature is now reviewed, thus providing context to subsequently test the viability of fault-based non-stoichiometry compensation in $SrTiO_3$.

A series of papers studying (001)-oriented $SrTiO_3$ crystals surface via scanning tunneling microscopy (STM) was published by Liang and Bonnell [161-163], mostly upon anneals in reducing conditions. It was reported that a short UHV anneal at 600 ºC led to the appearance of elongated clusters 15-50 Å in size aligned along a [100]-type direction. While no chemical analysis was performed, it was found that by extending the dwelling time at the same temperature, the clusters morphed into [100]-oriented rows, with typical 12 and 20 Å spacings. Although the periodicity is highly irregular in the images shown, these were attributed to the n = 1 and 2 cases of the SrO-rich $SrO{\cdot}(SrTiO_3)_n$ Ruddlesden-Popper phases, due to the proximity to the c-axis lattice parameter of Sr_2TiO_4 and Sr_3TiO_7 (12.6 and 20.4 Å [57]). Upon UHV annealing at 1300 ºC (unspecified time), surface islands of ~400 Å diameter and ~100 Å height formed. A combination of scanning tunneling spectroscopy and Auger electron spectroscopy (AES) was used to show that the islands were likely SrO. 2 Å steps within the islands, measured by STM, were attributed with little explanation to rocksalt strontium oxide. Rutherford backscattering spectroscopy results supported Sr surface enrichment only above 1300 ºC.

Another set of reports on surface enrichment in $SrTiO_3$ was published by Szot *et al.* [159, 160, 164, 165]. The first report, which examined several perovskite materials, dealt mainly with polycrystalline samples under oxidizing conditions [164]. While only the perovskite phase was detected via X-ray diffraction (XRD) at 500 ºC, secondary ion mass spectroscopy (SIMS) data was claimed to show the outermost 200-300 Å to be SrO-rich. Non-perovskite phases appear in the XRD patterns upon air annealing at 800 ºC for 2.2 hours. These were attributed to Ruddlesden-Popper phases (n = 1-6), as well as anatase, rutile and reduced TiO_x phases. The

latter is unconvincing given that only one peak was identified for each of TiO and Ti_4O_7 (and each such peak was shared with a RP phase); also, it is unclear how this would occur, as it would require a permanent oxygen loss in oxidizing conditions.

Their second paper [165] addressed both oxidizing (pO_2 = 200 Torr) and reducing conditions ($pO_2 \sim 10^{-7}$ Torr). Polycrystalline samples reduced at 950 ºC for 20 hours show XRD peaks assigned to RP phases (oddly, only n = 3 and 6) and reduced titanium oxides (TiO and Ti_2O). Almost all peaks ascribed to RP phases overlap (and are overwhelmed by) the main perovskite peaks; the rest are very small. SIMS depth profiles show Sr enrichment and Ti depletion in the outermost ~100 Å for oxidized crystals (1000 ºC for 40 hours); meanwhile, reduced samples exhibit Sr depletion and Ti enrichment for a depth up to 130 Å, except for the outermost 15 Å, where this is inverted. This Sr-rich layer is attributed to partial re-oxidation upon slow cooling. Rapidly quenching a reduced sample and using atomic force microscopy (AFM) results in droplet-like surface features with typical 500 nm diameter, which are attributed to SrO (in spite of being liquid-like and mobile at room temperature), in contradiction to their claim of reduction-induced Sr surface depletion.

Szot *et al.* published a third paper, in which $SrTiO_3$ single crystals were examined, with an emphasis on the (001) orientation [159]. In the 750-1000 ºC range, a 24-hour anneal in oxidizing conditions leads to the AFM observation of 11.8 Å steps, which are attributed to Sr_2TiO_4, the first RP phase, even though this is closer to a multiple of $SrTiO_3$ unit cells (11.7 vs. 12.6 Å). At 1100 ºC, droplets (with 1 μm typical diameter) appear on the surface after 24 hours and are assigned to SrO, as in the reduced samples of the previous paper, but these disappear after 120 hours. Instead, faceted crystallites were observed, and elemental analysis (not shown in the paper) indicates that these correspond to SrO_x; the authors speculate that these are the

result of the agglomeration of the droplet-like features. Szot *et al.* then develop in detail their discussion of the demixing process under oxidizing conditions in terms of the dismantling and surface-bound diffusion of bulk SrO layers, which results in the local collapse of the bulk structure, leading in turn to reduced Ti oxides or regions of TiO_2 with anatase (001)-like stacking, as well as Sr-rich RP phases near the surface and pure SrO on the surface itself. This dismantling/stacking fault mechanism will be examined in this section, as it is similar to what is seen in $SrLaAlO_4$.

A fourth report fills in the annealing temperature 1000-1100 ºC gap for $SrTiO_3$(001) single crystals in oxidizing conditions [160]. After 48 hours, 4-6 Å terraces are found on the surface upon slow cooling; meanwhile, quenching leads to droplet-like features again. The surface crystallites at higher temperatures are revisited, as high-resolution AFM images show lattice periodicities matching rocksalt SrO. Moreover, SIMS elemental mapping shows they are Sr-rich and contain no Ti.

Surface islands were also observed by Wei *et al.* on 5 at.% La-doped $SrTiO_3$(001) crystals upon heating to 1300 ºC for 120 hours in air [166, 167]. They were observed via photoemission electron microscopy and metastable impact electron microscopy and appear mostly as elongated, needle-like crystallites 5-50 μm long. Unlike any other report of such surface islands, metastable impact electron spectroscopy (MIES) data is said to suggest an overlayer of strontium peroxide (SrO_2) on the islands. Moreover, the authors use further MIES data to argue that each island is surrounded by a 2-3 micron-thick ring, or halo, which is tentatively attributed to TiO_2 or Ti_2O_3. The surface regions between islands is also found to be Sr-rich, following XPS and AES analysis; the authors, while admitting no strong evidence, speculate about the formation of RP phases on the surface. This level of La-doping was further

investigated by Gunhold *et al.* [168], who after 25 hours at 1300 ºC also observed the surface islands and labeled them as SrO_x. Step sizes of 12, 20 and 28 Å were measured by AFM between the islands and attributed to RP phases (n = 1-3) on the surface, with the c-axis normal to the surface plane. A sample with only 0.5 at.% La was also probed, and after 2 hours at 1300 ºC some surface microcrystals are observed, but the authors state that these are not SrO_x, although they do not describe how they reached this conclusion. These features disappear after 25 hours; 12 Å steps are found instead, again ascribed tentatively to Sr_2TiO_4. One ought to note that the AFM experiments indicate that in the limit of low doping, no SrO_x islands form, which contradicts their detection in undoped crystals by and Liang *et al.* and Szot *et al.* [159, 160, 162, 163].

The lack of surface islands for pure $SrTiO_3$ is further supported by Meyer *et al.* [169], who observed SrO surface islands on the (001) surfaces of donor-doped $SrTiO_3$ crystals but explained them as the result of the formation of bulk Sr vacancies as a compensation mechanism for the donor dopants, followed by the migration of Sr to the surface and its oxidation via the uptake of environmental oxygen. Optical micrographs of La-doped crystals annealed at 1350 ºC for 25 hours yielded the following observations: while lightly doped (0.1 at.%) samples exhibited no surface precipitates within optical resolution, 1%-doped samples showed needle-like islands (oriented along [110]-type directions) and 5% doping resulted in larger, less regularly shaped islands (with some preferential [110] orientation). The latter appeared to agglomerate into larger, regularly elongated crystallites after much longer annealing times. Nb-doped crystals (2 at.%) behaved similarly to annealed 1% La-doped samples. SEM-EDX and TEM-EDX elemental analysis showed the islands to be Sr-rich with no La/Nb present; the authors argue that they were likely rocksalt SrO, supported by lattice match considerations. No significant change

in stoichiometry was found between the bulk and the island-free surface regions. High-resolution TEM images showed no RP faults in either of these areas. No surface precipitates were seen below 1000 ºC via optical microscopy.

Rahmati *et al.* [170] also observed Sr-rich features in polycrystalline, Nb-doped (5 at.%) $SrTiO_3$ samples annealed at 1200 ºC for 30 hours in air and subsequently quenched to room temperature. Both faceted islands and smaller droplet-like features were found. Only two islands, on two different high-index orientations, were examined by EDX and transmission electron diffraction, and only one was determined to be rocksalt SrO.

Desu and Payne [171] also measured Sr surface enrichment in $SrTiO_3$, but in a reducing environment (10% H_2 + 90% N_2). This was measured with AES for single crystals at 1000 ºC and polycrystalline samples at 1380 ºC, although an O surface depletion was also observed, so the Sr surface enrichment cannot be explained by SrO alone. Similarly, Horvath *et al.* [172, 173] also measured similar Sr enrichment via AES, now with annealing at 800 ºC for 100 hours in three different environments. The enrichment was most pronounced with a mixture of 5% H_2 and 95% N_2, followed by a pure N_2 environment, while synthetic air gave the least Sr enrichment. Several dopants were introduced at levels below 1% but no effect on the Sr profile was detected.

As can be seen, the evidence for Sr/SrO surface segregation in $SrTiO_3$ is often conflicting and even self-contradictory. For the most part, it relates to high-temperature annealing (above ~1100 ºC), but a few reports exist for lower temperatures. The latter are in disagreement with a large body of work demonstrating the formation of Ti-rich surfaces at intermediate temperatures. This includes, for example, the periodic reconstructions examined in Chapter 3 [34, 89, 91-93] and the nanolines explored in Chapter 4 [107, 108, 113], which have been consistently shown by

AES [74, 75, 78, 84, 108] and XPS [104, 113] to be Ti-rich. Moreover, Herger *et al.* explicitly tested –and discarded– SrO-rich surfaces while fitting $SrTiO_3$(001) surface X-ray data [94].

Several reports on Ti-rich surface islands have also been published. For example, Silly and Castell [174] explored cycled UHV annealing of $SrTiO_3$(001) surfaces at 875 ºC for a total annealing time of 20 hours. Thin, epitaxial anatase TiO_2(001) islands with reconstructed domains were observed via STM. The islands grew from being roughly 10 nm wide to 100 nm upon further annealing at 1200 ºC, and remained surface-reconstructed. Marshall and Castell [175] further demonstrated that extended UHV annealing (20 hours) in the 930-1030 ºC range allows the epitaxial anatase (001) islands to reach dimensions larger than 1 μm.

Meanwhile, Gunhold *et al.* [176] used STM, SEM and spectroscopic techniques to observe and probe (001) surface islands in 0.1 at.% La-doped $SrTiO_3$. Small islands were seen after UHV annealing at 1000 ºC for 5 hours, but these grew to dimensions up to 2 μm by annealing at 1300 ºC for 40 hours. Scanning tunneling spectroscopy data indicates the islands are metallic, which is used in combination to AES data to attribute them to Ti_2O_3. In similar results, Lee *et al.* [85] observed surface islands by heating a crystal to above 970 ºC for over an hour, in a 1.5×10^{-8} Torr vacuum. The islands were observed by high-resolution transmission electron microscopy to grow on the (001) surfaces, but in this case lattice fringes were used to argue that the islands consisted of rocksalt TiO. No chemical characterization was performed.

Not all reports of Ti-rich surface islands relate to reducing conditions. Kazimirov *et al.* [177] annealed undoped $SrTiO_3$(001) crystals in flowing O_2 at 900-1100 ºC for 3 hours and observed via AFM surface crystallites with 50 nm average size. Grazing-incidence X-ray diffraction was used to attribute these to a monoclinic TiO phase, but it must be noted that this is highly implausible in oxidizing conditions, especially since no chemical analysis was carried out.

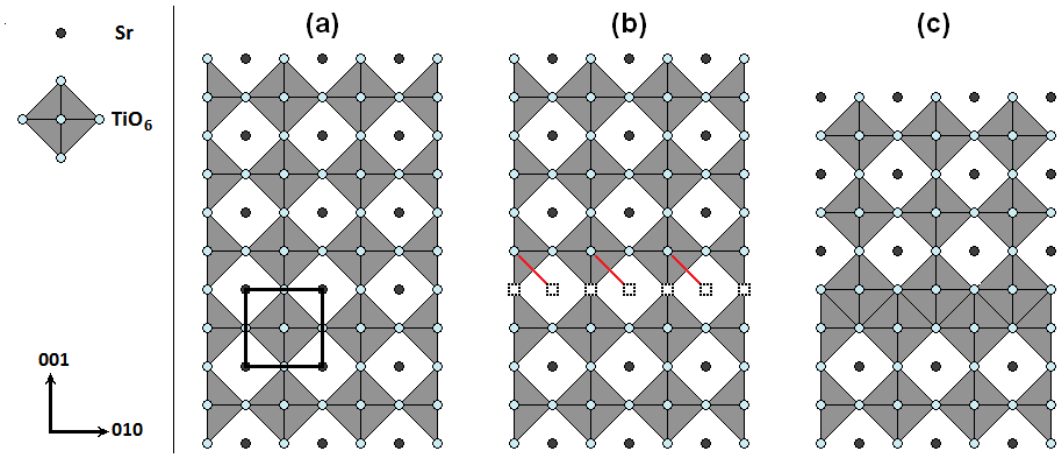

Fig. 6.9. TCS fault formation. (a) [100] projection of bulk $SrTiO_3$, unit cell outlined. (b) Removal of a SrO layer and subsequent <0 ½ ½> crystallographic shear, indicated by red diagonal lines; dotted empty squares denote vacant sites. (c) Resulting structure with TCS stacking fault. Adapted from Ref. [159].

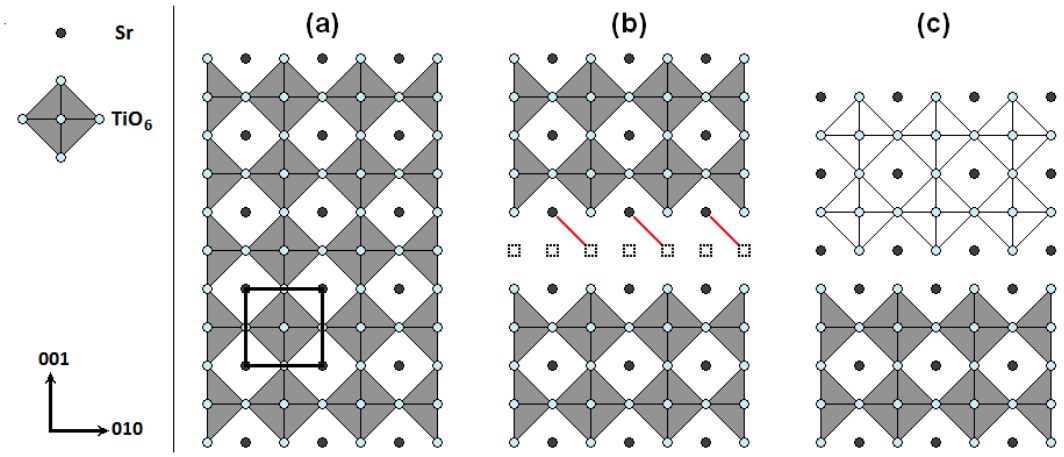

Fig. 6.10. RP fault formation. (a) [100] projection of bulk $SrTiO_3$, unit cell outlined. (b) Removal of a TiO_2 layer and subsequent <½ ½ ½> crystallographic shear, indicated by red diagonal lines; dotted empty squares denote vacant sites. (c) Resulting structure with RP stacking fault. White octahedra indicate an out-of-page half-unit-cell shift with respect to gray octahedra.

In light of the muddled literature, this section will examine two plausible theories regarding the decomposition of stoichiometric $SrTiO_3$ via bulk stacking faults and surface segregation.

The first, highly similar to what is seen in $SrLaAlO_4$, is what is dubbed the "simplified Szot mechanism". This consists of the dismantling of (001) SrO layers, with the diffusion of this material towards the surface. Deep in the bulk region, this leads to the collapse of the structure and the induction of crystallographic shears via the formation of TCS stacking faults with two contiguous bulk-like (001) TiO_2 layers (see subsection 2.3.2). Unlike the <½ ½ *z*> shear vector in SrO-poor $SrLaAlO_4$ stacking faults, this anatase (001)-like stacking requires a <½ 0 ½> shear, as shown schematically in Figure 6.9. As mentioned above, the complete mechanism proposed by Szot *et al.* describes the formation of RP faults and RP phases near the surface as intermediate structures. However, the ultimate, equilibrium state consists of pure rocksalt SrO precipitation at the surface, so this is what is studied in this chapter. Also, the formation of reduced Ti-based oxides is ignored, since this is highly unlikely under oxidizing conditions. The simplified Szot mechanism can be simply described by the following schematic equation:

$$SrTiO_3 \rightarrow \text{Surface SrO} + \text{Bulk TCS faults} \qquad \text{(Eq. 6.1)}$$

A second plausible situation is also tested, inspired by the simplified Szot mechanism, although very much diametrically opposite to it. The possibility is explored that the TiO_2 surface enrichment necessary for the DL (001) periodic reconstructions (described in previous chapters) arises from a hypothetically favorable formation of RP faults in the bulk (shown in Figure 6.10) and mild TiO_2 surface segregation. It must be noted that the surface enrichment in this case is fundamentally different, as the excess surface material consists of homogeneous thin coverage instead of islands or other large precipitates. This decomposition can be expressed as

$$SrTiO_3 \rightarrow \text{DL-}TiO_2\text{ Surface} + \text{Bulk RP faults} \qquad \text{(Eq. 6.2)}$$

and shall referred to as the "DL+RP" mechanism.

6.3.2. Methods

As usual, DFT calculations were performed using the full-electron-potential WIEN2k code [46] with the augmented plane wave + local orbital (APW+lo) basis set. Bulk structures were allowed to relax until the force on each atom was under 0.05 eV/Å. The following muffin-tin radii were consistently used: 2.40 (Sr), 1.72 (Ti) and 1.54 bohr (O). A maximum K value for the plane wave expansion of 6.5/1.54 bohr^{-1} was employed, as well as a k-point mesh equivalent to a 12×12×12 mesh for a bulk $SrTiO_3$ unit cell. The PBE [98] version of the generalized gradient approximation to the exchange-correlation functional was used. The lattice parameters in all bulk calculations were optimized independently.

For bulk phases in the SrO–TiO_2 pseudobinary system, the formation energies for the reaction

$$p{\cdot}\mathrm{SrO} + q{\cdot}\mathrm{TiO_2} \rightarrow (\mathrm{SrO})_p(\mathrm{TiO_2})_q \qquad \text{(Eq. 6.3)}$$

were calculated and normalized as follows:

$$\Delta E_f^{\mathrm{SrO}\oplus\mathrm{TiO_2}}\big((\mathrm{SrO})_p(\mathrm{TiO_2})_q\big) = (E_{(\mathrm{SrO})_p(\mathrm{TiO_2})_q} - p\cdot E_{\mathrm{SrO}} - q\cdot E_{\mathrm{TiO_2}})/(p+q)\,. \qquad \text{(Eq. 6.4)}$$

Alternatively, formation energies of the intergrowth phases can be calculated using $SrTiO_3$ and SrO/TiO_2 as reference states:

$$\mathrm{SrO} + n{\cdot}\mathrm{SrTiO_3} \rightarrow \mathrm{RP}_n \equiv \mathrm{SrO}{\cdot}(\mathrm{SrTiO_3})_n \qquad \text{(Eq. 6.5a)}$$

$$\mathrm{TiO_2} + n{\cdot}\mathrm{SrTiO_3} \rightarrow \mathrm{TCS}_n \equiv \mathrm{TiO_2}{\cdot}(\mathrm{SrTiO_3})_n\,. \qquad \text{(Eq. 6.5b)}$$

In this case, the energies are computed in accordance to the expressions

$$\Delta E_f^{\mathrm{SrO}\oplus\mathrm{SrTiO_3}}(\mathrm{RP}_n) = E_{\mathrm{RP}_n} - E_{\mathrm{SrO}} - n\cdot E_{\mathrm{SrTiO_3}} \qquad \text{(Eq. 6.6a)}$$

$$\Delta E_f^{\mathrm{TiO_2}\oplus\mathrm{SrTiO_3}}(\mathrm{TCS}_n) = E_{\mathrm{TCS}_n} - E_{\mathrm{TiO_2}} - n\cdot E_{\mathrm{SrTiO_3}} \qquad \text{(Eq. 6.6b)}$$

and are reported on a per-formula-unit basis.

Surfaces were also modeled to represent different levels of SrO/TiO_2 surface excess, using the repeated slab geometry. This was done for classical bulk-like truncations, as well as surfaces exhibiting terminations of 2 or 3 consecutive layers of either SrO or TiO_2. Following the ~~–~~2Ti" nomenclature in Chapter 5, these can be labeled 1Ti, 2Ti, 3Ti, 1Sr, 2Sr and 3Sr. 13 atomic layers for bulk-like truncations, 15 for double SrO/TiO_2 surface layers and 17 for triple SrO/TiO_2 layers, as well as at least 10 Å of vacuum thickness between contiguous slabs. Surface supercells were constrained along the in-plane axes to the optimized $SrTiO_3$ bulk lattice parameter of 3.938 Å. The force tolerance for the surface calculations was set to 0.1 eV/Å; all other DFT parameters were the same as for the bulk modeling.

6.3.3. Results

The optimal lattice parameters and relaxed bulk positions were calculated for the following phases in the $SrO–TiO_2$ pseudobinary system, all of which can be expressed as $(SrO)_p(TiO_2)_q$:

- Rocksalt SrO ($q = 0$)
- RP phases, $SrO\cdot(SrTiO_3)_n$, for n = 1-4, 9 ($q = p - 1$)
- $SrTiO_3$ ($q = p$)
- TCS phases, $TiO_2\cdot(SrTiO_3)_n$, for n = 1-3 ($q = p + 1$)
- Rutile TiO_2 ($p = 0$), the stable form of titanium dioxide.

The convex-hull construction is shown in Figure 6.11. As can be seen, all phases except the TCS fall on the construction. This demonstrates, as expected, that while the SrO-rich RP phases are thermodynamically favorable, the TiO_2-rich TCS phases are not. That is, given a starting composition matching any given TCS phase, the system is expected to dissociate into

pure rutile TiO_2 and $SrTiO_3$. This has much to do with the fact that the stacking of $SrTiO_3$-bulk-like TiO_2 layers qualitatively mirroring the anatase <001> stacking, which in anatase favors strong rumpling along this direction and leads an *a*-axis lattice constant of 3.78 Å [178], shorter than that of $SrTiO_3$. In a structure dominated by a perovskite or perovskite-like matrix, this rumpling is repressed, with a significant energy cost. As can be inferred from the dashed red line, the cohesiveness of rutile would have to be much weaker for the TCS phases to be stable.

Alternatively, one can tabulate the formation energies of RP/TCS phases from $SrTiO_3$ and SrO/TiO_2, as outlined in Equation 6.6. These numbers are shown in Table 6.1, along with values from three other DFT-based papers [60, 62, 64]. It is just as clear that, unlike the RP series, the TCS homologous series is energetically unfavorable, although in both cases the favorability improves with increasing *n* as the faults are further away from each other.

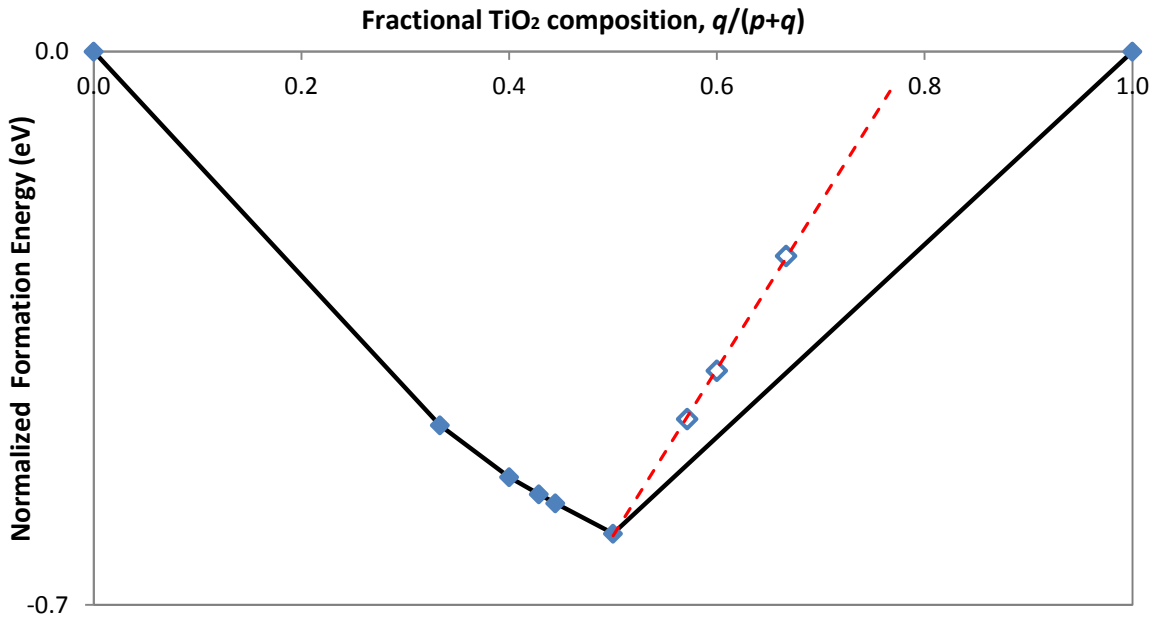

Fig. 6.11. Normalized bulk formation energies for $SrTiO_3$, RP and TCS phases from rocksalt SrO and rutile TiO_2. Convex-hull construction shown as solid black line. Dashed red line follows TCS phases.

Table 6.1. Formation energies of RP and TCS phases from SrO/TiO_2 and $SrTiO_3$, in eV per formula unit, following Eq. 6.6. Other published theoretical values are quoted for reference.

	$RP_n \equiv SrO\cdot(SrTiO_3)_n$		$TCS_n \equiv TiO_2\cdot(SrTiO_3)_n$	
n	This Work	Other	This Work	Other
1	–0.198	–0.152 [64], –0.200 [62], –0.158 [60]	0.444	
2	–0.252	–0.203 [64], –0.252 [62], –0.144 [60]	0.421	0.570 [60]
3	–0.261	–0.217 [64], –0.269 [62]	0.405	
4	–0.264	–0.215 [64]		

A useful exercise is to try to calculate the formation energy of a single RP/TCS fault. One way to do this is to use the available data points and extrapolate towards the limit of nearly pure $SrTiO_3$. The calculated formation energies for the n = 1-4 RP phases and n = 1-3 TCS phases are plotted in Figure 6.12 as a function of fractional SrO/TiO_2 content, $F_{SrO/TiO_2}=1/(n+1)$.

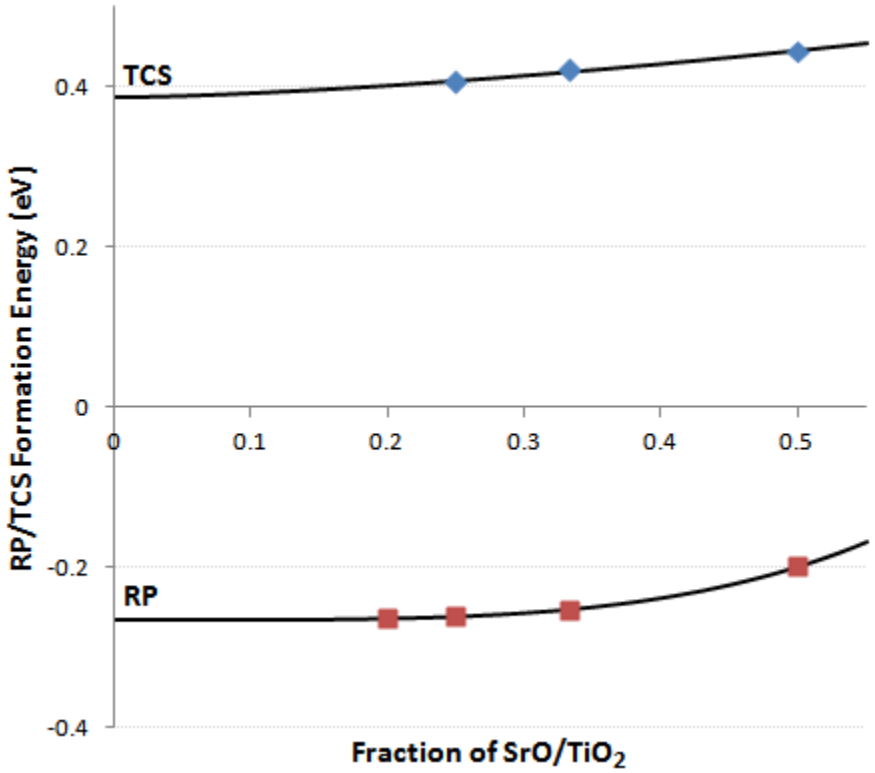

Fig. 6.12. RP/TCS formation energy, as defined by Eq. 6.3, as a function of SrO/TiO_2 content. Solid lines are power-law-plus-offset fits.

For the RP phases, the available data is fit to the power-law-plus-offset curve,

$$\Delta E_f^{\mathrm{SrO}\oplus\mathrm{SrTiO_3}}(\mathrm{RP}_n) = A \cdot {F_{\mathrm{SrO}}}^B + C, \quad B > 1, \qquad \text{(Eq. 6.7)}$$

since it has a slope of 0 as $n \to \infty$. An approximate formation energy for a single fault can be extracted by extrapolation to a specified fractional SrO content. The fit yields a large-*n* limit value of C = –0.266 eV. The TCS formation energies were fit by the same type of curve to obtain a single-fault limit value of +0.386 eV.

The decomposition ~~"r~~eactions" of interest are expressed by Eqs. 6.1 and 6.2. The formation energies of large-*n* RP/TCS phases can be exploited for this, in combination with the slab energy calculations. In general, we will estimate the enthalpy change of morphing a cleaved stoichiometric slab (represented by an average of 1Sr and 1Ti slabs) into a slab with a certain number (1-3) of consecutive SrO/TiO_2 bulk-like surface layers plus the number of bulk TCS/RP faults required to preserve the overall stoichiometry. Since the slabs have a fixed number of layers and the RP/TCS faults are modeled through a number of RP/TCS unit cells (which largely replace many $SrTiO_3$ bulk unit cells in the ~~"p~~roduct" system), an adequately balanced reaction must be reached in order to compute the enthalpy change. Throughout this process, the example of Eq. 6.2 will be developed after each step; again, this corresponds to a stoichiometric crystal forming Ti-rich DL surfaces and compensating the bulk via RP faults.

Since surfaces terminating in L layers of SrO/TiO_2 have L – 1/2 ML excess SrO/TiO_2, and since there are two surfaces per slab, an L(Sr/Ti) slab will need $\Lambda \equiv 2L - 1$ extra TiO_2/SrO planes in the bulk to preserve the ideal stoichiometry, assuming no other defects; that is, Λ TCS/RP stacking faults are necessary. These faults can be closely represented by TCS/RP phases of large *n*. Also, there are two (001) faults per unit cell, and a typical TEM sample 100

nm thick corresponds to a thickness of ~250 bulk $SrTiO_3$ unit cells, so this means that a target n value of $250/\Lambda$ should be suitable. In the case study mentioned, $L = 2$, $\Lambda = 3$ and $n \sim 83$.

All stabs use a base thickness of six bulk unit cells, which implies (math steps omitted) that the balanced reaction must take the form

$$½\left(1\text{Sr-slab}+1\text{Ti-slab}\right) \rightarrow L\text{Sr-slab} + \Lambda \cdot \text{TCS}_{n=250/\Lambda} - (\Lambda - ½ + \Lambda n) \cdot \text{SrTiO}_3 \qquad \text{(Eq. 6.8a)}$$

or,

$$½\left(1\text{Sr-slab}+1\text{Ti-slab}\right) \rightarrow L\text{Ti-slab} + \Lambda \cdot \text{RP}_{n=250/\Lambda} - (\Lambda - ½ + \Lambda n) \cdot \text{SrTiO}_3. \qquad \text{(Eq. 6.8b)}$$

For the example, this corresponds to

$$½\left(1\text{Sr-slab}+1\text{Ti-slab}\right) \rightarrow 2\text{Ti-slab} + 3\cdot\text{RP}_{n=83} - (2.5 + 3*83) \cdot \text{SrTiO}_3. \qquad \text{(Eq. 6.9)}$$

Using Equation 6.6, it is found that in general

$$\begin{aligned}\Delta H = E_{L\text{Sr-slab}} + \Lambda\cdot\left[\Delta E_f^{\text{SrO}\oplus\text{SrTiO}_3}\left(\text{TCS}_{n=250/\Lambda}\right) + E_{\text{TiO}_2}\right] \\ -[½(E_{1\text{Ti-slab}} + E_{1\text{Sr-slab}}) + (\Lambda - ½)\cdot E_{\text{SrTiO}_3}]\end{aligned} \qquad \text{(Eq. 6.10a)}$$

or,

$$\begin{aligned}\Delta H = E_{L\text{Ti-slab}} + \Lambda\cdot\left[\Delta E_f^{\text{TiO}_2\oplus\text{SrTiO}_3}\left(\text{RP}_{n=250/\Lambda}\right) + E_{\text{SrO}}\right] \\ -[½(E_{1\text{Ti-slab}} + E_{1\text{Sr-slab}}) + (\Lambda - ½)\cdot E_{\text{SrTiO}_3}].\end{aligned} \qquad \text{(Eq. 6.10b)}$$

In the example, this takes the form

$$\begin{aligned}\Delta H = E_{2\text{Ti-slab}} + 3\left[\Delta E_f^{\text{TiO}_2\oplus\text{SrTiO}_3}(\text{RP}_{n=83}) + E_{\text{SrO}}\right] \\ -[½(E_{1\text{Ti-slab}} + E_{1\text{Sr-slab}}) + 2.5*E_{\text{SrTiO}_3}].\end{aligned} \qquad \text{(Eq. 6.11)}$$

The resulting reaction enthalpies are listed in Table 6.2. In the particular case of the DL+RP example, the reaction is decidedly unfavorable at an enthalpic cost of 3.86 eV per 1×1 slab. However, it is more meaningful to replace the 2Ti surface by a DL reconstruction which has been experimentally observed. Using the calculated surface energy difference between the 2Ti and the "zigzag" 2×2 reconstruction (the lowest-energy observed DL surface) calculated in

Chapter 5, the slab energy of a 2×2 surface modeled with the same parameters can be estimated. Under this setting, the calculation yields an enthalpy cost of 1.64 eV per 1×1 slab.

Table 6.2. Enthalpic cost of reactions as defined by Equation 6.10, in eV per 1×1 slab.

Surface		SrO-rich	TiO_2-rich
Fault-type		TCS	RP
L	1	0.55	0.79
	2	4.18	3.86
	3	7.69	5.56
	2*		1.64

*With "zigzag" 2×2 surface reconstruction instead of 2Ti surface.

It should come as no surprise that adding more bulk stacking faults is increasingly unfavorable. Also, it is clear that the cost of forming a TCS fault makes it unviable for the Szot mechanism to occur.

6.4. Discussion

6.4.1. $SrLaAlO_4$: Surface Structure

The $SrLaAlO_4$ system does not easily form a periodic surface reconstruction such as those observed under similar conditions in $SrTiO_3$ and $LaAlO_3$ [34, 89, 91, 155]. This is believed to be related to the disorder in the structure, as Sr^{2+} and La^{3+} randomly occupy the same site. It may well be that the annealing time used at moderately high temperatures (<1200 ºC) was too short to allow for the surface to equilibrate, given the complex bulk structure. It is also possible that the surface exhibits only local order, essentially forming a 2D glassy surface structure (as suggested by Kienzle *et al.* for perovskite surfaces [92]) which would render the surface inscrutable by diffraction methods.

At high temperatures, the surfaces exhibit considerable SrO segregation. To the best of our knowledge, no such segregation behavior has been observed in materials with the perovskite-like K_2NiF_4 structure.

One important subject is that of the interface between $SrLaAlO_4$ and the segregated SrO, whose rocksalt structure is cubic with lattice constant a_{SrO} = 5.16 Å [179]. For simplicity, only bulk-like truncations are considered here. On the $SrLaAlO_4$(001) surface, the registry is fairly straightforward, as the SrO layer at the interface would be much like any (Sr/La)O (001) layer in $SrLaAlO_4$, regardless of whether the termination has AlO_2 or (Sr/La)O stoichiometry. This corresponds to a SrO(001) orientation, as illustrated in Figure 6.13. The lattice mismatch is only 3%, so epitaxial SrO accumulation is in principle possible.

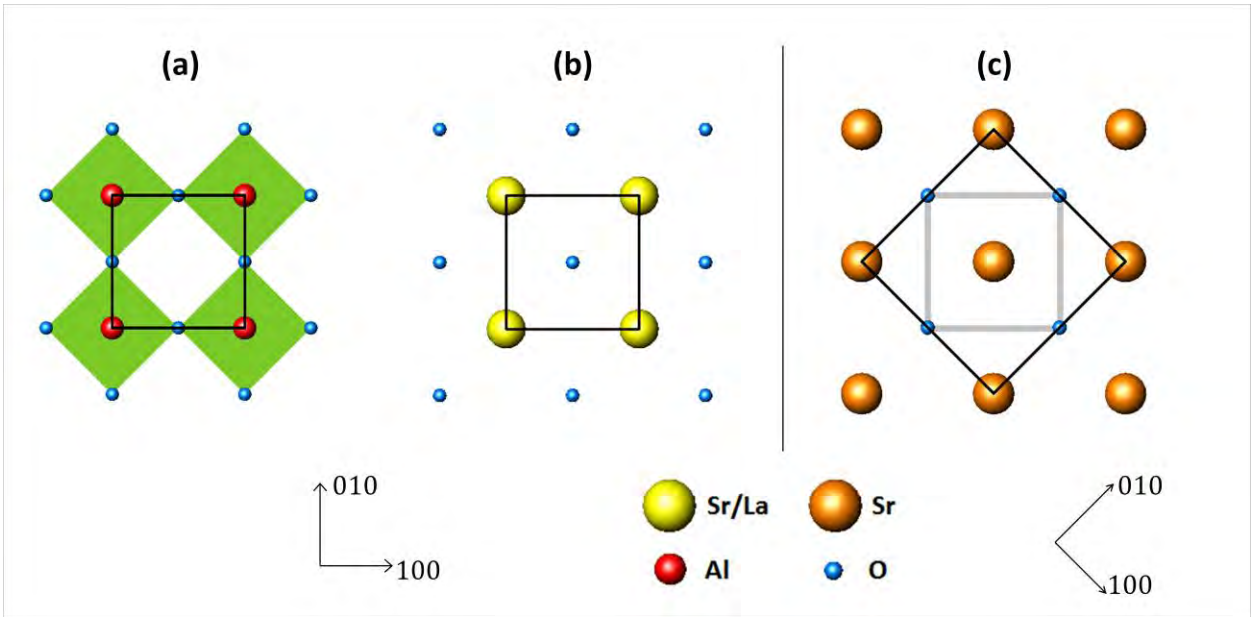

Fig. 6.13. (a) AlO_2 bulk-like $SrLaAlO_4$(001) truncation in plan view, with unit cell outlined. Green polyhedra correspond to 5-fold coordination. (b) (Sr/La)O bulk-like $SrLaAlO_4$(001) truncation in plan view, with unit cell outlined. (c) SrO(001) truncated surface in plan view, with unit cell outlined in black. Gray square indicates registry with $SrLaAlO_4$(001) unit cell.

On the {100} and {110}-type $SrLaAlO_4$ surfaces, the registry is clumsier. One can infer from Figure 6.4 that the {100} surfaces register best with a {110}-type rocksalt SrO surface. $SrLaAlO_4$(100) surfaces only have one possible type of termination, and while the natural stacking is qualitatively evident (see Figure 6.14), the problem is the lattice mismatch. The <010> (referenced to $SrLaAlO_4$) mismatch is again only 3%, but it is rather large along the $<001>_{SrLaAlO_4}$ direction at 22%. Meanwhile, the $SrLaAlO_4$(110) orientation has a $SrLaAlO_2$ termination and another with relative O_2 stoichiometry. The SrO(001) orientation appears again to be the most natural interface for the $SrLaAlO_2$ termination, although this corresponds again to a 22% mismatch along the $<001>_{SrLaAlO_4}$ axis (and 3% $<1\bar{1}0>_{SrLaAlO_4}$ mismatch), as shown in Figure 6.15. It is not immediately clear what the registry would be on the O_2 termination. Regardless, considerable $<001>_{SrLaAlO_4}$ strain and rumpling are to be expected at the interface of {100}- and {110}-type $SrLaAlO_4$ with SrO, so these are not low-energy interfaces.

6.4.2. $SrLaAlO_4$: SrO Surface Segregation

What is the driving force behind the segregation of SrO at the surface? One possible explanation for the observed surface segregation is that the original samples may not be as stoichiometric as advertised. $SrLaAlO_4$ crystal growth from a stoichiometric melt is known to produce crystals exhibiting cracking and undesired inclusions. Therefore, it is common to use some excess Sr precursor in the melt in order to obtain high-quality crystals [148]. This is typically explained as some Sr ions substituting for La (plus half an oxygen vacancy per cation substitution), which is easy to accommodate due to the nearly identical cationic radii [149]. Indeed, the commercial vendor from which the crystals were purchased acknowledges that 0.5% excess Sr (by weight) is regularly added to the starting mix for the growth of $SrLaAlO_4$ [180].

However, this does not forcibly imply that the resulting crystals are Sr-rich. In fact, the ICP-AES measurements yield a Sr/La ratio of 0.999±0.002 (and a Sr/Al ratio of 1.001±0.002), which indicates that the as-received crystals are stoichiometric, within the accuracy of the technique. Any Sr excess, if at all present, is negligible and cannot account for the observed level of surface segregation. Moreover, even in the case of higher Sr content, it is not clear that there would be a strong driving force for segregation other than the factors discussed above. In particular, the aforementioned size similarity between Sr^{2+} and La^{3+} implies that the resulting lattice strain would be small.

Another possible explanation is that segregation of SrO at the surface reduces the surface free energy. The registry models in the previous subsection are a starting point, but it is not definitively known what the $SrLaAlO_4$ surface structure is prior to the SrO segregation. In any case, it is very hard to accurately calculate the relevant surface and interfacial energies of a disordered solid solution such as this, but there are several things to note. The (001) orientation is already a low-energy case, as evidenced by its easy cleavage, and yet segregation on this surface is seen. Also, if surface energy lowering were the dominant driving force, it is unclear why one should see polycrystalline surface islands instead of homogeneous SrO surface coverage, which should in turn be only one or two monolayers since this interface would have very little epitaxial strain. Meanwhile, the SrO interface with {100} or {110} $SrLaAlO_4$ surfaces is inelegant, with long-range epitaxy next to impossible, so it is highly unlikely that the surface energy would be lowered enough to compensate for the large interfacial energy.

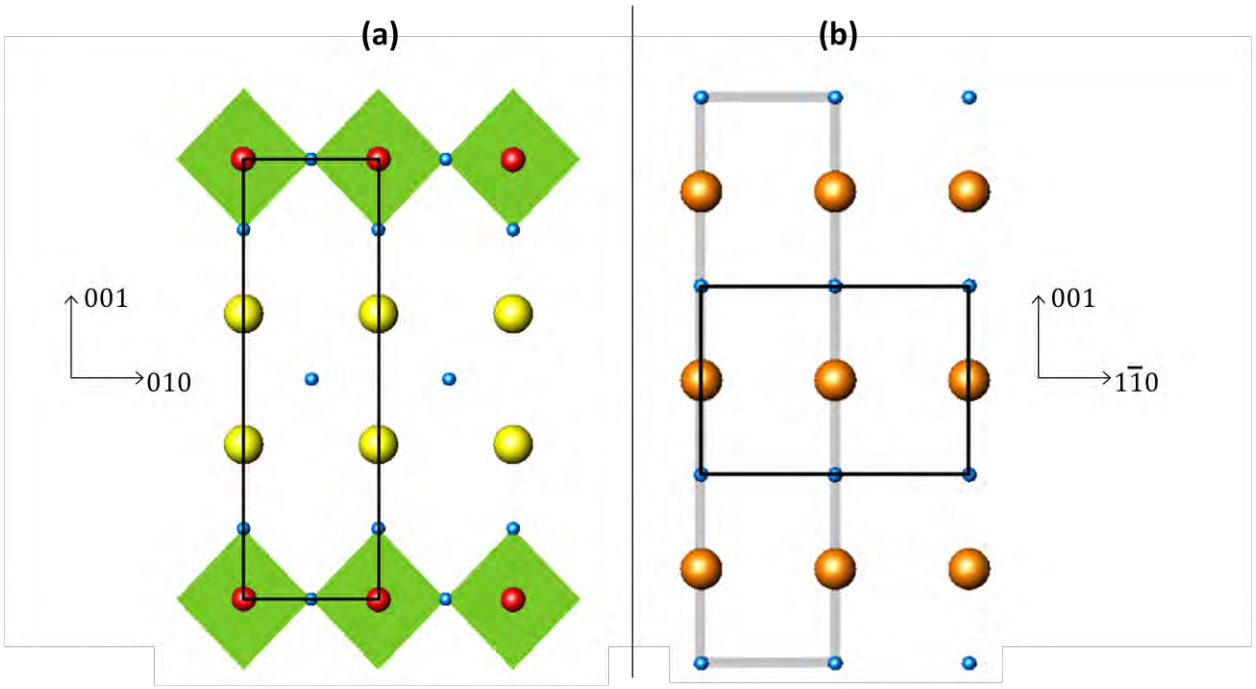

Fig. 6.14. (a) $SrLaAlO_4(100)$ bulk-like truncation in plan view, with unit cell outlined. (b) SrO(110) bulk-like truncation in plan view, with $(\sqrt{2}\times1)a_{SrO}$ cell outlined in black. Gray rectangle indicates natural registry with the $SrLaAlO_4(100)$ unit cell. Legend is the same as in Fig. 6.12.

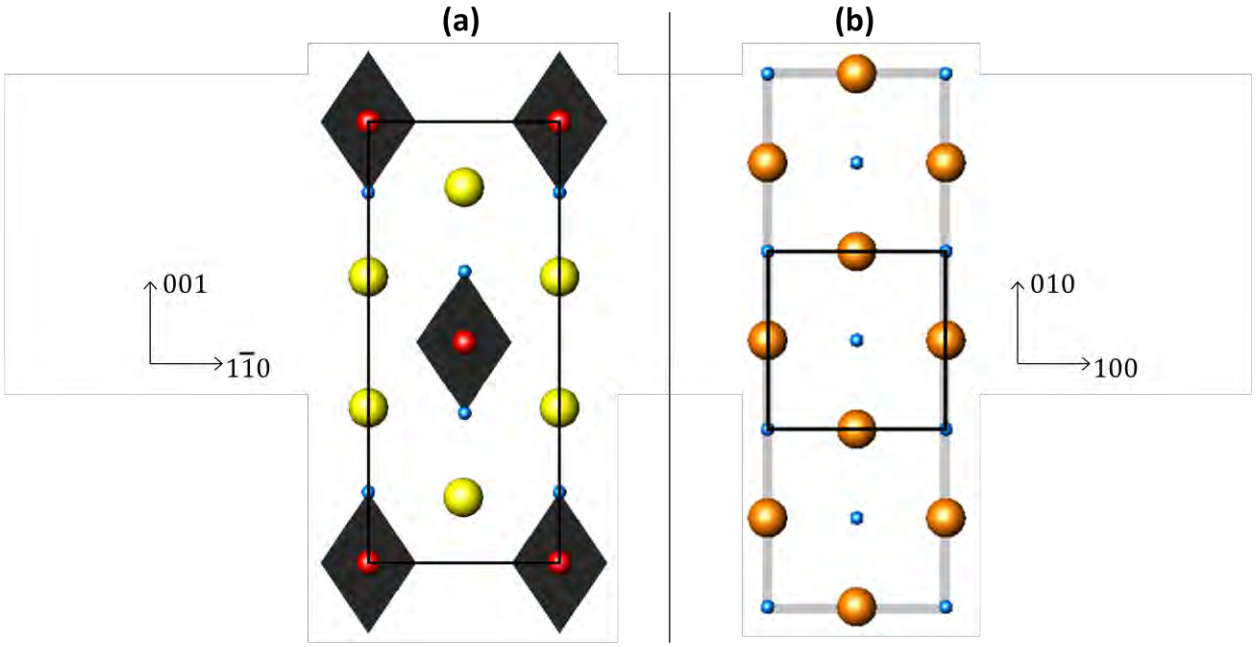

Fig. 6.15. (a) $SrLaAlO_2$ bulk-like $SrLaAlO_4(110)$ truncation in plan view, with $(\sqrt{2}a_{SrLaAlO4}\times c_{SrLaAlO4})$ cell outlined. Black polyhedra correspond to 4-fold coordinated Al, with two Al-bonded O in next (110) layer not shown. (b) SrO(001) bulk-like truncation in plan view, with unit cell outlined in black. Gray rectangle indicates registry with $SrLaAlO_4(110)$ cell shown in (a). Legend is the same as in Fig. 6.12.

There is a simpler explanation – one which implies that the observed segregation is mostly a bulk (not a surface) stabilization mechanism. Quite simply, the segregation is initially due to the increased contribution of the point defect configurational entropy (entropy of mixing) to the free energy of the system. Among valence-neutral point defects, one ought to expect Schottky-like disorder to dominate over Frenkel defects in a bulk structure of high packing density such as K_2NiF_4. Specifically in $SrLaAlO_4$, Sr-O vacancy pairs should be easier to form and more mobile than larger complexes involving La or Al vacancies, so they are expected to be the dominant defect. At high temperatures, the bulk concentration of Sr and O vacancies increases as their entropy outweighs the enthalpic cost of their formation. Also, as k_BT becomes comparable to the Sr/O diffusion activation barrier, these defects become not only more favorable, but also more mobile. This leads to SrO depletion in the bulk and, in the case of monocrystals the displaced atoms have only one place to go: the surface.

One ought to note, however, that $SrLaAlO_4$ is likely to have a relatively low tolerance for point defects; for sufficiently large bulk non-stoichiometry, planar fault compensation has been observed to dominate over classical point defect mechanisms in perovskite and perovskite-like materials [65, 156-158]. $SrLaAlO_4$ relies on the formation of stacking faults, which are easily accommodated, as discussed below. This allows for enhanced SrO surface segregation.

6.4.3. $SrLaAlO_4$: Inverse Ruddlesden-Popper Faults

As shown via high-resolution electron microscopy, the $SrLaAlO_4$ bulk accommodates for the large Sr and O deficiency by generating stacking faults. These are nucleated by Sr-O vacancy pairs, which agglomerate and cause the effective dismantling of a (001) SrO layer and a crystallographic shear. Said shear leads to the local alternation of AlO_2–LaO–AlO_2 layers in a

configuration of corner-sharing octahedra along the <001> direction. In short, this generates thin regions consisting of perovskite $LaAlO_3$, which is obviously highly stable. Moreover, the *a* lattice parameter of $SrLaAlO_4$ (3.756 Å) has a very small (<1%) mismatch with the pseudocubic $LaAlO_3$ lattice parameter (3.790 Å) [181], so the non-stoichiometry is effortlessly accommodated. This process is equivalent to the subtraction of a Ruddlesden-Popper fault, for it locally converts a RP phase ($AO{\cdot}(ABO_3)_n$; A = Sr/La, B = Al, n = 1) into a perovskite phase, not vice versa. These defects are therefore dubbed *inverse* RP faults.

Upon broader inspection, the resulting structure may also be attributed to a region of $SrLa_2Al_2O_7$, instead of $LaAlO_3$, as illustrated in Fig. 6.1(c). In fact, the $LaAlO_3$–$SrLaAlO_4$ phase diagram [182] shows only $SrLa_2Al_2O_7$ as a secondary phase in the regime of nearly pure $SrLaAlO_4$ for temperatures above 1300 ºC, which is coincidentally the upper limit in the present report. It is plausible that a longer or higher-temperature anneal would result in the ordering of the inverse RP faults with their (001) periodicity matching that of said phase.

Naturally, the low enthalpic cost of forming these planar defects is the main reason for their appearance. However, they still provide significant configurational entropy. A simple calculation can be performed for the entropic contribution of the inverse RP faults to the free energy. In one dimension, along <001>, this entropy term can be expressed as

$$-T{\cdot}\Delta S_{\text{conf}} = -k_{\text{B}}T\ln\Omega = -k_{\text{B}}T\ln\binom{N_{\text{S}}}{N_{\text{F}}} = -k_{\text{B}}T\ln\left(\frac{N_{\text{S}}!}{N_{\text{F}}!(N_{\text{S}}-N_{\text{F}})!}\right), \qquad \text{(Eq. 6.12)}$$

where Ω is the number of possible configurations, defined by the number of available sites (N_{S}) for an inverse RP fault and the actual number of faults (N_{F}). The former is specified by the sample thickness and the number of available fault sites per bulk unit cell (two in $SrLaAlO_4$). The value of this entropy term at an annealing temperature of 1300 ºC is shown in Table 6.3 for

several crystal thicknesses and N_F values. For a single inverse RP fault in a typical (001)-oriented $SrLaAlO_4$ TEM sample only 100 nm thick, this amounts roughly to –0.69 eV; this increases with thickness, which is consistent with the observation that the SrO surface islands are much larger in the thicker, as-received samples than in the thin regions examined via TEM.

Table 6.3. Entropic contribution of N_F inverse Ruddlesden-Popper faults in $SrLaAlO_4$ to the free energy of the system at 1300 ºC, as defined by Eq. 6.12, in eV.

		N_F		
		1	2	3
thickness (m)	10^{-7}	−0.69	−1.28	−1.81
	10^{-6}	−1.00	−1.90	−2.75
	10^{-5}	−1.31	−2.53	−3.69
	10^{-4}	−1.62	−3.15	−4.62
	10^{-3}	−1.93	−3.78	−5.56

If the overall transformation of the material is considered, what is observed is effectively a partial dissociation of strontium lanthanum aluminate into surface SrO and thin regions of bulk $LaAlO_3$; in doing so, the Sr-O vacancy formation is viewed as an intermediate step. Is this planar defect configurational entropy then large enough to compensate for their enthalpic cost of formation (albeit low) and possibly for an increase in surface/interfacial energy?

Again, exact composition and structure of stable $SrLaAlO_4$ surfaces is unknown; it is thus impossible to precisely estimate the enthalpic cost of the stacking fault formation and the generation of a SrO-$SrLaAlO_4$ interface. However, as a reference for comparison, the dissociation enthalpy of $SrLaAlO_4$ into bulk SrO and bulk $LaAlO_3$ is calculated to be 0.28 eV per formula unit (Table 6.4); as expected this decomposition is much easier than into three unary oxides. This value is comparable to the entropy term, but of course the faults generate more than

one formula unit of $LaAlO_3$, so the fault entropy component appears to be insufficient to compensate for this enthalpic cost – and yet, the faults clearly do form.

What other factors favor this effective dissociation? One overlooked aspect is the fact that the generation of faults does not mean that all point defects are annihilated; on the contrary, the feasibility of the planar defects just opens up a second pathway for the accommodation of bulk non-stoichiometry. Some vacancies will remain, and their configurational entropy is certainly much larger than for the stacking faults. Similarly, one ought to recognize that the inverse RP faults are finite along the [100]-type directions, which implies that their configurational entropy is not limited to the <001> axis. However, this also means that there is strain to be relieved at the edges of the faults, which has the opposite effect. The bottom line, even though one cannot at present rigorously quantify it, is that the often-overlooked defect-related entropy of mixing is the only plausible explanation for the observed SrO migration to the surface.

6.4.4. $SrTiO_3$: SrO Surface Segregation

It should be noted that Sr-O vacancy pairs also constitute the lowest-energy point defect in strontium titanate [183], so the SrO surface segregation in $SrTiO_3$, as in $SrLaAlO_4$, is associated, at least initially, with the increasing number of bulk defects with extended high-temperature annealing.

However, the significant Sr/SrO enrichment at $SrTiO_3$(001) surfaces at relatively low temperatures (under 1000 ºC), as reported most notably by Szot *et al.* and Horvath *et al.* [164, 172], is much less plausible, as the thermal energy is much smaller than the bulk diffusion activation barrier to be expected in a densely-packed system; the possibility of these samples

being originally SrO rich cannot be discounted. It must be noted that surface features convincingly attributable to rocksalt SrO do not appear in the literature at annealing temperatures below ~1100 ºC and even in this case, very long anneals (1 day or more) are required. The consensus in the literature, as mentioned above, indicates that $SrTiO_3$(001) surfaces stabilize upon relatively short anneals below ~1100 ºC by becoming Ti-rich. This regime will be revisited later.

Let us turn now to the simplified Szot mechanism, which, much like the experimental observations in $SrLaAlO_4$, describes the decomposition of $SrTiO_3$ into surface SrO and bulk stacking faults arising from the dismantling of (001) SrO planes; in this scheme, as described above, the result is a thin region of TiO_2 at each fault. Unlike the case of $SrLaAlO_4$, some modeling of the surface structures and of the TCS fault formation enthalpy is available. Although SrO segregation in this material is reported to take the form of surface islands (and not homogeneous coverage of many bulk-like layers), it is seen from Table 6.2 that the enthalpic cost of this mechanism balloons up with an increasing amount of surface SrO, as it requires more and more costly TCS faults; this is important considering that the reported islands are generally large, routinely reach characteristic dimensions in the micrometer scale.

The aforementioned calculation, however, omits the total change in free energy due to the configurational entropy component from the TCS faults. This contribution can be estimated, as outlined above for faults in $SrLaAlO_4$, adjusting only for the number of available fault sites in the perovskite structure. If one takes, for example, the case of 5 TCS faults (L = 3), the entropy term for a (fairly large) single crystal thickness of 1 mm at 1300 ºC is roughly –9.35 eV. This does not compensate for the 7.69 eV enthalpic cost, which is comparatively much larger as it is on a per 1×1 slab basis. As it stands, the simplified Szot mechanism is simply not viable.

Of course, as in $SrLaAlO_4$, not all SrO bulk deficiency must be compensated by planar faults. Vacancies would complement the TCS faults, and they will provide a sizable entropy contribution, as would finite TCS faults. However, the disparity is larger than in $SrLaAlO_4$ and it is hard to believe that this can make up for the high energy associated to the TCS faults. In the end, the anatase-like stacking, embedded in a perovskite matrix, is too strained to stabilize the bulk.

6.4.5. $SrTiO_3$: DL+RP Mechanism

Let us now examine the DL+RP mechanism, a hypothetical explanation for the recurring observation of a number of TiO_2-rich DL reconstructions. This scheme is also based on the formation of bulk planar defects, although now these are Ruddlesden-Popper faults. From a purely enthalpic approach, it can be seen from Table 6.2 that a stoichiometric crystal with ~~–z~~igzag"-2×2-reconstructed surfaces and 3 RP faults is less favorable that a fault-free crystal with equal fractions of SrO and TiO_2 bulk-like surface terminations, by 1.62 eV/1×1 slab.

Once more, one can resort to the fault configurational entropy. At 950 ºC, the typical annealing temperature for DL reconstructions (see Chapter 5), 3 RP faults within a typical TEM sample thickness of 100 nm corresponds to an entropy term of –1.56 eV. Again, one must remark that this value is independent of the slab volume. A realistic crystal will be much larger than a 1×1 slab, so (even though the entropic gain does increase with thickness) this in itself will be dwarfed by the overall enthalpic cost. Yet again, one could try to invoke additional configurational entropy due to point defects and finite faults; after all, the difference is not as insurmountable as for the simplified Szot mechanism.

However, this is where this hypothetical process fails. First, the amount of TiO_2 surface enrichment is rather low, at 1.5 excess ML, which means that in principle the bulk non-stoichiometry should be easily compensated for with only point defects. Second, the entropic argument implies that the amount of surface enrichment ought to be thickness-dependent. Most importantly, one ought to recall that Sr-O vacancy pairs are more favorable Schottky-type defects than Ti-based vacancy complexes, so there is no reason to expect TiO_2 to surface segregate like SrO does in $SrLaAlO_4$.

It must also be mentioned that TEM micrographs of (001)-oriented $SrTiO_3$ samples, annealed in the 900-1100 ºC range by, exhibit no discernible RP faults. TEM images from similar samples prepared by Dr. James Enterkin were also inspected, again with no evidence of bulk planar faults.

6.4.6. $SrTiO_3$ High-Temperature Stabilization

So what does happen upon annealing of $SrTiO_3$? At high temperatures, typically above ~1300 ºC, some SrO segregation should occur, although presumably not as much as in $SrLaAlO_4$, given the lack of an additional bulk stabilization mechanism beyond point defects alone. TCS faults are unfavorable and should not be expected to form.

For large TiO_2 excess in $SrTiO_3$, reduced $TiO_{x<2}$ Magnéli phases have been observed to precipitate out under reducing conditions [184], but this is unviable under oxidizing conditions, since this requires a permanent release of O. More likely, the migration of SrO will be capped by the solubility of Sr-O vacancy pairs so the bulk will never be severely TiO_2 rich. If it does, however, it is likely that rutile TiO_2 (rather than anatase-like faults) will precipitate, although the perovskite matrix does not easily accommodate for this.

It should be recalled that one last component of the original, extended mechanism described by Szot *et al.* [159, 160] is the formation of RP phases in the subsurface, largely as an intermediate accommodation for the excess Sr and O in the region, on its way to the surface. As mentioned in subsection 6.3.1, several authors interpret certain measured step heights close to c_{RP} lattice constants as evidence of RP phases. However, there are three issues with this. First, most of these are similarly close to multiples of $a_{\mathrm{SrTiO_3}}$. Second, any (001) plane within a RP phase is equivalent to the plane half a unit cell away, which means that if steps match the unit cell of an RP phase, steps half as large should also be observed. Finally, and this is especially true for higher-order RP phases, several (001) truncations should have very comparable stabilities [64], so again multiple step heights should be measured. While it cannot be ruled out that some would form, since they are indeed favorable defect, Meyer *et al.* [169] actively looked for RP faults (near the surface and in the vicinity of SrO islands) and found none.

6.4.7. Fault Non-Stoichiometry Compensation in Metal Oxides

SrO surface segregates in both materials studied here, but while planar faults form in SrO-poor $SrLaAlO_4$, they do not in $SrTiO_3$. Can one predict which oxides will exhibit this non-stoichiometry accommodation mechanism? A useful metric is the standard heat of dissociation of a metal oxide into simpler oxides, since this effectively represents what would be observed. Some examples are shown in Table 6.4, with values in eV per formula unit. It is found that the decomposition of $SrTiO_3$ into SrO and TiO_2 is much more unfavorable than that of $SrLaAlO_4$ into SrO and $LaAlO_3$, so it is not surprising that TCS faults are much more unfavorable than inverse RP faults.

What about Sr_2TiO_4, the n = 1 RP phase, which shares the K_2NiF_4 structure with $SrLaAlO_4$? Experimental measurements point to its dissociation into SrO and $SrTiO_3$ being actually less endothermic than the $SrLaAlO_4$ decomposition, so an annealed Sr_2TiO_4 is very likely to exhibit inverse RP faults and SrO surface segregation; indeed, Sr-O vacancy pairs should again be the dominant Schottky defect in the bulk. More generally, one can predict that oxides with intergrowth structures will compensate for the bulk depletion of one of its components via planar faults, since in essence all the bulk does is to locally lose the intergrowth. In this example, the loss of rocksalt material in a rocksalt/perovskite intergrowth is easily accommodated by a local perovskite region.

Can one look at another perovskite system, to compare to $SrTiO_3$? One natural choice would be the aforementioned $LaAlO_3$ system. However, these cations have 3+ formal valence and do not form rocksalt or anatase-like unary oxides. While one could speculate on which species would surface segregate, it is clear that (001) planar fault compensation would not be feasible.

Table 6.4. Standard heat of dissociation into simpler oxides, calculated from thermodynamic data [185-188].

	ΔH^0 (eV)	ΔG^0 (eV)
$SrLaAlO_4 \rightarrow SrO + LaAlO_3$	0.28	0.29*
$SrLaAlO_4 \rightarrow SrO + ½\ La_2O_3 + ½\ Al_2O_3$	1.00	1.00
$SrTiO_3 \rightarrow SrO + TiO_2$	1.41	1.43
$Sr_2TiO_4 \rightarrow SrO + SrTiO_3$	0.24	0.25

*$LaGaO_3$ standard entropy of formation from oxides used as estimate for $LaAlO_3$.

6.4.8. $SrTiO_3$(001) DL Reconstructions

The question of what drives the TiO_2 surface enrichment required for (001) DL reconstructions remains. Certainly, this is not due to TiO_2 surface segregation driven by an induced increase in Ti-O Schottky defects with temperature, stabilized in the bulk by RP faults, as discussed above. No conclusive answers are available here, but some ideas are worth reviewing.

In his doctoral dissertation [104], Enterkin speculated that higher annealing temperatures (under oxidizing conditions) or extended dwelling times led to larger surface TiO_2 content, after observing the less TiO_2-rich $(\sqrt{13}\times\sqrt{13})R33.7^\circ$ reconstruction as an intermediate surface en route to forming the 2×1 DL structure. However, no specific mechanism was proposed.

One other possibility is that the surface/subsurface area is SrO-poor as a result of sublimation phenomena, and that therefore the DL reconstructions are only a result of the TiO_2 richness. One must refer back to the literature, where sublimation-based arguments have been used to explain Sr surface *enrichment*, not depletion. Liang and Bonnell [161, 163] speculated that their observation of Sr-rich $SrTiO_3$ surfaces was partially due to Ti sublimation, arguing that Ti atoms are less strongly bound than Sr. On the other hand Szot *et al.* [159] argued the opposite, while also observing Sr/SrO-rich surfaces. At 1000 ºC, they claimed to detect a mass loss of 0.05% in 1 atm of O_2 via thermogravimetrical measurements. They further analyzed with fluorescence spectroscopy the material deposited opposite to the sample surface and identified it as mostly Sr, and attributing this to either pure Sr or its oxides. Szot *et al.* contend that this sublimation is one of the main driving forces for the $SrTiO_3$ decomposition, implying that the SrO migration to the surface was merely an intermediate step en route to full evaporation. However, the vapor pressure of SrO in air has been estimated [189] to be $\sim 10^{-15}$ Torr at 1000 ºC

(and Sr is much lower), which means said claims are implausible and that the role of sublimation is negligible.

One fact is that the multiple TiO_2 surface layers allow for much flexibility in the structural arrangement, as evidenced by the number of DL reconstructions; qualitatively, the only difference lies in the surface Ti positions. This enables many structures of higher stability than the ~~–2~~Ti" stacking of bulk-like TiO_2 layers (essentially a surface TCS fault). In contrast, no such flexibility exists with multiple layers of SrO: within each 1×1 cell, there is only one sensible site to place one Sr and one O atom. Naturally, this option is not available with bulk-like truncations either. Finally, while the same flexibility exists in, say, a triple-layer TiO_2 surface, it likely requires a high-energy TCS-like fault beneath the topmost layer.

6.5. Conclusions

Electron microscopy techniques and elemental microanalysis have demonstrated the preferential segregation of Sr and O at $SrLaAlO_4$ surfaces upon high-temperature annealing under oxidizing conditions, forming strontium oxide islands. This phenomenon is initially due to the increased configurational entropy of low-energy point defects but is ultimately enhanced by the easy accommodation for SrO loss in the bulk. The compensation mechanism for the large bulk non-stoichiometry consists predominantly of disordered inverse Ruddlesden-Popper faults. The dismantling of Sr-rich (001) layers results in crystallographic shear planes which in turn generate plausibly stable local structures such as perovskite-like $LaAlO_3$. Surface segregation and bulk stacking faults have not been directly observed as a coupled system in the past, which opens up a new channel for stabilization that may occur in other material systems.

SrO surface segregation in $SrTiO_3$, while less definitive than in $SrLaAlO_4$, is only plausible for very high annealing temperatures. In this chapter, the concepts of configurational entropy and stacking fault formation were employed to test the viability of similar non-stoichiometry accommodation mechanisms in bulk $SrTiO_3$, such as the formation of TCS faults to compensate for the SrO migration to the surface. This was found to be unrealistic through first-principles computations. The hypothesis that TiO_2-rich DL reconstructions may be explained through the generation of SrO-rich RP faults in the bulk was similarly refuted. More generally, one must infer that intergrowth structures are most likely to exploit fault-based accommodation mechanisms to compensate for bulk non-stoichiometry.

Conclusions are not always pleasant.
Helen Keller

Chapter 7. Conclusions and Future Directions

7.1. Periodic Reconstruction

Numerous structural models for $SrTiO_3$(001) periodic surface reconstructions which have been proposed in the literature have been tested. These models have been evaluated as alternatives to the family of double TiO_2 layer (DL) models supported by electron and X-ray diffraction. These notably include surface structures based on the periodic arrangement of Sr adatoms or oxygen vacancies, among others. The obvious appeal of these models is that they require less drastic atomic redistribution than do the DL surfaces.

However, these proposals fail on several counts and can be discarded; this provides further support for the air-stable, valence-neutral DL reconstruction models. The latter are not only derived from experimental results, but also yield reasonable bonding and good match to experimental scanning tunneling microscopy (STM) images, as determined from a first-principles simulation approach.

While the family of Sr-adatom models successfully reproduces the observed STM micrographs, it has several shortcomings. First, the bonding is highly questionable, as exemplified by the severe undercoordination of the Sr adatoms in the model for the 2×1 reconstruction. Second, most surface reconstructions have been shown to be air-stable, which these models clearly are not. Finally, the degree of reduction associated to the formation of these surfaces is highly unstable in practical conditions, as confirmed theoretically [83]; the small range of adatom density with any sort of stability window likely requires annealing in close proximity to a Sr or SrO source, which has never been part of the experimental treatment leading to the periodic reconstructions. Other structural models are similarly unsuccessful.

Two particular reconstructions are somewhat problematic. First, the (√5×√5)R26.6º or RT5 surface. No diffraction experiments have been carried out on this surface, which would be of great use and should be a target for future work. Based on the stability of the polyhedral quartet feature which characterizes the c(4×2) DL structure (see next section), a plausible RT5 structure using said motif was devised. This structure is not strictly a DL model, as it incorporates one Sr atom per surface cell to preserve the valence neutrality, but it does yield plausible bonding. However, it failed to reproduce the observation that the RT5 reconstruction can be imaged by STM at low bias voltages. Therefore, the atomic-scale structural solution for this reconstruction remains elusive. Future attempts (in the absence of diffraction data) should include a structure analogous to the solution recently found for the (√13×√13)R33.7º by Kienzle *et al.* [92], which is also TiO_2-rich.

The one DL model that is unsatisfactory is the 2×1 structure, ironically the first such model. Despite being supported by electron and X-ray diffraction data, it has an anomalously high surface energy and poor surface bonding; these attributes are largely associated to its

characteristic ―dangling" O atom. Moreover, STM observations strongly suggest that the ―brickwork" c(4×4) reconstruction that evolves from the 2×1 is structurally similar to it, but it is hard to devise a strictly DL model without further reducing the surface stability. This point will be revisited as the results of the water adsorption modeling are reviewed.

7.2. Recurrent Structural Motifs

A combination of experimental and simulated STM images, Auger electron spectroscopy (AES), X-ray photoelectron spectroscopy (XPS) and bonding analysis has been used to decipher the structure of the $SrTiO_3$(001) dilines and trilines, and in doing so the recurrence of certain patterns across several stable surface structures has been revealed.

First, the distinctive structural motif of the c(4×2) DL surface reconstruction is found not only in one of the ―square" 2×2 structures (as determined by Lin *et al.* [55]), but also within the nanolines; this is a testament to its local stability. The quartet of TiO_5 surface polyhedra gives rise to the characteristic bright STM spots in the diline structure, which is reasonable since the nanolines coexist with, and evolve from, a c(4×2)-reconstructed surface. This feature is likely to be observed in other surface reconstructions and in other alkali earth titanates. Also, in the context of glass-like tiling of TiO_5 surface polyhedra, which may form and subsist for long periods of time, the quartet motif should be one of the dominant local structures

Unlike the DL structures, dilines consist of three TiO_x surface layers, which is consistent with AES measurements. Meanwhile, trilines build on the diline structure, adding a ―backbone" between the rows of c(4×2)-like features. The backbone consists of a checkerboard-like Ti/O arrangement on the topmost layer. This produces an effectively reduced surface, with certain surface Ti sites approaching a formal 2+ valence state, consistent with the appearance of ―Ti^{2+}"

XPS shoulders. Like the c(4×2) quartet motif, this backbone structure produces an array of TiO_5 surface polyhedra. Moreover, each polyhedron is in an edge-sharing configuration with at least two other surface polyhedra, which is a pattern shared not only with the c(4×2) surface, but with all observed DL structures. This architecture is an efficient way to stabilize a TiO_2-rich surface: the surface Ti are coordinated to 5 oxygen atoms, and the surface O are coordinated to at least two Ti atoms. Again, the lone exception among the DL structures is the 2×1, which is complemented by a different stabilization mechanism (see below).

Simulated STM images were also used to decipher the structure of a characteristic triline backbone defect, which was found to consist of three O vacancies and four relocated Ti atoms. Its diffusion mechanism is clearly complicated, but this is consistent with its large diffusion activation barrier, as computed from experimental STM observation.

7.3. Water Adsorption

Through density functional theory (DFT) computations, DFT-based STM image simulations and bonding analysis, the importance of water adsorption (a frequently-overlooked phenomenon) on the stabilization of strontium titanate (001) surfaces has been demonstrated. It becomes clear that H_2O does not require surface defects to chemisorb, as it will do so readily even on fully-oxidized, valence-neutral reconstructions. This conclusion is believed to be applicable not only to other, less stable surface orientations, but to a very broad range of metal oxides (and likely to other adsorbate species).

It is clear that water plays two major stabilization roles and the $SrTiO_3$(001) family of DL surface reconstructions provides good examples. First, it may be incorporated in the stable

structures themselves, even in models determined from diffraction data, since light atoms are very weak scatterers. This is the case for the 2×1 surface: the addition of dissociatively chemisorbed water on this structure, particularly at half-monolayer coverage, resolves all the concerns engendered by the bare, strictly DL model. In this configuration, a hydroxyl group adsorbs on each severely underbonded surface Ti atom, while a lone H atom caps every "dangling" oxygen atom. This architecture lowers the surface energy of the 2×1 reconstruction significantly, rendering it comparable to all other DL models. Also, the hydrated model produces simulated STM images which are more consistent with experiment than the dry DL surface. Additionally, the revised structure supplies a natural structural model for the "brickwork" c(4×4) reconstruction, based on a simple process of partial dehydration. This model also succeeds in reproducing its corresponding experimental STM image. Finally, complementary XPS data from a collaborator [104] confirms that the $SrTiO_3$(001) 2×1 surface is hydroxylated and remains so at high temperatures.

The other role played by water is one of mediation. The characteristic example in this case is the (√2×√2)R45º ("RT2") DL structure, which is predicted to be the most stable of all bare DL models but has yet to be observed experimentally. However, this defining trait vanishes upon incorporation of adsorbed water: at half- and full-monolayer water coverage, the RT2 periodicity is no longer favored and in essence most reconstructions become energetically degenerate. This is related to the fact that the surface Ti in the DL RT2 structure are more shielded (less exposed) than in other DL surfaces, which requires larger displacement of the surface O. Ultimately, one must refer back to the typical experimental sample preparation stages. Without exception, these produce defective surfaces, so much chemisorbed water is part of the initial state. Upon annealing, a competition between dehydration and ordering processes

ensues; however, as long as the surface is not fully ordered, strong water adsorption sites remain. Since the adsorbed water (and derivatives) are much more mobile that heavier cations, the –wet" kinetics must dominate. Therefore, the dry thermodynamics are not as relevant as one might naïvely presume at first. In this context, it is clear that while the formation of other DL reconstructions is water-mediated, the RT2 is a kinetically inaccessible structure.

A fair question is whether or not the two functions are one and the same. That is, could all DL surfaces be always hydrated, such that dry DL structures are never the end product? This can be addressed again by referring to the XPS results from a collaborator [104]. It was indeed seen that the c(4×2) surface displayed O–H bonding, but this disappears fully upon annealing in the 300-400 ºC temperature range, and the reconstruction subsists thereafter. Hence, some bare DL models are attainable. In particular, the –zigzag" 2×2 should be, as it exhibits energy and bonding very similar to the c(4×2).

7.4. Surface Segregation

No periodic reconstruction was observed on strontium lanthanum aluminate (001) surfaces upon annealing in the temperature range typically used for materials such as $SrTiO_3$. This is likely related to the additional disorder in this oxide due to the shared occupancy of the 9-fold coordination site by Sr and La. Much like the idea of glass-like surfaces in $SrTiO_3$(001) surfaces [92], it is likely that a wide range of local structures with comparable energy coexist in a disordered fashion on $SrLaAlO_4$(001) surfaces. Future studies on this surface should attempt much longer anneals (the dwelling time in this case was typically 6 hours) at 900-1100 ºC, as this may eventually lead to an ordered surface.

At higher temperatures, which allow for significant bulk diffusion, segregation of rocksalt SrO occurs at the surfaces of single-crystalline $SrLaAlO_4$, as determined via a combination of high-resolution transmission electron microscopy (HREM), scanning electron microscopy and elemental analysis. The surfaces were not uniformly covered by SrO, which instead formed surface precipitates. This allows us to discard the possibility of the segregation being induced by a drive to lower the surface energy.

Instead, the strontium oxide segregation is at first due to the increased configurational entropy of the dominant bulk defect, which in this case is a Sr-O vacancy pair. As the number of vacancies rises, the displaced atoms can only go to the surface. The solubility of bulk vacancies in $SrLaAlO_4$ is small, but further segregation is enabled in this material due to a low-energy stacking-fault-based mechanism for non-stoichiometry compensation. In this process, vacancies agglomerate and gradually dismantle SrO (001) layers, which allows for the annihilation of vacancies through an easy crystallographic shear. This produces thin layers of essentially perovskite-like $LaAlO_3$, so these stacking faults are highly stable, while still providing significant configurational entropy. Indeed, the detection of SrO surface enrichment coincides with the observation, via HREM, of planar defects displaying lattice fringe shifts (with respect to the main matrix) consistent with these faults. Clearly, then, the observed segregation phenomenon is not actually a surface stabilization mechanism; segregation is fully expected to take place, for example, at grain boundaries in polycrystalline samples.

Interestingly, a similar decomposition mechanism has been proposed [159] to explain the observed SrO surface enrichment in $SrTiO_3$, although the claims of such segregation in strontium titanate are often self-contradictory and the evidence tenuous. Nonetheless, low levels of SrO segregation are certainly feasible and to be expected at high temperatures, since Sr-O vacancy

pairs are also the prevailing bulk defects in this material. However, analogous stacking fault stabilization is unviable, so less SrO segregation than in $SrLaAlO_4$ should be observed. The high energy of such faults arises because the removal of SrO layers in $SrTiO_3$ produces a heavily constrained region of consecutive TiO_2 layers. This stacking is similar to that along the anatase <001> axis, but in said material there is significant rumpling and lattice relaxation (with respect to the bulk-like TiO_2 layers in $SrTiO_3$).

One important question that remains regarding the DL surface reconstructions in $SrTiO_3$ is: what gives rise to this degree of TiO_2 surface richness? An interesting idea has been tested, based on a similar fault-based non-stoichiometry compensation mechanism. In this process, instead of dismantling SrO layers, TiO_2 layer would be removed and this material would migrate to the surface; this would create bulk stacking faults known as Ruddlesden-Popper faults, which are regularly seen in SrO-rich $SrTiO_3$. However, this process is also unrealistic: the configurational entropy is unlikely to compensate for the enthalpic cost of the faults and, once again, Ti-based vacancy complexes are not the dominant bulk defect, so the rise in temperature does not favor the migration of titanium. While this idea was worth exploring, it does not explain the TiO_2 surface enrichment necessary in DL surfaces.

Ultimately, the fault-based non-stoichiometry accommodation mechanism seen in $SrLaAlO_4$ is expected to be available for any intergrowth oxide, since the faults simply consist of the local removal of intergrown layers. This could be tested easily in other oxides of K_2NiF_4 or other intergrowth structures.

7.5. Scanning Tunneling Microscopy Simulations

A central component of the work presented in this work has been the use of DFT-based simulations of STM images. While this is described in 2.2.3 (and in more detail in Appendix A), it is important to discuss some of the limitations inherent to the approach used. The most obvious simplification in the method is that the electronic structure of the tip is not incorporated. While this is also true for the popular low-bias Tersoff-Hamann approximation, this may be significant. It is clear from Fig. 2.3 that if the tunneling depends on the local density of unoccupied sample states, it should also be roughly proportional to density of occupied tip states in the energy interval from $E_F^{\text{tip}} - e{\cdot}V_\text{b}$ to E_F^{tip}. The variation in the DOS in this range is likely to be larger when V_b is large, as it is in the experiments simulated. One way to address this would be to model the tungsten tip through an idealized geometry and add another multiplicative term to the calculation of the tunneling current. Instead of Eq. 2.7, the current would follow the following relation:

$$I_\text{t} \propto \int_0^{e\cdot V_\text{b}} \kappa(E_\text{F}+\varepsilon)^{-2}\,\rho(\boldsymbol{r}, E_\text{F}+\varepsilon)\rho^{\text{tip}}\left(\boldsymbol{r}, E_F^{\text{tip}} - e{\cdot}V_\text{b} + \varepsilon\right) d\varepsilon\,. \qquad \text{(Eq. 2.7)}$$

A related issue is that the tip-states are restricted to the radially-symmetric s-type states. The contribution of higher angular states should be increasingly significant when attempting to resolve smaller and smaller features. The difficulty with this is that while s-type states lead to terms proportional to the squared magnitude of the wavefunction (that is, the density), higher-order states invoke the squared magnitude of spatial wavefunction derivatives and double derivatives (and so on), which must in turn be adequately weighted. This can be done, in principle, but this is clearly a case of diminishing returns. Also, one must recognize that the

electronic structure of the tip is largely independent of the tip position as it is rastered across the surface, but the sample electronic structure is not and is therefore be dominant source of contrast in STM images. Changes in tip sharpness, shape or material are also generally ignored, except for the blurring parameter. Also, contact interactions of the tip with sample, including adsorbates, is not modeled.

It must be noted that other approaches to high-bias STM tunneling theory incorporate the tip-sample distance explicitly, using the expected exponential wavefunction decay into vacuum; see, for example, Ref. [190]. However, this quantity is hard to define and is, indirectly, what is being determined in constant-current STM mode. In the approach used in this work, the density decay into vacuum is implicitly accounted for, although the variation in the tunneling barrier width as a function of out-of-plane position may have some non-negligible effect.

7.6. Future Research

There exist several general extensions to the work presented here, other than the modest, specific proposals interspersed in the preceding subsections. One major point of emphasis should be the reproducibility of surface structure formation. For example, it is not unfair to say (in a tongue-in-cheek way) that at present the surface reconstruction formed on a $SrTiO_3$(001) sample is as dependent on the graduate student carrying out the sample preparation as on the annealing parameters. Different researchers observe very different surface traits under very similar conditions, as can be clearly seen from the muddled literature reviews in section 3.2 and subsection 6.3.1. Even within our research group, two samples annealed simultaneously and in close proximity have been observed to give rise to different surface periodicities. Clearly, the

exact details of sample preparation are quite important, presumably due to the varying degree of damage induced by the ion beam milling stage. Good control of the processing steps, which should clearly include parameters such as humidity or water vapor partial pressure (as demonstrated in Chapter 5), is indispensable. Without such control, long-term hopes of predictive rules and application-specific structure tailoring are unrealistic.

One important target should be to gradually move into less convenient, but more realistic systems. For catalytic applications, for example, surface area must be maximized, so nanoparticles are routinely used, not large monocrystals. It is reasonable to ask whether the structures observed in single-crystalline samples (e.g. DL periodic reconstructions) are also readily formed at the nanoscale. Indeed, there is ongoing work with well-controlled $SrTiO_3$ nanocuboids [191, 192] attempting to determine whether and how the surface structure is different.

Related to this point is the need to link the surface structure to performance in practical applications. Regarding heterogeneous catalysis, for instance, quantification of the catalytic activity and selectivity in specific chemical reactions should be performed. This could be done with single-crystalline samples, to allow for easier control over the surface structure. However, the answers to the previous two issues are also crucial here.

Finally, given that $SrTiO_3$ has been used as a model system, other perovskite surfaces should be examined to determine how general the findings in strontium titanate are. A system like $LaAlO_3$, where the cations have 3+ formal valence, shows (001) surface structures unseen in $SrTiO_3$ [155], which is unsurprising since the (001) planes are not valence-neutral. More relevant cases would be other members of the 2+/4+ perovskite family. For example, it has been predicted that the formation of Ruddlesden-Popper phases is more favorable in $BaTiO_3$ than in

$SrTiO_3$ [60]; does this influence the segregation behavior at high temperatures? What about a material like $CaTiO_3$, where the lighter A-site cation may show larger diffusivity?

Calcium brings about another subject: Ca impurities have been speculatively linked to the suppression of DL reconstructions [94], which may be related to the reproducibility issue mentioned above. This should be investigated further, by examining the (001) surface following controlled substitutional Ca-doping of $SrTiO_3$ or by simply testing whether these structures form in pure $CaTiO_3$. Similarly, a theoretical study of $SrTiO_3$, $BaTiO_3$, $SrZrO_3$ and $BaZrO_3$ (001) surfaces predicts that the DL reconstructions are thermodynamically stable among the titanates but not among the zirconates [97]; this can also be tested by reproducing the processing steps used in the $SrTiO_3$. In relation to this, water adsorption has been modeled and compared for both $SrTiO_3$ and $SrZrO_3$ (001) surfaces, but using bulk-like truncations only [126]. It would be productive to carry out further DFT modeling to test whether the DL reconstructions are stabilized in $SrZrO_3$ by water.

References

[1] A.T. Bell. "The impact of nanoscience on heterogeneous catalysis." *Science* 299: 1688-1691 (2003).

[2] C. Noguera. "Polar oxide surfaces." *J. Phys.: Condens. Matter* 12: R367-R410 (2000).

[3] P. Chaudhari, R. Koch, R. Laibowitz, T. McGuire, R. Gambino. "Critical-Current Measurements in Epitaxial Films of $YBa_2Cu_3O_{7-x}$ Compound." *Phys. Rev. Lett.* 58: 2684-2686 (1987).

[4] X.D. Qi, M. Wei, Y. Lin, Q.X. Jia, D. Zhi, J. Dho, M.G. Blamire, J.L. MacManus-Driscoll. "High-resolution x-ray diffraction and transmission electron microscopy of multiferroic $BiFeO_3$ films." *Appl. Phys. Lett.* 86: (2005).

[5] C. Aruta*, et al.* "Structure of superconducting $(BaCuO_x)_2/(CaCuO_2)_n$ superlattices on $SrTiO_3(001)$ investigated by X-ray scattering." *Physica Status Solidi A* 183: 353-364 (2001).

[6] J.A. Enterkin, W. Setthapun, J.W. Elam, S.T. Christensen, F.A. Rabuffetti, L.D. Marks, P.C. Stair, K.R. Poeppelmeier, C.L. Marshall. "Propane oxidation over $Pt/SrTiO_3$ nanocuboids." *ACS Catalysis* 1: 629-635 (2011).

[7] J.A. Enterkin, K.R. Poeppelmeier, L.D. Marks. "Oriented catalytic platinum nanoparticles on high surface area strontium titanate nanocubes." *Nano Lett.* 11: 993-997. (2011).

[8] A. Kudo, Y. Miseki. "Heterogeneous photocatalyst materials for water splitting." *Chem. Soc. Rev.* 38: 253-278 (2009).

[9] J.G. Mavroides, J.A. Kafalas, D.F. Kolesar. "Photoelectrolysis of water in cells with $SrTiO_3$ anodes." *Appl. Phys. Lett.* 28: 241-243 (1976).

[10] M.S. Wrighton, A.B. Ellis, P.T. Wolczanski, D.L. Morse, H.B. Abrahamson, D.S. Ginley. "Strontium-Titanate Photoelectrodes - Efficient Photoassisted Electrolysis of Water at Zero Applied Potential." *J. Am. Chem. Soc.* 98: 2774-2779 (1976).

[11] T. Puangpetch, T. Sreethawong, S. Yoshikawa, S. Chavadej. "Hydrogen production from photocatalytic water splitting over mesoporous-assembled $SrTiO_3$ nanocrystal-based photocatalysts." *J. Mol Catal. A-Chem.* 312: 97-106 (2009).

[12] J. Yin, J.H. Ye, Z.G. Zou. "Enhanced photoelectrolysis of water with photoanode Nb:$SrTiO_3$." *Appl. Phys. Lett.* 85: 689-691 (2004).

[13] D.W. Reagor, V.Y. Butko. "Highly conductive nanolayers on strontium titanate produced by preferential ion-beam etching." *Nature Materials* 4: 593-596 (2005).

[14] A.F. Santander-Syro*, et al.* "Two-dimensional electron gas with universal subbands at the surface of $SrTiO_3$." *Nature* 469: 189-193 (2011).

[15] W. Meevasana, P.D.C. King, R.H. He, S.K. Mo, M. Hashimoto, A. Tamai, P. Songsiriritthigul, F. Baumberger, Z.X. Shen. "Creation and control of a two-dimensional electron liquid at the bare $SrTiO_3$ surface." *Nature Materials* 10: 114-118 (2011).

[16] A. Ohtomo, H.Y. Hwang. "A high-mobility electron gas at the $LaAlO_3/SrTiO_3$ heterointerface." *Nature* 427: 423-426 (2004).

[17] C. Cen, S. Theil, J. Mannhard, J. Levy. "Oxide Nanoelectronics on Demand." *Science* 323: 1026-1030 (2009).

[18] R.A. McKee, F.J. Walker, M.F. Chisholm. "Crystalline oxides on silicon: The first five monolayers." *Physical Review Letters* 81: 3014-3017 (1998).

[19] R.A. McKee, F.J. Walker, M.F. Chisholm. "Physical structure and inversion charge at a semiconductor interface with a crystalline oxide." *Science* 293: 468-471 (2001).

[20] B.M. Kim, T. Brintlinger, E. Cobas, M.S. Fuhrer, H.M. Zheng, Z. Yu, R. Droopad, J. Ramdani, K. Eisenbeiser. "High-performance carbon nanotube transistors on $SrTiO_3$/Si substrates." *Appl. Phys. Lett.* 84: 1946-1948 (2004).

[21] K. Pennicott. "Semiconductors - GaAs meets its match." *Physics World* 14: 6-6 (2001).

[22] R. Droopad*, et al.*, in: M. Ilegems, G. Weimann, J. Wagner (Eds.), Compound Semiconductors 2002, pp. 1-8 (2003).

[23] Y. Liang, J. Kulik, T.C. Eschrich, R. Droopad, Z. Yu, P. Maniar. "Hetero-epitaxy of perovskite oxides on GaAs(001) by molecular beam epitaxy." *Appl. Phys. Lett.* 85: 1217-1219 (2004).

[24] D.S. Deak, F. Silly, K. Porfyrakis, M.R. Castell. "Template ordered open-grid arrays of paired endohedral fullerenes." *J. Am. Chem. Soc.* 128: 13976-13977 (2006).

[25] D.S. Deak, F. Silly, K. Porfyrakis, M.R. Castell. "Controlled surface ordering of endohedral fullerenes with a $SrTiO_3$ template." *Nanotechnology* 18: (2007).

[26] T. Hara, T. Ishiguro, N. Wakiya, K. Shinozaki. "Oxygen Sensing Properties of $SrTiO_3$ Thin Films." *Japanese Journal of Applied Physics* 47: 7486-7489 (2008).

[27] Y.L. Hu, H., D. Liu, Q. Zhao, P. Chang, J. Wu. "Low-temperature $SrTiO_3$ oxygen gas sensor for environment monitoring application." International Conference on Remote Sensing, Environment and Transportation Engineering, Nanjing, China, pp. 446-449 (2011).

[28] W. Menesklou, H.J. Schreiner, K.H. Hardtl, E. Ivers-Tiffee. "High temperature oxygen sensors based on doped $SrTiO_3$." *Sensors and Actuators B-Chemical* 59: 184-189 (1999).

[29] D.C. Johnson, A.L. Prieto. "Use of strontium titanate ($SrTiO_3$) as an anode material for lithium-ion batteries." *J. Power Sources* 196: 7736-7741 (2011).

[30] J.C. Ruiz-Morales, J. Canales-Vázquez, C. Savaniu, D. Marrero-López, W.Z. Zhou, J.T.S. Irvine. "Disruption of extended defects in solid oxide fuel cell anodes for methane oxidation." *Nature* 439: 568-571 (2006).

[31] O.A. Marina, N.L. Canfield, J.W. Stevenson. "Thermal, electrical, and electrocatalytical properties of lanthanum-doped strontium titanate." *Solid State Ionics* 149: 21-28 (2002).

[32] C. Kisielowski*, et al.* "Detection of Single Atoms and Buried Defects in Three Dimensions by Aberration-Corrected Electron Microscope with 0.5-Å Information Limit." *Microscopy and Microanalysis* 14: 469-477 (2008).

[33] L.D. Marks, D.J. Smith. "Direct surface imaging in small metal particles." *Nature* 303: 316-317 (1983).

[34] N. Erdman, K.R. Poeppelmeier, M. Asta, O. Warschkow, D.R. Ellis, L.D. Marks. "The structure and chemistry of the TiO_2-rich surface of $SrTiO_3$ (001)." *Nature* 419: 55-58 (2002).

[35] D.B. Williams, C.B. Carter. "Transmission Electron Microscopy: A Textbook for Materials Science." New York, Plenum Press (1996).

[36] T.J. Manning, W.R. Grow. "Inductively Coupled Plasma - Atomic Emission Spectrometry." *The Chemical Educator* 2: 1-19 (1997).

[37] A.M. Montaser, D.W. Golightly (Eds.). "Inductively Coupled Plasmas in Analytical Atomic Spectrometry." New York, VCH Publishers (1992).

[38] J.F. Moulder, W.F. Stickle, P.E. Sobol, K.D. Bomben. "Handbook of X-ray Photoelectron Spectroscopy." Eden Prairie, MN, Perkin-Elmer Corporation (1992).

[39] V.K. Lazarov, R. Plass, H.-C. Poon, D.K. Saldin, M. Weinert, S.A. Chambers, M. Gajdardziska-Josifovska. "Structure of the hydrogen-stabilized MgO(111)-(1×1) polar surface: Integrated experimental and theoretical studies." *Phys. Rev. B* 71: 115434 (2005).

[40] S. Yamamoto, H. Bluhm, K. Andersson, G. Ketteler, H. Ogasawara, M. Salmeron, A. Nilsson. "In situ x-ray photoelectron spectroscopy studies of water on metals and oxides at ambient conditions." *J. Phys.-Condens. Mat.* 20: (2008).

[41] H. Bluhm. "Photoelectron spectroscopy of surfaces under humid conditions." *J. Electron Spectrosc.* 177: 71-84 (2010).

[42] S.W. Knipe, J.R. Mycroft, A.R. Pratt, H.W. Nesbitt, G.M. Bancroff. "X-ray photoelectron spectroscopic study of water adsorption on iron sulphide minerals." *Geochim. Cosmochim. Ac.* 59: 1079-1090 (1995).

[43] C.J. Chen. "Introduction to Scanning Tunneling Microscopy." New York, Oxford University Press (1993).

[44] R. Armiento, A.E. Mattsson. "Functional designed to include surface effects in self-consistent density functional theory." *Physical Review B* 72: (2005).

[45] A.E. Mattsson, D.R. Jennison. "Computing accurate surface energies and the importance of electron self-energy in metal/metal-oxide adhesion." *Surface Science* 520: L611-L618 (2002).

[46] P. Blaha, K. Schwarz, G.K.H. Madsen, D. Kvasnicka, J. Luitz. "WIEN2k, An Augmented Plane Wave + Local Orbitals Program for Calculating Crystal Properties." Universität Wien, Austria (2010).

[47] A. Salinas-Sánchez, J.L. García-Muñoz, J. Rodríguez-Carvajal, R. Sáez-Puche, J.L. Martínez. "Structural characterization of R_2BaCuO_5 (R = Y, Lu, Yb, Tm, Er, Ho, Dy, Gd, Eu and Sm) oxides by X-ray and neutron diffraction." *J. Solid State Chem.* 100: 201-211 (1992).

[48] I.D. Brown. "Chemical and Steric Constraints in Inorganic Solids." *Acta Cryst. B-Stru.* 48: 553-572 (1992).

[49] J.A. Enterkin, A.E. Becerra-Toledo, K.R. Poeppelmeier, L.D. Marks. "A chemical approach to understanding oxide surfaces." *Surface Science, in press* (2011), doi:10.1016/j.susc.2011.10.018.

[50] J. Tersoff, D.R. Hamann. "Theory of the scanning tunneling microscope." *Phys. Rev. Lett.* 50: 1998-2001 (1983).

[51] T. Kubo, H. Nozoye. "Surface Structure of $SrTiO_3$(100)-($\sqrt{5}\times\sqrt{5}$)-R26.6°." *Phys. Rev. Lett.* 86: 1801-1804 (2001).

[52] T. Kubo, H. Nozoye. "Surface structure of $SrTiO_3$(100)." *Surface Science* 542: 177-191 (2003).

[53] K. Johnston, M.R. Castell, A.T. Paxton, M.W. Finnis. "$SrTiO_3$(001) 2×1 reconstructions: First-principles calculations of surface energy and atomic structure compared with scanning tunneling microscopy images." *Phys. Rev. B* 70: 085415 (2004).

[54] J.A. Enterkin, A.K. Subramanian, B.C. Russell, M.R. Castell, K.R. Poeppelmeier, L.D. Marks. "A homologous series of structures on the surface of $SrTiO_3$(110)." *Nature Materials* 9: 245-248 (2010).

[55] Y. Lin, A.E. Becerra-Toledo, F. Silly, K.R. Poeppelmeier, M.R. Castell, L.D. Marks. "The (2×2) reconstructions on the $SrTiO_3$ (001) surface: A combined scanning tunneling microscopy and density functional theory study." *Surface Science Letters* (2011).

[56] S.N. Ruddlesden, P. Popper. "New compounds of the K_2NiF_4 type." *Acta Cryst.* 10: 538-539 (1957).

[57] S.N. Ruddlesden, P. Popper. "The compound $Sr_3Ti_2O_7$ and its structure." *Acta Cryst.* 11: 54-55 (1958).

[58] M. McCoy, R.W. Grimes, W.E. Lee. "Phase stability and interfacial structures in the SrO–$SrTiO_3$ system." *Philos. Mag. A* 75: 833-846 (1997).

[59] C. Noguera. "Theoretical investigation of the Ruddlesden-Popper compounds $Sr_{n+1}Ti_nO_{3n+1}$ (n=1-3)." *Philos. Mag. Lett.* 80: 173-180 (2010).

[60] T. Suzuki, M. Fujitomo. "First-principles structural stability study of nonstoichiometry-related planar defects in $SrTiO_3$ and $BaTiO_3$." *J. Appl. Phys.* 89: 5622-5629 (2001).

[61] C.J. Fennie, K.M. Rabe. "Structural and dielectric properties of Sr_2TiO_4 from first principles." *Physical Review B* 68: (2003).

[62] O. Le Bacq, E. Salinas, A. Pisch, C. Bernard, A. Pasturel. "First-principles structural stability in the strontium–titanium–oxygen system." *Philos. Mag.* 86: 2283-2292 (2006).

[63] N.A. Benedek, C. Elsässer, M.W. Finnis. "First Principles Investigation of Polarisation at Interfaces in Multilayered Strontium Titanate." *J. Phys.: Conf. Ser.* 94: 012005 (2008).

[64] M. Zschornak, S. Gemming, E. Gutmann, T. Weissbach, H. Stoecker, T. Leisegang, T. Riedl, M. Traenkner, T. Gemming, D.C. Meyer. "Surface modeling and chemical solution deposition of $SrO(SrTiO_3)_n$ Ruddlesden-Popper phases." *Acta Materialia* 58: 4650-4659 (2010).

[65] R.J.D. Tilley. "Electron-Microscope Study of Perovskite-Related Oxides in Sr-Ti-O System." *J. Solid State Chem.* 21: 293-301 (1977).

[66] S. Sturm, A. Recnik, C. Scheu, M. Ceh. "Formation of Ruddlesden-Popper faults and polytype phases in SrO-doped $SrTiO_3$." *J. Mater. Res.* 15: 2131-2139 (2000).

[67] S. Sturm, A. Recnik, M. Ceh. "Nucleation and growth of planar faults in SrO-excess $SrTiO_3$." *J. Eur. Ceram. Soc.* 21: 2141-2144 (2001).

[68] S. Sturm, M. Shiojiri, M. Ceh. "Atomic-scale structural and compositional analyses of Ruddlesden-Popper planar faults in AO-excess $SrTiO_3$ (A = Sr^{2+}, Ca^{2+}, Ba^{2+}) ceramics." *J. Mater. Res.* 24: 2596-2604 (2009).

[69] W. Tian, X.Q. Pan, J.H. Haeni, D.G. Schlom. "Transmission electron microscopy study of n=1–5 $Sr_{n+1}Ti_nO_{3n+1}$ epitaxial thin films." *J. Mater. Res.* 16: 2013-2026 (2001).

[70] C.N.R. Rao, B. Raveau. "Transition Metal Oxides: Structure, Properties, and Synthesis of Ceramic Oxides." New York, Wiley-VCH (1998).

[71] T. Suzuki, Y. Nishi, M. Fujimoto. "Defect structure in homoepitaxial non-stoichiometric strontium titanate thin films." *Philos. Mag. A* 80: 621-637 (2000).

[72] M. Naito, H. Sato. "Reflection high-energy electron diffraction study on the $SrTiO_3$ surface-structure." *Physica C* 229: 1-11 (1994).

[73] Q.D. Jiang, J. Zegenhagen. "$SrTiO_3$(001) surfaces and growth of ultra-thin $GdBa_2Cu_3O_{7-x}$ films studied by LEED/AES and UHV STM." *Surface Science* 338: L882-L888 (1995).

[74] Q.D. Jiang, J. Zegenhagen. "$SrTiO_3$(001)-c(6×2): A long-range, atomically ordered surface stable in oxygen and ambient air." *Surface Science* 367: L42-L46 (1996).

[75] Q.D. Jiang, J. Zegenhagen. "c(6×2) and c(4×2)reconstruction of $SrTiO_3$(001)." *Surface Science* 425: 343-354 (1999).

[76] M.R. Castell. "Scanning tunneling microscopy of reconstructions on the $SrTiO_3$(001) surface." *Surface Science* 505: 1-13 (2002).

[77] M. Kawasaki, K. Takahashi, T. Maeda, T. Ryuta, M. Shinohara, O. Ishiyama, T. Yonezawa, M. Yoshimoto, H. Koinuma. "Atomic Control of the $SrTiO_3$ Crystal Surface." *Science* 266: 1540-1542 (1994).

[78] F. Silly, D.T. Newell, M.R. Castell. "$SrTiO_3$(001) reconstructions: the (2×2) to c(4×4) transition." *Surface Science* 600: L219-L223 (2006).

[79] K. Iwaya, R. Shimizu, T. Ohsawa, T. Hashizume, T. Hitosugi. "Stripe charge ordering in SrO-terminated $SrTiO_3$(001) surfaces." *Physical Review B* 83: 125117 (2011).

[80] T. Matsumoto, H. Tanaka, T. Kawai, S. Kawai. "STM-Imaging of a $SrTiO_3$(100) Surface with Atomic-Scale Resolution." *Surface Science* 278: L153-L158 (1992).

[81] H. Tanaka, T. Matsumoto, T. Kawai, S. Kawai. "Surface-Structure and Electronic Property of Reduced $SrTiO_3$(100) Surface Observed by Scanning Tunneling

Microscopy/Spectroscopy." *Japanese Journal of Applied Physics Part 1* 32: 1405-1409 (1993).

[82] M.S. Martín González, M.H. Aguirre, E. Emilio Mora, M.A. Alario-Franco, V. Pérez-Dieste, J. Ávila, M.C. Asensio. "In situ reduction of (100) $SrTiO_3$." *Solid State Sci.* 2: 519-524 (2000).

[83] L.M. Liborio, C.G. Sánchez, A.T. Paxton, M.W. Finnis. "Stability of Sr adatom model structures for $SrTiO_3$(001) surface reconstructions." *J. Phys.: Condens. Matter* 17: L223-L230 (2005).

[84] D.T. Newell, A. Harrison, F. Silly, M.R. Castell. "$SrTiO_3$(100)-($\sqrt{5}\times\sqrt{5}$)-R26.6° reconstruction: A surface resulting from phase separation in a reducing environment." *Physical Review B* 75: 205429 (2007).

[85] S.B. Lee, F. Phillip, W. Sigle, M. Rühle. "Nanoscale TiO island formation on the $SrTiO_3$(001) surface studied by in situ high-resolution transmission electron microscopy." *Ultramicroscopy* 104: 30-38 (2005).

[86] I. Shiraki, K. Miki. "$SrTiO_3$(100)-$\sqrt{5}\times\sqrt{5}$-R26.6 surface observed by high-resolution scanning tunneling microscopy." *Surface Science* 605: 1304-1307 (2011).

[87] L.D. Marks, W. Sinkler, E. Landree. "A feasible set approach to the crystallographic phase problem." *Acta Cryst.* A55: 601-612 (1999).

[88] L.D. Marks, N. Erdman, A. Subramanian. "Crystallographic direct methods for surfaces." *J. Phys.: Condens. Matter* 13: 10677-10688 (2001).

[89] N. Erdman, O. Warschkow, M. Asta, K.R. Poeppelmeier, D.R. Ellis, L.D. Marks. "Surface Structures of $SrTiO_3$ (001): A TiO_2-rich Reconstruction with a c(4×2) Unit Cell." *J. Am. Chem. Soc.* 125: 10050-10056 (2003).

[90] O. Warschkow, M. Asta, N. Erdman, K.R. Poeppelmeier, D.E. Ellis, L.D. Marks. "TiO_2-rich reconstructions of $SrTiO_3$(001): a theoretical study of structural patterns." *Surface Science* 573: 446-456 (2004).

[91] C.H. Lanier, A. Van de Walle, N. Erdman, E. Landree, O. Warschkow, A. Kazimirov, K.R. Poeppelmeier, J. Zegenhagen, M. Asta, L.D. Marks. "Atomic-scale structure of the $SrTiO_3$(001)-c(6×2) reconstruction: Experiments and first principles calculations." *Phys. Rev. B* 76: 045421 (2007).

[92] D.M. Kienzle, A.E. Becerra-Toledo, L.D. Marks. "Vacant-Site Octahedral Tilings on $SrTiO_3$ (001), the ($\sqrt{13}\times\sqrt{13}$)R33.7° Surface, and Related Structures." *Physical Review Letters* 106: 176102 (2011).

[93] R. Herger, P.R. Willmott, O. Bunk, C.M. Schlepütz, B.D. Patterson. "Surface of Strontium Titanate." *Phys. Rev. Lett.* 98: 076102 (2007).

[94] R. Herger, P.R. Willmott, O. Bunk, C.M. Schleputz, B.D. Patterson, B. Delley, V.L. Shneerson, P.F. Lyman, D.K. Saldin. "Surface structure of $SrTiO_3$(001)." *Physical Review B* 76: 195435 (2007).

[95] G. Koster, B.L. Kropman, G.J.H.M. Rijnders, D.H.A. Blank, H. Rogalla. "Quasi-ideal strontium titanate crystal surfaces through formation of strontium hydroxide." *Appl. Phys. Lett.* 73: 2920-2922 (1998).

[96] E. Heifets, S. Piskunov, E.A. Kotomin, Y.F. Zhukovskii, D.E. Ellis. "Electronic structure and thermodynamic stability of double-layered $SrTiO_3$(001) surfaces: Ab initio simulations." *Physical Review B* 75: 115417 (2007).

[97] N. Iles, F. Finocchi, K.D. Khodja. "A systematic study of ideal and double layer reconstructions of ABO_3(001) surfaces (A = Sr, Ba; B = Ti, Zr) from first principles." *Journal of Physics-Condensed Matter* 22: (2010).

[98] J.P. Perdew, K. Burke, M. Ernzerhof. "Generalized Gradient Approximation Made Simple." *Phys. Rev. Lett.* 77: 3865 (1996).

[99] J.P. Perdew, A. Ruzsinszky, G.I. Csonka, O.A. Vydrov, G.E. Scuseria, L.A. Constantin, X. Zhou, K. Burke. "Restoring the Density-Gradient Expansion for Exchange in Solids and Surfaces." *Phys. Rev. Lett.* 100: 136406 (2008).

[100] L.D. Marks, A.N. Chiaramonti, F. Tran, P. Blaha. "The small unit cell reconstructions of $SrTiO_3$(111)." *Surface Science* 603: 2179-2187 (2009).

[101] J. Ciston, A. Subramanian, D.M. Kienzle, L.D. Marks. "Why the case for clean surfaces does not hold water: Structure and morphology of hydroxylated nickel oxide (111)." *Surface Science* 604: 155-164 (2010).

[102] I.D. Brown, D. Altermatt. "Bond-Valence Parameters Obtained from a Systematic Analysis of the Inorganic Crystal-Structure Database." *Acta Cryst. B-Stru.* 41: 244-247 (1985).

[103] K. Knížek, http://www.fzu.cz/~knizek/kalvados/index.html.

[104] J.A. Enterkin. "A Chemical Approach to Understanding Oxide Surface Structure and Reactivity." Northwestern University, Department of Materials Science and Engineering, Evanston, IL (2010).

[105] D.K. Seo, K. Perdue, J. Ren, M.H. Whangbo. "Study of scanning tunneling microscopy images and probable relaxations of the $SrTiO_3$(100) surface by electronic structure calculations." *Surface Science* 370: 245-251 (1997).

[106] Z. Fang, K. Terakura. "Spin and orbital polarizations around oxygen vacancies on the (001) surfaces of $SrTiO_3$." *Surface Science* 470: L75-L80 (2000).

[107] M.R. Castell. "Nanostructures on the $SrTiO_3$(001) surface studied by STM." *Surface Science* 516: 33-42 (2002).

[108] D.S. Deak, F. Silly, D.T. Newell, M.R. Castell. "Ordering of TiO_2-Based Nanostructures on $SrTiO_3$(001) Surfaces." *J. Phys. Chem. B* 110: 9246-9251 (2006).

[109] H.L. Marsh, D.S. Deak, F. Silly, A.I. Kirkland, M.R. Castell. "Hot STM of nanostructure dynamics on $SrTiO_3$(001)." *Nanotechnology* 17: 3543-3548 (2006).

[110] F. Silly, M.R. Castell. "Encapsulated Pd Nanocrystals Supported by Nanoline-Structured $SrTiO_3$(001)." *J. Phys. Chem. B* 109: 12316-12319 (2005).

[111] M. Kawasaki, A. Ohtomo, T. Arakane, K. Takahashi, M. Yoshimoto, H. Koinuma. "Atomic control of $SrTiO_3$ surface for perfect epitaxy of perovskite oxides." *Appl. Surf. Sci.* 107: 102-106 (1996).

[112] R.W.G. Wyckoff. *Crystal Structures* 1: 85-237 (1963).

[113] M.S.J. Marshall, A.E. Becerra-Toledo, L.D. Marks, M.R. Castell. "Surface and Defect Structure of Oxide Nanowires on $SrTiO_3$." *Physical Review Letters* 107: 086102 (2011).

[114] M. Lontsi-Fomena, A. Villesuzanne, J.P. Doumerc, C. Frayret, M. Pouchard. "A density functional theory study of oxygen diffusion in $LaAlO_3$ and $SrTiO_3$." *Computational Materials Science* 44: 53-60 (2008).

[115] J. Carrasco, F. Illas, N. Lopez, E.A. Kotomin, Y.F. Zhukovskii, R.A. Evarestov, Y.A. Mastrikov, S. Piskunov, J. Maier. "First-principles calculations of the atomic and electronic structure of F centers in the bulk and on the (001) surface of $SrTiO_3$." *Physical Review B* 73: 064106 (2006).

[116] P. Agoston, K. Albe. "Thermodynamic stability, stoichiometry, and electronic structure of bcc-In_2O_3 surfaces." *Physical Review B* 84: 045311 (2011).

[117] A. Fahmi, C. Minot. "A theoretical investigation of water adsorption on titanium dioxide surfaces." *Surface Science* 304: 343-359 (1994).

[118] J. Goniakowski, M.J. Gillan. "The adsorption of H_2O on TiO_2 and SnO_2(110) studied by first-principles calculations." *Surface Science* 350: 145-158 (1996).

[119] J.W. Elam, C.E. Nelson, M.A. Cameron, M.A. Tolbert, S.M. George. "Adsorption of H_2O on a Single-Crystal α-Al_2O_3(0001) Surface." *J. Phys. Chem. B* 102: 7008-7015 (1998).

[120] X.D. Peng, M.A. Barteau. "Characterization of oxide layers on Mg(0001) and comparison of H_2O adsorption on surface and bulk oxides." *Surface Science* 233: 283-292 (1990).

[121] J. Ahdjoudj, C. Minot. "Adsorption of H_2O on metal oxides: a periodic ab-initio investigation." *Surface Science* 402-404: 104-109 (1998).

[122] L.-Q. Wang, K.F. Ferris, G.S. Herman. "Interactions of H_2O with $SrTiO_3$(100) surfaces." *J. Vac. Sci. Technol. A* 20: 239-244 (2002).

[123] S. Eriksen, P.D. Naylor, R.G. Egdell. "The Adsorption of Water on $SrTiO_3$ and TiO_2 - a Reappraisal." *Spectrochim. Acta A* 43: 1535-1538 (1987).

[124] N.B. Brookes, F.M. Quinn, G. Thornton. "H_2O Dissociation by $SrTiO_3$(100) Catalytic Step Sites." *Vacuum* 38: 405-408 (1988).

[125] L.-Q. Wang, K.F. Ferris, S. Azad, M.H. Engelhard. "Adsorption and Reaction of Methanol on Stoichiometric and Defective $SrTiO_3$(100) Surfaces." *J. Phys. Chem. B* 109: 4507-4513 (2005).

[126] R.A. Evarestov, A.V. Bandura, V.E. Alexandrov. "Adsorption of water on (001) surface of $SrTiO_3$ and $SrZrO_3$ cubic perovskites: Hybrid HF-DFT LCAO calculations." *Surface Science* 601: 1844-1856 (2007).

[127] B.B. Hinojosa, T. Van Cleve, A. Asthagiri. "A first-principles study of H_2O adsorption and dissociation on the $SrTiO_3$(100) surface." *Mol. Simulat.* 36: 604-617 (2010).

[128] S. Raghavan, A. Carvalho, F. Le Formal, N. Setter, S. Öberg, P.R. Briddon. "Adsorbate-localized states at water-covered (100) $SrTiO_3$ surfaces." *Appl. Phys. Lett.* 98: 012106 (2011).

[129] C. Di Valentin, A. Tilocca, A. Selloni, T.J. Beck, A. Klust, M. Batzill, Y. Losovyi, U. Diebold. "Adsorption of Water on Reconstructed Rutile TiO_2(011)-(2×1): Ti=O Double Bonds and Surface Reactivity." *J. Am. Chem. Soc.* 127: 9895-9903 (2005).

[130] J. Ciston, A. Subramanian, L.D. Marks. "Water-driven structural evolution of the polar MgO (111) surface: An integrated experimental and theoretical approach." *Phys. Rev. B* 79: 085421 (2009).

[131] A. Stroppa, G. Kresse. "The shortcomings of semi-local and hybrid functionals: what we can learn from surface science studies." *New J. Phys.* 10: (2008).

[132] J.P. Perdew, A. Ruzsinszky, G.I. Csonka, L.A. Constantin, J. Sun. "Workhorse Semilocal Density Functional for Condensed Matter Physics and Quantum Chemistry." *Phys. Rev. Lett.* 103: 026403 (2009).

[133] M.W. Chase. "NIST-JANAF Thermochemical Tables." Washington, D.C., American Chemical Society (1998).

[134] O. Warschkow, Y. Wang, A. Subramanian, M. Asta, L.D. Marks. "Structure and Local-Equilibrium Thermodynamics of the c(2×2) Reconstruction of Rutile TiO_2 (100)." *Physical Review Letters* 100: 086102 (2008).

[135] W.S. Benedict, N. Gailar, E.K. Plyler. "Rotation-Vibration Spectra of Deuterated Water Vapor." *J. Chem. Phys.* 24: 1139 (1956).

[136] N. Erdman, L.D. Marks. "$SrTiO_3$(001) surface structures under oxidizing conditions." *Surface Science* 526: 107-114 (2003).

[137] V.K. Lazarov, R. Plass, H.C. Poon, D.K. Saldin, M. Weinert, S.A. Chambers, M. Gajdardziska-Josifovska. "Structure of the hydrogen-stabilized MgO(111)-(1x1) polar surface: Integrated experimental and theoretical studies." *Phys. Rev. B* 71: (2005).

[138] L.-Q. Wang, D.R. Baer, M.H. Engelhard. "Creation of variable concentrations of defects on TiO_2(110) using low-density electron beams." *Surface Science* 320: 295-306 (1994).

[139] J.M. Tao, J.P. Perdew, V.N. Staroverov, G.E. Scuseria. "Climbing the Density Functional Ladder: Nonempirical Meta–Generalized Gradient Approximation Designed for Molecules and Solids." *Phys. Rev. Lett.* 91: 146401 (2003).

[140] X.Q. Liu, X.M. Chen, Y. Xiao. "Preparation and characterization of $LaSrAlO_4$ microwave dielectric ceramics." *Mat. Sci. Eng., B* 103: 276-280 (2003).

[141] R. Sobolewski, P. Gierlowski, W. Kula, S. Zarembinski, S.J. Lewandowski, M. Berkowski, A. Pajaczkowska, B.P. Gorshunov, D.B. Lyudmirski, O.I. Sirotinski. "High-T_c thin films on low microwave loss alkaline-rare-earth-aluminate crystals." *IEEE Transactions on Magnetics* 27: 876-879 (1991).

[142] R. Brown, V. Pendrick, D. Kalokitis, B.H.T. Chai. "Low-loss substrate for microwave application of high-temperature superconductor films." *Appl. Phys. Lett.* 57: 1351-1353 (1990).

[143] R.D. Shannon, R.A. Oswald, J.B. Parise, B.H.T. Chai, P. Byszewski, A. Pajaczkowska, R. Sobolewski. "Dielectric Constants and Crystal Structures of $CaYAlO_4$, $CaNdAlO_4$, and $SrLaAlO_4$, and Deviations from the Oxide Additivity Rule." *J. Solid State Chem.* 98: 90-98 (1992).

[144] M. Drozdowski, D. Kasprowicz, A. Pajaczkowska. "Characterization of the elastic and elasto-optic properties of $SrLaAlO_4$ and $SrLaGaO_4$ crystals using the Brillouin scattering method." *J. Mol. Struct.* 555: 119-129 (2000).

[145] J. Humlicek, R. Henn, M. Cardona. "Infrared vibrations in $LaSrGaO_4$ and $LaSrAlO_4$." *Phys. Rev. B* 61: 14554-14563 (2000).

[146] G.X. Chen, Y.J. Ge, C.Z. Bi, X.G. Qiu, B.R. Zhao. "Far-infrared optical properties of $SrLaAlO_4$ single crystal." *J. Appl. Phys.* 95: 3417-3421 (2004).

[147] I.A. Zvereva, L. Zueva, J. Choisnet. "Metastability of the K_2NiF_4 type structure of the solid solution $LaCa(Cr_xAl_{1-x})O_4$ ($0<=x<=0.10$)." *J. Mater. Sci.* 30: 3598-3602 (1995).

[148] P. Byszewski, A. Pajaczkowska, J. Sass, K. Mazur. "Crystallization of $CaNdAlO_4$ and $SrLaAlO_4$ compounds." *Cryst. Prop. Prep.* 36-38: 560-564 (1991).

[149] A. Pajaczkowska, P. Byszewski. "Anomalies in crystal growth by Czochralski technique." *J. Cryst. Growth* 128: 694-698 (1993).

[150] M. Berkowski, J. Fink-Finowicki, J. Sass, K. Mazur. "High quality (100) and (001) oriented substrates prepared from Czochralski grown $SrLaGaO_4$ and $SrLaAlO_4$ single crystals." *Acta Phys. Pol., A* 92: 201-204 (1997).

[151] J. Doerschel, I. Hähnert, R. Uecker. "Origin of imperfections in <100> $SrLaAlO_4$ crystals." *Acta Phys. Pol., A* 92: 157-162 (1997).

[152] A. Pajaczkowska, A. Gloubokov, A. Klos, C.F. Woensdregt. "Czochralski growth of $SrLaAlO_4$ and $SrLaGaO_4$ single crystals and its implications for the crystal morphology." *J. Cryst. Growth* 171: 387-391 (1997).

[153] W. Ryba-Romanowski, S. Golab, P. Deren, G. Dominiak-Dzik, W.A. Pisarski. "Investigation of as grown and induced structural defects in $SrLaXO_4$ (X= Al, Ga) crystals." *Acta Phys. Pol., A* 92: 191-196 (1997).

[154] D. Kasprowicz, M. Drozdowski, A. Pajaczkowska. "Influence of Growth Conditions on the Elastic Properties of $SrLaAlO_4$ and $SrLaGaO_4$ Crystals Studied by Brillouin Scattering Method." *Cryst. Res. Technol.* 26: 1123-1126 (2001).

[155] C.H. Lanier, J.M. Rondinelli, B. Deng, R. Kilaas, K.R. Poeppelmeier, L.D. Marks. "Surface Reconstruction with a Fractional Hole: $(\sqrt{5}\times\sqrt{5})R26.6^{\circ}$ $LaAlO_3$ (001)." *Phys. Rev. Lett.* 98: 086102 (2007).

[156] A.A. Dobrikov, O.V. Presnyakova, V.I. Zaitsev, V.V. Prisedskii, P.k. G.F. "Investigation of $PbTiO_3$ Crystal Lattice Defects by Transmission Electron Microscopy." *Kristall und Technik* 15: 207-212 (1980).

[157] V.V. Prisedsky, V.P. Komarov, G.F. Pan'ko, V.V. Klimov. "Crystallographic shear planes as nonstoichiometry defects in lead zirconate." *Ferroelectrics* 23: 23-34 (1980).

[158] K. Hawkins, T.J. White. "Defect structure and chemistry of $(Ca_xSr_{1-x})_{n+1}Ti_nO_{3n+1}$ layer perovskites." *Phil. Trans. R. Soc. Lond. A* 336: 541-569 (1991).

[159] K. Szot, W. Speier. "Surfaces of reduced and oxidized $SrTiO_3$ from atomic force microscopy." *Phys. Rev. B* 60: 5909-5926 (1999).

[160] K. Szot, W. Speier, U. Breuer, R. Meyer, J. Szade, R. Waser. "Formation of micro-crystals on the (100) surface of $SrTiO_3$ at elevated temperatures." *Surface Science* 460: 112-128 (2000).

[161] Y. Liang, D.A. Bonnell. "Atomic structures of reduced $SrTiO_3$(001) surfaces." *Surface Science* 285: L510-516 (1993).

[162] Y. Liang, D.A. Bonnell. "Structures and chemistry of the annealed $SrTiO_3$(001) surface." *Surface Science* 310: 128-134 (1994).

[163] Y. Liang, D. Bonnell. "Effects of Variations in Stoichiometry on the Surface Structure of $SrTiO_3$ (001)." *J. Am. Chem. Soc.* 78: 2633-40 (1995).

[164] K. Szot, M. Pawelczyk, J. Herion, C. Freiburg, J. Albers, R. Waser, J. Hulliger, J. Kwapulinski, J. Dec. "Nature of the surface layer in ABO_3-type perovskites at elevated temperatures." *Appl. Phys. A* 62: 335-343 (1996).

[165] K. Szot, W. Speier, J. Herion, C. Freiburg. "Restructuring of the surface region in $SrTiO_3$." *Appl. Phys. A* 64: 55-59 (1997).

[166] H. Wei, L. Beuermann, J. Helmbold, G. Borchardt, V. Kempter, G. Lilienkamp, W. Maus-Friedrichs. "Study of SrO segregation on $SrTiO_3$(100) surfaces." *Journal of the European Ceramic Society* 21: 1677-1680 (2001).

[167] H. Wei, W. Maus-Friedrichs, G. Lilienkamp, V. Kempter, J. Helmbold, K. Gömann, G. Borchardt. "Surface structure of oxygen annealed donor doped $SrTiO_3$(100) single crystals studied with spectroscopic electron microscopy." *Journal of Electroceramics* 8: 221-228 (2002).

[168] A. Gunhold, K. Gömann, L. Beuermann, M. Frerichs, G. Borchardt, V. Kempter, W. Maus-Friedrichs. "Geometric structure and chemical composition of $SrTiO_3$ surfaces heated under oxidizing and reducing conditions." *Surface Science* 507-510: 447-452 (2002).

[169] R. Meyer, R. Waser, J. Helmbold, G. Borchardt. "Cationic Surface Segregation in Donor-Doped $SrTiO_3$ Under Oxidizing Conditions." *J. Electroceramics* 9: 101-110 (2002).

[170] B. Rahmati, J. Fleig, W. Sigle, E. Bischoff, J. Maier, M. Rühle. "Oxidation of reduced polycrystalline Nb-doped $SrTiO_3$: Characterization of surface islands." *Surface Science* 595: 115-126 (2005).

[171] S.B. Desu, D.A. Payne. "Interfacial Segregation in Perovskites: II, Experimental Evidence." *J. Am. Chem. Soc.* 73: 3398-3406 (1990).

[172] G. Horvath. "Quantitative Methods for the Characterization of the Auger Peaks of $SrTiO_3$." *Surface and Interface Analysis* 23: 227-233 (1995).

[173] G. Horvath, J. Gerblinger, H. Meixner, J. Giber. "Segregation driving forces in perovskite titanates." *Sens. Actuators B* 32: 93-99 (1996).

[174] F. Silly, M.R. Castell. "Formation of single-domain anatase TiO_2(001)-(1×4) islands on $SrTiO_3$(001) after thermal annealing." *Appl. Phys. Lett.* 85: 3223-3225 (2004).

[175] M.S.J. Marshall, M.R. Castell. "Shape Transitions of Epitaxial Islands during Strained Layer Growth: Anatase TiO_2(001) on $SrTiO_3$(001)." *Physical Review Letters* 102: (2009).

[176] A. Gunhold, L. Beuermann, M. Frerichs, V. Kempter, K. Gömann, G. Borchardt, W. Maus-Friedrichs. "Island formation on 0.1 at.% La-doped $SrTiO_3$(100) at elevated temperatures under reducing conditions." *Surface Science* 523: 80-88 (2003).

[177] A. Kazimirov, D.M. Goodner, M.J. Bedzyk, J. Bai, C.R. Hubbard. "X-ray surface diffraction analysis of structural transformations on the (001) surface of oxidized $SrTiO_3$." *Surface Science* 492: L711-L716 (2001).

[178] M. Horn, C.F. Schwerdt, E.P. Meagher. "Refinement of Structure of Anatase at Several Temperatures." *Zeitschrift Für Kristallographie* 136: 273-281 (1972).

[179] J. Bashir, R.T.A. Khan, N.M. Butt, G. Heger. "Thermal atomic displacement parameters of SrO." *Powder Diffraction* 17: 222-224 (2002).

[180] MTI Corporation, personal communication.

[181] S. Geller, V.B. Bala. "Crystallographic Studies of Perovskite-like Compounds. II. Rare Earth Aluminates." *Acta Cryst.* 9: 1019-1025 (1956).

[182] V.F. Popova, E.A. Tugova, I.A. Zvereva, V.V. Gusarov. "Phase Equilibria in the $LaAlO_3$-$LaSrAlO_4$ System." *Glass Phys. Chem.* 30: 564-567 (2004).

[183] M.J. Akhtar, Z.U.N. Akhtar, R.A. Jackson, C.R.A. Catlow. "Computer Simulation Studies of Strontium Titanate." *J. Am. Chem. Soc.* 78: 421-428 (1995).

[184] M. Fujimoto, M. Watanabe. "Ti_nO_{2n-1} Magnéli phase formation in $SrTiO_3$ dielectrics." *J. Mater. Sci.* 20: 3683-3690 (1985).

[185] A.V. Novoselov, L.P. Ogodorova, G.V. Zimina, A. Pajaczkowska. "Thermodynamic Properties and Dissociation of $SrLaAlO_4$." *Inorg. Mater.* 36: 180-182 (2000).

[186] J. Cheng, A. Navrotsky. "Enthalpies of formation of $LaBO_3$ perovskites (B = Al, Ga, Sc, and In)." *J. Mater. Res.* 18: 2501-2508 (2003).

[187] "CRC Handbook of Chemistry and Physics." CRC Press (2007).

[188] K.J. Reddy, J.I. Drever, M.E. Essington, W.L. Lindsay. "Strontium Supplement to Technical Bulletin 134, Selection of Standard Free Energies of Formation for Use in Soil Chemistry." *Colorado State University Department of Agronomy* (1989).

[189] R.H. Lamoreaux, D.L. Hildenbrand. "High-Temperature Vaporization Behavior of Oxides II. Oxides of Be, Mg, Ca, Sr, Ba, B, Al, Ga, In, Tl, Si, Ge, Sn, Pb, Zn, Cd and Hg." *J. Phys. Chem. Ref. Data* 16: 419-443 (1987).

[190] J.M. Blanco, F. Flores, R. Pérez. "STM-theory: Image potential, chemistry and surface relaxation." *Progress in Surface Science* 81: 403-443 (2006).

[191] F.A. Rabuffetti, H.S. Kim, J.A. Enterkin, Y.M. Wang, C.H. Lanier, L.D. Marks, K.R. Poeppelmeier, P.C. Stair. "Synthesis-dependent first-order Raman scattering in $SrTiO_3$ nanocubes at room temperature." *Chemistry of Materials* 20: 5628-5635 (2008).

[192] F.A. Rabuffetti, P.C. Stair, K.R. Poeppelmeier. "Synthesis-Dependent Surface Acidity and Structure of $SrTiO_3$ Nanoparticles." *J. Phys. Chem. C* 114: 11056-11067 (2010).

[193] J. Bardeen. "Tunnelling from a Many-Particle Point of View." *Phys. Rev. Lett.* 6: 57-59 (1961).

[194] K. Stokbro, U. Quaade, F. Grey. "Electric field effects in scanning tunneling microscope imaging." *Appl. Phys. A* 66: S907-S910 (1998).

[195] L. Pauling. "Atomic Radii and Interatomic Distances in Metals." *Journal of the American Chemical Society* 69: 542-553 (1947).

[196] J.P. Perdew, M. Ernzerhof, K. Burke. "Rationale for mixing exact exchange with density functional approximations." *J. Chem. Phys.* 105: 9982 (1996).

[197] F. Tran, P. Blaha. "Accurate Band Gaps of Semiconductors and Insulators with a Semilocal Exchange-Correlation Potential." *Phys. Rev. Lett.* 102: (2009).

[198] F. Tran, P. Blaha, K. Schwarz, P. Novak. "Hybrid exchange-correlation energy functionals for strongly correlated electrons: Applications to transition-metal monoxides." *Physical Review B* 74: 155108 (2006).

[199] P. Novak, J. Kunes, L. Chaput, W.E. Pickett. "Exact exchange for correlated electrons." *Physica Status Solidi B-Basic Solid State Physics* 243: 563-572 (2006).

List of Publications

Portions of the material included in this dissertation have been or will be published elsewhere by the author as follows:

Chapter 3.

Y. Lin, A.E. Becerra-Toledo, F. Silly, K.R. Poeppelmeier, M.R. Castell, L.D. Marks. "A (2×2) reconstruction on the $SrTiO_3$(001) surface: a combined STM and DFT study." *Surface Science* 605: L51-L55 (2011).

Chapter 4.

M.S.J. Marshall, A.E. Becerra-Toledo, L.D. Marks, M.R. Castell. "Surface and Defect Structure of Oxide Nanowires on $SrTiO_3$." *Physical Review Letters* 107: 086102 (2011).

A.E. Becerra-Toledo, M.S.J. Marshall, M.R. Castell, L.D. Marks. "c(4×2) and Related Structural Units on the $SrTiO_3$(001) Surface: STM, DFT and Structure." In preparation, title subject to change.

Chapter 5.

A.E. Becerra-Toledo, M.R. Castell, L.D. Marks. "Water Adsorption on $SrTiO_3$(001): I. Experimental and Simulated Scanning Tunneling Microscopy." Submitted (2011).

A.E. Becerra-Toledo, J.A. Enterkin, D.M. Kienzle, L.D. Marks. "Water Adsorption on $SrTiO_3$(001): II. Water, Water, Everywhere." Submitted (2011).

Chapter 6.

A.E. Becerra-Toledo, L.D. Marks. "Strontium oxide segregation at $SrLaAlO_4$ surfaces." *Surface Science* 604: 1476-1480 (2010).

Appendix A. STM Image Simulations: Theory & Implementation

A.1. STM Imaging Theory

The experimental scanning tunneling micrographs of $SrTiO_3$ surfaces from our collaborators are all unusual since they high biasing voltages; this is necessary since strontium titanate is an insulator. Unfortunately, this renders the popular versions of scanning tunneling microscopy (STM) imaging theory unusable, since they assume a small bias. The present section reviews the background to the existing theory and the modifications made to enable the generation of DFT-based high-bias STM micrograph simulations.

A.1.1. Bardeen Theory and the Tersoff-Hamann Approximation

Bardeen pioneered the theory of tunneling and modeled the system as a metal-insulator-metal junction. Instead of trying to solve the Schrödinger Equation for the whole system, he first

addressed each electrode (tip and sample, in STM) separately and treated their wavefunctions as being roughly orthogonal [190]. The tunneling rate from the ν^{th} tip state to the μ^{th} sample state was calculated upon application of time-dependent perturbation theory, and this was in turn incorporated to find an expression for the tunneling current. The derivation is long; see Ref. [43] for a good review. For low temperatures, the tunneling current is given by

$$I_t \propto \int_{E_F}^{E_F + e\,V_b} \rho_T(\varepsilon - e\,V_b)\rho(\varepsilon) \sum_{\mu\nu} \left|M_{\mu\nu}\right|^2 \left(\varepsilon_\mu - \varepsilon_\nu\right) d\varepsilon \,. \qquad \text{(Eq. A.1)}$$

where $\rho_T(\varepsilon)$ and $\rho(\varepsilon)$ are the local density of states of energy ε for the tip and sample, respectively, E_F is the Fermi energy of the sample, e is the charge of an electron and V_b is the bias voltage. Also, $M_{\mu\nu}$ is a tunneling matrix element, defined as a surface integral over a separating surface which must lie completely within the barrier (vacuum) region which separates the tip and the surface:

$$M_{\mu\nu} = \frac{\hbar^2}{2m_e} \int d\boldsymbol{S} \cdot \left(\chi_\nu^* \nabla \psi_\mu - \psi_\mu \nabla \chi_\nu^*\right) . \qquad \text{(Eq. A.2)}$$

Moreover, if M is assumed to be independent of energy within the range from E_F to $E_F + e \cdot V_b$, as may be the case for small the bias, then under Bardeen Theory the tunneling current is specifically dependent not only on the electronic structure of the sample, but also on the electronic structure of the tip. In general, however, the latter is not known. Tersoff and Hamann addressed this by simplifying the system [50]. The tip was modeled as a locally spherical potential well, incorporating only s-type orbitals and otherwise treating it as a structureless geometric point. They used the low-V_b, low-temperature Bardeen tunneling current and evaluated the tunneling matrix M under the s-orbital treatment. This results in the following relation for the tunneling current from a tip with the center of its apex atom at position $\boldsymbol{r}$:

$$I_{\mathrm{t}} \propto \rho(\boldsymbol{r}, E_{\mathrm{F}}) \equiv \sum_{\mu} \left|\psi_{\mu}(\boldsymbol{r})\right|^2 \ \left(\varepsilon_{\mu} - E_{\mathrm{F}}\right). \qquad \text{(Eq. A.3)}$$

This central result is the famous Tersoff-Hamann approximation. Very simply, it states that the tunneling current is proportional to the sample's local density of states around its Fermi energy. Just as importantly, this is a powerful outcome, as it enables the use of *ab initio* methods such as density functional theory. It comes as no surprise, therefore, that it has been used extensively to generate STM micrograph simulations. Unfortunately, the Tersoff-Hamann approximation holds for low biases only (under 100 meV).

A.1.2. High-Bias STM Imaging Theory

Stokbro *et al.* [191] attempted to extend the Tersoff-Hamann approximation to the high-bias regime, although their resulting equations incorrectly weight the energy levels. In what follows, a similar derivation will be presented, which in turn closely follows the description by Chen [43]. It starts with the modified Bardeen tunneling current,

$$I_t = \frac{2\pi e}{\hbar} \sum_{\mu\nu} \left[f(\varepsilon_{\nu} - e\, V_{\mathrm{b}}) - f\left(\varepsilon_{\mu}\right)\right] \left|M_{\mu\nu}\right|^2 \ \left(\varepsilon_{\mu} - \varepsilon_{\nu}\right), \qquad \text{(Eq. A.4)}$$

The tip wavefunctions χ_{ν}, which obey Schrödinger's equation, are then addressed:

$$(\nabla^2 - \kappa(\varepsilon)^2)\chi_{\nu}(\boldsymbol{d}) = 0\ , \qquad \text{(Eq. A.5)}$$

where

$$\kappa(\varepsilon) = \hbar^{-1}\sqrt{2m_e(\phi_t + E_{\mathrm{F}} + e\, V_{\mathrm{b}} - \varepsilon)} \qquad \text{(Eq. A.6)}$$

is the inverse decay length of electron states in vacuum of energy ε. Also, $\boldsymbol{d}$ is the distance from the center of the atom at the tip apex, ϕ_t is the tip workfunction and m_{e} is the mass of an electron. The tip wavefunctions must have the form

$$\chi_\nu(\boldsymbol{d}) = \sum_{lm} C_{lm}^{\nu} f_{lm}(\kappa(\varepsilon)\varrho) Y_l^m \,. \qquad \text{(Eq. A.7)}$$

Here, $\varrho \equiv |\boldsymbol{d} - \boldsymbol{r}|$. When substituting Eq. A.7 into Eq. A.5, and given that the tip wavefunction must converge far away from the tip, it is found that the radial functions $f_{lm}(\kappa(\varepsilon)\varrho)$ depend only on *l* and correspond to the spherical modified Bessel functions:

$$f_{lm}(u) = k_l(u) = (-u)^l \left(\frac{d}{u\,du}\right)^l \frac{e^{-u}}{u}. \qquad \text{(Eq. A.8)}$$

For s-type tip states,

$$f_{00}(\kappa(\varepsilon)\varrho) = k_0(\kappa(\varepsilon)\varrho) = \frac{e^{-\kappa(\varepsilon)\varrho}}{\kappa(\varepsilon)\varrho}. \qquad \text{(Eq. A.9)}$$

Therefore, the tip wavefunctions have the general form:

$$\chi_\nu(\boldsymbol{r}) = \sum_{lm} C_{lm}^{\nu} k_l(\kappa(\varepsilon)\varrho) Y_l^m \,. \qquad \text{(Eq. A.10)}$$

For the s-type tip states,

$$\chi_s(\boldsymbol{d}) = \frac{C_{00}}{\sqrt{4\pi}} \frac{e^{-\kappa(\varepsilon)\varrho}}{\kappa(\varepsilon)\varrho}. \qquad \text{(Eq. A.11)}$$

In order to evaluate the tunneling matrix elements for these states, it is necessary to make use of Green's functions. For Eq. A.5, this corresponds [43] to

$$(\nabla^2 - \kappa(\varepsilon)^2) G(\boldsymbol{d} - \boldsymbol{r}) = - \quad (\boldsymbol{d} - \boldsymbol{r}) \,, \qquad \text{(Eq. A.12)}$$

where, given the boundary condition of convergence far from the tip apex,

$$G(\boldsymbol{d} - \boldsymbol{r}) = \frac{e^{-\kappa(\varepsilon)\varrho}}{4\pi\varrho} = \frac{\kappa(\varepsilon)}{4\pi} k_0(\kappa(\varepsilon)\varrho) \,. \qquad \text{(Eq. A.13)}$$

Therefore, the s-type tip wavefunction can be expressed in terms of the Green's function:

$$\chi_s(\boldsymbol{d}) = \frac{\sqrt{4\pi}C_{00}}{\kappa(\varepsilon)} G(\boldsymbol{d}-\boldsymbol{r}) \,. \qquad \text{(Eq. A.14)}$$

Evaluating the tunneling matrix element for s-type tip states, it is found that

$$M_{\mu s} = \frac{2\pi C_{00}\hbar^2}{\kappa(\varepsilon) m_e} \int d\boldsymbol{S} \cdot [\, G(\boldsymbol{d}-\boldsymbol{r}) \nabla\psi_\mu - \psi_\mu \nabla G(\boldsymbol{d}-\boldsymbol{r})] \,. \qquad \text{(Eq. A.15)}$$

This can be converted, by Green's theorem, into a volume integral over the tip side of the separation surface:

$$M_{\mu s} = \frac{2\pi C_{00}\hbar^2}{\kappa(\varepsilon) m_e} \int\limits_{\Omega} d\boldsymbol{V} \cdot [\, G(\boldsymbol{d}-\boldsymbol{r}) \nabla^2\psi_\mu - \psi_\mu \nabla^2 G(\boldsymbol{d}-\boldsymbol{r})] \,. \qquad \text{(Eq. A.16)}$$

Since ψ_μ satisfies Eq. A.5 in this region,

$$M_{\mu s} = \frac{2\pi C_{00}\hbar^2}{\kappa(\varepsilon) m_e} \psi_\mu(\boldsymbol{r}) \,. \qquad \text{(Eq. A.17)}$$

By approximating the Fermi functions as step functions, one arrives at the expression for the tunneling current:

$$I_\mathrm{t} = \frac{8\pi^3\hbar^3 C_{00}^2 e}{m_e^2} \int_{E_\mathrm{F}}^{E_\mathrm{F}+e\cdot V_\mathrm{b}} \kappa(\varepsilon)^{-2} \sum\nolimits_\mu \left|\psi_\mu(\boldsymbol{r})\right|^2 \, (\varepsilon_\mu - \varepsilon)\, d\varepsilon \,, \qquad \text{(Eq. A.18)}$$

which changes the proportionality relation to

$$I_\mathrm{t} \propto \int_{E_\mathrm{F}}^{E_\mathrm{F}+e\cdot V_\mathrm{b}} \kappa(\varepsilon)^{-2}\, \rho(\boldsymbol{r},\varepsilon)\, d\varepsilon \,. \qquad \text{(Eq. A.19)}$$

Stokbro *et al.* [191] used a different expansion for the tip wavefunctions which directly led, for s-type tip states to the incorrect relation

$$I_\mathrm{t} \propto \int_{E_\mathrm{F}}^{E_\mathrm{F}+e\cdot V_\mathrm{b}} e^{2\kappa(\varepsilon)R}\, \rho(\boldsymbol{r},\varepsilon)\, d\varepsilon \,, \qquad \text{(Eq. A.20)}$$

where R is the radius of curvature of the tip. This result mistakenly gives more weight to the lower-energy states, despite the larger effective tunneling barrier.

A.2. DFT Implementation

This section describes how to implement the high-bias imaging theory above in the context of the full-electron potential WIEN2k DFT code [46]. WIEN2k is the software used throughout this work, not only for STM micrograph simulations, but also for total-energy calculations and bond valence sum analysis.

A.2.1. DFT Relaxation and Convergence

WIEN2k can only be run for periodic systems, by defining a unit cell or supercell. In order to model a surface with this code, a repeated slab model is used, with two important constraints: that the slab is thick enough, and that the vacuum separation between slabs is also large enough. The latter is typically 10-15 Å, but for STM simulations this is an especially important factor, as it limits how far away from the surface you can sample the density (essentially limiting the tip-sample distance).

In DFT codes, the electron density distribution is solved iteratively. After the geometry of the system is inputted, an initial electron density "guess" is necessary to determine the potential, which in turn is used to solve the Schrödinger-like Kohn-Sham equations which yield a new density. The latter is then used at the start of the next cycle to determine the new potential, and so on. Each such iteration is called a self-consistent field (SCF) cycle and if the problem is well-posed, the electron density distribution will converge to a stable solution. In the case of simple bulk calculations, there are often many high-symmetry sites and no atomic relaxation is

allowable. For surfaces, however, relaxation is possible at the very least in the out-of-plane direction. In DFT, after density convergence has been attained, it can be used to calculate the force on each atom. The magnitude and direction of the force can be used to nudge each atom, and the new set of positions is used to get a new converged electron density distribution. This can be repeated until the forces are minimized; a small threshold, typically 1 eV/Å, is enforced so that the relaxation stops once all atomic forces are below this value.

In order to generate STM image simulations from the DFT outputs, one must start from a fully-relaxed and density-converged structure, so that unoccupied states can then be artificially populated in an appropriate manner.

A.2.2. Artificial Population of States

Before going further, it is useful to understand how the SCF cycles are performed in the WIEN2k code. There are five main routines, each of which has an important role:

1. ~~–la~~pw0": This generates the potential from the starting electron density
2. ~~–la~~pw1": This takes the potential generated and uses it for the Kohn-Sham equations to calculate the valence eigenvectors and eigenvalues (energies), thereby generating the valence band structure
3. ~~–la~~pw2": This populates the valence eigenstates
4. ~~–lc~~ore": This calculates the core states and their densities (orbitals are treated either as core or band states)
5. ~~–m~~ixer": This generates a new density by mixing the previous density with the one outputted by ~~–la~~pw2" and ~~–lc~~ore"

It is then clear that ―lapw2" should be tweaked in order to populate the appropriate states. Following Equation A.19, the states from $E = E_F$ up to $E = E_{max} = E_F + e \cdot V_b$ need to be populated. In itself, this is not enough. The population at each energy must be multiplied by the weighting factor $\kappa(\varepsilon)^{-2}$. Since the tip is not explicitly modeled, its workfunction can be approximated by the workfunction of the sample, which corresponds to the difference between the vacuum energy (E_{vac}) and the Fermi energy. These two values can be found by typing the following in the case folder from the DFT outputs:

```
grep :VZER* *.scf0
grep :FER *.scf
```

The upper energy bound (E_{max}, defined by the biasing voltage used for the experimental images to be compared to the simulations) is also necessary and can be calculated for several different voltages, if necessary, but must always be converted into Rydberg units, which are used for all energies in the WIEN2k outputs, including E_F and E_{vac}.

A ―lapw2STM" routine has been created, by using the same source code as for ―lapw2", except for the ―fermi5.f" module, which uses E_{vac}, E_{max} and E_{min} (any value between E_F and the conduction band minimum, which can be found by inspecting the ―case.output2" file) and thus applies the weighted population of unoccupied states. The ―lapw2STM" routine can be executed on its own as follows:

```
x lapw2STM -p -emin [E_min]
```

and reads the file ―STM.lapw2" in the case folder as follows:

- First line: E_{max}
- Second line: 1.5 (vestige from a previous incarnation that used the incorrect Stokbro *et al.* [191] weighting; this was read as the tip radius in Å, but this is no longer relevant)

- Third line: E_{vac}

More useful than this is to run a script "a2stm.sh" which allows to explore different voltages. This is done by reading another file in the case folder called "EMAX", which lists the different E_{max} values, each followed by a label related to the voltage to which it corresponds. For the sake of clarity, let us look at an example. If one is interested in three voltages (say, 1.7 V, 2.0 V and 2.3 V), they can labeled "lo", "md" and "hi" and the E_{max} value can be calculated for each case. One would then use an "EMAX" file that looks something like this:

```
-----------------EMAX--------------------------
0.339754 lo
0.361803 md
0.383852 hi
-----------------------------------------------
```

Below is an example of the "a2stm.sh" script, with comments (preceded by "#") to help explain it:

```
------------------a2stm.sh---------------------
#!/bin/sh
#Read the folder name to use later to read and write files:
LFILE=$(basename `pwd`)
mkdir CLMfiles                #Creates subfolder to save case.clmval files
mkdir OUT2                    #Creates subfolder to save case.output2 files

#Set Emin, Evac:
EMIN=0.285                    #Any value between E_F and conduction band edge
EVAC=0.69642                  #From case.scf0

#Use "volt" variable to loop through voltage labels from EMAX
for volt in lo md hi; do        #Labels must be changed if EMAX labels change
   grep $volt EMAX > STM.lapw2  #Read an entire line from EMAX
   emx=$(awk -F " " '{ print $1 }' STM.lapw2)     #Read E_max only from line
   echo $emx > STM.lapw2            #Print E_max to input file for STM.lapw2
   echo 1.5 >> STM.lapw2            #Print vestigial second line of STM.lapw2
   echo $EVAC >> STM.lapw2          #Print E_vac as third line of STM.lapw2
  #Run lapw2STM with right E_min
   user_x lapw2STM -p -emin $EMIN
   cp $LFILE.clmval CLMfiles/$LFILE.clmval_$volt #Save each case.clmval file
   cp $LFILE.output2 OUT2/$LFILE.output2_$volt   #Save each case.output2 file
done
-----------------------------------------------
```

A.2.3. Volume Sampling of Artificial Density

At this point, the artificial state population has been completed. The pre-existing "lapw5" routine in WIEN2k can then be exploited, as it is designed to sample the density across a plane, generating a matrix of densities. It uses the "case.clmval" file as an input, which is why each of these (one per voltage) was saved with the previous script. The "lapw5" routine also uses the "case.in5" as input, which defines the plane to be sampled, the sampling intervals, etc. The density map is saved to a new file "case.rho". The routine is described in more detail in the WIEN2k user guide [46], but an example of "case.in5" follows below:

```
-----------------------2x2.in5-----------------
0 50 0   100     # Origin of plot: x,y,z, common denominator
0 50 150 100     # x-end of plot
150 50 0 100     # y-end of plot
6 6 6            # x,y,z Number of unit cells used to sample density
61 61            # Number of sampling points along x, y directions
RHO              # RHO/DIFF/OVER; ADD/SUB or blank
ANG VAL NODEBUG  # Further options, detailed in userguide
-----------------------------------------------
```

For a constant-height STM simulation, sampling a single plane (parallel to the surface) at a specified height would suffice. However, for constant-current simulations one needs to sample not a plane, but a volume, so as to generate not a 2D matrix, but a 3D array. Naturally, one can employ the "lapw5" routine and sample several parallel planes, which can be stacked later to form such an array. Therefore, a new script "stm.sh" will be used to loop over heights.

Before proceeding, however, one ought to decide what volume to sample. This involves setting the in-plane bounds ("x" and "y" co-ordinates in "case.in5") and the out-of-plane (or height) range. For the latter, the upper bound should be the middle of the vacuum, $z = 0.5$ if the slab is centered at $z = 0$. Beyond that value, one is closer to the next surface than the one being probed, which is why it is especially important for STM simulations that the vacuum spacing

between slabs has been set to be large. The lower bound should be determined by the surface structure; the best way to determine this is by visualizing the slab using software such as ATOMS and determining where the outermost atoms are. The optimal choice for this bound is a height (as a fractional coordinate, rounded to 2 decimal places, e.g. $z = 0.21$) which is just below the lowest of the atoms exposed to the vacuum. In principle, one could sample all the way down to the center of the slab, but this is computationally expensive and is unphysical, as the tip should not penetrate into the material.

The in-plane bounds should also save computational expense; while sampling the whole surface cell would work, whenever possible one should take advantage of any additional in-plane symmetry. Take for example the $SrTiO_3(001)$ "zigzag" 2×2 surface reconstruction, presented in Chapter 3. It has p2gm symmetry, consisting of a glide plane and 2-fold rotational symmetry. This implies that one fourth of the surface cell suffices to generate the rest of the surface via symmetry operations and it is therefore unnecessary to sample the whole unit cell.

While this is true, this will not be enough if in-plane blurring is to be later applied. As shall be seen below, a blurring effect (to account for thermal vibration and tip size) is added by weighting the data from nearby pixels. So if only the smallest symmetry element is sampled, spurious edge effects will arise due to pixels near the borders not having the same number of neighbors as pixels far away from the edges. This can be solved by expanding the in-plane bounds. Typically the radius of the blurring convolution feature (see below) will not exceed 2.0 Å. Therefore, that much is added to all four sides (lower and upper bounds in x and y directions). Ultimately, this additional border area will not be part of the simulated image, but will have solved our edge issues.

Now that the volume to be sampled has been established, here is an example of the aforementioned ―a5stm.sh" file, with comments:

```
-----------------------a5stm.sh----------------
#!/bin/sh
#Read the folder name to use later to read and write files:
LFILE=$(basename `pwd`)
#Define in-plane limits to sampling planes as fractional coordinates
#(First four are numerators)
x0=0       #x-axis origin
xf=150     #x-axis end
y0=0       #y-axis origin
yf=150     #y-axis end
denom=100  #Common denominator, as used in case.in5

#Use "volt" variable to loop through voltage labels
for volt in lo md hi; do     #Change voltage labels as necessary
   cp CLMfiles/$LFILE.clmval_$volt $LFILE.clmval   #Load case.clmval file
   zperc=21        #Starting height as percentage of long axis
   zheight=21      #Height numerator to match denom, needed if denom not 100
   bias=$volt"_"   #Extra variable to avoid filenaming problem later
#Loop over heights up to middle of vacuum
  until [ $zperc -gt 50 ]; do
   #Build case.in5 file line by line:
   #Make sure you have the right axes
   echo "$y0" $zheight" "$x0" "$denom > $LFILE.in5
   echo "$y0" $zheight" "$xf" "$denom >> $LFILE.in5
   echo "$yf" $zheight" "$x0" "$denom >> $LFILE.in5
   echo "6 6 6" >> $LFILE.in5
   #Edit below to match dimensions (use 20 pixels per SrTiO3 unit cell)
   echo "61 61" >> $LFILE.in5
   echo "RHO" >> $LFILE.in5
   echo "ANG VAL NODEBUG" >> $LFILE.in5
   x lapw5          #Sample artificial density
   cp $LFILE.rho $LFILE.rho_$bias$zperc   #Save density matrix file
   zheight=$((zheight+1))    #Change 1 to 2 if denom=200, and so on
   zperc=$((zperc+1))
  done
done
------------------------------------------------
```

As can be seen, the density matrix for each height is saved; in the example above, the files will be named (for the ―md" voltage case) from ―case.rho_md_21" to ―case.rho_md_50".

A.2.4. Blurring, Matrix Stacking and Generation of Isosurface

Next, the density matrices must be stacked to generate a 3D array. An additional complication is that all "case.rho…" files are formatted in an inconvenient way; an example is shown below. The first line lists the matrix dimensions $m \times n$ (61×61 here) as well as the dimensions of the plane sampled (in Bohr units). After that, the matrix follows, but listed in rows of 5 (the densities are in units of electrons per $Å^3$). Therefore, one task is to rearrange each matrix into its meaningful $m \times n$ form. For this and all further steps, the "case.rho…" files shall be exported to MATLAB.

```
------------------------2x2.rho_md_45----------------------
   61   61  22.36200  22.36200
  0.2223595E-05  0.2191511E-05  0.2427449E-05  0.2640669E-05  0.2357882E-05
  0.2120249E-05  0.2166101E-05  0.2154077E-05  0.2262763E-05  0.2255312E-05
  0.2251182E-05  0.2316274E-05  0.2327494E-05  0.2285896E-05  0.2131272E-05
  0.2202484E-05  0.2198283E-05  0.2135310E-05  0.2045486E-05  0.2020479E-05
  0.2105237E-05  0.2323246E-05  0.2465173E-05  0.2394108E-05  0.2150548E-05
[…]
-----------------------------------------------------------
```

One first, short MATLAB script is used to take stack the matrices from a particular voltage, keeping for now the 5-column configuration. The script itself, called "rhoreader.m" is shown below, with comments (each preceded by "%").

```
-----------------rhoreader.m----------------------
function Rho3d=rhoreader(casename,EM,x00,y00,minZ)

x0=x00;         %Number of sampling steps in x-direction from case.in5
y0=y00;         %Number of sampling steps in y-direction
zmin=minZ;      %Lowest sampled z as percentage
zmax=50;        %Highest sampled z

z0=zmax+1-zmin;     %Number of matrices to stack
zz=ceil(x0*y0/5);   %Number of rows in 5-column rho-file matrix

RhoArr=zeros(zz,5,z0);   %All-zeroes 3D array to be filled by planes
for i=1:z0               %Loop over planes
    j=i+zmin-1;          %Use correct height index
```

```
    str=strcat(casename, '.rho_', EM, '_', int2str(j)); %Rho file to be read
    RhoArr(:,:,i)=dlmread(str,'',1,0);    %Fill each layer of array
end
Rho3d=RhoArr;
-------------------------------------------------
```

To invoke this script, one would type, for example,

>> rhoreader(_2x2', _md', 61, 61, 21);

This outputs a 3D array which should now be saved, for example, as —2x2STMmd". One would then rerun the script to generate –z2x2STMlo" and –z2x2STMhi". These arrays should be saved to the hard drive, to avoid having to run this script again and to allow for the deletion of the –case.rho…" files. (As an aside, the name of the array should not start with a number to avoid future trouble; that is why the letter –z" was added.)

The final step is to run another script, –STMblur.m" which does the following: it rearranges the 3D array so each layer is in the proper $m \times n$ form; it applies the radially-symmetric in-plane blurring; it generates a constant-density isosurface using a specified input density; it colors the isosurface with coloring scaled with the height at each position on the surface; and, it images the colored 3D surface, viewing it down the normal axis. Since the coloring conveys the information in the out-of-plane direction, the isosurface resembles a two-dimensional STM micrograph. This major script follows in detail, commented:

```
--------------------STMblur.m--------------------------------
function y=STMblur(array,dens0,blur,x00,y00,zmin0)

x0=x00;          %Number of sampling steps in x-direction from case.in5
y0=y00;          %Number of sampling steps in y-direction
zmin=zmin0;      %Lowest sampled z as percentage
zmax=50;         %Highest sampled z
m=blur;          %Radius of blurring convolution matrix, in pixels

z0=zmax+1-zmin; %Number of planes sampled
zz=ceil(x0*y0/5);  %Number of rows in 5-column rho-file matrix
rho0=dens0;      %Specified constant density value for isosurface
total=zeros(y0,x0,z0);     %All-zeroes array of correct dimensions
```

```
for z=1:size(array,3) %Loop over planes
    %Convert each Mx5 matrix into a Px1 vector
    k=1;
    vector=zeros(zz*5); %All-zeroes vector to hold single layer
    for j=1:zz          %Loop over each row from rho-file matrix
        for i=1:5
            vector(k)=array(j,i,z); %Fill vector
            k=k+1;
        end
    end
    %Convert each Px1 vector into an nxm matrix
    k=1;
    partial=zeros(x0,y0);
    for x=1:x0
        for y=1:y0
            partial(x,y)=vector(k);
            k=k+1;
        end
    end
    B=partial';  %Transpose into a proper mxn matrix

    %Convolution matrix for blurring:
    F=zeros(2*m+1,2*m+1); A1=F; A2=F;  %Create 2 all-zeros matrices
    for x=1:2*m+1
        A1(:,x)=x-m-1;   %Matrix with equal rows, each from -m to m
    end
    for y=1:2*m+1
        A2(y,:)=y-m-1;   %Matrix with equal columns, each from -m to m
    end
    for x=1:2*m+1
       for y=1:2*m+1
         D=sqrt(A1(x,y)^2+A2(x,y)^2); %Radial distance
         %Generate convolution matrix
         %Uncomment one of next three blurring modes:
         %if D>m F(x,y)=0; else F(x,y)=exp(-(D^2)/((81/200)*m^2)); end %gauss
         %if D>m F(x,y)=0; else F(x,y)=cos(D*pi/(2*m)); end           %cosine
         if D>m F(x,y)=0; else F(x,y)=1; end                    %top-hat disc
        end
    end
    N=0;
    for x=1:2*m+1
        for y=1:2*m+1
            N=N+F(x,y);
        end
    end
    F=F/N; %Normalization of convolution matrix so sum of elements is 1
    total(:,:,z)=imfilter(B,F);  %Blurring added via convolution
end

figure()                    %Open figure window
%Coloring matrix
colors1=zeros(y0,x0,z0);
for p=1:z0
    %Set each layer to one color value, match fractional z height
    colors1(:,:,p)=zmin+p-1;
```

```
end

bckg=patch(isosurface(colors1,zmin)); %Black background
hold on
%Generate isosurface
[faces,verts,colors] = isosurface(total,rho0,colors1);
patch('Vertices', verts, 'Faces', faces, ...
    'FaceVertexCData', colors, ...
    'FaceColor','interp', ...
    'edgecolor', 'interp');
colormap gray   %can change to other scales (eg. hot, gray)
%Edit colorbar tick locations at will
colorbar('SouthOutside','XTick',[15 20 25 30 35 36 37 38 39 40 45 50])
daspect([1 1 1]); %Set aspect ratio to keep proportional dimensions
xlim([1 x0]); ylim([1 y0]);zlim([1 z0]);  %Bounds to image on MATLAB
set(gca,'XTickLabel',[],'YTickLabel',[],'ZTickLabel',[])
title({'\rho [e/au^3]=',rho0, 'm [Angs] =', m/5});  %Title for figure
-----------------------------------------------------
```

In order to invoke the "STMblur.m" script, one would type, for example,

>> STMblur(z2x2STMmd, 3e-5, 10, 61, 61, 21);

One important question is the choice of isosurface density. Clearly, the electron density is analogous to the tunneling current, as seen in Eq. A.19. However, there is no possible transformation from an experimental current value (typically in nA) to a density value (in electrons per $Å^3$). Two approaches are thus possible. The first, if the experimental corrugation is known, is to aim to match said corrugation; in practice, however, this still yields a broad range of possible values. The second, if no corrugation information is available, is to use other successful simulations as reference; this is also vague, as the range of states imaged (even for the same bias voltage) and weighting factor are not necessarily equal from system to system. However, while this does appear to yield too much freedom to the operator, it must be emphasized that it is not possible to generate an image arbitrarily; the simulated images remain severely constrained by the system in question.

Back to the "STMblur.m" script: the blurring modes will be addressed in the next subsection, but the output of the script shall be examined first. A typical example is shown in

Fig. A.1(a). However, this image includes the buffer border area that was added to avoid the border effects, so the relevant section (outlined in red in Fig. A.1(b)) must be cut out and the known symmetry operations must be exploited to finalize the simulation via tessellation. The full simulated micrograph for this surface is presented in Fig. 3.14 after some contrast and brightness adjustment.

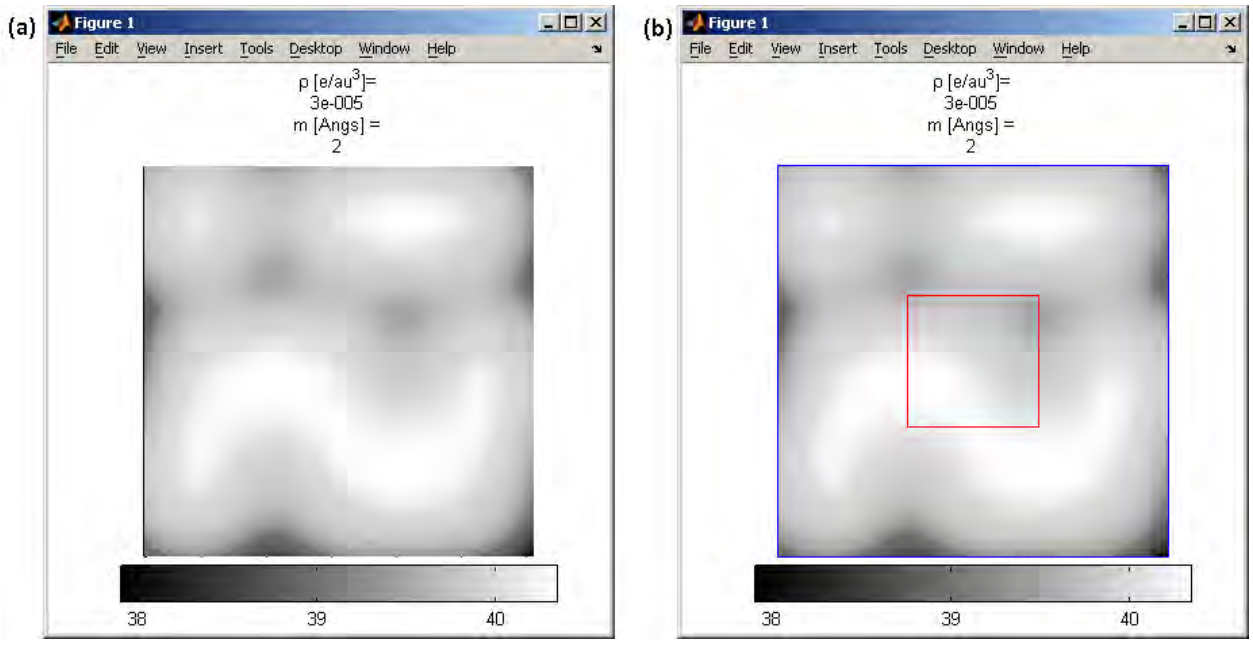

Fig. A.1. (a) MATLAB figure output. (b) Relevant symmetry element outlined in red.

A.2.5. Tests

A.2.5.1. Blurring

The added blurring is designed to account for the tip size and additional thermal vibrations. This is done via a radially-symmetric convolution feature, such that the density at a position is averaged with the densities at neighboring positions. In the implementation detailed above, this convolution is done in-plane only. Successful test simulations used a convolution feature of radius 2.0 Å, which was thereafter consistently used. This is a reasonable value under the approximation of a tip ending in a single W atom (tungsten tips were used for all experimental imaging), since the radius is 1.4 Å [192]; adding a small correction due to thermal vibrations would account for the difference.

The "STMblur.m" script includes three blurring options, one of which must be activated by uncommenting its definition line. These are shown in Fig. A.2 and are defined as follows, with respect to the characteristic radius m:

$$F(r \le m) = \begin{cases} \exp(-r^2/(0.9m)^2), & \text{Gaussian} \\ \cos(\pi r/2m), & \text{Half-cosine} \\ 1, & \text{Top-hat} \end{cases} \qquad \text{(Eq. A.24)}$$

and, $F(r > m) = 0$.

The differences in the simulations were found to be minor. The top-hat convolution feature was generally used, although the half-cosine blurring was applied in Ref. [55]. The effect of blurring with increasing convolution feature radius is shown in Fig. A.3 for a trial structure.

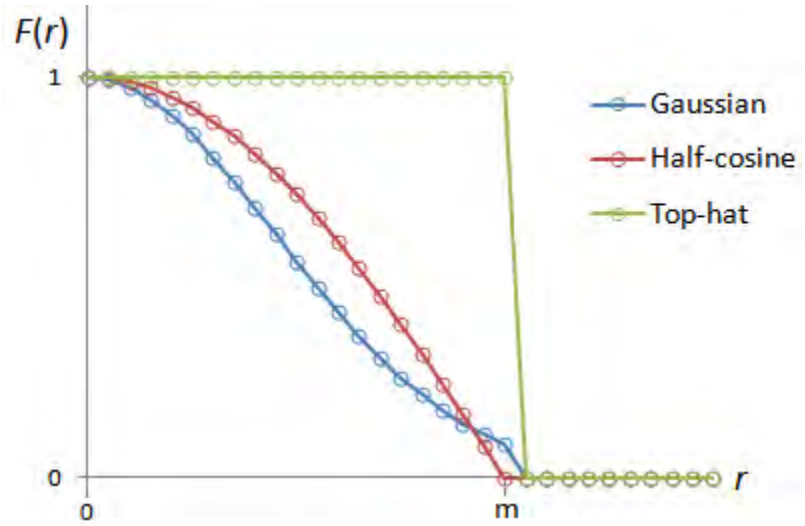

Fig. A.2. Different radially-symmetric convolution motifs for blurring.

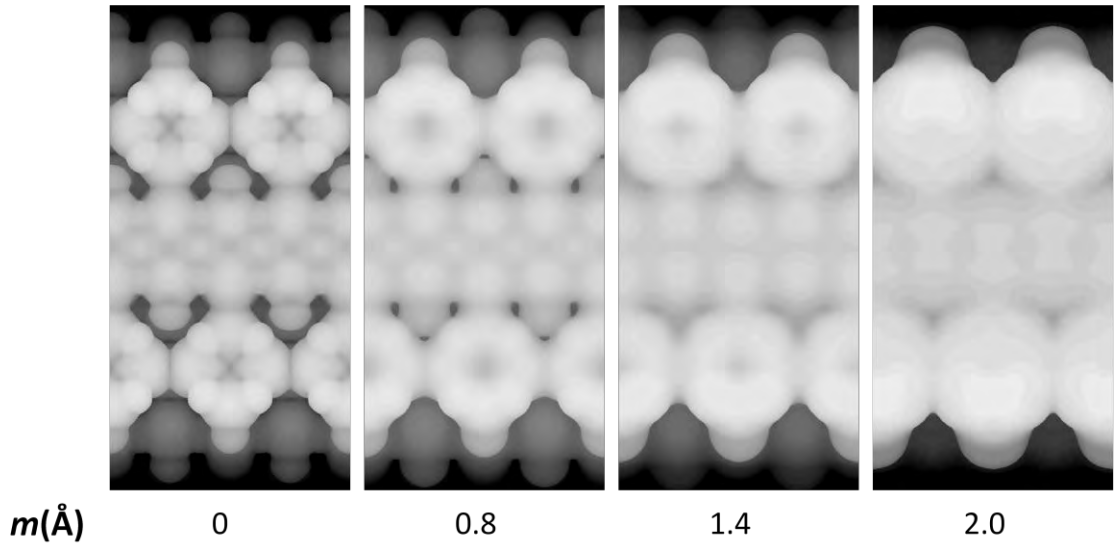

Fig. A.3. Effect of blurring motif radius on the simulated STM image for a trial triline case, with top-hat blurring.

A.2.5.2. Electric Field

Stokbro *et al.* [191] pointed out that a large bias voltage gives rise to an electric field that will have some effect on the electron density distribution. Therefore, the DFT calculations may need to be calculated incorporating an additional potential to simulate an external planar electric

field with strength determined by the bias. Such an artificial potential was added to a trial structure to determine its effect. The structure was relaxed again. The simulated STM images with and without said potential are shown in Figure A.4. While the eigenstate energies certainly did change, they did so mostly with respect to the vacuum energy, and the atomic displacements were small. As can be seen, this makes almost no difference in the STM simulations for the material in question. Therefore, given the additional computational expense, this was neglected thereafter.

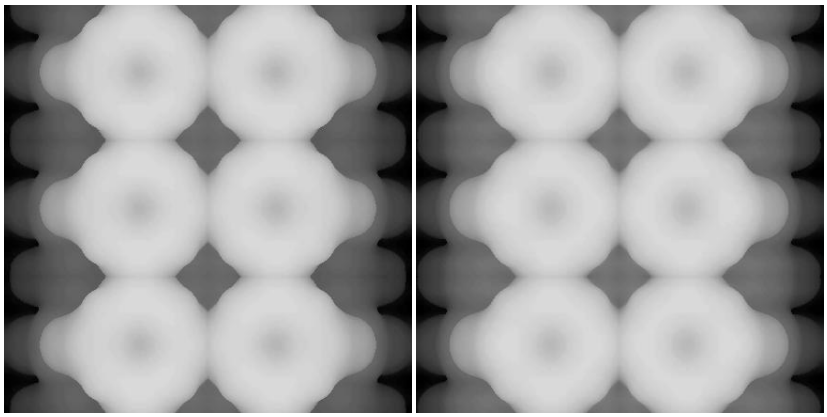

Fig. A.4. STM simulations for a trial diline structure with 1.5 V bias voltage: (left) without and (right) with an artificial planar electric field.

A.2.5.3. Exchange-Correlation Functionals

One other important parameter is, of course, the exchange correlation functional, since the PBE functional is known to overestimate the hybridization between d orbitals in transition metals (e.g. Ti) and sp orbitals in oxygen. While the d electron density in $SrTiO_3$ is relatively small, this was potentially an issue, which is why other functionals were tested on early structural models. In particular, the hybrid PBE0 [193] functional, the PBE+U approach, as well as the modified Becke-Johnson LDA [194] were all examined. All of these alternative

functionals increase the ionicity of the system. The eigenstate energies clearly shifted, but no discernible differences were found within the spatial resolution available in experimental micrographs; an example of the effect is shown in Fig. A.5 for a trial diline model. Based again on computational expense considerations, the PBE exchange-correlation functional was consistently used.

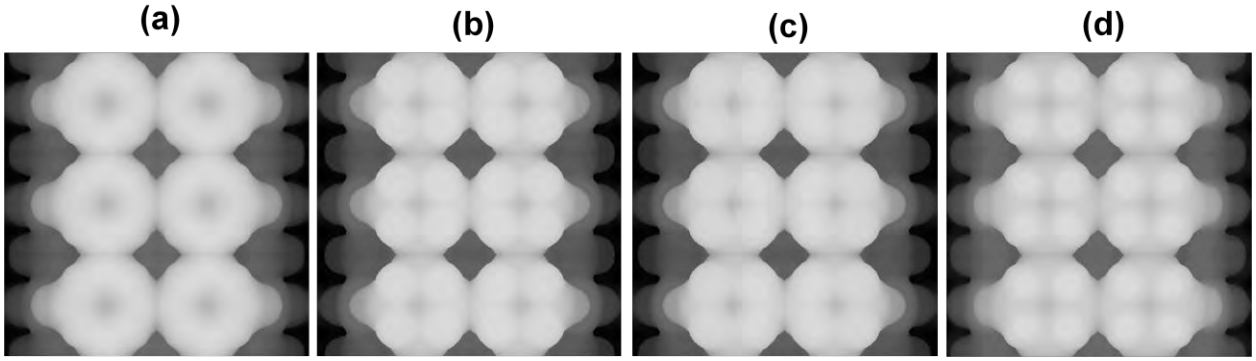

Fig. A.5. Simulated STM image for a trial diline structure with different xc functionals: (a) PBE, (b) PBE0, (c) PBE+U, and (d) modified Becke-Johnson LDA.

Appendix B. PBEsol0 Error

It is well established that the more ionic an oxide is, the more hygroscopic it is. It is also well established that many of the exchange-correlation functionals used in DFT underestimate the ionicity of oxides. The effect is best known in the middle of the transition metal series; for instance, for nickel and iron oxides where conventional functionals give rather bad results for chemisorption (see Ref. [101] and references therein), overestimating the hybridization of the metal d-states with the oxygen states. Even for titanium in $SrTiO_3$ there is an effect, despite there being an almost empty d-shell [100]. Therefore it is important when considering water chemisorption to do a reasonable job correcting for this.

The most common method currently used is to add some component of exact exchange, ideally for all atoms but this is very costly computationally. A simpler, faster method is to use an on-site Hartree-Fock hybrid method [195, 196]. A question with this approach is how much exact exchange to use. To determine, Professor Laurence D. Marks calculated the atomization energies of some representative TiO_x molecules, similar to Ref. [100], and varied the amount of

exact exchange. As an independent verification, after the calculations were completed the band gap size, the energy of the dissociation reaction

$$SrTiO_3 \rightarrow SrO + TiO_2$$

and the ratio of the (001) to (110) surface energies were checked to ensure that the results of the fitting were reasonable. The results are shown in Figure B.1 (in eV/atom) and from this it can be concluded that an appropriate fraction is 0.5(1). This is a relatively large number compared to the optimal value found for the common PBE functional, where 0.2 is common; this is reasonable, since the PBEsol functional is more covalent than PBE. The optimized PBEsol value gives a noticeably better value of 1.36 eV for the decomposition energy of $SrTiO_3$ to SrO and TiO_3 compared to previous work [100], a better band gap of ~2.8(1) eV as well as a good absolute fit to the ratio of the surface free-energy of $SrTiO_3$ (001) to (110) from Wulff construction measurements [54], none of these being part of the fitting. It should be noted that the results are not ideal, and to do better one almost certainly needs to include some correction for the oxygen atoms.

From Ref. [100], the average error in the atomization energies of the three TiO_x molecules is 0.32 eV/atom for PBE0, compared to 0.08 eV/atom for PBEsol0 (PBEsol with an exact exchange fraction of 0.5). The PBE0 surface energy error has previously been estimated to be 0.1 eV per 1×1 $SrTiO_3$(001) cell. Erring on the cautious side, a value of 0.05 eV/1×1 has been used in this study as a reasonable PBEsol0 error estimate.

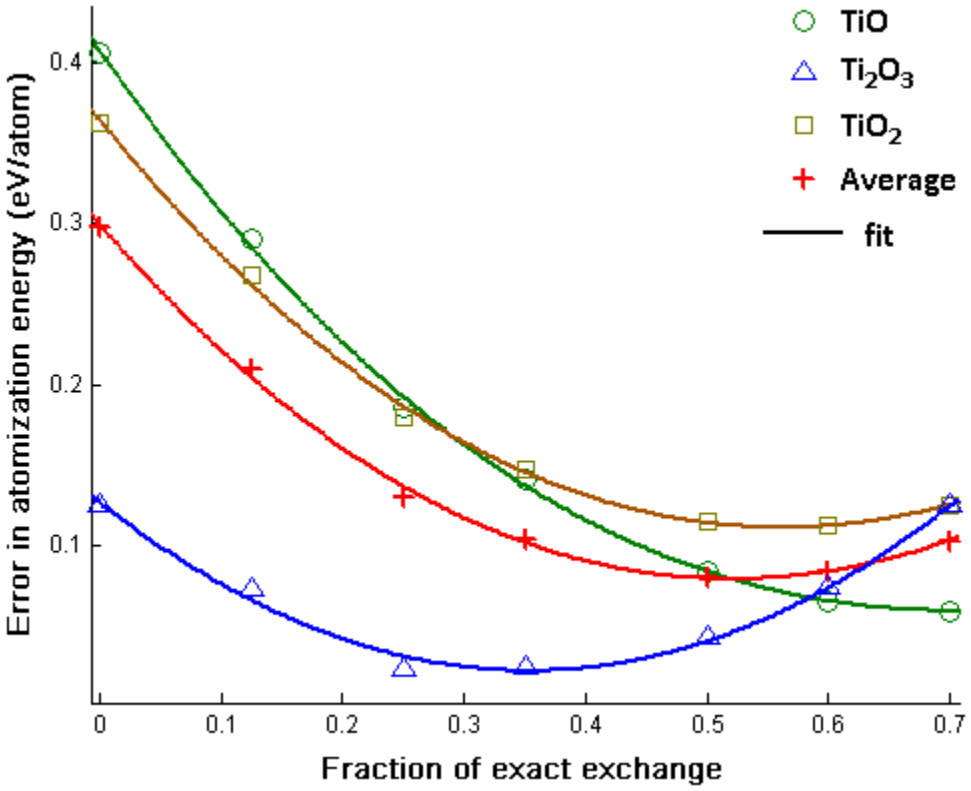

Fig. B.1. Error in atomization energy for several TiO_x molecules as a function of exact-exchange fraction, courtesy of Prof. Laurence D. Marks.

Appendix C. Functional Effect on BVS

As can be seen in Table C.1, the BVS numbers for the dry $SrTiO_3$(001) reconstructions differ considerably from those published by Enterkin *et al*. [49]. The difference lies in the exchange-correlation functional used. In an article demonstrating the usefulness of BVS in studying surface structures, Enterkin *et al.* used the PBE functional, a popular flavor of the generalized gradient approximation. On the other hand, the results reported in Chapter 5 of this dissertation use a hybrid version of the PBEsol functional (0.5 fraction of exact exchange) to determine the relaxed structure; the revTPSS correction to the total energy is applied with no change to the atomic positions, so this does not affect the BVS analysis.

The discrepancy is most obvious with atoms near the surface and the BVS values with the PBE functional are (with very few exceptions) larger in magnitude than with PBEsol0, which implies shorter bonds. The PBE numbers yield some contradictory predictions. For example:

1. Except for atom Ti2 in the 2×1, top-layer Ti have better BVS (ie. closer to +4) than second-layer Ti, in spite of being coordinated to fewer O.

2. The "dangling" oxygen atom (O1) in the dry 2×1 model, bound only to Ti1, has the same BVS as O2, which is coordinated to three Ti atoms.
3. The RT2 structure has a higher SII than the 2×2, in spite of its significantly lower surface energy.

Table C.1. Bond valence sums and surface instability indices for dry $SrTiO_3$(001) reconstruction models. PBE values are taken from Ref. [49], while PBEsol0 results are from Tables 5.2-5.5.

	2×1			**RT2**			**2×2**			**c(4×2)**		
	SII			SII			SII			SII		
		PBE	PBEsol0		PBE	PBEsol0		PBE	PBEsol0		PBE	PBEsol0
		0.22	0.28		0.15	0.13		0.14	0.17		0.17	0.18
	BVS			BVS			BVS			BVS		
		PBE	PBEsol0		PBE	PBEsol0		PBE	PBEsol0		PBE	PBEsol0
Top layer	Ti1	3.92	3.64	Ti1	4.00	3.82	Ti1	4.03	3.78	Ti1	4.07	3.86
	Ti2	3.65	3.45	O1	−2.14	−2.04	Ti2	3.94	3.70	Ti2	4.03	3.70
	O1	−1.74	−1.54	O2	−1.93	−1.84	O1	−1.95	−1.83	O1	−1.93	−1.81
	O2	−1.74	−1.68				O2	−2.17	−2.09	O2	−2.20	−2.18
	O3	−2.25	−2.20				O3	−2.01	−1.87	O3	−2.02	−1.89
	O4	−2.02	−1.88							O4	−2.56	−2.39
2nd layer	Ti3	4.11	4.01	Ti2	4.21	4.08	Ti3	3.98	3.88	Ti3	4.35	4.20
	Ti4	4.25	4.15	O3	−2.04	−1.98	Ti4	4.29	4.16	Ti4	4.02	3.96
	O5	−2.14	−2.05	O4	−2.25	−2.19	O4	−2.03	−1.93	Ti5	4.30	4.23
	O6	−1.94	−1.91				O5	−2.15	−2.06	O5	−2.03	−1.94
	O7	−1.93	−1.95				O6	−1.92	−1.93	O6	−2.15	−2.06
	O8	−2.40	−2.31				O7	−2.31	−2.24	O7	−2.20	−2.16
										O8	−1.94	−1.95

These problems disappear with PBEsol0: in particular, the RT2 clearly has the lowest SII of the four structures, and the 2×1 sees its SII go up, a picture which is much more consistent with the DFT energetics. There are two factors that contribute to the discrepancy between functionals:

1. The difference in the optimized lattice parameter. In each case, the lowest-energy bulk $SrTiO_3$ lattice constant was first calculated, then enforced for the surface calculations; for PBE, the optimal value is 3.944 Å, while PBEsol0 predicts 3.893 Å, much closer to the experimental constant of 3.905 Å. For the BVS calculations, the supercell is contracted/expanded isotropically so that the in-plane lattice constant matches the experimental value; this is necessary since the R_0 and b parameters are empirically determined. The contraction of the PBE supercell is more substantial than the expansion of PBEsol0, which may especially affect the out-of-plane component of bond lengths. However, this factor alone does not explain the observed discrepancy, which affects the near-surface atoms much more strongly.

2. The inherently different degree of bond covalency. The PBE functional overestimates the Ti-d/O-sp hybridization, making Ti–O bonds more covalent (and therefore shorter) than they should be. PBEsol0 does not only predict the lattice parameter better, it increases the ionicity of said bonds too.

Let us examine the dry 2×1 model in more detail, since it is where the largest deviations are found. The four atoms with the largest discrepancy are Ti1 (discrepancy of 0.28 valence units), Ti2 (0.20), O1 (0.20) and O4 (0.14), as labeled in the corresponding CIF. Only two bonds per surface cell involve a pair of these atoms: Ti2–O4 and Ti1–O1.

In the case of Ti2–O4, the bond is oriented mostly in-plane. In spite of the different lattice parameters, the bond lengths are originally almost the same for each functional (1.768 Å with PBE, 1.770 Å with PBEsol0); this is possible because O4 is only bound in-plane to Ti2. However, upon cell resizing, a large discrepancy arises: the bond lengths become 1.751 Å with PBE and 1.776 Å for PBEsol0. This corresponds roughly to a discrepancy of 0.08 valence units for this bond alone.

The Ti1–O1 bond is a more interesting case, since it has significant components both in and out-of-plane. The out-of-plane portion of the bond length is a clear example that the functionals give inherently different bond lengths: before any volume normalization, the PBE bond length is 1.303 Å vs. 1.342 Å for PBEsol0. While the resizing step does enhance the disparity (1.290 Å vs. 1.346 Å), it is a smaller contribution. The in-plane bond length is actually larger for PBE than for PBEsol0 (0.972 Å vs. 0.960 Å), but the supercell resizing makes them essentially equal. The overall bond length discrepancy changes from 2.5 pm without volume normalization to 4.6 pm with it, which demonstrates that both factors discussed above may play comparable roles.

This discussion highlights that the choice of DFT exchange-correlation functional is of crucial importance for chemical analysis through bond valence sum calculations, and further validates the use of the PBEsol0 functional in our study.

Appendix D. CIF Files

All relevant structures are listed in this appendix in the Crystallographic Information File (CIF) format.

D.1. Chapter 3 CIF Files

D.1.1. 2×1TiO_2

```
data_Wien2k_Data
_cell_length_a    3.892979
_cell_length_b    7.785958
_cell_length_c   38.930564
_cell_angle_alpha   90.000000
_cell_angle_beta    90.000000
_cell_angle_gamma   90.000000
_symmetry_space_group_name_H-M         'Pmmm   '
_symmetry_space_group_number   47
loop_
_symmetry_equiv_pos_as_xyz
   +x,+y,+z
   -x,-y,-z
   -x,-y,+z
   -x,+y,-z
   -x,+y,+z
   +x,-y,-z
   +x,-y,+z
   +x,+y,-z
```

```
loop_
_atom_site_label
_atom_site_type_symbol
_atom_site_fract_x
_atom_site_fract_y
_atom_site_fract_z
Ti1  Ti  0.00000000  0.50000000  0.30109099
O1   O   0.50000000  0.34739098  0.30430186
Sr1  Sr  0.50000000  0.23248202  0.24947929
O2   O   0.00000000  0.50000000  0.25491677
O3   O   0.00000000  0.00000000  0.24940021
Ti2  Ti  0.00000000  0.50000000  0.20017012
Ti3  Ti  0.00000000  0.00000000  0.20131945
O4   O   0.50000000  0.00000000  0.19751771
O5   O   0.50000000  0.50000000  0.20364670
O6   O   0.00000000  0.25278495  0.20085485
Sr2  Sr  0.50000000  0.24524599  0.15013067
O7   O   0.00000000  0.50000000  0.15110366
O8   O   0.00000000  0.00000000  0.14957113
Ti4  Ti  0.00000000  0.50000000  0.10011251
Ti5  Ti  0.00000000  0.00000000  0.10018881
O9   O   0.00000000  0.25069321  0.10009816
O10  O   0.50000000  0.50000000  0.10074151
O11  O   0.50000000  0.00000000  0.09938035
Sr3  Sr  0.50000000  0.24890043  0.05002946
O12  O   0.00000000  0.00000000  0.04990282
O13  O   0.00000000  0.50000000  0.05021938
Ti6  Ti  0.00000000  0.50000000  0.00000000
Ti7  Ti  0.00000000  0.00000000  0.00000000
O14  O   0.50000000  0.00000000  0.00000000
O15  O   0.50000000  0.50000000  0.00000000
O16  O   0.00000000  0.25034075  0.00000000
#End data_Wien2k_Data
```

D.1.2. 2×1Ti_2O_3

```
data_Wien2k_Data
_cell_length_a    3.892979
_cell_length_b    7.785958
_cell_length_c   38.930564
_cell_angle_alpha   90.000000
_cell_angle_beta    90.000000
_cell_angle_gamma   90.000000
_symmetry_space_group_name_H-M         'Pmmm   '
_symmetry_space_group_number   47
loop_
_symmetry_equiv_pos_as_xyz
   +x,+y,+z
```

```
   -x,-y,-z
   -x,-y,+z
   -x,+y,-z
   -x,+y,+z
   +x,-y,-z
   +x,-y,+z
   +x,+y,-z
loop_
_atom_site_label
_atom_site_type_symbol
_atom_site_fract_x
_atom_site_fract_y
_atom_site_fract_z
Ti1  Ti  0.00000000  0.25675374  0.29826198
O1   O   0.50000000  0.23133339  0.30077344
O2   O   0.00000000  0.50000000  0.30183544
Sr1  Sr  0.50000000  0.00000000  0.24918868
Sr2  Sr  0.50000000  0.50000000  0.24942503
O3   O   0.00000000  0.23984497  0.25122814
Ti2  Ti  0.00000000  0.24952604  0.19914086
O4   O   0.00000000  0.00000000  0.20004386
O5   O   0.00000000  0.50000000  0.20260392
O6   O   0.50000000  0.25121905  0.20097542
Sr3  Sr  0.50000000  0.50000000  0.14895829
Sr4  Sr  0.50000000  0.00000000  0.14900296
O7   O   0.00000000  0.25275147  0.15033714
Ti3 Ti  0.00000000  0.25014522  0.09955216
O8   O   0.00000000  0.50000000  0.10024008
O9   O   0.00000000  0.00000000  0.10059878
O10  O   0.50000000  0.24986362  0.10037499
Sr5 Sr  0.50000000  0.50000000  0.04961056
Sr6 Sr  0.50000000  0.00000000  0.04962378
O11  O   0.00000000  0.24980324  0.05006474
Ti4 Ti  0.00000000  0.24997464  0.00000000
O12  O   0.50000000  0.25000749  0.00000000
O13  O   0.00000000  0.50000000  0.00000000
O14  O   0.00000000  0.00000000  0.00000000
#End data_Wien2k_Data
```

D.1.3. 2×1-Sr

```
data_Wien2k_Data
_cell_length_a    7.888971
_cell_length_b    3.944485
_cell_length_c   40.000000
_cell_angle_alpha   90.000000
_cell_angle_beta    90.000000
_cell_angle_gamma   90.000000
_symmetry_space_group_name_H-M         'Pmmm    '
```

```
_symmetry_space_group_number   47
loop_
_symmetry_equiv_pos_as_xyz
   +x,+y,+z
   -x,-y,-z
   -x,-y,+z
   -x,+y,-z
   -x,+y,+z
   +x,-y,-z
   +x,-y,+z
   +x,+y,-z
loop_
_atom_site_label
_atom_site_type_symbol
_atom_site_fract_x
_atom_site_fract_y
_atom_site_fract_z
Sr1  Sr  0.00000000  0.00000000  0.19091580
Ti1  Ti  0.74098378  0.50000000  0.14496749
O1   O   0.00000000  0.50000000  0.15802170
O2   O   0.50000000  0.50000000  0.14366474
O3   O   0.75419810  0.00000000  0.15313389
Sr2  Sr  0.00000000  0.00000000  0.09471755
Sr3  Sr  0.50000000  0.00000000  0.09665048
O4   O   0.76792844  0.50000000  0.10025318
Ti2  Ti  0.74992759  0.50000000  0.04805590
O5   O   0.50000000  0.50000000  0.05138324
O6   O   0.00000000  0.50000000  0.04824027
O7   O   0.75004512  0.00000000  0.05017968
Sr4  Sr  0.00000000  0.00000000  0.00000000
Sr5  Sr  0.50000000  0.00000000  0.00000000
O8   O   0.74383709  0.50000000  0.00000000
#End data_Wien2k_Data
```

D.1.4. c(4×4)bw-Sr

```
data_Wien2k_Data
_cell_length_a   15.777941
_cell_length_b   15.777941
_cell_length_c   27.959909
_cell_angle_alpha   90.000000
_cell_angle_beta    90.000000
_cell_angle_gamma   90.000000
_symmetry_space_group_name_H-M         'Cmmm  '
_symmetry_space_group_number   65
loop_
_symmetry_equiv_pos_as_xyz
   +x,+y,+z
   -x,-y,+z
   -x,+y,-z
   +x,-y,-z
   -x,-y,-z
   +x,+y,-z
   +x,-y,+z
   -x,+y,+z
```

```
   +x+1/2,+y+1/2,+z
   -x+1/2,-y+1/2,+z
   -x+1/2,+y+1/2,-z
   +x+1/2,-y+1/2,-z
   -x+1/2,-y+1/2,-z
   +x+1/2,+y+1/2,-z
   +x+1/2,-y+1/2,+z
   -x+1/2,+y+1/2,+z
   +x+1/2,+y+1/2,+z
   -x+1/2,-y+1/2,+z
   -x+1/2,+y+1/2,-z
   +x+1/2,-y+1/2,-z
   -x+1/2,-y+1/2,-z
   +x+1/2,+y+1/2,-z
   +x+1/2,-y+1/2,+z
   -x+1/2,+y+1/2,+z
   +x,+y,+z
   -x,-y,+z
   -x,+y,-z
   +x,-y,-z
   -x,-y,-z
   +x,+y,-z
   +x,-y,+z
   -x,+y,+z
loop_
_atom_site_label
_atom_site_type_symbol
_atom_site_fract_x
_atom_site_fract_y
_atom_site_fract_z
Sr01  Sr  0.50000000  0.25094289  0.26880619
Sr02  Sr  0.00000000  0.50000000  0.27107849
Ti03  Ti  0.36706886  0.12563721  0.20837531
Ti04  Ti  0.62697455  0.37890018  0.20764617
O005  O   0.74908611  0.62532903  0.21517780
O006  O   0.62483009  0.50000000  0.21111815
O007  O   0.87859922  0.50000000  0.21796694
O008  O   0.00000000  0.12669721  0.21852270
O009  O   0.00000000  0.37434088  0.22014348
O010  O   0.12173216  0.25068540  0.21803497
Sr11  Sr  0.74890182  0.50000000  0.13814532
Sr12  Sr  0.00000000  0.50000000  0.13845318
Sr13  Sr  0.50000000  0.50000000  0.14090194
Sr14  Sr  0.25000000  0.25000000  0.13911737
Sr15  Sr  0.00000000  0.25079796  0.13739188
O016  O   0.62574354  0.37303398  0.14319845
O017  O   0.37476138  0.12502900  0.14371033
Ti18  Ti  0.62498926  0.37518133  0.06887029
Ti19  Ti  0.37479795  0.12511520  0.06882247
O020  O   0.62500996  0.50000000  0.07157718
O021  O   0.74978685  0.62512627  0.07137965
O022  O   0.87520845  0.50000000  0.07157915
O023  O   0.00000000  0.12517105  0.07172189
O024  O   0.00000000  0.37507208  0.07141948
O025  O   0.12492127  0.25041175  0.07131087
```

```
Sr26  Sr  0.50000000  0.50000000  0.00000000
Sr27  Sr  0.00000000  0.50000000  0.00000000
Sr28  Sr  0.74978795  0.50000000  0.00000000
Sr29  Sr  0.25000000  0.25000000  0.00000000
O030  O   0.37510537  0.12487590  0.00000000
O031  O   0.62490938  0.37516150  0.00000000
Sr32  Sr  0.00000000  0.25031481  0.00000000
#End data_Wien2k_Data
```

D.1.5. c(4×2)-Sr

```
data_Wien2k_Data
_cell_length_a    7.888971
_cell_length_b   15.777941
_cell_length_c   27.959909
_cell_angle_alpha   90.000000
_cell_angle_beta    90.000000
_cell_angle_gamma   90.000000
_symmetry_space_group_name_H-M         'Cmmm  '
_symmetry_space_group_number   65
loop_
_symmetry_equiv_pos_as_xyz
   +x,+y,+z
   -x,-y,+z
   -x,+y,-z
   +x,-y,-z
   -x,-y,-z
   +x,+y,-z
   +x,-y,+z
   -x,+y,+z
   +x+1/2,+y+1/2,+z
   -x+1/2,-y+1/2,+z
   -x+1/2,+y+1/2,-z
   +x+1/2,-y+1/2,-z
   -x+1/2,-y+1/2,-z
   +x+1/2,+y+1/2,-z
   +x+1/2,-y+1/2,+z
   -x+1/2,+y+1/2,+z
loop_
_atom_site_label
_atom_site_type_symbol
_atom_site_fract_x
_atom_site_fract_y
_atom_site_fract_z
Sr01  Sr  0.50000000  0.00000000  0.26713799
Ti02  Ti  0.24404943  0.12805564  0.20757173
O003  O   0.00000000  0.37589563  0.22081210
O004  O   0.50000000  0.37446570  0.21167493
O005  O   0.25254443  0.00000000  0.22022295
O006  O   0.25000000  0.25000000  0.21122738
Sr07  Sr  0.00000000  0.00000000  0.14185215
Sr08  Sr  0.50000000  0.24890259  0.14116385
Sr09  Sr  0.50000000  0.00000000  0.13606253
O010  O   0.24370014  0.37801021  0.14318128
Ti11  Ti  0.24941562  0.12512857  0.06875557
```

```
O012  O   0.25000000  0.25000000  0.07170637
O013  O   0.50000000  0.37493241  0.07175060
O014  O   0.00000000  0.37520773  0.07079586
O015  O   0.25022172  0.00000000  0.07089033
Sr16  Sr  0.50000000  0.24966815  0.00000000
Sr17  Sr  0.50000000  0.00000000  0.00000000
Sr18  Sr  0.00000000  0.00000000  0.00000000
O019  O   0.25100894  0.37458745  0.00000000
#End data_Wien2k_Data
```

D.1.6. RT5-Sr

```
data_Wien2k_Data
_cell_length_a    8.820138
_cell_length_b    8.820138
_cell_length_c   27.959909
_cell_angle_alpha   90.000000
_cell_angle_beta    90.000000
_cell_angle_gamma   90.000000
_symmetry_space_group_name_H-M         'P4/m   '
_symmetry_space_group_number   83
loop_
_symmetry_equiv_pos_as_xyz
   +x,+y,+z
   -x,-y,-z
   -x,-y,+z
   +y,-x,-z
   +y,-x,+z
   -y,+x,-z
   -y,+x,+z
   +x,+y,-z
loop_
_atom_site_label
_atom_site_type_symbol
_atom_site_fract_x
_atom_site_fract_y
_atom_site_fract_z
Sr01  Sr  0.00000000  0.00000000  0.26584737
Ti02  Ti  0.10597581  0.30838589  0.20685186
Ti03  Ti  0.50000000  0.50000000  0.20621486
O004  O   0.00000000  0.50000000  0.21072568
O005  O   0.29984551  0.40002529  0.21064208
O006  O   0.19714606  0.10086964  0.21912820
O007  O   0.09855382  0.29414907  0.14244409
Sr08  Sr  0.39859203  0.20062811  0.14107410
Sr09  Sr  0.00000000  0.00000000  0.13632991
O010  O   0.50000000  0.50000000  0.14161064
Ti11  Ti  0.10051321  0.30064895  0.06877938
Ti12  Ti  0.50000000  0.50000000  0.06911931
O013  O   0.29941640  0.40006681  0.07122403
O014  O   0.19949339  0.10007644  0.07079367
O015  O   0.00000000  0.50000000  0.07158872
Sr16  Sr  0.00000000  0.00000000  0.00000000
O017  O   0.50000000  0.50000000  0.00000000
O018  O   0.10003154  0.30099597  0.00000000
```

```
Sr19  Sr  0.39984470  0.20068787  0.00000000
#End data_Wien2k_Data
```

D.1.7. RT5-Q

```
data_Wien2k_Data
_cell_length_a    8.820138
_cell_length_b    8.820138
_cell_length_c   37.546106
_cell_angle_alpha   90.000000
_cell_angle_beta    90.000000
_cell_angle_gamma   90.000000
loop_
_symmetry_equiv_pos_as_xyz
   +x,+y,+z
   -x,-y,-z
   -x,-y,+z
   +y,-x,-z
   +y,-x,+z
   -y,+x,-z
   -y,+x,+z
   +x,+y,-z
loop_
_atom_site_label
_atom_site_type_symbol
_atom_site_fract_x
_atom_site_fract_y
_atom_site_fract_z
Ti01  Ti  0.11652369  0.21280500  0.36233883
O002  O   0.00000000  0.00000000  0.35573328
O003  O   0.92571132  0.25298231  0.38043844
O004  O   0.39004246  0.77890708  0.35627658
Sr05  Sr  0.50000000  0.50000000  0.35478777
O006  O   0.10197707  0.19928874  0.31049875
O007  O   0.50000000  0.00000000  0.30087856
O008  O   0.69549278  0.40523197  0.30104817
Ti09  Ti  0.00000000  0.00000000  0.30450019
Ti10  Ti  0.42100673  0.80185252  0.30564165
Sr11  Sr  0.89773476  0.29949368  0.25417264
Sr12  Sr  0.50000000  0.50000000  0.25299144
O013  O   0.00000000  0.00000000  0.25589481
O014  O   0.38397416  0.80620087  0.25398989
O015  O   0.09898663  0.19734387  0.20253928
O016  O   0.50000000  0.00000000  0.20288213
O017  O   0.70175847  0.40240391  0.20353250
Ti18  Ti  0.00000000  0.00000000  0.20104580
Ti19  Ti  0.39951203  0.80105367  0.20375132
Sr20  Sr  0.89948875  0.30090046  0.15209883
Sr21  Sr  0.50000000  0.50000000  0.15229720
O022  O   0.00000000  0.00000000  0.15168152
O023  O   0.39696659  0.79933783  0.15242683
O024  O   0.09996602  0.19969600  0.10114323
O025  O   0.50000000  0.00000000  0.10162472
O026  O   0.70017369  0.40053463  0.10146354
Ti27  Ti  0.00000000  0.00000000  0.10073349
```

```
Ti28  Ti  0.39959781  0.79989411  0.10164074
Sr29  Sr  0.89980453  0.30083363  0.05066405
Sr30  Sr  0.50000000  0.50000000  0.05075060
O031  O   0.00000000  0.00000000  0.05054747
O032  O   0.39992502  0.79994892  0.05075924
Ti33  Ti  0.00000000  0.00000000  0.00000000
O034  O   0.09999275  0.19991601  0.00000000
Ti35  Ti  0.39973633  0.79986789  0.00000000
O036  O   0.50000000  0.00000000  0.00000000
O037  O   0.70001416  0.40002066  0.00000000
#End data_Wien2k_Data
```

D.2. Chapter 4 CIF Files

D.2.1. D1 Diline

```
data_Wien2k_Data
_cell_length_a   23.539582
_cell_length_b    7.846534
_cell_length_c   34.999986
_cell_angle_alpha   90.000000
_cell_angle_beta    90.000000
_cell_angle_gamma   90.000000
_symmetry_space_group_name_H-M          'Pmmm   '
_symmetry_space_group_number   47
loop_
_symmetry_equiv_pos_as_xyz
   +x,+y,+z
   -x,-y,-z
   -x,-y,+z
   -x,+y,-z
   -x,+y,+z
   +x,-y,-z
   +x,-y,+z
   +x,+y,-z
loop_
_atom_site_label
_atom_site_type_symbol
_atom_site_fract_x
_atom_site_fract_y
_atom_site_fract_z
O0001  O   0.00000000  0.50000000  0.30068279
O0002  O   0.23421013  0.70363010  0.32470769
O0003  O   0.09946506  0.70029009  0.32561196
Ti004  Ti  0.07878493  0.50000000  0.30322221
O0005  O   0.16594099  0.00000000  0.29529790
Ti006  Ti  0.16683542  0.76522767  0.30387141
Ti007  Ti  0.25616520  0.50000000  0.30254948
O0008  O   0.16642844  0.50000000  0.29195637
O0009  O   0.33019035  0.50000000  0.29598983
O0010  O   0.08511693  0.00000000  0.22481164
O0011  O   0.08114200  0.50000000  0.24581737
O0012  O   0.41246372  0.50000000  0.22679488
```

Ti013	Ti	0.33617566	0.00000000	0.23225459
Ti014	Ti	0.16679705	0.00000000	0.23262860
O0015	O	0.24605903	0.00000000	0.22325296
O0016	O	0.41497914	0.00000000	0.22263531
O0017	O	0.32934557	0.77002594	0.24641756
O0018	O	0.00000000	0.76978919	0.24816489
O0019	O	0.16625488	0.75622197	0.24859076
O0020	O	0.24836635	0.50000000	0.24111976
Ti021	Ti	0.17016260	0.50000000	0.23561537
Ti022	Ti	0.33889144	0.50000000	0.24303008
Ti023	Ti	0.00000000	0.00000000	0.23335703
Ti024	Ti	0.00000000	0.50000000	0.23844745
O0025	O	0.08211069	0.25489975	0.16172921
O0026	O	0.24059682	0.25429405	0.16252639
O0027	O	0.42224228	0.26624694	0.16274639
Ti028	Ti	0.08124817	0.50000000	0.16652763
Ti029	Ti	0.08298003	0.00000000	0.16982322
Ti030	Ti	0.42243375	0.00000000	0.17303758
Ti031	Ti	0.40793521	0.50000000	0.17539072
Ti032	Ti	0.25035659	0.50000000	0.16633999
Ti033	Ti	0.25163686	0.00000000	0.16948227
O0034	O	0.50000000	0.00000000	0.16186061
O0035	O	0.33253455	0.00000000	0.17385565
O0036	O	0.32920319	0.50000000	0.17854259
O0037	O	0.16293308	0.50000000	0.18276288
O0038	O	0.16420712	0.00000000	0.17596773
O0039	O	0.00000000	0.00000000	0.17699657
O0040	O	0.00000000	0.50000000	0.18416426
Sr041	Sr	0.50000000	0.24740343	0.11448380
Sr042	Sr	0.33537942	0.24435340	0.11360891
Sr043	Sr	0.16449797	0.24304363	0.11076914
Sr044	Sr	0.00000000	0.24320754	0.10905512
O0045	O	0.25330582	0.00000000	0.11220584
O0046	O	0.25373822	0.50000000	0.11433460
O0047	O	0.08071340	0.50000000	0.11421091
O0048	O	0.08261437	0.00000000	0.11283968
O0049	O	0.41759004	0.50000000	0.11114258
O0050	O	0.40915487	0.00000000	0.11091900
O0051	O	0.07941493	0.25118915	0.05634484
O0052	O	0.24219290	0.25202741	0.05633350
O0053	O	0.40995621	0.24919898	0.05438248
Ti054	Ti	0.08463195	0.50000000	0.05479367
Ti055	Ti	0.08448139	0.00000000	0.05590173
Ti056	Ti	0.25301806	0.50000000	0.05529437
Ti057	Ti	0.25298651	0.00000000	0.05594271
Ti058	Ti	0.41858981	0.50000000	0.05810958
Ti059	Ti	0.41837924	0.00000000	0.05793442
O0060	O	0.16415167	0.50000000	0.05990472
O0061	O	0.00000000	0.00000000	0.05594132
O0062	O	0.00000000	0.50000000	0.05629534
O0063	O	0.16433789	0.00000000	0.05779589
O0064	O	0.33055175	0.50000000	0.05690964
O0065	O	0.33082345	0.00000000	0.05306807
O0066	O	0.50000000	0.50000000	0.05569741
O0067	O	0.50000000	0.00000000	0.06088877

```
Sr068  Sr  0.50000000  0.25186233  0.00000000
Sr069  Sr  0.33789767  0.24878977  0.00000000
Sr070  Sr  0.16809456  0.24482373  0.00000000
Sr071  Sr  0.00000000  0.24593696  0.00000000
O0072  O   0.24596799  0.00000000  0.00000000
O0073  O   0.24872609  0.50000000  0.00000000
O0074  O   0.08651470  0.50000000  0.00000000
O0075  O   0.08481159  0.00000000  0.00000000
O0076  O   0.41690243  0.50000000  0.00000000
O0077  O   0.42366114  0.00000000  0.00000000
#End data_Wien2k_Data
```

D.2.2. D2 Diline

```
data_Wien2k_Data
_symmetry_cell_setting     orthorhombic
_cell_length_a   23.539592
_cell_length_b    7.846531
_cell_length_c   35.000000
_cell_angle_alpha   90.000000
_cell_angle_beta    90.000000
_cell_angle_gamma   90.000000
_symmetry_space_group_name_H-M          'Pmmm   '
_symmetry_space_group_number   47
loop_
_symmetry_equiv_pos_as_xyz
   +x,+y,+z
   -x,-y,-z
   -x,-y,+z
   -x,+y,-z
   -x,+y,+z
   +x,-y,-z
   +x,-y,+z
   +x,+y,-z
loop_
  _atom_site_label
  _atom_site_fract_x
  _atom_site_fract_y
  _atom_site_fract_z
  _atom_site_U_iso_or_equiv
  _atom_site_occupancy
  _atom_site_type_symbol
O1    O   0.50000000  0.50000000  0.29508739
O2    O   0.26761022  0.70430564  0.32342877
O3    O   0.40361722  0.70278992  0.31574815
Ti4   Ti  0.42199601  0.50000000  0.29225281
O5    O   0.33313361  0.00000000  0.29243299
Ti6   Ti  0.33358706  0.76357614  0.29922182
Ti7   Ti  0.24611420  0.50000000  0.30225636
O8    O   0.33144753  0.50000000  0.28723879
O9    O   0.17184971  0.50000000  0.29362546
O10   O   0.41454173  0.00000000  0.22424320
O11   O   0.41367944  0.50000000  0.23259770
O12   O   0.00000000  0.50000000  0.15756685
Ti13  Ti  0.16050650  0.00000000  0.23011682
```

Ti14	Ti	0.33183889	0.00000000	0.23137712
O15	O	0.25191405	0.00000000	0.22392906
O16	O	0.08368293	0.00000000	0.22214290
O17	O	0.16213399	0.75592381	0.23948307
O18	O	0.50000000	0.76036202	0.24027416
O19	O	0.33180563	0.75503187	0.24441565
O20	O	0.24873927	0.50000000	0.23952696
Ti21	Ti	0.33265798	0.50000000	0.23024914
Ti22	Ti	0.17042898	0.50000000	0.24066525
Ti23	Ti	0.50000000	0.00000000	0.23025322
Ti24	Ti	0.50000000	0.50000000	0.23453014
O25	O	0.41466224	0.25393065	0.16446979
O26	O	0.24926867	0.25231492	0.16338307
O27	O	0.08181430	0.25485024	0.16268999
Ti28	Ti	0.41872459	0.50000000	0.16855628
Ti29	Ti	0.41556496	0.00000000	0.16865099
Ti30	Ti	0.07715429	0.00000000	0.17148536
Ti31	Ti	0.08080017	0.50000000	0.16080960
Ti32	Ti	0.24133270	0.50000000	0.16537160
Ti33	Ti	0.24778398	0.00000000	0.16933082
O34	O	0.00000000	0.00000000	0.16069273
O35	O	0.16646233	0.00000000	0.17354111
O36	O	0.16420711	0.50000000	0.18076733
O37	O	0.32808061	0.50000000	0.17711325
O38	O	0.33309857	0.00000000	0.17499492
O39	O	0.50000000	0.00000000	0.17501068
O40	O	0.50000000	0.50000000	0.17356404
Sr41	Sr	0.00000000	0.23961984	0.11247751
Sr42	Sr	0.16539627	0.23770144	0.11384573
Sr43	Sr	0.33243861	0.24911047	0.11337691
Sr44	Sr	0.50000000	0.25069865	0.11293409
O45	O	0.25050003	0.00000000	0.11217372
O46	O	0.23894649	0.50000000	0.11310603
O47	O	0.41922145	0.50000000	0.11377679
O48	O	0.41761428	0.00000000	0.11343436
O49	O	0.09941983	0.50000000	0.11066796
O50	O	0.08904539	0.00000000	0.11002427
O51	O	0.41703559	0.25027345	0.05605403
O52	O	0.25078436	0.25177888	0.05586929
O53	O	0.08349026	0.25259954	0.05507397
Ti54	Ti	0.41557878	0.50000000	0.05662383
Ti55	Ti	0.41682511	0.00000000	0.05630893
Ti56	Ti	0.24840142	0.50000000	0.05454881
Ti57	Ti	0.25037863	0.00000000	0.05640153
Ti58	Ti	0.08248812	0.50000000	0.05434167
Ti59	Ti	0.08365877	0.00000000	0.05694809
O60	O	0.33304004	0.50000000	0.06242684
O61	O	0.50000000	0.00000000	0.05726932
O62	O	0.50000000	0.50000000	0.05533647
O63	O	0.33464262	0.00000000	0.05769957
O64	O	0.16734984	0.50000000	0.04780835
O65	O	0.16863875	0.00000000	0.05440431
O66	O	0.00000000	0.50000000	0.06408252
O67	O	0.00000000	0.00000000	0.05679889
Sr68	Sr	0.00000000	0.23811585	0.00000000

```
Sr69  Sr  0.16621386  0.24117690  0.00000000
Sr70  Sr  0.33351066  0.24604289  0.00000000
Sr71  Sr  0.50000000  0.25060993  0.00000000
O72   O   0.25459084  0.00000000  0.00000000
O73   O   0.26114496  0.50000000  0.00000000
O74   O   0.41130861  0.50000000  0.00000000
O75   O   0.41734643  0.00000000  0.00000000
O76   O   0.07147114  0.50000000  0.00000000
O77   O   0.08339184  0.00000000  0.00000000
#End data_Wien2k_Data
```

D.2.3. T1 Triline

```
data_Wien2k_Data
_cell_length_a    7.846531
_cell_length_b   31.999987
_cell_length_c   31.386096
_cell_angle_alpha   90.000000
_cell_angle_beta    90.000000
_cell_angle_gamma   90.000000
_symmetry_space_group_name_H-M          'Pmma   '
_symmetry_space_group_number   51
loop_
_symmetry_equiv_pos_as_xyz
   +x,+y,+z
   -x,-y,-z
   -x,+y,-z
   +x,-y,+z
   -x+1/2,+y,+z
   +x+1/2,-y,-z
   -x+1/2,-y,+z
   +x+1/2,+y,-z
loop_
_atom_site_label
_atom_site_type_symbol
_atom_site_fract_x
_atom_site_fract_y
_atom_site_fract_z
O0001  O   0.75000000  0.32277814  0.13049566
O0002  O   0.55083919  0.34874482  0.30379571
O0003  O   0.54826163  0.35531342  0.20260264
Ti004  Ti  0.75000000  0.33218606  0.18608258
O0005  O   0.25000000  0.32344471  0.25123219
Ti006  Ti  0.48461298  0.32927415  0.25196920
Ti007  Ti  0.75000000  0.32313395  0.31797188
O0008  O   0.25000000  0.31453937  0.37991394
O0009  O   0.98395560  0.33350626  0.43902647
O0010  O   0.25000000  0.31012780  0.49863085
Ti011  Ti  0.75000000  0.31964392  0.44026578
Ti012  Ti  0.25000000  0.31871761  0.43681544
O0013  O   0.75000000  0.31522224  0.25007934
O0014  O   0.75000000  0.31494745  0.37447506
O0015  O   0.25000000  0.24517987  0.18759073
O0016  O   0.75000000  0.26324234  0.18676066
O0017  O   0.75000000  0.25447109  0.43648127
```

Ti018	Ti	0.25000000	0.25908265	0.37018557
Ti019	Ti	0.25000000	0.25348740	0.24740377
O0020	O	0.25000000	0.24398716	0.30859466
O0021	O	0.25000000	0.25516602	0.43541889
O0022	O	0.50420179	0.25349179	0.37025441
O0023	O	0.49660001	0.26245450	0.12026555
O0024	O	0.49075207	0.26986983	0.24811670
O0025	O	0.75000000	0.25738528	0.30869672
O0026	O	0.00000000	0.24701304	0.50000000
O0027	O	0.25000000	0.24234482	0.06115365
Ti028	Ti	0.25000000	0.25134636	0.49869057
Ti029	Ti	0.75000000	0.25396531	0.25023425
Ti030	Ti	0.75000000	0.25224330	0.37569330
Ti031	Ti	0.25000000	0.25101601	0.11807166
Ti032	Ti	0.75000000	0.26548039	0.12811509
O0033	O	0.50248845	0.17872902	0.18668509
O0034	O	0.50195598	0.17738842	0.30808060
O0035	O	0.49871896	0.17744633	0.43541905
Ti036	Ti	0.75000000	0.18139807	0.18139181
Ti037	Ti	0.25000000	0.18616970	0.18523367
Ti038	Ti	0.25000000	0.18122596	0.43327142
Ti039	Ti	0.75000000	0.18026021	0.43848198
Ti040	Ti	0.75000000	0.18058209	0.31222544
Ti041	Ti	0.25000000	0.18474019	0.31151514
Ti042	Ti	0.25000000	0.18691591	0.05563250
Ti043	Ti	0.75000000	0.17658384	0.06245299
O0044	O	0.25000000	0.17497798	0.99792235
O0045	O	0.99526219	0.17760080	0.06129083
O0046	O	0.25000000	0.18459739	0.50167991
O0047	O	0.25000000	0.18666854	0.37359323
O0048	O	0.75000000	0.18807264	0.37164811
O0049	O	0.75000000	0.19636500	0.24668469
O0050	O	0.25000000	0.19181671	0.24818632
O0051	O	0.25000000	0.19005602	0.12417554
O0052	O	0.75000000	0.19686582	0.12399701
Sr053	Sr	0.50000000	0.12570545	0.50000000
Sr054	Sr	0.49924891	0.12379789	0.37289961
Sr055	Sr	0.49622178	0.12302511	0.24760341
Sr056	Sr	0.48689928	0.12460055	0.12373136
Sr057	Sr	0.00000000	0.12318878	0.00000000
O0058	O	0.25000000	0.12026542	0.06640624
O0059	O	0.75000000	0.12133024	0.07257412
O0060	O	0.25000000	0.12184943	0.31153614
O0061	O	0.75000000	0.12356008	0.31028227
O0062	O	0.75000000	0.12419330	0.18245428
O0063	O	0.25000000	0.12221702	0.18769360
O0064	O	0.75000000	0.12292458	0.43490317
O0065	O	0.25000000	0.12302059	0.43702606
O0066	O	0.50119004	0.06098787	0.18760968
O0067	O	0.50093376	0.06065359	0.31202532
O0068	O	0.50003430	0.06055537	0.43716478
Ti069	Ti	0.75000000	0.05974356	0.18804387
Ti070	Ti	0.25000000	0.06149101	0.18458543
Ti071	Ti	0.75000000	0.06014913	0.31301283
Ti072	Ti	0.25000000	0.06172896	0.30933998

```
Ti073  Ti  0.75000000  0.06049266  0.43927128
Ti074  Ti  0.25000000  0.06086055  0.43484267
Ti075  Ti  0.25000000  0.06251757  0.05936662
Ti076  Ti  0.75000000  0.05924418  0.06545574
O0077  O   0.25000000  0.06400685  0.99934304
O0078  O   0.99751207  0.06020796  0.06241030
O0079  O   0.75000000  0.06475081  0.24866208
O0080  O   0.25000000  0.05964447  0.12607323
O0081  O   0.75000000  0.05627240  0.12549956
O0082  O   0.25000000  0.06109917  0.25057533
O0083  O   0.75000000  0.06215514  0.37269315
O0084  O   0.25000000  0.06195110  0.37618662
O0085  O   0.75000000  0.06270045  0.49824222
Sr086  Sr  0.50000000  0.00000000  0.50000000
Sr087  Sr  0.49724652  0.00000000  0.37340604
Sr088  Sr  0.49568125  0.00000000  0.24884689
Sr089  Sr  0.49222382  0.00000000  0.12403069
Sr090  Sr  0.00000000  0.00000000  0.00000000
O0091  O   0.25000000  0.00000000  0.06134311
O0092  O   0.75000000  0.00000000  0.06037487
O0093  O   0.25000000  0.00000000  0.31421182
O0094  O   0.75000000  0.00000000  0.30978246
O0095  O   0.75000000  0.00000000  0.19120164
O0096  O   0.25000000  0.00000000  0.18925729
O0097  O   0.75000000  0.00000000  0.43632609
O0098  O   0.25000000  0.00000000  0.43901942
#End data_Wien2k_Data
```

D.2.4. T2 Triline

```
data_Wien2k_Data
_symmetry_cell_setting     orthorhombic
_cell_length_a   31.386123
_cell_length_b    7.846531
_cell_length_c   32.000000
_cell_angle_alpha   90.000000
_cell_angle_beta    90.000000
_cell_angle_gamma   90.000000
_symmetry_space_group_name_H-M         'Pbmm   '
_symmetry_space_group_number   51
loop_
_symmetry_equiv_pos_as_xyz
    +x,+y,+z
    -x,-y,-z
    -x,-y,+z
    +x,+y,-z
    +x,-y+1/2,+z
    -x,+y+1/2,-z
    +x,-y+1/2,-z
    -x,+y+1/2,+z
loop_
_atom_site_label
_atom_site_type_symbol
_atom_site_fract_x
_atom_site_fract_y
```

```
_atom_site_fract_z
O1    O   0.12838864  0.75000000  0.32234252
O2    O   0.30279951  0.55113936  0.34784964
O3    O   0.20100577  0.54757522  0.35464235
Ti4   Ti  0.18445319  0.75000000  0.33134976
O5    O   0.24978378  0.25000000  0.32275407
Ti6   Ti  0.25049326  0.48535922  0.32854383
Ti7   Ti  0.31663210  0.75000000  0.32174670
O8    O   0.37509537  0.25000000  0.31404932
O9    O   0.44125087  0.00028331  0.33111411
O10   O   0.49877799  0.25000000  0.32127909
Ti11  Ti  0.50000000  0.00000000  0.31349521
Ti12  Ti  0.43458931  0.75000000  0.31249575
Ti13  Ti  0.43052357  0.25000000  0.31502271
O14   O   0.24904086  0.75000000  0.31520469
O15   O   0.37464792  0.75000000  0.31727122
O16   O   0.18661005  0.25000000  0.24538545
O17   O   0.18563538  0.75000000  0.26401788
O18   O   0.43578493  0.75000000  0.25036708
Ti19  Ti  0.36616106  0.25000000  0.25571563
Ti20  Ti  0.24508629  0.25000000  0.25307778
O21   O   0.30779279  0.25000000  0.24464320
O22   O   0.43505869  0.25000000  0.25646230
O23   O   0.37011175  0.50510500  0.25392339
O24   O   0.11964168  0.49725624  0.26215943
O25   O   0.24694464  0.49216934  0.26924560
O26   O   0.30739631  0.75000000  0.25677775
O27   O   0.50000000  0.00000000  0.25446917
O28   O   0.06089369  0.25000000  0.24220860
Ti29  Ti  0.50209991  0.25000000  0.25362948
Ti30  Ti  0.24816455  0.75000000  0.25339545
Ti31  Ti  0.37279051  0.75000000  0.25141647
Ti32  Ti  0.11800665  0.25000000  0.25103147
Ti33  Ti  0.12677328  0.75000000  0.26463930
O34   O   0.18607137  0.50262411  0.17829492
O35   O   0.30749053  0.50312377  0.17785056
O36   O   0.43648032  0.50167428  0.18086567
Ti37  Ti  0.18072941  0.75000000  0.18073124
Ti38  Ti  0.18474411  0.25000000  0.18469073
Ti39  Ti  0.43659816  0.25000000  0.18379326
Ti40  Ti  0.43757637  0.75000000  0.18634259
Ti41  Ti  0.31138702  0.75000000  0.18046178
Ti42  Ti  0.31105665  0.25000000  0.18275426
Ti43  Ti  0.05573292  0.25000000  0.18634650
Ti44  Ti  0.06227679  0.75000000  0.17655150
O45   O   0.99783417  0.25000000  0.17474465
O46   O   0.06132808  0.99543752  0.17733122
O47   O   0.49902721  0.25000000  0.18793664
O48   O   0.37250809  0.25000000  0.18874959
O49   O   0.37121915  0.75000000  0.18553307
O50   O   0.24509060  0.75000000  0.19599714
O51   O   0.24749025  0.25000000  0.19225155
O52   O   0.12381817  0.25000000  0.18999732
O53   O   0.12342473  0.75000000  0.19762630
Sr54  Sr  0.50000000  0.50000000  0.12684867
```

```
Sr55  Sr  0.37490494  0.50100439  0.12571150
Sr56  Sr  0.24775661  0.49643239  0.12241080
Sr57  Sr  0.12329663  0.48691061  0.12370430
Sr58  Sr  0.00000000  0.00000000  0.12277011
O59   O   0.06691800  0.25000000  0.12034532
O60   O   0.07297285  0.75000000  0.12106485
O61   O   0.31111570  0.25000000  0.12283124
O62   O   0.30892481  0.75000000  0.12322245
O63   O   0.18036891  0.75000000  0.12355267
O64   O   0.18749796  0.25000000  0.12258596
O65   O   0.43684176  0.75000000  0.12307683
O66   O   0.43665103  0.25000000  0.12547164
O67   O   0.18738343  0.50084492  0.06095548
O68   O   0.31205816  0.50058569  0.06065997
O69   O   0.43737250  0.49867153  0.06166478
Ti70  Ti  0.18821599  0.75000000  0.05960504
Ti71  Ti  0.18527058  0.25000000  0.06099388
Ti72  Ti  0.31353737  0.75000000  0.06068237
Ti73  Ti  0.31091393  0.25000000  0.06112125
Ti74  Ti  0.43957808  0.75000000  0.06309641
Ti75  Ti  0.43578358  0.25000000  0.06144684
Ti76  Ti  0.05954660  0.25000000  0.06252643
Ti77  Ti  0.06514073  0.75000000  0.05902954
O78   O   0.99956788  0.25000000  0.06522168
O79   O   0.06242371  0.99792666  0.06022365
O80   O   0.24810646  0.75000000  0.06518017
O81   O   0.12620826  0.25000000  0.05929927
O82   O   0.12482147  0.75000000  0.05426269
O83   O   0.25090377  0.25000000  0.06155949
O84   O   0.37305840  0.75000000  0.06249437
O85   O   0.37575113  0.25000000  0.06303984
O86   O   0.49977079  0.75000000  0.06272027
Sr87  Sr  0.50000000  0.50000000  0.00000000
Sr88  Sr  0.37556441  0.50121934  0.00000000
Sr89  Sr  0.24972345  0.49629570  0.00000000
Sr90  Sr  0.12387583  0.49194524  0.00000000
Sr91  Sr  0.00000000  0.00000000  0.00000000
O92   O   0.06068847  0.25000000  0.00000000
O93   O   0.05752998  0.75000000  0.00000000
O94   O   0.31437552  0.25000000  0.00000000
O95   O   0.30934978  0.75000000  0.00000000
O96   O   0.19212685  0.75000000  0.00000000
O97   O   0.18983798  0.25000000  0.00000000
O98   O   0.43677884  0.75000000  0.00000000
O99   O   0.43758502  0.25000000  0.00000000
#End data_Wien2k_Data
```

D.2.5. T3 Triline

```
data_Wien2k_Data
_cell_length_a    7.846531
_cell_length_b   30.291748
_cell_length_c   31.386096
```

```
_cell_angle_alpha   90.000000
_cell_angle_beta    90.000000
_cell_angle_gamma   90.000000
_symmetry_space_group_name_H-M          'Pmmm   '
_symmetry_space_group_number   47
loop_
_symmetry_equiv_pos_as_xyz
   +x,+y,+z
   -x,-y,-z
   -x,-y,+z
   -x,+y,-z
   -x,+y,+z
   +x,-y,-z
   +x,-y,+z
   +x,+y,-z
loop_
_atom_site_label
_atom_site_type_symbol
_atom_site_fract_x
_atom_site_fract_y
_atom_site_fract_z
O0001  O   0.50000000  0.27244132  0.12587443
O0002  O   0.30199156  0.30769664  0.30097404
O0003  O   0.29956243  0.30341429  0.19945204
Ti004  Ti  0.50000000  0.27746174  0.18023034
O0005  O   0.00000000  0.27538518  0.24981954
Ti006  Ti  0.23510863  0.28118450  0.24953728
Ti007  Ti  0.50000000  0.28178671  0.31444431
O0008  O   0.00000000  0.26704223  0.37496615
O0009  O   0.74731926  0.27333160  0.43694437
O0010  O   0.00000000  0.27675377  0.50000000
O0011  O   0.50000000  0.27552467  0.50000000
Ti012  Ti  0.75128134  0.20687596  0.43714494
Ti013  Ti  0.50000000  0.26940984  0.44035049
Ti014  Ti  0.00000000  0.27024618  0.43936063
O0015  O   0.50000000  0.26571209  0.25282716
O0016  O   0.50000000  0.26679383  0.37187458
O0017  O   0.00000000  0.19308768  0.18936871
O0018  O   0.50000000  0.20794040  0.18747710
O0019  O   0.50000000  0.20129955  0.43396967
Ti020  Ti  0.00000000  0.21079503  0.36434999
Ti021  Ti  0.00000000  0.20108057  0.24509026
O0022  O   0.00000000  0.19482092  0.30973603
O0023  O   0.00000000  0.20138976  0.43320563
O0024  O   0.25260497  0.20219939  0.37662014
O0025  O   0.23576396  0.21262988  0.12509489
O0026  O   0.24304836  0.21869512  0.24997731
O0027  O   0.50000000  0.20553656  0.31045536
O0028  O   0.74975617  0.20250535  0.50000000
O0029  O   0.00000000  0.19006025  0.06295670
O0030  O   0.50000000  0.19309158  0.06186225
Ti031  Ti  0.50000000  0.20729378  0.50000000
Ti032  Ti  0.00000000  0.20808028  0.50000000
Ti033  Ti  0.50000000  0.20171396  0.24399045
Ti034  Ti  0.50000000  0.20313533  0.36637908
```

Ti035	Ti	0.00000000	0.20097725	0.11942780
Ti036	Ti	0.50000000	0.20946175	0.11559314
O0037	O	0.25305076	0.12382715	0.18916858
O0038	O	0.25334565	0.12268580	0.31130647
O0039	O	0.25227584	0.13353620	0.43808218
Ti040	Ti	0.50000000	0.12663627	0.18262663
Ti041	Ti	0.00000000	0.12802791	0.18416425
Ti042	Ti	0.00000000	0.12727927	0.43660176
Ti043	Ti	0.50000000	0.12672492	0.43838130
Ti044	Ti	0.50000000	0.12485526	0.31180152
Ti045	Ti	0.00000000	0.12768627	0.31225370
Ti046	Ti	0.00000000	0.13139079	0.05695403
Ti047	Ti	0.50000000	0.13228519	0.05725624
O0048	O	0.50000000	0.11976341	0.00000000
O0049	O	0.00000000	0.11819791	0.00000000
O0050	O	0.74705623	0.12199066	0.06113397
O0051	O	0.00000000	0.13609371	0.50000000
O0052	O	0.50000000	0.13422864	0.50000000
O0053	O	0.00000000	0.13367564	0.37557030
O0054	O	0.50000000	0.13565098	0.37332585
O0055	O	0.50000000	0.14128946	0.25081364
O0056	O	0.00000000	0.13700241	0.25146332
O0057	O	0.00000000	0.13333279	0.12619355
O0058	O	0.50000000	0.13758401	0.12662244
Sr059	Sr	0.24790156	0.06287689	0.50000000
Sr060	Sr	0.24708836	0.06446178	0.37177248
Sr061	Sr	0.24683866	0.06519051	0.24525099
Sr062	Sr	0.24853590	0.06737291	0.11876674
Sr063	Sr	0.25171702	0.06574382	0.00000000
O0064	O	0.00000000	0.06204827	0.06826194
O0065	O	0.50000000	0.06228558	0.06866264
O0066	O	0.00000000	0.06481353	0.31529619
O0067	O	0.50000000	0.06481721	0.31372963
O0068	O	0.50000000	0.06545801	0.19050071
O0069	O	0.00000000	0.06483201	0.19182772
O0070	O	0.50000000	0.06722063	0.43788330
O0071	O	0.00000000	0.06729206	0.43901344
O0072	O	0.25076522	0.00000000	0.19162223
O0073	O	0.25055589	0.00000000	0.31608707
O0074	O	0.24995634	0.00000000	0.43947587
Ti075	Ti	0.50000000	0.00000000	0.18425791
Ti076	Ti	0.00000000	0.00000000	0.18434222
Ti077	Ti	0.50000000	0.00000000	0.31001645
Ti078	Ti	0.00000000	0.00000000	0.31017211
Ti079	Ti	0.50000000	0.00000000	0.43650457
Ti080	Ti	0.00000000	0.00000000	0.43671944
Ti081	Ti	0.00000000	0.00000000	0.06071846
Ti082	Ti	0.50000000	0.00000000	0.06103033
O0083	O	0.50000000	0.00000000	0.00000000
O0084	O	0.00000000	0.00000000	0.00000000
O0085	O	0.74988153	0.00000000	0.06324950
O0086	O	0.50000000	0.00000000	0.25313377
O0087	O	0.00000000	0.00000000	0.12828328
O0088	O	0.50000000	0.00000000	0.12831424
O0089	O	0.00000000	0.00000000	0.25347635

```
O0090  O   0.50000000  0.00000000  0.37727810
O0091  O   0.00000000  0.00000000  0.37791722
O0092  O   0.50000000  0.00000000  0.50000000
O0093  O   0.00000000  0.00000000  0.50000000
#End data_Wien2k_Data
```

D.2.6. T4 Triline

```
data_Wien2k_Data
_cell_length_a    7.846531
_cell_length_b   31.999987
_cell_length_c   31.386096
_cell_angle_alpha   90.000000
_cell_angle_beta    90.000000
_cell_angle_gamma   90.000000
_symmetry_space_group_name_H-M          'Pmma   '
_symmetry_space_group_number   51
loop_
_symmetry_equiv_pos_as_xyz
   +x,+y,+z
   -x,-y,-z
   -x,+y,-z
   +x,-y,+z
   -x+1/2,+y,+z
   +x+1/2,-y,-z
   -x+1/2,-y,+z
   +x+1/2,+y,-z
loop_
_atom_site_label
_atom_site_type_symbol
_atom_site_fract_x
_atom_site_fract_y
_atom_site_fract_z
O0001  O   0.75000000  0.32104987  0.13058130
O0002  O   0.55128363  0.34455744  0.30641251
O0003  O   0.54849676  0.35248837  0.20314213
Ti004  Ti  0.75000000  0.32951961  0.18624490
O0005  O   0.25000000  0.32477235  0.25231125
Ti006  Ti  0.48286820  0.32690662  0.25262127
Ti007  Ti  0.75000000  0.31835054  0.31620758
O0008  O   0.99874302  0.32633740  0.43898955
O0009  O   0.25000000  0.32163383  0.49891132
Ti010  Ti  0.00000000  0.31236399  0.50000000
Ti011  Ti  0.75000000  0.30872346  0.43234594
Ti012  Ti  0.25000000  0.30853982  0.43667645
O0013  O   0.75000000  0.31297281  0.25160650
O0014  O   0.25000000  0.24358186  0.18856603
O0015  O   0.75000000  0.26248060  0.18664592
O0016  O   0.75000000  0.25053109  0.43621584
Ti017  Ti  0.25000000  0.24735101  0.36876144
Ti018  Ti  0.25000000  0.24981372  0.24729290
O0019  O   0.25000000  0.24299384  0.30848879
O0020  O   0.25000000  0.24921682  0.43538870
O0021  O   0.48639541  0.26066802  0.37131998
O0022  O   0.49475900  0.26153366  0.12110303
```

O0023	O	0.48841652	0.26842542	0.24832017
O0024	O	0.75000000	0.25252246	0.30911434
O0025	O	0.00000000	0.25340023	0.50000000
O0026	O	0.25000000	0.24086053	0.06164357
Ti027	Ti	0.25000000	0.25100518	0.49826761
Ti028	Ti	0.75000000	0.25175480	0.25041737
Ti029	Ti	0.75000000	0.25114952	0.37181262
Ti030	Ti	0.25000000	0.25001057	0.11833532
Ti031	Ti	0.75000000	0.26347054	0.12863078
O0032	O	0.50166282	0.17740957	0.18638410
O0033	O	0.50323304	0.17796536	0.30848015
O0034	O	0.50223949	0.18074920	0.43627574
Ti035	Ti	0.75000000	0.17949103	0.18099340
Ti036	Ti	0.25000000	0.18387671	0.18432480
Ti037	Ti	0.25000000	0.18399764	0.43843545
Ti038	Ti	0.75000000	0.18453230	0.43605304
Ti039	Ti	0.75000000	0.18086018	0.31230585
Ti040	Ti	0.25000000	0.18096677	0.30994164
Ti041	Ti	0.25000000	0.18533780	0.05510886
Ti042	Ti	0.75000000	0.17563875	0.06227507
O0043	O	0.25000000	0.17452643	0.99787366
O0044	O	0.99451217	0.17695100	0.06136885
O0045	O	0.25000000	0.18583842	0.50004912
O0046	O	0.25000000	0.18718705	0.37260450
O0047	O	0.75000000	0.18434304	0.37215287
O0048	O	0.75000000	0.19484408	0.24419964
O0049	O	0.25000000	0.19033675	0.24837075
O0050	O	0.25000000	0.18926454	0.12479758
O0051	O	0.75000000	0.19650168	0.12386727
Sr052	Sr	0.50000000	0.12613858	0.50000000
Sr053	Sr	0.49968116	0.12445375	0.37508534
Sr054	Sr	0.49785992	0.12167436	0.24798839
Sr055	Sr	0.48696141	0.12292615	0.12363577
Sr056	Sr	0.00000000	0.12171858	0.00000000
O0057	O	0.25000000	0.11965580	0.06698637
O0058	O	0.75000000	0.12044570	0.07219760
O0059	O	0.25000000	0.12230000	0.31140592
O0060	O	0.75000000	0.12252673	0.30931252
O0061	O	0.75000000	0.12282969	0.17993332
O0062	O	0.25000000	0.12150536	0.18773887
O0063	O	0.75000000	0.12240541	0.43665875
O0064	O	0.25000000	0.12401704	0.43715700
O0065	O	0.50128500	0.06052076	0.18719654
O0066	O	0.49988157	0.06056025	0.31193672
O0067	O	0.49892649	0.06139225	0.43734849
Ti068	Ti	0.75000000	0.05893414	0.18899962
Ti069	Ti	0.25000000	0.06077359	0.18480691
Ti070	Ti	0.75000000	0.06075768	0.31436166
Ti071	Ti	0.25000000	0.06046887	0.31019687
Ti072	Ti	0.75000000	0.06242016	0.44078583
Ti073	Ti	0.25000000	0.06158814	0.43476870
Ti074	Ti	0.25000000	0.06215600	0.05877743
Ti075	Ti	0.75000000	0.05846398	0.06613558
O0076	O	0.25000000	0.06507018	0.00016709
O0077	O	0.99736303	0.05998475	0.06240925

```
O0078  O   0.75000000  0.06498086  0.24733873
O0079  O   0.25000000  0.05886639  0.12667944
O0080  O   0.75000000  0.05383217  0.12442258
O0081  O   0.25000000  0.06126134  0.25141917
O0082  O   0.75000000  0.06189267  0.37245957
O0083  O   0.25000000  0.06259199  0.37586986
O0084  O   0.75000000  0.06203751  0.49914068
Sr085  Sr  0.50000000  0.00000000  0.50000000
Sr086  Sr  0.50129628  0.00000000  0.37592390
Sr087  Sr  0.49658504  0.00000000  0.25006084
Sr088  Sr  0.49055456  0.00000000  0.12400235
Sr089  Sr  0.00000000  0.00000000  0.00000000
O0090  O   0.25000000  0.00000000  0.06059302
O0091  O   0.75000000  0.00000000  0.05709639
O0092  O   0.25000000  0.00000000  0.31433294
O0093  O   0.75000000  0.00000000  0.30892429
O0094  O   0.75000000  0.00000000  0.19201192
O0095  O   0.25000000  0.00000000  0.19016963
O0096  O   0.75000000  0.00000000  0.43646215
O0097  O   0.25000000  0.00000000  0.43763348
#End data_Wien2k_Data
```

D.2.7. Backbone Defect BD1

```
data_Wien2k_Data
_cell_length_a   15.693094
_cell_length_b   24.999990
_cell_length_c   15.692994
_cell_angle_alpha   90.000000
_cell_angle_beta    90.000000
_cell_angle_gamma   90.000000
_symmetry_space_group_name_H-M          'Pmmm    '
_symmetry_space_group_number   47
loop_
_symmetry_equiv_pos_as_xyz
   +x,+y,+z
   -x,-y,-z
   -x,-y,+z
   -x,+y,-z
   -x,+y,+z
   +x,-y,-z
   +x,-y,+z
   +x,+y,-z
loop_
_atom_site_label
_atom_site_type_symbol
_atom_site_fract_x
_atom_site_fract_y
_atom_site_fract_z
O0001  O   0.90774732  0.71794100  0.89864487
O0002  O   0.59988389  0.71612586  0.89580793
O0003  O   0.62687982  0.73594561  0.61674565
O0004  O   0.84411136  0.71718721  0.60308590
Ti005  Ti  0.87267651  0.74411405  0.00000000
Ti006  Ti  0.63396546  0.74158288  0.00000000
```

Ti007	Ti	0.00000000	0.75830566	0.86335104
O0008	O	0.74463692	0.76069613	0.50000000
O0009	O	0.00000000	0.76954030	0.00000000
O0010	O	0.75221370	0.25167960	0.00000000
O0011	O	0.74828370	0.24115648	0.25146453
Ti012	Ti	0.74753376	0.75310048	0.63685192
Ti013	Ti	0.62084959	0.76004720	0.50000000
Ti014	Ti	0.87988198	0.25704651	0.50000000
O0015	O	0.86968911	0.82144075	0.00000000
O0016	O	0.62915830	0.81656317	0.00000000
O0017	O	0.00000000	0.84304425	0.88030495
O0018	O	0.75058396	0.15663493	0.12238451
O0019	O	0.75466209	0.83274582	0.63160754
O0020	O	0.00000000	0.15670785	0.37975654
Ti021	Ti	0.72891826	0.83128620	0.76255494
Ti022	Ti	0.00000000	0.16864650	0.26021227
Ti023	Ti	0.00000000	0.83510982	0.50000000
Ti024	Ti	0.75021125	0.84359570	0.50000000
O0025	O	0.63142936	0.83532285	0.50000000
O0026	O	0.87899178	0.81750704	0.50000000
O0027	O	0.91886900	0.78796282	0.77022774
O0028	O	0.61930366	0.83207081	0.75597435
Ti029	Ti	0.75124355	0.83618748	0.00000000
Ti030	Ti	0.00000000	0.15193847	0.00000000
O0031	O	0.00000000	0.92556895	0.00000000
O0032	O	0.74990429	0.08813375	0.00000000
O0033	O	0.75156911	0.91402793	0.75379096
O0034	O	0.00000000	0.08452054	0.25283296
O0035	O	0.75247382	0.92428750	0.50000000
O0036	O	0.00000000	0.08772298	0.50000000
Ti037	Ti	0.00000000	0.92354321	0.62482253
Ti038	Ti	0.74900470	0.07830230	0.37416672
Ti039	Ti	0.75229334	0.92398312	0.87297405
Ti040	Ti	0.00000000	0.07559010	0.12938734
O0041	O	0.87492425	0.92774832	0.62528210
O0042	O	0.62611094	0.92596869	0.62560741
O0043	O	0.87444052	0.92984610	0.87573366
O0044	O	0.62305313	0.92890436	0.87659781
Sr045	Sr	0.87780405	0.00000000	0.00000000
Sr046	Sr	0.62425056	0.00000000	0.00000000
O0047	O	0.00000000	0.00000000	0.86312953
O0048	O	0.74874126	0.00000000	0.11916796
Sr049	Sr	0.87397820	0.00000000	0.74616002
Sr050	Sr	0.62341132	0.00000000	0.74761187
O0051	O	0.00000000	0.00000000	0.61951577
O0052	O	0.74836473	0.00000000	0.36642739
Sr053	Sr	0.86938773	0.00000000	0.50000000
Sr054	Sr	0.62552656	0.00000000	0.50000000
Ti055	Ti	0.50000000	0.74902995	0.86708091
O0056	O	0.50000000	0.25770477	0.50000000
O0057	O	0.50000000	0.75892906	0.00000000
O0058	O	0.50000000	0.75225699	0.75020015
Ti059	Ti	0.50000000	0.24101187	0.37027134
O0060	O	0.50000000	0.83323319	0.87886490
O0061	O	0.50000000	0.16226043	0.37447779

```
Ti062  Ti  0.50000000  0.16379865  0.24922106
Ti063  Ti  0.50000000  0.83304329  0.50000000
Ti064  Ti  0.50000000  0.16278573  0.00000000
O0065  O   0.50000000  0.91188422  0.00000000
O0066  O   0.50000000  0.07948015  0.24978750
O0067  O   0.50000000  0.08106198  0.50000000
Ti068  Ti  0.50000000  0.92206199  0.62365603
Ti069  Ti  0.50000000  0.07591299  0.12817190
O0070  O   0.50000000  0.00000000  0.87996549
O0071  O   0.50000000  0.00000000  0.62389678
O0072  O   0.00000000  0.25290350  0.50000000
#End data_Wien2k_Data
```

D.2.8. Backbone Defect BD2

```
data_Wien2k_Data
_cell_length_a   15.693094
_cell_length_b   24.999990
_cell_length_c   15.692994
_cell_angle_alpha   90.000000
_cell_angle_beta    90.000000
_cell_angle_gamma   90.000000
_symmetry_space_group_name_H-M         'Pmmm   '
_symmetry_space_group_number   47
loop_
_symmetry_equiv_pos_as_xyz
   +x,+y,+z
   -x,-y,-z
   -x,-y,+z
   -x,+y,-z
   -x,+y,+z
   +x,-y,-z
   +x,-y,+z
   +x,+y,-z
loop_
_atom_site_label
_atom_site_type_symbol
_atom_site_fract_x
_atom_site_fract_y
_atom_site_fract_z
O0001  O   0.90764293  0.72026104  0.89580327
O0002  O   0.59939995  0.71561535  0.89562841
O0003  O   0.62912861  0.73630938  0.61613960
O0004  O   0.85142341  0.71969292  0.60367634
Ti005  Ti  0.87358526  0.74385631  0.00000000
Ti006  Ti  0.63484419  0.74047190  0.00000000
Ti007  Ti  0.00000000  0.76040032  0.86026180
O0008  O   0.74740043  0.76001930  0.50000000
O0009  O   0.00000000  0.76879631  0.00000000
O0010  O   0.75261817  0.25430981  0.00000000
O0011  O   0.75044798  0.24130501  0.25217945
Ti012  Ti  0.75088974  0.75379877  0.63615176
Ti013  Ti  0.62178936  0.75996184  0.50000000
Ti014  Ti  0.88330849  0.25523508  0.50000000
O0015  O   0.86886420  0.82038108  0.00000000
```

O0016	O	0.63047331	0.81542694	0.00000000
O0017	O	0.00000000	0.84359351	0.88159954
O0018	O	0.75129835	0.15719937	0.12283124
O0019	O	0.75657714	0.83274393	0.63180195
O0020	O	0.00000000	0.15393155	0.38012831
Ti021	Ti	0.72927328	0.83111599	0.76253811
Ti022	Ti	0.00000000	0.16537137	0.26110355
Ti023	Ti	0.00000000	0.83779511	0.50000000
Ti024	Ti	0.75022230	0.84368507	0.50000000
O0025	O	0.63201051	0.83537169	0.50000000
O0026	O	0.88234240	0.81831172	0.50000000
O0027	O	0.91923136	0.79115449	0.76978413
O0028	O	0.61947009	0.83152451	0.75614577
Ti029	Ti	0.75111161	0.83566065	0.00000000
Ti030	Ti	0.00000000	0.15400338	0.00000000
O0031	O	0.00000000	0.92269353	0.00000000
O0032	O	0.74944477	0.08940675	0.00000000
O0033	O	0.75194314	0.91410143	0.75408183
O0034	O	0.00000000	0.08296968	0.25021878
O0035	O	0.75194483	0.92467608	0.50000000
O0036	O	0.00000000	0.07699343	0.50000000
Ti037	Ti	0.00000000	0.92571771	0.62415584
Ti038	Ti	0.74917146	0.07832321	0.37467757
Ti039	Ti	0.75189250	0.92384287	0.87291829
Ti040	Ti	0.00000000	0.07516279	0.12850278
O0041	O	0.87388713	0.92886853	0.62559520
O0042	O	0.62501616	0.92532994	0.62662286
O0043	O	0.87459817	0.92963936	0.87679201
O0044	O	0.62365046	0.92908772	0.87692708
Sr045	Sr	0.87711155	0.00000000	0.00000000
Sr046	Sr	0.62437146	0.00000000	0.00000000
O0047	O	0.00000000	0.00000000	0.87002072
O0048	O	0.74962144	0.00000000	0.11794086
Sr049	Sr	0.87360945	0.00000000	0.74685734
Sr050	Sr	0.62294375	0.00000000	0.74686566
O0051	O	0.00000000	0.00000000	0.63539527
O0052	O	0.74618413	0.00000000	0.36713595
Sr053	Sr	0.86775388	0.00000000	0.50000000
Sr054	Sr	0.62517119	0.00000000	0.50000000
Ti055	Ti	0.50000000	0.74885306	0.86700121
O0056	O	0.50000000	0.25773496	0.50000000
O0057	O	0.50000000	0.75913280	0.00000000
O0058	O	0.50000000	0.75199863	0.74966931
Ti059	Ti	0.50000000	0.24116408	0.37058906
O0060	O	0.50000000	0.83362764	0.87924189
O0061	O	0.50000000	0.16272049	0.37455555
Ti062	Ti	0.50000000	0.16401612	0.24929767
Ti063	Ti	0.50000000	0.83277749	0.50000000
Ti064	Ti	0.50000000	0.16326063	0.00000000
O0065	O	0.50000000	0.91185683	0.00000000
O0066	O	0.50000000	0.07982313	0.24879959
O0067	O	0.50000000	0.08134853	0.50000000
Ti068	Ti	0.50000000	0.92188123	0.62352173
Ti069	Ti	0.50000000	0.07592878	0.12821566
O0070	O	0.50000000	0.00000000	0.87924051

```
O0071  O   0.50000000  0.00000000  0.62394756
#End data_Wien2k_Data
```

D.2.9. Backbone Defect BD3

```
data_Wien2k_Data
_cell_length_a   15.693054
_cell_length_b   24.999990
_cell_length_c   15.692994
_cell_angle_alpha   90.000000
_cell_angle_beta    90.000000
_cell_angle_gamma   90.000000
_symmetry_space_group_name_H-M          'Pmmm   '
_symmetry_space_group_number   47
loop_
_symmetry_equiv_pos_as_xyz
   +x,+y,+z
   -x,-y,-z
   -x,-y,+z
   -x,+y,-z
   -x,+y,+z
   +x,-y,-z
   +x,-y,+z
   +x,+y,-z
loop_
_atom_site_label
_atom_site_type_symbol
_atom_site_fract_x
_atom_site_fract_y
_atom_site_fract_z
O0001  O   0.90695015  0.71165006  0.89980553
O0002  O   0.59989786  0.71497522  0.89574781
O0003  O   0.61190606  0.72355528  0.61436772
O0004  O   0.76500249  0.65637809  0.63991813
Ti005  Ti  0.87128258  0.73844866  0.00000000
Ti006  Ti  0.63403462  0.74051865  0.00000000
Ti007  Ti  0.00000000  0.75151859  0.86476221
O0008  O   0.74737200  0.74572242  0.50000000
O0009  O   0.00000000  0.76382835  0.00000000
O0010  O   0.75170053  0.25360529  0.00000000
O0011  O   0.75107506  0.24429664  0.26524810
Ti012  Ti  0.73694990  0.71810340  0.63158261
Ti013  Ti  0.62138376  0.75359812  0.50000000
O0014  O   0.87112045  0.81770045  0.00000000
O0015  O   0.62912250  0.81623043  0.00000000
O0016  O   0.00000000  0.84010143  0.88079887
O0017  O   0.75188468  0.15833249  0.12679755
O0018  O   0.75588911  0.83991285  0.62407353
O0019  O   0.00000000  0.15935181  0.37904021
Ti020  Ti  0.73047865  0.82376843  0.75051726
Ti021  Ti  0.00000000  0.17482878  0.25912488
Ti022  Ti  0.00000000  0.83832953  0.50000000
Ti023  Ti  0.77491193  0.82971682  0.50000000
O0024  O   0.62438253  0.82442830  0.50000000
O0025  O   0.88365080  0.81597235  0.50000000
```

```
O0026  O   0.91918916  0.78239316  0.77150270
O0027  O   0.61977201  0.82739515  0.74863894
Ti028  Ti  0.75312915  0.83503094  0.00000000
Ti029  Ti  0.00000000  0.15740179  0.00000000
O0030  O   0.00000000  0.91920529  0.00000000
O0031  O   0.75139296  0.08982417  0.00000000
O0032  O   0.75116891  0.91446609  0.74919200
O0033  O   0.00000000  0.09040515  0.25019133
O0034  O   0.75912431  0.91012993  0.50000000
O0035  O   0.00000000  0.08742347  0.50000000
Ti036  Ti  0.00000000  0.92327835  0.62863284
Ti037  Ti  0.74828172  0.07976910  0.37569995
Ti038  Ti  0.75054731  0.92054523  0.86912974
Ti039  Ti  0.00000000  0.07612417  0.13246719
O0040  O   0.87718353  0.92975577  0.62668201
O0041  O   0.62619828  0.92718763  0.62384028
O0042  O   0.87651640  0.92998353  0.87555659
O0043  O   0.62396304  0.92787377  0.87560059
Sr044  Sr  0.87306144  0.00000000  0.00000000
Sr045  Sr  0.62606078  0.00000000  0.00000000
O0046  O   0.00000000  0.00000000  0.85813581
O0047  O   0.74863351  0.00000000  0.12448983
Sr048  Sr  0.87037613  0.00000000  0.74789767
Sr049  Sr  0.62406102  0.00000000  0.75007646
O0050  O   0.00000000  0.00000000  0.62696195
O0051  O   0.74876553  0.00000000  0.38202402
Sr052  Sr  0.87182426  0.00000000  0.50000000
Sr053  Sr  0.62107897  0.00000000  0.50000000
Ti054  Ti  0.50000000  0.74758271  0.86785665
O0055  O   0.50000000  0.24579057  0.50000000
O0056  O   0.50000000  0.75784475  0.00000000
O0057  O   0.50000000  0.74961753  0.75145913
Ti058  Ti  0.50000000  0.24484684  0.36561759
O0059  O   0.50000000  0.83312443  0.87845942
O0060  O   0.50000000  0.16275400  0.37695759
Ti061  Ti  0.50000000  0.16403085  0.24944662
Ti062  Ti  0.50000000  0.84366671  0.50000000
Ti063  Ti  0.50000000  0.16320273  0.00000000
O0064  O   0.50000000  0.91285664  0.00000000
O0065  O   0.50000000  0.07806851  0.24904589
O0066  O   0.50000000  0.08076187  0.50000000
Ti067  Ti  0.50000000  0.92157131  0.62956316
Ti068  Ti  0.50000000  0.07743725  0.12631335
O0069  O   0.50000000  0.00000000  0.88305898
O0070  O   0.50000000  0.00000000  0.62564857
#End data_Wien2k_Data
```

D.2.10. Backbone Defect BD4 (Square, In-Phase Configuration)

```
data_Wien2k_Data
_cell_length_a   15.693054
_cell_length_b   24.999990
_cell_length_c   15.692994
_cell_angle_alpha   90.000000
_cell_angle_beta    90.000000
```

```
_cell_angle_gamma   90.000000
_symmetry_space_group_name_H-M          'Pmmm   '
_symmetry_space_group_number   47
loop_
_symmetry_equiv_pos_as_xyz
   +x,+y,+z
   -x,-y,-z
   -x,-y,+z
   -x,+y,-z
   -x,+y,+z
   +x,-y,-z
   +x,-y,+z
   +x,+y,-z
loop_
_atom_site_label
_atom_site_type_symbol
_atom_site_fract_x
_atom_site_fract_y
_atom_site_fract_z
O0001  O   0.90031434  0.71717621  0.89236691
O0002  O   0.59833190  0.71517669  0.89553926
O0003  O   0.61930839  0.73388590  0.61625573
O0004  O   0.85968156  0.75698586  0.61972265
Ti005  Ti  0.86500040  0.73890985  0.00000000
Ti006  Ti  0.63066533  0.74024815  0.00000000
Ti007  Ti  0.00000000  0.75305794  0.87488681
O0008  O   0.74212556  0.74903215  0.50000000
O0009  O   0.00000000  0.75478829  0.00000000
O0010  O   0.74890868  0.25713565  0.00000000
O0011  O   0.73895525  0.24375356  0.25317124
Ti012  Ti  0.74460224  0.75565164  0.62988152
Ti013  Ti  0.61929680  0.75717746  0.50000000
Ti014  Ti  0.87784949  0.17038949  0.37221166
O0015  O   0.87144431  0.81310167  0.00000000
O0016  O   0.63069476  0.81592109  0.00000000
O0017  O   0.00000000  0.83593212  0.87982961
O0018  O   0.75214258  0.15727363  0.12047123
O0019  O   0.74654750  0.83558519  0.63348125
O0020  O   0.00000000  0.16587619  0.37088786
Ti021  Ti  0.73142016  0.82695018  0.76640623
Ti022  Ti  0.00000000  0.16108728  0.24030401
Ti023  Ti  0.00000000  0.84915028  0.50000000
Ti024  Ti  0.74363731  0.83729631  0.50000000
O0025  O   0.62620409  0.83403140  0.50000000
O0026  O   0.87330499  0.83702341  0.50000000
O0027  O   0.88035989  0.82842869  0.74739625
O0028  O   0.62010073  0.83460376  0.75788909
Ti029  Ti  0.74974436  0.83632557  0.00000000
Ti030  Ti  0.00000000  0.16507405  0.00000000
O0031  O   0.00000000  0.91165427  0.00000000
O0032  O   0.75101182  0.08974488  0.00000000
O0033  O   0.74915992  0.91830099  0.75386477
O0034  O   0.00000000  0.08121407  0.24456906
O0035  O   0.74896323  0.92271168  0.50000000
O0036  O   0.00000000  0.06990769  0.50000000
```

```
Ti037  Ti  0.00000000  0.92326792  0.62424697
Ti038  Ti  0.74194235  0.07715432  0.37532416
Ti039  Ti  0.75050920  0.92405614  0.87178785
Ti040  Ti  0.00000000  0.07586279  0.12387707
O0041  O   0.87560960  0.91499063  0.62714638
O0042  O   0.62625476  0.92894363  0.62568956
O0043  O   0.87531092  0.92987699  0.87733150
O0044  O   0.62370297  0.92854963  0.87788336
Sr045  Sr  0.87338334  0.00000000  0.00000000
Sr046  Sr  0.62243149  0.00000000  0.00000000
O0047  O   0.00000000  0.00000000  0.88412886
O0048  O   0.74877299  0.00000000  0.11528780
Sr049  Sr  0.87476031  0.00000000  0.75188397
Sr050  Sr  0.62168109  0.00000000  0.75345389
O0051  O   0.00000000  0.00000000  0.63527554
O0052  O   0.75974342  0.00000000  0.37099104
Sr053  Sr  0.87074618  0.00000000  0.50000000
Sr054  Sr  0.62009963  0.00000000  0.50000000
Ti055  Ti  0.50000000  0.74950303  0.86707195
O0056  O   0.50000000  0.25672877  0.50000000
O0057  O   0.50000000  0.75967658  0.00000000
O0058  O   0.50000000  0.75318942  0.75104035
Ti059  Ti  0.50000000  0.24131528  0.36784311
O0060  O   0.50000000  0.83376102  0.87947759
O0061  O   0.50000000  0.16180692  0.37416861
Ti062  Ti  0.50000000  0.16211477  0.24864098
Ti063  Ti  0.50000000  0.83277475  0.50000000
Ti064  Ti  0.50000000  0.16145729  0.00000000
O0065  O   0.50000000  0.91362839  0.00000000
O0066  O   0.50000000  0.07755164  0.25081615
O0067  O   0.50000000  0.08152868  0.50000000
Ti068  Ti  0.50000000  0.92191315  0.62478594
Ti069  Ti  0.50000000  0.07719303  0.12754916
O0070  O   0.50000000  0.00000000  0.87799026
O0071  O   0.50000000  0.00000000  0.62130377
#End data_Wien2k_Data
```

D.2.11. Backbone Defect BD4 (Square, Out-of-Phase Configuration)

```
data_Wien2k_Data
_cell_length_a   15.693054
_cell_length_b   24.999990
_cell_length_c   15.692994
_cell_angle_alpha   90.000000
_cell_angle_beta    90.000000
_cell_angle_gamma   90.000000
_symmetry_space_group_name_H-M         'Pmmm   '
_symmetry_space_group_number   47
loop_
_symmetry_equiv_pos_as_xyz
   +x,+y,+z
   -x,-y,-z
   -x,-y,+z
   -x,+y,-z
   -x,+y,+z
```

```
   +x,-y,-z
   +x,-y,+z
   +x,+y,-z
loop_
_atom_site_label
_atom_site_type_symbol
_atom_site_fract_x
_atom_site_fract_y
_atom_site_fract_z
O0001  O   0.35120829  0.28282541  0.10490277
O0002  O   0.64333162  0.24387435  0.37683064
Ti003  Ti  0.38265490  0.25710462  0.00000000
Ti004  Ti  0.24998713  0.25092181  0.13172983
O0005  O   0.24216358  0.74889934  0.50000000
O0006  O   0.25064991  0.24041035  0.00000000
O0007  O   0.50000000  0.74720392  0.00000000
O0008  O   0.24243641  0.24798268  0.24754707
Ti009  Ti  0.37996715  0.17256949  0.37239444
Ti010  Ti  0.24137638  0.75666078  0.63206783
O0011  O   0.37832617  0.18143487  0.00000000
O0012  O   0.25070787  0.16623119  0.12218806
O0013  O   0.50000000  0.84040611  0.87951499
O0014  O   0.50000000  0.16313961  0.36932978
O0015  O   0.24854908  0.83783439  0.62774202
Ti016  Ti  0.50000000  0.15473763  0.23427237
Ti017  Ti  0.23310700  0.83608639  0.75508892
Ti018  Ti  0.24534301  0.16594322  0.50000000
Ti019  Ti  0.50000000  0.15019539  0.50000000
O0020  O   0.62359125  0.16682569  0.50000000
O0021  O   0.38180259  0.16998521  0.25297449
Ti022  Ti  0.50000000  0.16130119  0.00000000
Ti023  Ti  0.25225911  0.83917742  0.00000000
O0024  O   0.25040769  0.08474702  0.00000000
O0025  O   0.50000000  0.91846537  0.00000000
O0026  O   0.50000000  0.07779685  0.24756582
O0027  O   0.25035804  0.92078686  0.74890412
O0028  O   0.50000000  0.07010468  0.50000000
O0029  O   0.25055709  0.91788956  0.50000000
Ti030  Ti  0.24237130  0.07584728  0.37436933
Ti031  Ti  0.50000000  0.92391008  0.62532267
Ti032  Ti  0.50000000  0.07638243  0.11984604
Ti033  Ti  0.24963573  0.92288800  0.87238179
O0034  O   0.37763686  0.08709803  0.37541287
O0035  O   0.37412937  0.07258199  0.12353061
Sr036  Sr  0.37217422  0.00000000  0.00000000
O0037  O   0.25168806  0.00000000  0.12365063
O0038  O   0.50000000  0.00000000  0.88285511
Sr039  Sr  0.37567752  0.00000000  0.24310043
O0040  O   0.26253897  0.00000000  0.37667645
O0041  O   0.50000000  0.00000000  0.63222805
Sr042  Sr  0.37424718  0.00000000  0.50000000
O0043  O   0.84841040  0.28524590  0.10273647
O0044  O   0.12069864  0.26520527  0.38230642
Ti045  Ti  0.88225119  0.25819956  0.00000000
O0046  O   0.00000000  0.25771459  0.50000000
```

```
O0047  O   0.00000000  0.74704345  0.00000000
O0048  O   0.00000000  0.75939330  0.74786626
Ti049  Ti  0.00000000  0.24126030  0.36928679
Ti050  Ti  0.11924390  0.24300762  0.50000000
O0051  O   0.87827766  0.18304719  0.00000000
O0052  O   0.00000000  0.84431152  0.87946097
O0053  O   0.00000000  0.16280551  0.36906275
Ti054  Ti  0.00000000  0.17017629  0.23731145
Ti055  Ti  0.00000000  0.16775491  0.50000000
O0056  O   0.12654996  0.16653271  0.50000000
O0057  O   0.87692625  0.16353454  0.24635046
Ti058  Ti  0.00000000  0.16367121  0.00000000
O0059  O   0.00000000  0.91167467  0.00000000
O0060  O   0.00000000  0.07916066  0.24714236
O0061  O   0.00000000  0.07997774  0.50000000
Ti062  Ti  0.00000000  0.92062724  0.62457811
Ti063  Ti  0.00000000  0.07590167  0.12668865
O0064  O   0.87295058  0.07033194  0.37565754
O0065  O   0.87334688  0.07079243  0.12311948
Sr066  Sr  0.87231938  0.00000000  0.00000000
O0067  O   0.00000000  0.00000000  0.88600750
Sr068  Sr  0.87784162  0.00000000  0.24673305
O0069  O   0.00000000  0.00000000  0.62610744
Sr070  Sr  0.88248145  0.00000000  0.50000000
#End data_Wien2k_Data
```

D.2.12. Backbone Defect BD4 (Zigzag Configuration)

```
data_Wien2k_Data
_symmetry_cell_setting     orthorhombic
_cell_length_a   31.386123
_cell_length_b   15.693061
_cell_length_c   32.000000
_cell_angle_alpha   90.000000
_cell_angle_beta    90.000000
_cell_angle_gamma   90.000000
_symmetry_space_group_name_H-M         'P2/m   '
_symmetry_space_group_number   10
loop_
_symmetry_equiv_pos_as_xyz
   +x,+y,+z
   -x,+y,-z
   -x,-y,-z
   +x,-y,+z
loop_
_atom_site_label
_atom_site_type_symbol
_atom_site_fract_x
_atom_site_fract_y
_atom_site_fract_z
O   O   0.12987434  0.50000000  0.17486728
O   O   0.87239292  0.24897046  0.17645570
O   O   0.30857780  0.39927448  0.15898528
O   O   0.69823549  0.15092174  0.15027983
O   O   0.69774714  0.35351613  0.15303792
```

O	O	0.20463221	0.39861352	0.14615755
O	O	0.79965307	0.14798739	0.14444999
O	O	0.80040830	0.35212048	0.14547904
Ti	Ti	0.18586874	0.50000000	0.16898972
Ti	Ti	0.81657232	0.24930834	0.16794875
O	O	0.25047073	0.24957978	0.17844991
O	O	0.75296345	0.50000000	0.17781082
Ti	Ti	0.25332756	0.36667544	0.17288951
Ti	Ti	0.25026042	0.13123363	0.17072818
Ti	Ti	0.75117713	0.61676403	0.17179219
Ti	Ti	0.31393027	0.50000000	0.18641851
Ti	Ti	0.68439226	0.25079038	0.17665094
O	O	0.37451238	0.24035235	0.18590017
O	O	0.44190157	0.12037621	0.16581699
O	O	0.43754862	0.36104140	0.18419609
O	O	0.56146859	0.35986578	0.18602579
O	O	0.49885160	0.24385231	0.18199834
Ti	Ti	0.49949162	0.11995418	0.18483530
Ti	Ti	0.43458061	0.37770597	0.24602206
Ti	Ti	0.56454818	0.24808513	0.18667393
Ti	Ti	0.43196677	0.25015021	0.18289109
Ti	Ti	0.56403551	0.37903607	0.24649143
O	O	0.25244092	0.50000000	0.18549040
O	O	0.75144615	0.25053124	0.18351995
O	O	0.62686799	0.24514621	0.18207284
O	O	0.18593841	0.25006676	0.25274261
O	O	0.81703697	0.50000000	0.25203365
O	O	0.18556724	0.50000000	0.23322390
O	O	0.81482637	0.24955617	0.23503401
O	O	0.43493418	0.50000000	0.24146820
O	O	0.56508876	0.24520897	0.24963927
Ti	Ti	0.36456702	0.23244998	0.24205809
Ti	Ti	0.63456212	0.50000000	0.25414591
Ti	Ti	0.24372762	0.24851630	0.24681519
Ti	Ti	0.75395278	0.50000000	0.24855765
O	O	0.30767860	0.24865088	0.25379085
O	O	0.69297862	0.50000000	0.24861776
O	O	0.43382247	0.24555214	0.24536246
O	O	0.56481503	0.50000000	0.24459138
O	O	0.37439973	0.37867177	0.24411723
O	O	0.62893031	0.12406261	0.24637259
O	O	0.62437103	0.37953716	0.24568605
O	O	0.11926823	0.37342821	0.23538008
O	O	0.11884621	0.12572097	0.23587751
O	O	0.88203837	0.62798934	0.23711062
O	O	0.88108778	0.12181614	0.23601491
O	O	0.24824959	0.37256878	0.23181159
O	O	0.24661435	0.12725207	0.23056643
O	O	0.75396387	0.62291897	0.23189765
O	O	0.30981915	0.50000000	0.25113835
O	O	0.69155780	0.25113106	0.24127171
O	O	0.50007278	0.12529413	0.24501309
O	O	0.49963550	0.37186874	0.24821484
O	O	0.06033256	0.24986619	0.25622273
O	O	0.93976892	0.50000000	0.25526473

O	O	0.94013150	0.00000000	0.25661096
Ti	Ti	0.50098654	0.24283392	0.24774684
Ti	Ti	0.49859708	0.50000000	0.25415189
Ti	Ti	0.24877191	0.50000000	0.24765375
Ti	Ti	0.75342742	0.25048888	0.24565135
Ti	Ti	0.37147683	0.50000000	0.25585277
Ti	Ti	0.62905825	0.23416225	0.24677654
Ti	Ti	0.11752780	0.25024171	0.24699542
Ti	Ti	0.88208890	0.50000000	0.24797190
Ti	Ti	0.12646225	0.50000000	0.23380142
Ti	Ti	0.12589330	0.00000000	0.23438617
Ti	Ti	0.87469320	0.25105186	0.23470711
O	O	0.18467853	0.37442955	0.32105538
O	O	0.18582738	0.87676736	0.32066809
O	O	0.81380691	0.12548782	0.32064065
O	O	0.81477297	0.37324542	0.31999539
O	O	0.30767533	0.37511688	0.32108285
O	O	0.69248046	0.12627735	0.32078756
O	O	0.69246659	0.37415601	0.31915577
O	O	0.43623541	0.37095361	0.31157967
O	O	0.56413022	0.12476913	0.31945984
O	O	0.56322316	0.37231455	0.31205798
Ti	Ti	0.18056163	0.50000000	0.31932562
Ti	Ti	0.18072800	0.00000000	0.31848034
Ti	Ti	0.81941299	0.24987126	0.31825510
Ti	Ti	0.18371030	0.25108652	0.31508933
Ti	Ti	0.81589153	0.50000000	0.31137136
Ti	Ti	0.43510822	0.24289025	0.31753280
Ti	Ti	0.56239238	0.50000000	0.31407039
Ti	Ti	0.43741659	0.50000000	0.31174262
Ti	Ti	0.56270353	0.24235169	0.31570644
Ti	Ti	0.30831095	0.50000000	0.31608299
Ti	Ti	0.68864474	0.24997165	0.31879029
Ti	Ti	0.31117803	0.25107854	0.31600954
Ti	Ti	0.69199674	0.50000000	0.31294981
Ti	Ti	0.05625350	0.25015345	0.31231044
Ti	Ti	0.94466939	0.50000000	0.31136710
Ti	Ti	0.94416284	0.00000000	0.31226936
Ti	Ti	0.06279998	0.50000000	0.32231157
Ti	Ti	0.06230284	0.00000000	0.32281316
Ti	Ti	0.93818344	0.24979693	0.32278890
O	O	0.99833765	0.24996053	0.32499035
O	O	0.00265953	0.50000000	0.32343709
O	O	0.00212041	0.00000000	0.32498296
O	O	0.06196069	0.62393830	0.32209787
O	O	0.06168379	0.12338234	0.32201722
O	O	0.93899019	0.37315098	0.32138695
O	O	0.93879515	0.12670659	0.32210202
O	O	0.49866328	0.24602294	0.31312973
O	O	0.50002840	0.50000000	0.31619047
O	O	0.37188477	0.24754055	0.30880164
O	O	0.62690543	0.50000000	0.31527991
O	O	0.37147774	0.50000000	0.31652927
O	O	0.62880519	0.24931096	0.31185992
O	O	0.24239439	0.50000000	0.30825826

O	O	0.75472008	0.24972736	0.30342270
O	O	0.24694723	0.24975321	0.30695590
O	O	0.75470602	0.50000000	0.31102385
O	O	0.12326073	0.24924631	0.30789540
O	O	0.87835894	0.50000000	0.30783301
O	O	0.87663252	0.00000000	0.30861145
O	O	0.12292239	0.50000000	0.29939487
O	O	0.12325465	0.00000000	0.30063075
O	O	0.87701529	0.24840022	0.30129523
Sr	Sr	0.49936732	0.37549717	0.37391761
Sr	Sr	0.49997017	0.12310867	0.37639286
Sr	Sr	0.37313498	0.37805403	0.37499288
Sr	Sr	0.62668806	0.12411858	0.37638285
Sr	Sr	0.62652950	0.37778990	0.37362317
Sr	Sr	0.24742810	0.37611448	0.37707202
Sr	Sr	0.24722134	0.12630828	0.37678129
Sr	Sr	0.75260362	0.62217557	0.37574237
Sr	Sr	0.75260715	0.12415719	0.37682068
Sr	Sr	0.12298393	0.37036987	0.37704363
Sr	Sr	0.12343475	0.12947382	0.37603753
Sr	Sr	0.87687218	0.61930423	0.37495320
Sr	Sr	0.87672855	0.12043121	0.37558127
Sr	Sr	0.00017642	0.12496888	0.37626080
Sr	Sr	0.00014230	0.37594817	0.37606503
O	O	0.06815205	0.24960824	0.37900444
O	O	0.93337243	0.50000000	0.37832942
O	O	0.93203664	0.00000000	0.37891098
O	O	0.07287972	0.50000000	0.37777482
O	O	0.07330834	0.00000000	0.37826327
O	O	0.92696391	0.25042536	0.37805068
O	O	0.31229671	0.24936178	0.37655657
O	O	0.69012349	0.50000000	0.37762953
O	O	0.30779873	0.50000000	0.37735453
O	O	0.68982402	0.25156608	0.37542830
O	O	0.17920619	0.50000000	0.37564931
O	O	0.18102506	0.00000000	0.37597376
O	O	0.81921857	0.24994169	0.37539306
O	O	0.18529036	0.24909504	0.37676807
O	O	0.81665596	0.50000000	0.37731078
O	O	0.81399072	0.00000000	0.37681374
O	O	0.43735890	0.50000000	0.37619792
O	O	0.56399383	0.25389126	0.37524244
O	O	0.43339495	0.25333973	0.37453890
O	O	0.56306979	0.50000000	0.37623896
O	O	0.18724317	0.37471774	0.43832142
O	O	0.81244434	0.12512181	0.43858167
O	O	0.81302869	0.37449542	0.43844838
O	O	0.18763845	0.87520225	0.43893843
O	O	0.31206876	0.37395229	0.43896649
O	O	0.68781156	0.12496933	0.43816495
O	O	0.68818151	0.37462047	0.43889190
O	O	0.31230942	0.87523318	0.43917786
O	O	0.43729931	0.37419801	0.43814234
O	O	0.43731886	0.12506334	0.43778369
O	O	0.56281497	0.12503685	0.43721656

O	O	0.56271595	0.62583921	0.43862958
Ti	Ti	0.18621232	0.50000000	0.44196120
Ti	Ti	0.18637704	0.00000000	0.44109797
Ti	Ti	0.81321347	0.25055330	0.44049323
Ti	Ti	0.18590910	0.25040685	0.43857718
Ti	Ti	0.81363056	0.50000000	0.43603593
Ti	Ti	0.81418020	0.00000000	0.43790291
Ti	Ti	0.31163165	0.50000000	0.43853200
Ti	Ti	0.68810301	0.25094795	0.44005332
Ti	Ti	0.31095238	0.25075320	0.43782415
Ti	Ti	0.68838660	0.50000000	0.43612490
Ti	Ti	0.43756270	0.50000000	0.43613382
Ti	Ti	0.56215776	0.25153596	0.43679851
Ti	Ti	0.43641560	0.25108539	0.44004918
Ti	Ti	0.56290693	0.50000000	0.43729748
Ti	Ti	0.06093451	0.24999492	0.43587907
Ti	Ti	0.93806060	0.50000000	0.43547255
Ti	Ti	0.93886840	0.00000000	0.43567080
Ti	Ti	0.06239753	0.50000000	0.44195644
Ti	Ti	0.06279528	0.00000000	0.44188601
Ti	Ti	0.93695328	0.25019932	0.44175619
O	O	0.99944382	0.24961841	0.43331324
O	O	0.00091828	0.50000000	0.43330499
O	O	0.00066447	0.00000000	0.43338460
O	O	0.06249212	0.62530904	0.43964488
O	O	0.06254069	0.12465383	0.43975311
O	O	0.93782286	0.37456084	0.43944984
O	O	0.93757628	0.12504551	0.43944736
O	O	0.24793212	0.50000000	0.43611515
O	O	0.75108462	0.25007634	0.43382987
O	O	0.24931051	0.00000000	0.43487936
O	O	0.12589847	0.24955600	0.44279738
O	O	0.87554545	0.50000000	0.44247111
O	O	0.87419819	0.00000000	0.44241964
O	O	0.12455318	0.50000000	0.44403487
O	O	0.87470773	0.24958747	0.44434013
O	O	0.12539445	0.00000000	0.44445306
O	O	0.25019458	0.24964741	0.43590816
O	O	0.75143832	0.50000000	0.43737217
O	O	0.74980497	0.00000000	0.43672213
O	O	0.37369408	0.50000000	0.43658864
O	O	0.62605327	0.24984606	0.43751368
O	O	0.37470881	0.24951747	0.43950947
O	O	0.62570510	0.50000000	0.43774835
O	O	0.50002620	0.50000000	0.43802987
O	O	0.49990988	0.24960801	0.43480876
Sr	Sr	0.50000000	0.37940603	0.50000000
Sr	Sr	0.50000000	0.12508867	0.50000000
Sr	Sr	0.37491304	0.37881400	0.50037617
Sr	Sr	0.62522196	0.12574211	0.49997285
Sr	Sr	0.24976056	0.37736036	0.50064026
Sr	Sr	0.24932645	0.12546733	0.50019120
Sr	Sr	0.12398847	0.37607577	0.50061497
Sr	Sr	0.12398423	0.12515944	0.50022430
Sr	Sr	0.00000000	0.12509691	0.50000000

Sr	Sr	0.00000000	0.37554931	0.50000000
O	O	0.05799495	0.24983632	0.50036397
O	O	0.94253298	0.50000000	0.50020927
O	O	0.94193315	0.00000000	0.50020721
O	O	0.30982254	0.24931767	0.50086271
O	O	0.68931819	0.50000000	0.50087952
O	O	0.68867679	0.00000000	0.50025755
O	O	0.18935964	0.50000000	0.49966803
O	O	0.80793242	0.25023534	0.49971382
O	O	0.19163491	0.00000000	0.49983045
O	O	0.43652523	0.50000000	0.49979198
O	O	0.56113638	0.24886633	0.50000503
O	O	0.43635418	0.00000000	0.50040360
O	O	0.12818214	0.00000000	0.17596157
O	O	0.30299306	0.89968513	0.15158161
O	O	0.20083794	0.89759873	0.14454063
Ti	Ti	0.18394120	0.00000000	0.16787147
O	O	0.75085409	0.00000000	0.17764478
Ti	Ti	0.75012432	0.11814582	0.17033591
Ti	Ti	0.31652809	0.00000000	0.17766667
O	O	0.62559781	0.00000000	0.18636436
O	O	0.55830025	0.87904015	0.16689276
O	O	0.50140031	0.00000000	0.17463309
Ti	Ti	0.43529899	0.00000000	0.18584040
Ti	Ti	0.56883724	0.00000000	0.18385954
O	O	0.24935141	0.00000000	0.18353292
O	O	0.37412166	0.00000000	0.18333523
O	O	0.81369895	0.00000000	0.25274718
O	O	0.18526031	0.00000000	0.23384912
O	O	0.43564128	0.00000000	0.24891746
Ti	Ti	0.63337311	0.00000000	0.24326238
Ti	Ti	0.75579419	0.00000000	0.24576761
O	O	0.69128710	0.00000000	0.25368473
O	O	0.56558874	0.00000000	0.24372008
O	O	0.36937571	0.88030377	0.24637558
O	O	0.75264990	0.12246271	0.23022406
O	O	0.30792603	0.00000000	0.24224559
Ti	Ti	0.49870531	0.00000000	0.24324794
Ti	Ti	0.24766249	0.00000000	0.24606405
Ti	Ti	0.37363917	0.00000000	0.24834212
Ti	Ti	0.88253901	0.00000000	0.24707743
O	O	0.30709070	0.87681028	0.32121826
O	O	0.43575684	0.87713401	0.32008018
Ti	Ti	0.81596059	0.00000000	0.31422399
Ti	Ti	0.56321201	0.00000000	0.31604375
Ti	Ti	0.43838866	0.00000000	0.31376962
Ti	Ti	0.31123081	0.00000000	0.31902545
Ti	Ti	0.68913651	0.00000000	0.31586812
O	O	0.50114445	0.00000000	0.31087305
O	O	0.62740123	0.00000000	0.31017074
O	O	0.37163496	0.00000000	0.31310523
O	O	0.24506795	0.00000000	0.30329009
O	O	0.75260816	0.00000000	0.30631605
Sr	Sr	0.37286019	0.87619433	0.37626679
O	O	0.68910922	0.00000000	0.37612516

```
O   O   0.30984427  0.00000000  0.37616799
O   O   0.43851930  0.00000000  0.37630785
O   O   0.56345314  0.00000000  0.37426614
Ti  Ti  0.31125465  0.00000000  0.44005115
Ti  Ti  0.68913489  0.00000000  0.43770439
Ti  Ti  0.43723645  0.00000000  0.43617175
Ti  Ti  0.56336772  0.00000000  0.43990675
O   O   0.37412540  0.00000000  0.43634418
O   O   0.62544050  0.00000000  0.43695708
O   O   0.50021886  0.00000000  0.43797750
#End data_Wien2k_Data
```

D.3. Chapter 5 CIF Files

D.3.1. 1TiMol

```
data_Wien2k_Data
_cell_length_a    3.892979
_cell_length_b    3.892979
_cell_length_c   38.929790
_cell_angle_alpha   90.000000
_cell_angle_beta    90.000000
_cell_angle_gamma   90.000000
_symmetry_space_group_name_H-M         'P-1'
loop_
_symmetry_equiv_pos_as_xyz
   +x,+y,+z
   -x,-y,-z
loop_
_atom_site_label
_atom_site_type_symbol
_atom_site_fract_x
_atom_site_fract_y
_atom_site_fract_z
Ow  O   0.10106668  0.06138625  0.69235300
H1  H   0.08296647  0.82209331  0.68468424
H2  H   0.33801800  0.07571131  0.70331436
Ti1 Ti  0.97538594  0.04431353  0.74840711
O1  O   0.99198282  0.54020604  0.74879413
O2  O   0.49305891  0.04153005  0.74471011
Sr1 Sr  0.48261933  0.54059884  0.79501919
O3  O   0.99253056  0.03139187  0.79714596
Ti2 Ti  0.99022603  0.02552168  0.84817510
O4  O   0.99210900  0.52299440  0.84823376
O5  O   0.49162988  0.01939584  0.84747145
Sr2 Sr  0.49176700  0.52037299  0.89806444
O6  O   0.99419981  0.01597238  0.89845488
Ti3 Ti  0.99531211  0.01024843  0.94919056
O7  O   0.99578979  0.50948576  0.94907498
O8  O   0.49586783  0.00896026  0.94895723
Sr3 Sr  0.50000000  0.50000000  0.00000000
O9  O   0.00000000  0.00000000  0.00000000
```

```
#End data_Wien2k_Data
```

D.3.2. 1TiDiss

```
data_Wien2k_Data
_cell_length_a    3.892979
_cell_length_b   38.929790
_cell_length_c    3.892979
_cell_angle_alpha   90.000000
_cell_angle_beta    90.000000
_cell_angle_gamma   90.000000
_symmetry_space_group_name_H-M         'P112/m'
loop_
_symmetry_equiv_pos_as_xyz
   +x,+y,+z
   -x,-y,-z
   -x,-y,+z
   +x,+y,-z
loop_
_atom_site_label
_atom_site_type_symbol
_atom_site_fract_x
_atom_site_fract_y
_atom_site_fract_z
Ow  O   0.95100598  0.70157700  0.00000000
H1  H   0.14937177  0.68631547  0.00000000
H2  H   0.85051330  0.72547573  0.50000000
Ti1 Ti  0.01255645  0.74995075  0.00000000
O1  O   0.48431659  0.75475799  0.00000000
O2  O   0.94403318  0.74924275  0.50000000
Sr1 Sr  0.50116647  0.80126273  0.50000000
O3  O   0.99164050  0.80053929  0.00000000
Ti2 Ti  0.99567613  0.85044814  0.00000000
O4  O   0.49543248  0.85108144  0.00000000
O5  O   0.99504105  0.85015924  0.50000000
Sr2 Sr  0.49698386  0.90046159  0.50000000
O6  O   0.99643020  0.90035692  0.00000000
Ti3 Ti  0.99792820  0.95018859  0.00000000
O7  O   0.49831767  0.95027038  0.00000000
O8  O   0.99823769  0.95017354  0.50000000
Sr3 Sr  0.50000000  0.00000000  0.50000000
O9  O   0.00000000  0.00000000  0.00000000
#End data_Wien2k_Data
```

D.3.3. 2×1

```
data_Wien2k_Data
_cell_length_a   38.930564
_cell_length_b    7.785958
_cell_length_c    3.892979
_cell_angle_alpha   90.000000
_cell_angle_beta    90.000000
_cell_angle_gamma   90.000000
_symmetry_space_group_name_H-M         'P112/m'
_symmetry_space_group_number   10
loop_
```

```
_symmetry_equiv_pos_as_xyz
   +x,+y,+z
   -x,-y,-z
   -x,-y,+z
   +x,+y,-z
loop_
_atom_site_label
_atom_site_type_symbol
_atom_site_fract_x
_atom_site_fract_y
_atom_site_fract_z
Ti1   Ti  0.30742815  0.71553424  0.50000000
Ti2   Ti  0.30127317  0.02013078  0.00000000
O1    O   0.34190561  0.59219459  0.50000000
O2    O   0.31271840  0.97126420  0.50000000
O3    O   0.29714872  0.75183046  0.00000000
O4    O   0.29609762  0.24603716  0.00000000
Ti3   Ti  0.24723554  0.26361724  0.00000000
Ti4   Ti  0.24542344  0.73809176  0.00000000
O5    O   0.25270781  0.99854764  0.00000000
O6    O   0.25083448  0.72982443  0.50000000
O7    O   0.24168060  0.25281503  0.50000000
O8    O   0.23870292  0.50146284  0.00000000
Sr1   Sr  0.19837282  0.00944825  0.50000000
Sr2   Sr  0.19663078  0.48961766  0.50000000
O9    O   0.19823848  0.78090960  0.00000000
O10   O   0.19673874  0.22282830  0.00000000
Ti5   Ti  0.14806155  0.24762216  0.00000000
Ti6   Ti  0.14791935  0.75098142  0.00000000
O11   O   0.15150958  0.50033174  0.00000000
O12   O   0.14890277  0.74939062  0.50000000
O13   O   0.14717367  0.25049112  0.50000000
O14   O   0.14386544  0.99905584  0.00000000
Sr3   Sr  0.09863799  0.49870056  0.50000000
Sr4   Sr  0.09854119  0.00058605  0.50000000
O15   O   0.09891545  0.73541235  0.00000000
O16   O   0.09846681  0.26358398  0.00000000
Ti7   Ti  0.04935625  0.74943186  0.00000000
Ti8   Ti  0.04932299  0.25007483  0.00000000
O17   O   0.04720757  0.49989883  0.00000000
O18   O   0.04901257  0.24931852  0.50000000
O19   O   0.04963209  0.74997986  0.50000000
O20   O   0.05131166  0.99960517  0.00000000
Sr5   Sr  0.00000000  0.50000000  0.50000000
Sr6   Sr  0.00000000  0.00000000  0.50000000
O21   O   0.99986312  0.24041631  0.00000000
#End data_Wien2k_Data
```

D.3.4. 2×1DissA

```
data_Wien2k_Data
_cell_length_a   38.930564
_cell_length_b    7.785958
_cell_length_c    3.892979
_cell_angle_alpha   90.000000
```

```
_cell_angle_beta    90.000000
_cell_angle_gamma   90.000000
_symmetry_space_group_name_H-M         'P-1'
_symmetry_space_group_number    2
loop_
_symmetry_equiv_pos_as_xyz
   +x,+y,+z
   -x,-y,-z
loop_
_atom_site_label
_atom_site_type_symbol
_atom_site_fract_x
_atom_site_fract_y
_atom_site_fract_z
Ow1 O   0.35441323  0.08004118  0.99949407
H1  H   0.37415470  0.00416195  0.00024481
H2  H   0.35420019  0.52031523  0.49953448
Ti1 Ti  0.30566534  0.75027662  0.50065051
Ti2 Ti  0.30787009  0.05777018  0.00134504
O1  O   0.34619255  0.63862725  0.49972475
O2  O   0.30880744  0.98563646  0.50105506
O3  O   0.29958770  0.75886521  0.00064300
O4  O   0.29626253  0.27958605  0.99999718
Ti3 Ti  0.24778300  0.27488858  0.99678267
Ti4 Ti  0.24657707  0.75733120  0.00008412
O5  O   0.25469326  0.01066131  0.99995413
O6  O   0.25516799  0.73894679  0.50019592
O7  O   0.24207892  0.26721811  0.50015006
O8  O   0.23869336  0.51829369  0.99930556
Sr1 Sr  0.19949564  0.02490131  0.50014795
Sr2 Sr  0.19719900  0.49903644  0.49890694
O9  O   0.19941829  0.79616032  0.00033184
O10 O   0.19694797  0.23180214  0.00221261
Ti5 Ti  0.14828569  0.25521643  0.00007517
Ti6 Ti  0.14836893  0.75831013  0.99948084
O11 O   0.15255495  0.50793754  0.00014312
O12 O   0.14944497  0.75478583  0.49994327
O13 O   0.14756478  0.25557051  0.50063179
O14 O   0.14319858  0.00528484  0.00066017
Sr3 Sr  0.09890341  0.50346339  0.49988562
Sr4 Sr  0.09877118  0.00510747  0.49988040
O15 O   0.09930159  0.73406458  0.00016723
O16 O   0.09857829  0.27417155  0.00025790
Ti7 Ti  0.04957402  0.75156130  0.00012444
Ti8 Ti  0.04933927  0.25204886  0.00006189
O17 O   0.04592892  0.50192993  0.00007456
O18 O   0.04917986  0.25101983  0.50008704
O19 O   0.04977113  0.75160185  0.50014297
O20 O   0.05275880  0.00164084  0.00013113
Sr5 Sr  0.00000000  0.50000000  0.50000000
Sr6 Sr  0.00000000  0.00000000  0.50000000
O21 O   0.99981798  0.23314368  0.99992801
#End data_Wien2k_Data
```

D.3.5. 2×1SatB

```
data_Wien2k_Data
_cell_length_a   39.452831
_cell_length_b    7.785958
_cell_length_c    3.892979
_cell_angle_alpha   90.000000
_cell_angle_beta    90.000000
_cell_angle_gamma   90.000000
_symmetry_space_group_name_H-M         'P112/m'
_symmetry_space_group_number    10
loop_
_symmetry_equiv_pos_as_xyz
   +x,+y,+z
   -x,-y,+z
   -x,-y,-z
   +x,+y,-z
loop_
_atom_site_label
_atom_site_type_symbol
_atom_site_fract_x
_atom_site_fract_y
_atom_site_fract_z
Ow1  O   0.14878087  0.55978883  0.50000000
H1   H   0.13011520  0.47799235  0.50000000
H2   H   0.19736168  0.88085155  0.00000000
Ow2  O   0.14333258  0.25888081  0.00000000
H3   H   0.13075548  0.15091302  0.00000000
H4   H   0.19095625  0.87234612  0.50000000
Ti1  Ti  0.19008561  0.22912820  0.00000000
Ti2  Ti  0.19416283  0.52899460  0.50000000
O1   O   0.18659104  0.99363076  0.00000000
O2   O   0.19579388  0.48038653  0.00000000
O3   O   0.20066115  0.26354929  0.50000000
O4   O   0.20561830  0.77013967  0.50000000
Ti3  Ti  0.25650314  0.76874654  0.50000000
Ti4  Ti  0.25356467  0.25553174  0.50000000
O5   O   0.24753708  0.51268960  0.50000000
O6   O   0.24733503  0.24496535  0.00000000
O7   O   0.25991453  0.76474120  0.00000000
O8   O   0.26118212  0.01256868  0.50000000
Sr1  Sr  0.30135805  0.51527644  0.00000000
Sr2  Sr  0.30296302  0.00858124  0.00000000
O9   O   0.30141416  0.28895789  0.50000000
O10  O   0.30469275  0.72992435  0.50000000
Ti5  Ti  0.35309470  0.75752168  0.50000000
Ti6  Ti  0.35220589  0.25939923  0.50000000
O11  O   0.34791518  0.00925265  0.50000000
O12  O   0.35121314  0.25948859  0.00000000
O13  O   0.35371615  0.75959582  0.00000000
O14  O   0.35746648  0.50723380  0.50000000
Sr3  Sr  0.40158871  0.00523019  0.00000000
Sr4  Sr  0.40162022  0.50591384  0.00000000
O15  O   0.40114854  0.23414303  0.50000000
O16  O   0.40218767  0.77754543  0.50000000
```

```
Ti7  Ti  0.45065789  0.25287537  0.50000000
Ti8  Ti  0.45108518  0.75301522  0.50000000
O17  O   0.45492856  0.00314958  0.50000000
O18  O   0.45133258  0.75294751  0.00000000
O19  O   0.45039669  0.25314708  0.00000000
O20  O   0.44688655  0.50297920  0.50000000
Sr5  Sr  0.50000000  0.00000000  0.00000000
Sr6  Sr  0.50000000  0.50000000  0.00000000
O21  O   0.50025043  0.72963370  0.50000000
#End data_Wien2k_Data
```

D.3.6. RT2

```
data_Wien2k_Data
_cell_length_a    5.578345
_cell_length_b   37.920506
_cell_length_c    5.578345
_cell_angle_alpha   90.000000
_cell_angle_beta    90.000000
_cell_angle_gamma   90.000000
_symmetry_space_group_name_H-M         'Pmma'
_symmetry_space_group_number   51
loop_
_symmetry_equiv_pos_as_xyz
   +x,+y,+z
   -x,-y,-z
   -x,+y,-z
   +x,-y,+z
   -x+1/2,+y,+z
   +x+1/2,-y,-z
   -x+1/2,-y,+z
   +x+1/2,+y,-z
loop_
_atom_site_label
_atom_site_type_symbol
_atom_site_fract_x
_atom_site_fract_y
_atom_site_fract_z
Ti1  Ti  0.00000000  0.31161758  0.50000000
O1   O   0.25000000  0.30364213  0.74789119
O2   O   0.75000000  0.33198032  0.67214518
Ti2  Ti  0.75000000  0.25283429  0.23173074
O3   O   0.00000000  0.25940421  0.50000000
O4   O   0.50000000  0.24533204  0.00000000
Sr1  Sr  0.75000000  0.20238002  0.74760021
O5   O   0.75000000  0.20267405  0.30269457
Ti3  Ti  0.25000000  0.15188167  0.74966793
O6   O   0.00000000  0.15653300  0.00000000
O7   O   0.50000000  0.14680582  0.50000000
Sr2  Sr  0.25000000  0.10107271  0.25133785
O8   O   0.25000000  0.10121115  0.79405459
Ti4  Ti  0.25000000  0.05058572  0.75022384
O9   O   0.00000000  0.04607506  0.00000000
O10  O   0.50000000  0.05495435  0.50000000
Sr3  Sr  0.25000000  0.00000000  0.24902446
```

```
O11  O   0.25000000  0.00000000  0.70727225
#End data_Wien2k_Data
```

D.3.7. RT2Diss

```
data_Wien2k_Data
_cell_length_a    5.505504
_cell_length_b    5.505504
_cell_length_c   39.452831
_cell_angle_alpha   90.000000
_cell_angle_beta    90.000000
_cell_angle_gamma   90.000000
_symmetry_space_group_name_H-M         'P-1'
_symmetry_space_group_number    2
loop_
_symmetry_equiv_pos_as_xyz
   +x,+y,+z
   -x,-y,-z
loop_
_atom_site_label
_atom_site_type_symbol
_atom_site_fract_x
_atom_site_fract_y
_atom_site_fract_z
Ow   O   0.93641788  0.02391235  0.35780319
H1   H   0.03901719  0.92597828  0.37263040
H2   H   0.70820612  0.39735324  0.30642604
Ti1a Ti  0.51944525  0.02247674  0.70465887
Ti1b Ti  0.99418641  0.98800755  0.31223618
O1a  O   0.77339652  0.78152741  0.70635479
O1b  O   0.24309584  0.24009720  0.70556694
O2a  O   0.28358127  0.78148953  0.69215131
O2b  O   0.74160593  0.21713734  0.68396015
Ti2a Ti  0.75893853  0.73176763  0.24251445
Ti2b Ti  0.23628392  0.25950755  0.24316018
O3a  O   0.47857379  0.97481586  0.24813591
O3b  O   0.01434171  0.99974549  0.75705623
O4a  O   0.00244972  0.49975854  0.23654730
O4b  O   0.49469157  0.51628909  0.75930762
Sr1a Sr  0.74406933  0.24096873  0.19522540
Sr1b Sr  0.25255954  0.75010573  0.19540306
O5a  O   0.72505271  0.77947105  0.19485693
O5b  O   0.26637351  0.21019691  0.19504135
Ti3a Ti  0.24846387  0.24743334  0.14615715
Ti3b Ti  0.74759929  0.74586203  0.14594713
O6a  O   0.49824550  0.49678952  0.14795369
O6b  O   0.00175856  0.50327307  0.84910459
O7a  O   0.99855099  0.99649844  0.14390610
O7b  O   0.50095117  0.00265538  0.85845680
Sr2a Sr  0.24860078  0.74839161  0.09745798
Sr2b Sr  0.74905552  0.24730037  0.09750540
O8a  O   0.23907615  0.28256476  0.09745105
O8b  O   0.75826492  0.71295900  0.09736173
Ti4a Ti  0.24922637  0.24895628  0.04873107
Ti4b Ti  0.74982145  0.74900440  0.04864903
```

```
O9a  O   0.49924744  0.49938848  0.04593440
O9b  O   0.00060002  0.50132369  0.95541717
O10a O   0.00028753  0.99824817  0.05146752
O10b O   0.49982975  0.00061571  0.94719274
Sr3  Sr  0.25028961  0.74960145  0.00003045
O11  O   0.25621042  0.21488002  0.00001190
#End data_Wien2k_Data
```

D.3.8. RT2SatD

```
data_Wien2k_Data
_cell_length_a    5.505504
_cell_length_b    5.505504
_cell_length_c   39.452831
_cell_angle_alpha   90.000000
_cell_angle_beta    90.000000
_cell_angle_gamma   90.000000
_symmetry_space_group_name_H-M          'P-1'
_symmetry_space_group_number    2
loop_
_symmetry_equiv_pos_as_xyz
   +x,+y,+z
   -x,-y,-z
loop_
_atom_site_label
_atom_site_type_symbol
_atom_site_fract_x
_atom_site_fract_y
_atom_site_fract_z
Ow   O   0.96346644  0.99760265  0.35163770
H1   H   0.12234822  0.96530553  0.36274907
H2   H   0.70986411  0.42380309  0.30389820
H3   H   0.78907390  0.43469276  0.69628460
Ow2  O   0.45042236  0.95888395  0.35079876
H4   H   0.59688241  0.99377029  0.36433384
Ti1a Ti  0.53325050  0.01599267  0.69637320
Ti1b Ti  0.96716128  0.00228021  0.30499048
O1a  O   0.77774227  0.76717628  0.70390489
O1b  O   0.27437031  0.24479415  0.70428262
O2a  O   0.28768616  0.75744493  0.69613723
O2b  O   0.78796221  0.25511568  0.69954187
Ti2a Ti  0.73528572  0.73803604  0.24421989
Ti2b Ti  0.23460696  0.25730277  0.24442733
O3a  O   0.47668370  0.99324816  0.25083409
O3b  O   0.02488814  0.99575773  0.75063003
O4a  O   0.98720737  0.50052605  0.23862559
O4b  O   0.51275040  0.50472324  0.75932134
Sr1a Sr  0.73741895  0.24652082  0.19737183
Sr1b Sr  0.23987266  0.74950760  0.19740104
O5a  O   0.72281137  0.79293755  0.19636321
O5b  O   0.25157260  0.20386007  0.19649845
Ti3a Ti  0.24061190  0.24853923  0.14719361
Ti3b Ti  0.74213202  0.74898455  0.14713021
O6a  O   0.49047135  0.49995317  0.14949999
O6b  O   0.00948066  0.50237758  0.84691541
```

```
O7a  O   0.99238413  0.99824367  0.14506718
O7b  O   0.50707266  0.00025273  0.85827215
Sr2a Sr  0.24444633  0.75021315  0.09826133
Sr2b Sr  0.74560240  0.24842463  0.09834453
O8a  O   0.22343770  0.28537423  0.09822516
O8b  O   0.76451841  0.71331996  0.09821018
Ti4a Ti  0.24718641  0.25009096  0.04909067
Ti4b Ti  0.74698532  0.74963988  0.04905954
O9a  O   0.49587945  0.50111376  0.04772838
O9b  O   0.00353797  0.50145550  0.95638369
O10a O   0.99825033  0.99872571  0.05044290
O10b O   0.50188154  0.99954769  0.94545376
Sr3  Sr  0.25061682  0.74963637  0.00006917
O11  O   0.27167846  0.21616558  0.00002189
#End data_Wien2k_Data
```

D.3.9. Zigzag 2×2

```
data_Wien2k_Data
_cell_length_a    7.785958
_cell_length_b   38.930564
_cell_length_c    7.785958
_cell_angle_alpha   90.000000
_cell_angle_beta    90.000000
_cell_angle_gamma   90.000000
_symmetry_space_group_name_H-M          'Pccm'
_symmetry_space_group_number   49
loop_
_symmetry_equiv_pos_as_xyz
   +x,+y,+z
   -x,-y,+z
   -x,+y,-z+1/2
   +x,-y,-z+1/2
   -x,-y,-z
   +x,+y,-z
   +x,-y,+z+1/2
   -x,+y,+z+1/2
loop_
_atom_site_label
_atom_site_type_symbol
_atom_site_fract_x
_atom_site_fract_y
_atom_site_fract_z
Ti1  Ti  0.50000000  0.30537631  0.75000000
Ti2  Ti  0.78459803  0.30600669  0.50000000
O1   O   0.29180352  0.32499768  0.79456362
O2   O   0.48221003  0.29736831  0.50000000
O3   O   0.01196245  0.29745870  0.50000000
Ti3  Ti  0.01567154  0.24938150  0.50000000
Ti4  Ti  0.49335883  0.24623504  0.50000000
O4   O   0.75128731  0.25683649  0.50000000
O5   O   0.50000000  0.25351623  0.75000000
O6   O   0.00000000  0.24271116  0.75000000
O7   O   0.25769470  0.23843670  0.50000000
Sr1  Sr  0.76289708  0.19800344  0.74695925
```

```
O8   O   0.53946969  0.19919982  0.50000000
O9   O   0.97158849  0.19766201  0.50000000
Ti5  Ti  0.99881363  0.14908618  0.50000000
Ti6  Ti  0.50121155  0.14848036  0.50000000
O10  O   0.25121232  0.15329008  0.50000000
O11  O   0.50000000  0.14990003  0.75000000
O12  O   0.00000000  0.14782771  0.75000000
O13  O   0.74979134  0.14371300  0.50000000
Sr2  Sr  0.24862567  0.09904025  0.74948806
O14  O   0.48314462  0.09948582  0.50000000
O15  O   0.01720978  0.09905398  0.50000000
Ti7  Ti  0.49851021  0.04961166  0.50000000
Ti8  Ti  0.00143618  0.04970739  0.50000000
O16  O   0.25045906  0.04778902  0.50000000
O17  O   0.74960521  0.05113359  0.50000000
O18  O   0.00000000  0.04935534  0.75000000
O19  O   0.50000000  0.05031450  0.75000000
Sr3  Sr  0.24911773  0.00000000  0.75000000
O20  O   0.00000000  0.00000000  0.50000000
O21  O   0.50000000  0.00000000  0.50000000
#End data_Wien2k_Data
```

D.3.10. 2×2Mol

```
data_Wien2k_Data
_cell_length_a    7.785958
_cell_length_b   38.930564
_cell_length_c    7.785958
_cell_angle_alpha   90.000000
_cell_angle_beta    90.000000
_cell_angle_gamma   90.000000
_symmetry_space_group_name_H-M          'Pccm'
_symmetry_space_group_number   49
loop_
_symmetry_equiv_pos_as_xyz
   +x,+y,+z
   -x,-y,+z
   -x,+y,-z+1/2
   +x,-y,-z+1/2
   -x,-y,-z
   +x,+y,-z
   +x,-y,+z+1/2
   -x,+y,+z+1/2
loop_
_atom_site_label
_atom_site_type_symbol
_atom_site_fract_x
_atom_site_fract_y
_atom_site_fract_z
Ow   O   0.88994607  0.36335562  0.50000000
H1   H   0.82134382  0.37008526  0.60038266
Ti1  Ti  0.50000000  0.30374291  0.75000000
Ti2  Ti  0.79674611  0.30809511  0.50000000
O1   O   0.29549281  0.32490519  0.79182235
O2   O   0.47692825  0.29683988  0.50000000
```

```
O3   O   0.02037828  0.29668063  0.50000000
Ti3  Ti  0.01377826  0.24861409  0.50000000
Ti4  Ti  0.49433110  0.24595755  0.50000000
O4   O   0.75246116  0.25825235  0.50000000
O5   O   0.50000000  0.25250780  0.75000000
O6   O   0.00000000  0.24203586  0.75000000
O7   O   0.25754315  0.23762922  0.50000000
Sr1  Sr  0.76301190  0.19758150  0.74766825
O8   O   0.54374546  0.19901452  0.50000000
O9   O   0.96909918  0.19709897  0.50000000
Ti5  Ti  0.99905554  0.14855184  0.50000000
Ti6  Ti  0.50168391  0.14840249  0.50000000
O10  O   0.25164840  0.15335999  0.50000000
O11  O   0.50000000  0.14950468  0.75000000
O12  O   0.00000000  0.14750836  0.75000000
O13  O   0.74985495  0.14286525  0.50000000
Sr2  Sr  0.24892643  0.09873642  0.74929567
O14  O   0.48130578  0.09930652  0.50000000
O15  O   0.01964166  0.09878467  0.50000000
Ti7  Ti  0.49841971  0.04953001  0.50000000
Ti8  Ti  0.00156890  0.04953674  0.50000000
O16  O   0.25039308  0.04746603  0.50000000
O17  O   0.74981355  0.05127659  0.50000000
O18  O   0.00000000  0.04932412  0.75000000
O19  O   0.50000000  0.04974689  0.75000000
Sr3  Sr  0.24936128  0.00000000  0.75000000
O20  O   0.00000000  0.00000000  0.50000000
O21  O   0.50000000  0.00000000  0.50000000
#End data_Wien2k_Data
```

D.3.11. 2×2SatD

```
data_Wien2k_Data
_cell_length_a    7.785958
_cell_length_b   38.930609
_cell_length_c    7.785958
_cell_angle_alpha   90.000000
_cell_angle_beta    90.000000
_cell_angle_gamma   90.000000
_symmetry_space_group_name_H-M         'P2/c11'
loop_
_symmetry_equiv_pos_as_xyz
   +x,+y,+z
   -x,-y,-z
   -x,+y,+z+1/2
   +x,-y,-z+1/2
loop_
_atom_site_label
_atom_site_type_symbol
_atom_site_fract_x
_atom_site_fract_y
_atom_site_fract_z
Ow1  O   0.79511343  0.35579383  0.45556855
Ow2  O   0.49368275  0.35864119  0.75430220
H1   H   0.38632616  0.36636458  0.81447680
```

```
H2   H   0.79150724  0.36994700  0.55919146
H3   H   0.17026044  0.30465753  0.64086715
H4   H   0.83785720  0.69381332  0.67207966
Ti1  Ti  0.50483960  0.31246802  0.74177898
Ti2  Ti  0.80463192  0.30794275  0.48263939
O1a  O   0.25607088  0.30669593  0.74020420
O1b  O   0.75394366  0.68875054  0.77011324
O2   O   0.52124083  0.30272142  0.49196237
O3   O   0.03631051  0.29796180  0.48966966
Ti3  Ti  0.01475605  0.24717995  0.50093796
Ti4  Ti  0.50214160  0.24934946  0.49664495
O4   O   0.76108428  0.25615452  0.49459377
O5   O   0.50484351  0.25531822  0.74654067
O6   O   0.99896795  0.24325794  0.74718389
O7   O   0.26017508  0.24170632  0.49949848
Sr1a Sr  0.75603360  0.19992480  0.74642548
Sr2b Sr  0.24395780  0.80005320  0.74832556
O8   O   0.53546288  0.20112170  0.49820671
O9   O   0.97626070  0.19792321  0.49706619
Ti5  Ti  0.99998099  0.14906180  0.49909270
Ti6  Ti  0.50158411  0.15001600  0.49945567
O10  O   0.25181946  0.15393013  0.49960820
O11  O   0.50043721  0.15117654  0.74933456
O12  O   0.99959379  0.14822850  0.74887960
O13  O   0.74982933  0.14523280  0.49897480
Sr2a Sr  0.24963788  0.09973955  0.74953593
Sr2b Sr  0.75023516  0.90023924  0.75028425
O14  O   0.48543543  0.10029010  0.49971351
O15  O   0.01625554  0.09934217  0.49907959
Ti7  Ti  0.49866746  0.05003157  0.49990727
Ti8  Ti  0.00137098  0.04978793  0.49982707
O16  O   0.25052159  0.04828787  0.49983072
O17  O   0.74977730  0.05142341  0.49992694
O18  O   0.00009435  0.04960211  0.74978118
O19  O   0.49993528  0.05026864  0.74990125
Sr3a Sr  0.24983986  0.00000000  0.75000000
Sr3b Sr  0.75011034  0.00000000  0.75000000
O20  O   0.00000000  0.00000000  0.50000000
O21  O   0.50000000  0.00000000  0.50000000
#End data_Wien2k_Data
```

D.3.12. c(4×2)

```
data_Wien2k_Data
_cell_length_a    7.785958
_cell_length_b   15.571916
_cell_length_c   38.930516
_cell_angle_alpha   90.000000
_cell_angle_beta    90.000000
_cell_angle_gamma   90.000000
_symmetry_space_group_name_H-M          'Cmmm'
_symmetry_space_group_number   65
loop_
_symmetry_equiv_pos_as_xyz
   +x,+y,+z
```

```
   -x,-y,-z
   -x,-y,+z
   -x,+y,-z
   -x,+y,+z
   +x,-y,-z
   +x,-y,+z
   +x,+y,-z
   +x+1/2,+y+1/2,+z
   -x+1/2,-y+1/2,-z
   -x+1/2,-y+1/2,+z
   -x+1/2,+y+1/2,-z
   -x+1/2,+y+1/2,+z
   +x+1/2,-y+1/2,-z
   +x+1/2,-y+1/2,+z
   +x+1/2,+y+1/2,-z
loop_
_atom_site_label
_atom_site_type_symbol
_atom_site_fract_x
_atom_site_fract_y
_atom_site_fract_z
Ti1  Ti  0.76119347  0.00000000  0.30532427
Ti2  Ti  0.00000000  0.36123139  0.30452437
O1   O   0.20994768  0.39503974  0.32346526
O2   O   0.00000000  0.00000000  0.29822089
O3   O   0.00000000  0.24819283  0.29702529
O4   O   0.50000000  0.00000000  0.29655596
Ti3  Ti  0.50000000  0.00000000  0.24613267
Ti4  Ti  0.00000000  0.24103021  0.24875240
Ti5  Ti  0.00000000  0.00000000  0.24562024
O5   O   0.00000000  0.37543777  0.25303385
O6   O   0.75039306  0.00000000  0.25382000
O7   O   0.00000000  0.12153151  0.24174282
O8   O   0.25000000  0.25000000  0.24207505
Sr1  Sr  0.24813942  0.13191307  0.19772028
O9   O   0.00000000  0.00000000  0.19755512
O10  O   0.00000000  0.25726660  0.19720343
O11  O   0.50000000  0.00000000  0.19891679
Ti6  Ti  0.50000000  0.00000000  0.14753364
Ti7  Ti  0.00000000  0.00000000  0.14833553
Ti8  Ti  0.00000000  0.25082140  0.14825604
O12  O   0.00000000  0.12565737  0.14865586
O13  O   0.25000000  0.25000000  0.14717729
O14  O   0.50000000  0.12394302  0.14736967
O15  O   0.25051406  0.00000000  0.14909880
Sr2  Sr  0.24963841  0.12552322  0.09875151
O16  O   0.00000000  0.00000000  0.09906453
O17  O   0.00000000  0.25024464  0.09860705
O18  O   0.50000000  0.00000000  0.09867048
Ti9  Ti  0.50000000  0.00000000  0.04928214
Ti10 Ti  0.00000000  0.00000000  0.04943863
Ti11 Ti  0.00000000  0.25004675  0.04931882
O19  O   0.00000000  0.12491403  0.04945459
O20  O   0.25000000  0.25000000  0.04908407
O21  O   0.50000000  0.12499556  0.04914130
```

```
O22  O   0.24992812  0.00000000  0.04957499
Sr3  Sr  0.24978791  0.12512914  0.00000000
O23  O   0.00000000  0.00000000  0.00000000
O24  O   0.00000000  0.24941310  0.00000000
O25  O   0.50000000  0.00000000  0.00000000
#End data_Wien2k_Data
```

D.3.13. c(4×2)Mol

```
data_Wien2k_Data
_cell_length_a    7.785958
_cell_length_b   15.571916
_cell_length_c   39.602027
_cell_angle_alpha   90.000000
_cell_angle_beta    90.000000
_cell_angle_gamma   90.000000
_symmetry_space_group_name_H-M          'Cmmm'
_symmetry_space_group_number   65
loop_
_symmetry_equiv_pos_as_xyz
   +x,+y,+z
   -x,-y,-z
   -x,-y,+z
   -x,+y,-z
   -x,+y,+z
   +x,-y,-z
   +x,-y,+z
   +x,+y,-z
   +x+1/2,+y+1/2,+z
   -x+1/2,-y+1/2,-z
   -x+1/2,-y+1/2,+z
   -x+1/2,+y+1/2,-z
   -x+1/2,+y+1/2,+z
   +x+1/2,-y+1/2,-z
   +x+1/2,-y+1/2,+z
   +x+1/2,+y+1/2,-z
loop_
_atom_site_label
_atom_site_type_symbol
_atom_site_fract_x
_atom_site_fract_y
_atom_site_fract_z
Ow1  O   0.00000000  0.31151203  0.35500235
H1   H   0.10139277  0.34515782  0.36175029
Ti1  Ti  0.76103444  0.00000000  0.29826128
Ti2  Ti  0.00000000  0.35725895  0.30178358
O1   O   0.21786824  0.39565826  0.31741830
O2   O   0.00000000  0.00000000  0.29191029
O3   O   0.00000000  0.24580996  0.29150894
O4   O   0.50000000  0.00000000  0.29231527
Ti3  Ti  0.50000000  0.00000000  0.24216768
Ti4  Ti  0.00000000  0.24179711  0.24424198
Ti5  Ti  0.00000000  0.00000000  0.24045211
O5   O   0.00000000  0.37562476  0.25015379
O6   O   0.75027575  0.00000000  0.24822733
```

```
O7   O   0.00000000  0.12191515  0.23706818
O8   O   0.25000000  0.25000000  0.23773730
Sr1  Sr  0.24836217  0.13168887  0.19422051
O9   O   0.00000000  0.00000000  0.19360027
O10  O   0.00000000  0.25863272  0.19372462
O11  O   0.50000000  0.00000000  0.19567986
Ti6  Ti  0.50000000  0.00000000  0.14492731
Ti7  Ti  0.00000000  0.00000000  0.14530274
Ti8  Ti  0.00000000  0.25091249  0.14578307
O12  O   0.00000000  0.12578209  0.14611538
O13  O   0.25000000  0.25000000  0.14480573
O14  O   0.50000000  0.12379070  0.14472325
O15  O   0.25046019  0.00000000  0.14623403
Sr2  Sr  0.25000160  0.12564131  0.09701093
O16  O   0.00000000  0.00000000  0.09716830
O17  O   0.00000000  0.25041184  0.09693355
O18  O   0.50000000  0.00000000  0.09690413
Ti9  Ti  0.50000000  0.00000000  0.04838474
Ti10 Ti  0.00000000  0.00000000  0.04844589
Ti11 Ti  0.00000000  0.25000637  0.04853669
O19  O   0.00000000  0.12486933  0.04864045
O20  O   0.25000000  0.25000000  0.04831215
O21  O   0.50000000  0.12495286  0.04828239
O22  O   0.24991776  0.00000000  0.04862542
Sr3  Sr  0.25005872  0.12526506  0.00000000
O23  O   0.00000000  0.00000000  0.00000000
O24  O   0.00000000  0.24942334  0.00000000
O25  O   0.50000000  0.00000000  0.00000000
#End data_Wien2k_Data
```

D.3.14. c(4×2)SatD

```
data_Wien2k_Data
_cell_length_a    7.785958
_cell_length_b   15.571916
_cell_length_c   39.601996
_cell_angle_alpha   90.000000
_cell_angle_beta    90.000000
_cell_angle_gamma   90.000000
_symmetry_space_group_name_H-M         'Cmmm'
_symmetry_space_group_number   65
loop_
_symmetry_equiv_pos_as_xyz
   +x,+y,+z
   -x,-y,-z
   -x,-y,+z
   -x,+y,-z
   -x,+y,+z
   +x,-y,-z
   +x,-y,+z
   +x,+y,-z
   +x+1/2,+y+1/2,+z
   -x+1/2,-y+1/2,-z
   -x+1/2,-y+1/2,+z
   -x+1/2,+y+1/2,-z
```

```
   -x+1/2,+y+1/2,+z
   +x+1/2,-y+1/2,-z
   +x+1/2,-y+1/2,+z
   +x+1/2,+y+1/2,-z
loop_
_atom_site_label
_atom_site_type_symbol
_atom_site_fract_x
_atom_site_fract_y
_atom_site_fract_z
Ow1  O   0.00000000  0.33576869  0.34943206
H1   H   0.00000000  0.38429665  0.36494857
Ow2  O   0.75376650  0.00000000  0.35113248
H2   H   0.83207610  0.00000000  0.37010322
H3   H   0.34183133  0.33310305  0.29765094
Ti1  Ti  0.76266650  0.00000000  0.30487332
Ti2  Ti  0.00000000  0.34462131  0.30349194
O1   O   0.24383924  0.37557445  0.30084698
O2   O   0.00000000  0.00000000  0.29518778
O3   O   0.00000000  0.23173299  0.29175688
O4   O   0.50000000  0.00000000  0.29893733
Ti3  Ti  0.50000000  0.00000000  0.24554778
Ti4  Ti  0.00000000  0.24339888  0.24187923
Ti5  Ti  0.00000000  0.00000000  0.24322878
O5   O   0.00000000  0.37376827  0.25060091
O6   O   0.75029161  0.00000000  0.25059128
O7   O   0.00000000  0.12268064  0.23740455
O8   O   0.25000000  0.25000000  0.23816972
Sr1  Sr  0.25118859  0.12721939  0.19572097
O9   O   0.00000000  0.00000000  0.19526155
O10  O   0.00000000  0.26000944  0.19375316
O11  O   0.50000000  0.00000000  0.19810378
Ti6  Ti  0.50000000  0.00000000  0.14610491
Ti7  Ti  0.00000000  0.00000000  0.14672691
Ti8  Ti  0.00000000  0.25056358  0.14579695
O12  O   0.00000000  0.12572060  0.14689750
O13  O   0.25000000  0.25000000  0.14513053
O14  O   0.50000000  0.12350797  0.14537223
O15  O   0.25066648  0.00000000  0.14746871
Sr2  Sr  0.24996671  0.12526383  0.09758540
O16  O   0.00000000  0.00000000  0.09800128
O17  O   0.00000000  0.25043448  0.09712844
O18  O   0.50000000  0.00000000  0.09764887
Ti9  Ti  0.50000000  0.00000000  0.04874389
Ti10 Ti  0.00000000  0.00000000  0.04886195
Ti11 Ti  0.00000000  0.25001409  0.04862411
O19  O   0.00000000  0.12480450  0.04890600
O20  O   0.25000000  0.25000000  0.04848268
O21  O   0.50000000  0.12490814  0.04852227
O22  O   0.24994417  0.00000000  0.04897762
Sr3  Sr  0.24991579  0.12505832  0.00000000
O23  O   0.00000000  0.00000000  0.00000000
O24  O   0.00000000  0.24929843  0.00000000
O25  O   0.50000000  0.00000000  0.00000000
#End data_Wien2k_Data
```

D.3.15. 2Ti

```
data_Wien2k_Data
_cell_length_a    3.892979
_cell_length_b    3.892979
_cell_length_c   38.930564
_cell_angle_alpha   90.000000
_cell_angle_beta    90.000000
_cell_angle_gamma   90.000000
_symmetry_space_group_name_H-M          'Pmmm'
loop_
_symmetry_equiv_pos_as_xyz
   +x,+y,+z
   -x,-y,-z
   -x,-y,+z
   -x,+y,-z
   -x,+y,+z
   +x,-y,-z
   +x,-y,+z
   +x,+y,-z
loop_
_atom_site_label
_atom_site_type_symbol
_atom_site_fract_x
_atom_site_fract_y
_atom_site_fract_z
Ti1  Ti  0.00000000  0.50000000  0.69078129
O1   O   0.50000000  0.50000000  0.68052334
O2   O   0.00000000  0.00000000  0.69758093
Ti2  Ti  0.00000000  0.00000000  0.74818802
O3   O   0.50000000  0.00000000  0.75411370
O4   O   0.00000000  0.50000000  0.74115481
Sr1  Sr  0.50000000  0.50000000  0.79841231
O5   O   0.00000000  0.00000000  0.79841994
Ti3  Ti  0.00000000  0.00000000  0.84876779
O6   O   0.50000000  0.00000000  0.84927704
O7   O   0.00000000  0.50000000  0.84792884
Sr2  Sr  0.50000000  0.50000000  0.89901776
O8   O   0.00000000  0.00000000  0.89909174
Ti4  Ti  0.00000000  0.00000000  0.94952481
O9   O   0.50000000  0.00000000  0.94946269
O10  O   0.00000000  0.50000000  0.94936969
Sr3  Sr  0.50000000  0.50000000  0.00000000
O11  O   0.00000000  0.00000000  0.00000000
#End data_Wien2k_Data
```

D.3.16. 2TiMol

```
data_Wien2k_Data
_cell_length_a    3.892979
_cell_length_b    3.892979
_cell_length_c   38.864876
_cell_angle_alpha   90.000000
_cell_angle_beta    90.000000
_cell_angle_gamma   90.000000
```

```
_symmetry_space_group_name_H-M         'P-1'
loop_
_symmetry_equiv_pos_as_xyz
   +x,+y,+z
   -x,-y,-z
loop_
_atom_site_label
_atom_site_type_symbol
_atom_site_fract_x
_atom_site_fract_y
_atom_site_fract_z
Ow  O   0.07139046  0.56919239  0.63769609
H1  H   0.32085842  0.55039755  0.64960534
H2  H   0.02918594  0.35248036  0.62572655
Ti1 Ti  0.94561874  0.53017753  0.69182244
O1  O   0.48905926  0.52672236  0.68232335
O2  O   0.98875022  0.02843411  0.69876314
Ti2 Ti  0.01745804  0.02576649  0.74959540
O3  O   0.50100804  0.02667397  0.75532666
O4  O   0.98948862  0.52632687  0.74297668
Sr1 Sr  0.50991136  0.52182582  0.79975681
O5  O   0.00115699  0.01645064  0.79970638
Ti3 Ti  0.00436045  0.01397515  0.84990468
O6  O   0.50362583  0.01328540  0.85068650
O7  O   0.00410406  0.51347124  0.84924834
Sr2 Sr  0.50281625  0.50914416  0.89996806
O8  O   0.00242344  0.00848457  0.89994917
Ti4 Ti  0.00137916  0.00431305  0.94998788
O9  O   0.50129008  0.00413111  0.95009133
O10 O   0.00118725  0.50423682  0.94993789
Sr3 Sr  0.50000000  0.50000000  0.00000000
O11 O   0.00000000  0.00000000  0.00000000
#End data_Wien2k_Data
```

D.3.17. 2TiMolR2

```
data_Wien2k_Data
_cell_length_a    5.505504
_cell_length_b    5.505504
_cell_length_c   38.864876
_cell_angle_alpha   90.000000
_cell_angle_beta    90.000000
_cell_angle_gamma   90.000000
_symmetry_space_group_name_H-M         'P-1'
loop_
_symmetry_equiv_pos_as_xyz
   +x,+y,+z
   -x,-y,-z
loop_
_atom_site_label
_atom_site_type_symbol
_atom_site_fract_x
_atom_site_fract_y
_atom_site_fract_z
Ow   O   0.32302517  0.69533525  0.64779748
```

```
H1   H   0.51663565  0.50799131  0.64818246
H2   H   0.19772912  0.65998811  0.63074770
Ti1a Ti  0.77148768  0.24216810  0.69114188
Ti1b Ti  0.21627304  0.79931403  0.69123725
O1a  O   0.64534698  0.38033305  0.65417307
O1b  O   0.99210172  0.01308381  0.67822057
O2a  O   0.00996662  0.51254482  0.70020499
O2b  O   0.49820946  0.00600671  0.70004363
Ti2a Ti  0.50178117  0.00929542  0.75057235
Ti2b Ti  0.00280515  0.51038058  0.75050314
O3a  O   0.25260806  0.26553710  0.75611333
O3b  O   0.74698123  0.76003014  0.75572985
O4a  O   0.74910123  0.26311321  0.74306686
O4b  O   0.24130120  0.77141809  0.74411050
Sr1a Sr  0.50254494  0.50814700  0.80069521
Sr1b Sr  1.00165278  0.00849596  0.80040017
O5a  O   0.99455641  0.50752622  0.80057072
O5b  O   0.50257251  0.01170638  0.80057643
Ti3a Ti  0.50021716  0.00701138  0.85060377
Ti3b Ti  1.00017375  0.50689328  0.85057642
O6a  O   0.24907643  0.25683990  0.85119621
O6b  O   0.75044033  0.75819538  0.85152485
O7a  O   0.24970575  0.75734780  0.84954449
O7b  O   0.74846365  0.25855954  0.85047097
Sr2a Sr  0.50067240  0.50426864  0.90049280
Sr2b Sr  1.00000282  0.00445615  0.90045540
O8a  O   0.00177017  0.50619609  0.90041679
O8b  O   0.49699315  0.00445486  0.90042513
Ti4a Ti  1.00023802  0.50240434  0.95023117
Ti4b Ti  0.49974416  0.00221707  0.95024330
O9a  O   0.24947909  0.25215317  0.95052157
O9b  O   0.75013229  0.75288101  0.95016450
O10a O   0.24980147  0.75247340  0.95044624
O10b O   0.74909212  0.25319088  0.94995444
Sr3a Sr  0.50000000  0.50000000  0.00000000
Sr3b Sr  0.00000000  0.00000000  0.00000000
O11a O   0.00000000  0.50000000  0.00000000
O11b O   0.50000000  0.00000000  0.00000000
#End data_Wien2k_Data
```

D.3.18. c(4×4)A

```
data_Wien2k_Data
_cell_length_a   34.445686
_cell_length_b   15.777941
_cell_length_c   15.777941
_cell_angle_alpha   90.000000
_cell_angle_beta    90.000000
_cell_angle_gamma   90.000000
_symmetry_space_group_name_H-M         'A112/m'
_symmetry_space_group_number   12
loop_
_symmetry_equiv_pos_as_xyz
   +x,+y,+z
   -x,-y,-z
```

```
   -x,-y,+z
   +x,+y,-z
   -x,-y+1/2,-z+1/2
   -x,-y+1/2,+z+1/2
   +x,+y+1/2,-z+1/2
   +x,+y+1/2,+z+1/2
loop_
_atom_site_label
_atom_site_type_symbol
_atom_site_fract_x
_atom_site_fract_y
_atom_site_fract_z
O1   O   0.27639789  0.30414371  0.00000000
O2   O   0.24245788  0.49001748  0.00000000
Ti1  Ti  0.23803521  0.36537919  0.00000000
Ti2  Ti  0.24135069  0.02066088  0.37966915
O3   O   0.22695963  0.37446429  0.37594870
O4   O   0.22578782  0.12767514  0.37639363
O5   O   0.17561775  0.50196669  0.37835519
O6   O   0.17530340  0.36782835  0.00000000
Ti3  Ti  0.17095576  0.12628040  0.37509885
Ti4  Ti  0.16797942  0.36288638  0.37738956
O7   O   0.16420237  0.13180779  0.00000000
O8   O   0.16087153  0.24945414  0.37426060
O9   O   0.11549462  0.38858689  0.37264061
Sr1  Sr  0.11679852  0.00504636  0.00000000
Sr2  Sr  0.11280959  0.24971851  0.00000000
O10  O   0.11153472  0.11475405  0.37495254
O11  O   0.05971120  0.25081782  0.37494360
O12  O   0.05881848  0.37545526  0.00000000
Ti5  Ti  0.05728508  0.12387752  0.37444740
Ti6  Ti  0.05563072  0.37511976  0.37525386
O13  O   0.05554160  0.12575444  0.00000000
O14  O   0.05278644  0.50023963  0.37505610
O15  O   0.99887403  0.13310451  0.37496981
Sr3  Sr  0.00017249  0.25038748  0.00000000
Sr4  Sr  0.00000000  0.00000000  0.00000000
O16  O   0.27966217  0.31533052  0.24966947
O17  O   0.24267212  0.48867421  0.26049909
Ti7  Ti  0.23502839  0.37412767  0.25086089
Ti8  Ti  0.22834332  0.01305280  0.11957400
O18  O   0.22872145  0.38175989  0.12661132
O19  O   0.22538697  0.12509651  0.12380943
O20  O   0.17567053  0.50195958  0.12452934
O21  O   0.17742499  0.36789228  0.25039838
Ti9  Ti  0.17036105  0.13957264  0.12497117
Ti10 Ti  0.16887024  0.37744057  0.12341462
O22  O   0.16424554  0.12834345  0.24932260
O23  O   0.16213487  0.25542096  0.12523755
O24  O   0.11539778  0.39043467  0.12636234
Sr5  Sr  0.11544087  0.00529106  0.24810979
Sr6  Sr  0.11245135  0.24702345  0.24986586
O25  O   0.11223001  0.11609674  0.12483522
O26  O   0.06046258  0.25094066  0.12487676
O27  O   0.05818940  0.37535971  0.25009785
```

```
Ti11 Ti  0.05769026  0.12427363  0.12449922
Ti12 Ti  0.05578749  0.37550713  0.12552120
O28  O   0.05522155  0.12591649  0.24968012
O29  O   0.05278538  0.50014586  0.12496181
O30  O   0.99915902  0.13334545  0.12468887
Sr7  Sr  0.00000000  0.25000000  0.25000000
Sr8  Sr  0.00000000  0.00000000  0.24938437
O31  O   0.27806217  0.30041724  0.50000000
O32  O   0.24506407  0.48664522  0.50000000
Ti13 Ti  0.23970011  0.36089001  0.50000000
O33  O   0.17445493  0.36562967  0.50000000
O34  O   0.16399665  0.12864774  0.50000000
Sr9  Sr  0.11400344  0.00535927  0.50000000
Sr10 Sr  0.11187676  0.24285951  0.50000000
O35  O   0.05879442  0.37549483  0.50000000
O36  O   0.05502811  0.12584622  0.50000000
Sr11 Sr  0.00000000  0.00000000  0.50000000
O37  O   0.29344713  0.03284427  0.36852342
H1   H   0.31458106  0.99366289  0.38017082
H2   H   0.28798873  0.25658780  0.25399861
#End data_Wien2k_Data
```

D.3.19. c(4×4)B

```
data_Wien2k_Data
_cell_length_a   34.445686
_cell_length_b   15.777941
_cell_length_c   15.777941
_cell_angle_alpha   90.000000
_cell_angle_beta    90.000000
_cell_angle_gamma   90.000000
_symmetry_space_group_name_H-M         'A112/m'
_symmetry_space_group_number   12
loop_
_symmetry_equiv_pos_as_xyz
   +x,+y,+z
   -x,-y,-z
   -x,-y,+z
   +x,+y,-z
   -x,-y+1/2,-z+1/2
   -x,-y+1/2,+z+1/2
   +x,+y+1/2,-z+1/2
   +x,+y+1/2,+z+1/2
loop_
_atom_site_label
_atom_site_type_symbol
_atom_site_fract_x
_atom_site_fract_y
_atom_site_fract_z
O1   O   0.27691324  0.55442289  0.12456588
O2   O   0.24340779  0.73608365  0.13182869
Ti1  Ti  0.23442324  0.62087778  0.12544538
Ti2  Ti  0.23985754  0.26988213  0.00000000
O3   O   0.22856974  0.63017760  0.00000000
O4   O   0.22629985  0.37850265  0.00000000
```

O5	O	0.17738397	0.75269659	0.00000000
O6	O	0.17734023	0.61675054	0.12468390
Ti3	Ti	0.17119768	0.37923683	0.00000000
Ti4	Ti	0.16855630	0.62044625	0.00000000
O7	O	0.16415865	0.37881321	0.12474881
O8	O	0.16232165	0.50254896	0.00000000
O9	O	0.11574991	0.63933670	0.00000000
Sr1	Sr	0.11585378	0.25415300	0.12396206
Sr2	Sr	0.11249048	0.49589905	0.12343507
O10	O	0.11191201	0.36597725	0.00000000
O11	O	0.05967744	0.50096371	0.00000000
O12	O	0.05824060	0.62513521	0.12465470
Ti5	Ti	0.05749430	0.37327469	0.00000000
Ti6	Ti	0.05533330	0.62488372	0.00000000
O13	O	0.05531676	0.37587828	0.12503907
O14	O	0.05287266	0.74988480	0.00000000
O15	O	0.99922644	0.38195757	0.00000000
Sr3	Sr	0.00000000	0.50000000	0.12506147
Sr4	Sr	0.00022370	0.24975030	0.12543645
O16	O	0.28228614	0.56368099	0.37353009
O17	O	0.24363440	0.73817948	0.36927664
Ti7	Ti	0.24094879	0.61404680	0.37610671
Ti8	Ti	0.22927718	0.26184268	0.24592897
O18	O	0.22685306	0.62359324	0.25051765
O19	O	0.22510935	0.37372719	0.24907658
O20	O	0.17557427	0.75084153	0.25240238
O21	O	0.17381038	0.61682672	0.37479348
Ti9	Ti	0.16988189	0.38381480	0.24991349
Ti10	Ti	0.16790380	0.61710559	0.25498818
O22	O	0.16401479	0.37861275	0.37384690
O23	O	0.16064952	0.50139375	0.24878602
O24	O	0.11527066	0.63942703	0.24783348
Sr5	Sr	0.11516616	0.25448984	0.37552450
Sr6	Sr	0.11227755	0.49608847	0.37739072
O25	O	0.11196247	0.36326178	0.24968814
O26	O	0.06023480	0.50047690	0.24991540
O27	O	0.05844574	0.62512949	0.37472696
Ti11	Ti	0.05745606	0.37344857	0.24984847
Ti12	Ti	0.05576343	0.62484604	0.24979992
O28	O	0.05527203	0.37569544	0.37491924
O29	O	0.05265280	0.74985199	0.24986051
O30	O	0.99908058	0.38265867	0.24978308
Sr7	Sr	0.00000000	0.50000000	0.37507087
Ti13	Ti	0.23919930	0.27142881	0.50000000
O31	O	0.22880359	0.62792008	0.50000000
O32	O	0.22558562	0.37907676	0.50000000
O33	O	0.17687665	0.75174834	0.50000000
Ti14	Ti	0.17068430	0.38009818	0.50000000
Ti15	Ti	0.16923266	0.62130880	0.50000000
O34	O	0.16195528	0.50202089	0.50000000
O35	O	0.11525464	0.63954596	0.50000000
O36	O	0.11173971	0.36524241	0.50000000
O37	O	0.05959236	0.50079662	0.50000000
Ti16	Ti	0.05701724	0.37308864	0.50000000
Ti17	Ti	0.05618093	0.62533911	0.50000000

```
O38  O   0.05307419  0.75030742  0.50000000
O39  O   0.99898682  0.38159439  0.50000000
O40  O   0.29241444  0.28489833  0.00000000
O41  O   0.29140596  0.28136563  0.50000000
H1   H   0.31532407  0.24886320  0.50000000
H2   H   0.31375482  0.24446796  0.00000000
H3   H   0.28149989  0.49355907  0.12616271
#End data_Wien2k_Data
```

D.4. Chapter 6 CIF Files

D.4.1. 1Sr Surface

```
data_Wien2k_Data
_cell_length_a    3.937746
_cell_length_b    3.937746
_cell_length_c   33.944806
_cell_angle_alpha   90.000000
_cell_angle_beta    90.000000
_cell_angle_gamma   90.000000
_symmetry_space_group_name_H-M         'P4/mmm '
_symmetry_space_group_number  123
loop_
_symmetry_equiv_pos_as_xyz
   +x,+y,+z
   -x,-y,-z
   -x,-y,+z
   -x,+y,-z
   -x,+y,+z
   -y,-x,-z
   -y,-x,+z
   +y,-x,-z
   +y,-x,+z
   -y,+x,-z
   -y,+x,+z
   +y,+x,-z
   +y,+x,+z
   +x,-y,-z
   +x,-y,+z
   +x,+y,-z
loop_
_atom_site_label
_atom_site_type_symbol
_atom_site_fract_x
_atom_site_fract_y
_atom_site_fract_z
Sr001  Sr  0.50000000  0.50000000  0.15971134
Sr002  Sr  0.50000000  0.50000000  0.27084926
Sr003  Sr  0.50000000  0.50000000  0.38507476
Sr004  Sr  0.50000000  0.50000000  0.50000000
Ti005  Ti  0.00000000  0.00000000  0.20942438
Ti006  Ti  0.00000000  0.00000000  0.32659215
Ti007  Ti  0.00000000  0.00000000  0.44224558
```

```
O0008  O   0.00000000  0.50000000  0.21071517
O0009  O   0.00000000  0.50000000  0.32690575
O0010  O   0.00000000  0.50000000  0.44236599
O0011  O   0.00000000  0.00000000  0.15309818
O0012  O   0.00000000  0.00000000  0.26911567
O0013  O   0.00000000  0.00000000  0.38454738
O0014  O   0.00000000  0.00000000  0.50000000
#End data_Wien2k_Data
```

D.4.2. 2Sr Surface

```
data_Wien2k_Data
_cell_length_a    3.937746
_cell_length_b    3.937746
_cell_length_c   38.744805
_cell_angle_alpha   90.000000
_cell_angle_beta    90.000000
_cell_angle_gamma   90.000000
_symmetry_space_group_name_H-M         'P4/mmm '
_symmetry_space_group_number  123
loop_
_symmetry_equiv_pos_as_xyz
   +x,+y,+z
   -x,-y,-z
   -x,-y,+z
   -x,+y,-z
   -x,+y,+z
   -y,-x,-z
   -y,-x,+z
   +y,-x,-z
   +y,-x,+z
   -y,+x,-z
   -y,+x,+z
   +y,+x,-z
   +y,+x,+z
   +x,-y,-z
   +x,-y,+z
   +x,+y,-z
loop_
_atom_site_label
_atom_site_type_symbol
_atom_site_fract_x
_atom_site_fract_y
_atom_site_fract_z
Sr001  Sr  0.50000000  0.50000000  0.20001570
Sr002  Sr  0.50000000  0.50000000  0.29830117
Sr003  Sr  0.50000000  0.50000000  0.39895208
Sr004  Sr  0.50000000  0.50000000  0.50000000
Ti005  Ti  0.00000000  0.00000000  0.24612628
Ti006  Ti  0.00000000  0.00000000  0.34793141
Ti007  Ti  0.00000000  0.00000000  0.44936092
O0008  O   0.00000000  0.50000000  0.24688530
O0009  O   0.00000000  0.50000000  0.34809626
O0010  O   0.00000000  0.50000000  0.44935437
O0011  O   0.00000000  0.00000000  0.19516261
```

```
O0012  O   0.00000000  0.00000000  0.29751402
O0013  O   0.00000000  0.00000000  0.39874750
O0014  O   0.00000000  0.00000000  0.50000000
O0015  O   0.50000000  0.50000000  0.13640924
Sr016  Sr  0.00000000  0.00000000  0.13416453
#End data_Wien2k_Data
```

D.4.3. 3Sr Surface

```
data_Wien2k_Data
_cell_length_a    3.937746
_cell_length_b    3.937746
_cell_length_c   43.744783
_cell_angle_alpha   90.000000
_cell_angle_beta    90.000000
_cell_angle_gamma   90.000000
_symmetry_space_group_name_H-M         'P4/mmm '
_symmetry_space_group_number  123
loop_
_symmetry_equiv_pos_as_xyz
   +x,+y,+z
   -x,-y,-z
   -x,-y,+z
   -x,+y,-z
   -x,+y,+z
   -y,-x,-z
   -y,-x,+z
   +y,-x,-z
   +y,-x,+z
   -y,+x,-z
   -y,+x,+z
   +y,+x,-z
   +y,+x,+z
   +x,-y,-z
   +x,-y,+z
   +x,+y,-z
loop_
_atom_site_label
_atom_site_type_symbol
_atom_site_fract_x
_atom_site_fract_y
_atom_site_fract_z
Sr001  Sr  0.50000000  0.50000000  0.23403898
Sr002  Sr  0.50000000  0.50000000  0.32131973
Sr003  Sr  0.50000000  0.50000000  0.41047782
Sr004  Sr  0.50000000  0.50000000  0.50000000
Ti005  Ti  0.00000000  0.00000000  0.27504479
Ti006  Ti  0.00000000  0.00000000  0.36535839
Ti007  Ti  0.00000000  0.00000000  0.45515005
O0008  O   0.00000000  0.50000000  0.27567483
O0009  O   0.00000000  0.50000000  0.36558420
O0010  O   0.00000000  0.50000000  0.45512972
O0011  O   0.00000000  0.00000000  0.23043670
O0012  O   0.00000000  0.00000000  0.32065900
O0013  O   0.00000000  0.00000000  0.41032332
```

```
O0014  O   0.00000000  0.00000000  0.50000000
O0015  O   0.50000000  0.50000000  0.17456767
Sr016  Sr  0.00000000  0.00000000  0.17439476
Sr017  Sr  0.50000000  0.50000000  0.11890932
O0018  O   0.00000000  0.00000000  0.11945574
#End data_Wien2k_Data
```

D.4.4. 1Ti Surface

```
data_Wien2k_Data
_cell_length_a    3.937746
_cell_length_b    3.937746
_cell_length_c   33.944806
_cell_angle_alpha   90.000000
_cell_angle_beta    90.000000
_cell_angle_gamma   90.000000
_symmetry_space_group_name_H-M         'P4/mmm '
_symmetry_space_group_number  123
loop_
_symmetry_equiv_pos_as_xyz
   +x,+y,+z
   -x,-y,-z
   -x,-y,+z
   -x,+y,-z
   -x,+y,+z
   -y,-x,-z
   -y,-x,+z
   +y,-x,-z
   +y,-x,+z
   -y,+x,-z
   -y,+x,+z
   +y,+x,-z
   +y,+x,+z
   +x,-y,-z
   +x,-y,+z
   +x,+y,-z
loop_
_atom_site_label
_atom_site_type_symbol
_atom_site_fract_x
_atom_site_fract_y
_atom_site_fract_z
Ti001  Ti  0.00000000  0.00000000  0.15838402
Ti002  Ti  0.00000000  0.00000000  0.27110949
Ti003  Ti  0.00000000  0.00000000  0.38542282
Ti004  Ti  0.00000000  0.00000000  0.50000000
Sr005  Sr  0.50000000  0.50000000  0.20835918
Sr006  Sr  0.50000000  0.50000000  0.32705745
Sr007  Sr  0.50000000  0.50000000  0.44251234
O0008  O   0.00000000  0.00000000  0.21256287
O0009  O   0.00000000  0.00000000  0.32781354
O0010  O   0.00000000  0.00000000  0.44263855
O0011  O   0.50000000  0.00000000  0.15591159
O0012  O   0.50000000  0.00000000  0.27064366
O0013  O   0.50000000  0.00000000  0.38535741
```

```
O0014  O   0.50000000  0.00000000  0.50000000
#End data_Wien2k_Data
```

D.4.5. 2Ti Surface

```
data_Wien2k_Data
_cell_length_a    3.937746
_cell_length_b    3.937746
_cell_length_c   38.744805
_cell_angle_alpha   90.000000
_cell_angle_beta    90.000000
_cell_angle_gamma   90.000000
_symmetry_space_group_name_H-M          'Pmmm   '
_symmetry_space_group_number   47
loop_
_symmetry_equiv_pos_as_xyz
   +x,+y,+z
   -x,-y,-z
   -x,-y,+z
   -x,+y,-z
   -x,+y,+z
   +x,-y,-z
   +x,-y,+z
   +x,+y,-z
loop_
_atom_site_label
_atom_site_type_symbol
_atom_site_fract_x
_atom_site_fract_y
_atom_site_fract_z
Ti001  Ti  0.00000000  0.50000000  0.63908526
O0002  O   0.50000000  0.50000000  0.62872545
O0003  O   0.00000000  0.00000000  0.64535363
Ti004  Ti  0.00000000  0.00000000  0.69578941
Ti005  Ti  0.00000000  0.00000000  0.79733290
Ti006  Ti  0.00000000  0.00000000  0.89871474
Ti007  Ti  0.00000000  0.00000000  0.00000000
Sr008  Sr  0.50000000  0.50000000  0.74687419
Sr009  Sr  0.50000000  0.50000000  0.84806570
Sr010  Sr  0.50000000  0.50000000  0.94934777
O0011  O   0.00000000  0.00000000  0.74651405
O0012  O   0.00000000  0.00000000  0.84804419
O0013  O   0.00000000  0.00000000  0.94936744
O0014  O   0.50000000  0.00000000  0.70194860
O0015  O   0.00000000  0.50000000  0.68907927
O0016  O   0.50000000  0.00000000  0.79812388
O0017  O   0.00000000  0.50000000  0.79661260
O0018  O   0.50000000  0.00000000  0.89879286
O0019  O   0.00000000  0.50000000  0.89860685
O0020  O   0.50000000  0.00000000  0.00000000
O0021  O   0.00000000  0.50000000  0.00000000
#End data_Wien2k_Data
```

D.4.6. 3Ti Surface

```
data_Wien2k_Data
_cell_length_a    3.937746
_cell_length_b    3.937746
_cell_length_c   43.744783
_cell_angle_alpha   90.000000
_cell_angle_beta    90.000000
_cell_angle_gamma   90.000000
_symmetry_space_group_name_H-M         'Pmmm   '
_symmetry_space_group_number   47
loop_
_symmetry_equiv_pos_as_xyz
   +x,+y,+z
   -x,-y,-z
   -x,-y,+z
   -x,+y,-z
   -x,+y,+z
   +x,-y,-z
   +x,-y,+z
   +x,+y,-z
loop_
_atom_site_label
_atom_site_type_symbol
_atom_site_fract_x
_atom_site_fract_y
_atom_site_fract_z
Ti001  Ti  0.00000000  0.50000000  0.67864236
O0002  O   0.50000000  0.50000000  0.67096737
O0003  O   0.00000000  0.00000000  0.68599106
Ti004  Ti  0.00000000  0.00000000  0.73109335
Ti005  Ti  0.00000000  0.00000000  0.82060188
Ti006  Ti  0.00000000  0.00000000  0.91030252
Ti007  Ti  0.00000000  0.00000000  0.00000000
Sr008  Sr  0.50000000  0.50000000  0.77563294
Sr009  Sr  0.50000000  0.50000000  0.86544849
Sr010  Sr  0.50000000  0.50000000  0.95515195
O0011  O   0.00000000  0.00000000  0.77576432
O0012  O   0.00000000  0.00000000  0.86547813
O0013  O   0.00000000  0.00000000  0.95515983
O0014  O   0.50000000  0.00000000  0.73571347
O0015  O   0.00000000  0.50000000  0.72501727
O0016  O   0.50000000  0.00000000  0.82120361
O0017  O   0.00000000  0.50000000  0.82000712
O0018  O   0.50000000  0.00000000  0.91037623
O0019  O   0.00000000  0.50000000  0.91022661
O0020  O   0.50000000  0.00000000  0.00000000
O0021  O   0.00000000  0.50000000  0.00000000
O0022  O   0.50000000  0.00000000  0.61871443
O0023  O   0.00000000  0.50000000  0.63465363
Ti024  Ti  0.50000000  0.50000000  0.62810143
#End data_Wien2k_Data
```

D.4.7. Sr_2TiO_4

```
data_Wien2k_Data
_cell_length_a    3.921750
_cell_length_b    3.921750
_cell_length_c   12.647645
_cell_angle_alpha   90.000000
_cell_angle_beta    90.000000
_cell_angle_gamma   90.000000
_symmetry_space_group_name_H-M         'I4/mmm '
_symmetry_space_group_number  139
loop_
_symmetry_equiv_pos_as_xyz
   +x,+y,+z
   +x,-y,-z
   -y,+x,-z
   -x,-y,-z
   +y,+x,-z
   -y,-x,-z
   +x,+y,-z
   +x,-y,+z
   -y,+x,+z
   +y,-x,-z
   -x,+y,-z
   -x,-y,+z
   +y,+x,+z
   -y,-x,+z
   +y,-x,+z
   -x,+y,+z
   +x+1/2,+y+1/2,+z+1/2
   +x+1/2,-y+1/2,-z+1/2
   -y+1/2,+x+1/2,-z+1/2
   -x+1/2,-y+1/2,-z+1/2
   +y+1/2,+x+1/2,-z+1/2
   -y+1/2,-x+1/2,-z+1/2
   +x+1/2,+y+1/2,-z+1/2
   +x+1/2,-y+1/2,+z+1/2
   -y+1/2,+x+1/2,+z+1/2
   +y+1/2,-x+1/2,-z+1/2
   -x+1/2,+y+1/2,-z+1/2
   -x+1/2,-y+1/2,+z+1/2
   +y+1/2,+x+1/2,+z+1/2
   -y+1/2,-x+1/2,+z+1/2
   +y+1/2,-x+1/2,+z+1/2
   -x+1/2,+y+1/2,+z+1/2
loop_
_atom_site_label
_atom_site_type_symbol
_atom_site_fract_x
_atom_site_fract_y
_atom_site_fract_z
Ti001  Ti  0.00000000  0.00000000  0.00000000
O0002  O   0.00000000  0.50000000  0.00000000
O0003  O   0.00000000  0.00000000  0.15828907
Sr004  Sr  0.00000000  0.00000000  0.35476222
```

```
#End data_Wien2k_Data
```

D.4.8. $Sr_3Ti_2O_7$

```
data_Wien2k_Data
_cell_length_a    3.934532
_cell_length_b    3.934532
_cell_length_c   20.467198
_cell_angle_alpha   90.000000
_cell_angle_beta    90.000000
_cell_angle_gamma   90.000000
_symmetry_space_group_name_H-M         'I4/mmm '
_symmetry_space_group_number  139
loop_
_symmetry_equiv_pos_as_xyz
   +x,+y,+z
   +x,-y,-z
   -y,+x,-z
   -x,-y,-z
   +y,+x,-z
   -y,-x,-z
   +x,+y,-z
   +x,-y,+z
   -y,+x,+z
   +y,-x,-z
   -x,+y,-z
   -x,-y,+z
   +y,+x,+z
   -y,-x,+z
   +y,-x,+z
   -x,+y,+z
   +x+1/2,+y+1/2,+z+1/2
   +x+1/2,-y+1/2,-z+1/2
   -y+1/2,+x+1/2,-z+1/2
   -x+1/2,-y+1/2,-z+1/2
   +y+1/2,+x+1/2,-z+1/2
   -y+1/2,-x+1/2,-z+1/2
   +x+1/2,+y+1/2,-z+1/2
   +x+1/2,-y+1/2,+z+1/2
   -y+1/2,+x+1/2,+z+1/2
   +y+1/2,-x+1/2,-z+1/2
   -x+1/2,+y+1/2,-z+1/2
   -x+1/2,-y+1/2,+z+1/2
   +y+1/2,+x+1/2,+z+1/2
   -y+1/2,-x+1/2,+z+1/2
   +y+1/2,-x+1/2,+z+1/2
   -x+1/2,+y+1/2,+z+1/2
loop_
_atom_site_label
_atom_site_type_symbol
_atom_site_fract_x
_atom_site_fract_y
_atom_site_fract_z
Ti001  Ti  0.00000000  0.00000000  0.09778388
O0002  O   0.00000000  0.00000000  0.00000000
```

```
O0003  O   0.00000000  0.50000000  0.09637586
O0004  O   0.00000000  0.00000000  0.19380359
Sr005  Sr  0.00000000  0.00000000  0.50000000
Sr006  Sr  0.00000000  0.00000000  0.31567346
#End data_Wien2k_Data
```

D.4.9. $Sr_4Ti_3O_{10}$

```
data_Wien2k_Data
_cell_length_a    3.937815
_cell_length_b    3.937815
_cell_length_c   28.330946
_cell_angle_alpha   90.000000
_cell_angle_beta    90.000000
_cell_angle_gamma   90.000000
_symmetry_space_group_name_H-M         'I4/mmm '
_symmetry_space_group_number  139
loop_
_symmetry_equiv_pos_as_xyz
   +x,+y,+z
   +x,-y,-z
   -y,+x,-z
   -x,-y,-z
   +y,+x,-z
   -y,-x,-z
   +x,+y,-z
   +x,-y,+z
   -y,+x,+z
   +y,-x,-z
   -x,+y,-z
   -x,-y,+z
   +y,+x,+z
   -y,-x,+z
   +y,-x,+z
   -x,+y,+z
   +x+1/2,+y+1/2,+z+1/2
   +x+1/2,-y+1/2,-z+1/2
   -y+1/2,+x+1/2,-z+1/2
   -x+1/2,-y+1/2,-z+1/2
   +y+1/2,+x+1/2,-z+1/2
   -y+1/2,-x+1/2,-z+1/2
   +x+1/2,+y+1/2,-z+1/2
   +x+1/2,-y+1/2,+z+1/2
   -y+1/2,+x+1/2,+z+1/2
   +y+1/2,-x+1/2,-z+1/2
   -x+1/2,+y+1/2,-z+1/2
   -x+1/2,-y+1/2,+z+1/2
   +y+1/2,+x+1/2,+z+1/2
   -y+1/2,-x+1/2,+z+1/2
   +y+1/2,-x+1/2,+z+1/2
   -x+1/2,+y+1/2,+z+1/2
loop_
_atom_site_label
_atom_site_type_symbol
_atom_site_fract_x
```

```
_atom_site_fract_y
_atom_site_fract_z
Ti001  Ti  0.00000000  0.00000000  0.00000000
Ti002  Ti  0.00000000  0.00000000  0.14037492
O0003  O   0.00000000  0.50000000  0.00000000
O0004  O   0.00000000  0.00000000  0.06951474
O0005  O   0.00000000  0.50000000  0.13911079
O0006  O   0.00000000  0.00000000  0.20947640
Sr007  Sr  0.00000000  0.00000000  0.43156980
Sr008  Sr  0.00000000  0.00000000  0.29780444
#End data_Wien2k_Data
```

D.4.10. $Sr_5Ti_4O_{13}$

```
data_Wien2k_Data
_cell_length_a    3.940580
_cell_length_b    3.940580
_cell_length_c   36.159829
_cell_angle_alpha   90.000000
_cell_angle_beta    90.000000
_cell_angle_gamma   90.000000
_symmetry_space_group_name_H-M         'I4/mmm '
_symmetry_space_group_number  139
loop_
_symmetry_equiv_pos_as_xyz
   +x,+y,+z
   +x,-y,-z
   -y,+x,-z
   -x,-y,-z
   +y,+x,-z
   -y,-x,-z
   +x,+y,-z
   +x,-y,+z
   -y,+x,+z
   +y,-x,-z
   -x,+y,-z
   -x,-y,+z
   +y,+x,+z
   -y,-x,+z
   +y,-x,+z
   -x,+y,+z
   +x+1/2,+y+1/2,+z+1/2
   +x+1/2,-y+1/2,-z+1/2
   -y+1/2,+x+1/2,-z+1/2
   -x+1/2,-y+1/2,-z+1/2
   +y+1/2,+x+1/2,-z+1/2
   -y+1/2,-x+1/2,-z+1/2
   +x+1/2,+y+1/2,-z+1/2
   +x+1/2,-y+1/2,+z+1/2
   -y+1/2,+x+1/2,+z+1/2
   +y+1/2,-x+1/2,-z+1/2
   -x+1/2,+y+1/2,-z+1/2
   -x+1/2,-y+1/2,+z+1/2
   +y+1/2,+x+1/2,+z+1/2
   -y+1/2,-x+1/2,+z+1/2
```

```
   +y+1/2,-x+1/2,+z+1/2
   -x+1/2,+y+1/2,+z+1/2
loop_
_atom_site_label
_atom_site_type_symbol
_atom_site_fract_x
_atom_site_fract_y
_atom_site_fract_z
Ti001  Ti  0.00000000  0.00000000  0.05450138
O0002  O   0.00000000  0.00000000  0.00000000
O0003  O   0.00000000  0.50000000  0.05437101
O0004  O   0.00000000  0.00000000  0.10880245
Sr005  Sr  0.00000000  0.00000000  0.50000000
Sr006  Sr  0.50000000  0.50000000  0.10782912
Ti007  Ti  0.00000000  0.00000000  0.16431243
O0008  O   0.00000000  0.50000000  0.16331275
O0009  O   0.00000000  0.00000000  0.21832802
Sr010  Sr  0.50000000  0.50000000  0.21266564
#End data_Wien2k_Data
```

D.4.11. $SrTi_2O_5$

```
data_Wien2k_Data
_cell_length_a    3.946382
_cell_length_b    3.883240
_cell_length_c   12.377643
_cell_angle_alpha   90.000000
_cell_angle_beta    90.000000
_cell_angle_gamma   90.000000
_symmetry_space_group_name_H-M          'Pmmm   '
_symmetry_space_group_number   47
loop_
_symmetry_equiv_pos_as_xyz
   +x,+y,+z
   -x,-y,-z
   -x,-y,+z
   -x,+y,-z
   -x,+y,+z
   +x,-y,-z
   +x,-y,+z
   +x,+y,-z
loop_
_atom_site_label
_atom_site_type_symbol
_atom_site_fract_x
_atom_site_fract_y
_atom_site_fract_z
Sr001  Sr  0.50000000  0.50000000  0.00000000
O0002  O   0.00000000  0.00000000  0.00000000
O0003  O   0.50000000  0.00000000  0.17507884
Ti004  Ti  0.50000000  0.00000000  0.34183921
Sr005  Sr  0.00000000  0.50000000  0.50000000
Ti006  Ti  0.00000000  0.00000000  0.15810654
O0007  O   0.00000000  0.50000000  0.14416807
O0008  O   0.00000000  0.00000000  0.32481364
```

```
O0009  O   0.50000000  0.50000000  0.35581336
O0010  O   0.50000000  0.00000000  0.50000000
#End data_Wien2k_Data
```

D.4.12. $Sr_2Ti_3O_8$

```
data_Wien2k_Data
_cell_length_a    3.966998
_cell_length_b    3.887658
_cell_length_c   20.471371
_cell_angle_alpha   90.000000
_cell_angle_beta    90.000000
_cell_angle_gamma   90.000000
_symmetry_space_group_name_H-M         'Pmmm   '
_symmetry_space_group_number   47
loop_
_symmetry_equiv_pos_as_xyz
   +x,+y,+z
   -x,-y,-z
   -x,-y,+z
   -x,+y,-z
   -x,+y,+z
   +x,-y,-z
   +x,-y,+z
   +x,+y,-z
loop_
_atom_site_label
_atom_site_type_symbol
_atom_site_fract_x
_atom_site_fract_y
_atom_site_fract_z
Sr001  Sr  0.00000000  0.50000000  0.09849493
O0002  O   0.00000000  0.00000000  0.00000000
O0003  O   0.50000000  0.00000000  0.09749132
O0004  O   0.00000000  0.00000000  0.20526811
Ti005  Ti  0.00000000  0.00000000  0.50000000
Ti006  Ti  0.00000000  0.00000000  0.30638017
Ti007  Ti  0.50000000  0.00000000  0.00000000
Ti008  Ti  0.50000000  0.00000000  0.19373951
Sr009  Sr  0.50000000  0.50000000  0.40120605
O0010  O   0.50000000  0.00000000  0.50000000
O0011  O   0.00000000  0.50000000  0.50000000
O0012  O   0.00000000  0.50000000  0.31556857
O0013  O   0.50000000  0.00000000  0.29489102
O0014  O   0.50000000  0.50000000  0.18442715
O0015  O   0.00000000  0.00000000  0.40247253
O0016  O   0.50000000  0.50000000  0.00000000
#End data_Wien2k_Data
```

D.4.13. $Sr_3Ti_4O_{11}$

```
data_Wien2k_Data
_cell_length_a    3.899187
_cell_length_b    3.938178
_cell_length_c   28.180045
_cell_angle_alpha   90.000000
```

```
_cell_angle_beta    90.000000
_cell_angle_gamma   90.000000
_symmetry_space_group_name_H-M          'Pmmm   '
_symmetry_space_group_number   47
loop_
_symmetry_equiv_pos_as_xyz
   +x,+y,+z
   -x,-y,+z
   -x,+y,-z
   +x,-y,-z
   -x,-y,-z
   +x,+y,-z
   +x,-y,+z
   -x,+y,+z
loop_
_atom_site_label
_atom_site_type_symbol
_atom_site_fract_x
_atom_site_fract_y
_atom_site_fract_z
O0001  O   0.00000000  0.00000000  0.00000000
O0002  O   0.00000000  0.00000000  0.14010349
O0003  O   0.50000000  0.00000000  0.06925863
O0004  O   0.50000000  0.00000000  0.20262297
O0005  O   0.00000000  0.00000000  0.42918545
O0006  O   0.50000000  0.50000000  0.29736369
O0007  O   0.00000000  0.50000000  0.07083657
O0008  O   0.00000000  0.50000000  0.21802460
O0009  O   0.00000000  0.00000000  0.28196768
O0010  O   0.00000000  0.50000000  0.50000000
O0011  O   0.00000000  0.50000000  0.35985374
O0012  O   0.50000000  0.50000000  0.43080559
Sr013  Sr  0.50000000  0.00000000  0.50000000
Sr014  Sr  0.50000000  0.50000000  0.00000000
Sr015  Sr  0.50000000  0.50000000  0.14142334
Sr016  Sr  0.50000000  0.00000000  0.35863694
Ti017  Ti  0.00000000  0.00000000  0.06985751
Ti018  Ti  0.00000000  0.50000000  0.29076370
Ti019  Ti  0.00000000  0.00000000  0.20918198
Ti020  Ti  0.00000000  0.50000000  0.43013946
#End data_Wien2k_Data
```